



## DISSERTATION

# **Micropore evolution in polymer-derived ceramics**

ausgeführt zum Zwecke der Erlangung des akademischen Grades einer

Doktorin der technischen Wissenschaften

unter der Leitung von

Dr. Thomas Konegger und Prof. Dr. Roland Haubner

164-03-CT, Institut für Chemische Technologien und Analytik

eingereicht an der Technischen Universität Wien

Fakultät für Technische Chemie

von

**Dipl.-Ing. Christina Drechsel, BSc.**

1027201

Wien, Mai 2021

## ACKNOWLEDGEMENTS

First of all, I want to thank my supervisors Thomas Konegger and Roland Haubner for giving me the opportunity to do my PhD thesis at the Institute of Chemical Technologies and Analytics at the TU Wien. As I already got to know him from my time at the institute during my master's thesis, Thomas was always kind and friendly, dedicated and always had time and an open ear for me, when necessary.

Also, I want to thank Rajendra Bordia, who welcomed me to his research group at Clemson University for a research stay in spring 2018, which gave me the opportunity to benefit from the excellent equipment and his expertise, as well as on a personal level from the many friendships I was able to make during my stay, including Michelle Greenough, who helped me with the laboratory work during my stay.

I am very thankful for Herwig Peterliks (and his research groups) help with the SAXS investigations, especially the in-situ SAXS measurements, which were time- and energyconsuming, but made it possible to manage a novel type of pore formation observation under pyrolysis conditions.

For the help with various analyses I want to thank....

...Christian Gierl-Mayer for the TGA-MS measurements

.... Klaudia Hradil and Werner Artner for their help with the PDF measurements

...Christian Hametner and Michael Puchberger for the NMR measurements

...Bernhard Lendl for the access to IR measurements

and the research group around Karin Föttinger, which provided the possibility of physisorption measurements.

I am grateful for the funding by the Austrian Science Fund (FWF): P29058-N34, making this project possible.

Also, I want to thank the Christiana-Hörbiger-Award, which funded a great part of my research stay at the Clemson University.

And last but not least my friends and family, who supported me in all possible ways during the time of my thesis. This includes also my colleagues at the institute, who made the recent years a joyful and exciting experience, while sharing all ups and downs.

## ABSTRACT

Polymer-derived ceramics have become an interesting material for many applications, including separation processes, due to microporosity forming during the polymer-ceramic-conversion. The identification of reactions and mechanisms leading to the formation of transient pores in two commercially available precursors is supposed to contribute towards a deeper understanding of the generation of porosity in polymer-derived ceramics in general. By systematically varying parameters during all processing stages and in-depth characterization of the samples regarding elemental composition, structural evolution (IR, NMR, PDF), pore characteristics (gas sorption, SAXS) and decomposition behaviour (TGA-MS), correlations between processing and pore size and –stability shall be clarified. Modification in the polymer stage was performed by testing the influence of an increased molecular weight as well as copolymerisation with styrene. The precursor structure itself was modified by substitution with different organic side groups. The changes during the crosslinking process involve the type and amount of initiator and different crosslinking mechanisms such as thermally induced crosslinking and hydrosilylation with linker molecules. Pyrolysis experiments were conducted at temperatures as high as 900 °C under inert (N<sub>2</sub>) or reactive (NH<sub>3</sub>) atmosphere.

The modifications of the precursor were successful. Yet, they had only minor effects on the microporosity. The same is true for the crosslinking step, except for the hydrosilylation experiments, which showed an influence of the linker molecule divinylbenzene DVB on the decomposition behaviour, resulting in different composition, structural features and a shift of the micropore size to smaller values. The pyrolysis atmosphere had the strongest influence on the microporosity, which can be retained up to the highest pyrolysis temperatures of 900 °C if ammonia is used. The elemental composition of the different starting materials converges through reaction with ammonia resulting in the same pore size, independent of the starting material. All the above-mentioned findings show, that the micropore size is not already determined by the structure of the precursor. Due to the differences in decomposition behaviour, the elemental composition of the micropore forming entities changes and consequently changes the pore size. All these processes were additionally investigated and confirmed using innovative in-situ SAXS measurements, simulating the pyrolysis under gas flow. The elemental composition of micropore forming entities in the material during the polymer-ceramic conversion plays the major role in the micropore formation, which can be predefined by the precursor, but adjusted using different pyrolysis atmospheres. These findings are a step towards the clarification of pore generation in PDCs which is crucial for future applications.

## KURZFASSUNG

Polymer-abgeleitete Keramiken (PDCs) sind vielversprechende Materialien für verschiedenste Anwendungsbereiche, durch die während der Umwandlung entstehende Mikroporosität auch für den Bereich der (Gas-)trennung. Die Mechanismen der Porenentwicklung in polymer-abgeleiteter Keramik wurden anhand zweier kommerziell erhältlicher Prekursoren, einem Polyvinylsilazan PSZ und einem Polycarbosilan PCS untersucht. Parameter während der Prozessierung wurden systematisch verändert, und durch simultane umfassende Charakterisierung hinsichtlich Zusammensetzung, Struktur (IR, NMR, PDF) und Porenstruktur (Physisorption, SAXS) sowie Zersetzungverhalten (TGA-MS), sollten Zusammenhänge mit Porengröße und –stabilität gefunden werden. Dadurch wird ein generelles tieferes Verständnis der Porenentwicklung in PDCs angestrebt. Nach Charakterisierung der Ausgangsmaterialien, wurden Veränderungen im Polymerstadium, wie die Erhöhung des Molekulargewichts, Copolymerisation, sowie Substitution der N-H Gruppe mit organischen Resten untersucht. Die Untersuchungen im Vernetzungsschritt beliefen sich auf Typ und Menge des Initiators und Änderung des Mechanismus zu rein thermisch induzierter Vernetzung bzw. Hydrosilylierung mit verschiedenen Linkern. Pyrolyseversuche wurden bis zu Temperaturen von 900 °C unter inerter (N<sub>2</sub>) sowie reaktiver (NH<sub>3</sub>) Atmosphäre durchgeführt.

Die Modifikationen im Polymerstadium waren erfolgreich, zeigten aber nur geringe Auswirkungen auf die Mikroporosität. Ebenso konnte im Vernetzungsschritt nur durch Änderung des Mechanismus und Einsatz von Divinylbenzol als Linker eine Änderung des Zersetzungsverhaltens und daraus resultierend eine veränderte Zusammensetzung, chemische Struktur und eine Verschiebung des Maximums der Porengröße festgestellt werden. Die größten Unterschiede konnten durch eine reaktive Pyrolyseatmosphäre erreicht werden, die zu Mikroporosität in allen Proben bis 900 °C führte. Gemeinsam mit einer Angleichung der elementaren Zusammensetzung im fortschreitenden Pyrolyseprozess, konnte auch eine annähernd gleiche Porengröße unabhängig vom Startmaterial gefunden werden. Die Ergebnisse wurden durch neuartige in-situ SAXS Untersuchungen, die die Pyrolyse unter Gasfluss simulieren, bestätigt, die klare Unterschiede in der Porenentwicklung je nach Atmosphäre zeigen. Die Ergebnisse zeigen, dass die Zusammensetzung von porenbildenden strukturellen Einheiten, die durch den Precursor vordefiniert und durch die Pyrolyseatmosphäre beeinflusst werden kann, im Temperaturbereich der tatsächlichen Zersetzung entscheidend ist. Diese Ergebnisse stellen einen wichtigen Schritt in Richtung der Aufklärung der Porenentwicklung in PDCs dar, die ein entscheidender Faktor für zukünftige Anwendungen ist.



# TABLE OF CONTENTS

Acknowledgements .....	2
Abstract.....	3
Kurzfassung.....	4
1. Introduction .....	1
2. Objectives of this work.....	3
3. Systematic approach and structure of this work.....	4
4. Theoretical Background .....	6
4.1 Polymer derived ceramics .....	6
4.2 Processing of PDCs.....	7
4.3 Preceramic polymers .....	7
4.4 Crosslinking .....	10
4.5 Polymer-ceramic conversion.....	12
4.6 Porosity in PDCs.....	16
4.7 Applications of PDCs.....	16
4.8 Historical overview of research fields of PDCs.....	18
4.9 Pore characterization of microporous materials.....	23
5. Experimental Procedure .....	30
5.1 Materials.....	30
5.2 Processing .....	31
5.3 Characterization methods.....	32
6. FOCUS I – CHARACTERIZATION OF THE UNALTERED PRECURSORS.....	37
6.1 Experimental Procedure – Focus I.....	37
6.2 Results and Discussion – Focus I.....	37
6.3 Summary and conclusions – Focus I.....	63
7. FOCUS II – MODIFICATION IN THE PRECURSOR STAGE BY INCREASE OF MOLECULAR WEIGHT AND COPOLYMERISATION.....	64

7.1	Experimental Procedure – Focus II.....	64
7.2	Results – Focus II.....	65
7.3	Conclusions – Focus II.....	75
8.	FOCUS III – MODIFICATIONS OF THE PRECURSOR BY INCORPORATION OF ORGANIC SIDEGROUPS .....	76
8.1	Experimental Procedure – Focus III .....	76
8.2	Results – Focus III .....	79
8.3	Conclusions – Focus III .....	99
9.	FOCUS IV – MODIFICATIONS DURING THE CROSSLINKING STEP .....	100
9.1	Experimental procedure – Focus IV .....	100
9.2	Results – Focus IV .....	102
9.3	Conclusions – Focus IV .....	146
10.	FOCUS V – EFFECT OF PYROLYSIS CONDITIONS ON MICROPOROUS FORMATION IN POLYMER-DERIVED CERAMICS.....	147
10.1	Experimental Procedure - Focus V.....	147
10.2	Results - Pyrolysis in nitrogen atmosphere .....	149
10.3	Conclusions - Pyrolysis in nitrogen atmosphere .....	160
10.4	Results - Pyrolysis in diluted ammonia.....	161
10.5	Conclusions - Pyrolysis in diluted ammonia.....	175
10.6	Results - Pyrolysis in concentrated ammonia.....	176
10.7	Conclusions - Pyrolysis in concentrated ammonia.....	199
10.8	Results - Further pyrolysis experiments with 80DVB in nitrogen.....	201
10.9	Conclusions - Pyrolysis experiments with 80DVB.....	208
11.	FOCUS VI – IN SITU SAXS INVESTIGATIONS.....	209
11.1	Design of the sample holder .....	209
11.2	Experimental procedure – Focus VI.....	213
11.3	Results – Focus VI.....	213
11.4	Conclusions – Focus VI.....	218

12.	FOCUS VII – STABILITY AGAINST OXIDATION .....	219
12.1	Experimental procedure – Focus VII .....	219
12.2	Results – Focus VII .....	220
12.3	Conclusions – Focus VII .....	226
13.	Summary .....	227
13.1	Focus I – Unaltered Precursors.....	227
13.2	Focus II and III - Modifications in the precursor stage .....	227
13.3	Focus IV – Modifications in the crosslinking stage .....	228
13.4	Focus V and VI – Effect of pyrolysis conditions on the microporosity .....	230
13.5	Focus VII - Oxidation stability .....	233
14.	Conclusions.....	234
15.	Outlook .....	236
	References .....	237
	CV - Christina Drechsel .....	243

## 1. INTRODUCTION

Recently, there was a rise in public awareness for environmental problems, leading to intensive research towards renewable energy generation and sustainability. An important role plays the improvement of catalysis or separation processes, which could lead e.g. to the reduction of process temperatures, a decrease in processing steps or longer life time of parts. This often goes along with increasing requirements regarding the materials used, which have to withstand high mechanical, thermal and chemical stresses. Ceramics fulfil most requirements due to their excellent high temperature properties regarding mechanical and chemical stability and creep resistance, especially in comparison to metal or polymeric alternatives.

For applications in separation processes or as catalyst support, porous ceramics are promising candidates, especially non-oxide ceramics due to even superior high temperature mechanical properties and oxidation resistance. Besides the traditional powder based processing of ceramics, which is rather difficult in case of non-oxide ceramics, a new field of research arose in the last decades, the development of polymer-derived ceramics. A typically silicon based polymer, like a polysiloxane, polysilazane or polycarbosilane, is used as precursor depending on the elements that shall be present in the resulting ceramic in which it is then converted via pyrolysis. These provide an interesting alternative to powder based processing, since a polymer is used as starting compound, which can easily be shaped and is converted to a ceramic afterwards. Besides advantages in processing, this approach also makes new materials systems, like mixed non-oxide ceramics (e.g. SiCN), accessible by variation of the precursor composition, at relatively low processing temperatures. While the initial research was done on the production of SiC fibers by Yajima et al. [1], the advantages of PDCs, like easy shaping, low process temperatures and accessibility of new materials systems, led to their application in a variety of fields, but usually only in special applications, which cannot be achieved using the powder based route, like fibers, coatings or MEMS. [2-6]

An additional phenomenon that makes PDCs interesting candidates for the application in separation processes is the development of microporosity during the polymer-ceramic conversion. Together with the excellent high temperature properties, they thereby become interesting candidates for (hot) gas separation membranes, e.g. in hydrogen separation in steam reforming processes. [7-11] Unfortunately, the micropores collapse or become inaccessible if pyrolysis is conducted in an inert atmosphere. [12] This led to intense research towards stabilization of the porosity up to higher temperatures. Major work in this direction was performed by Dismukes et al. [13], who presented different approaches for increased pore

stability, including the use of fillers or instruction of metals in the ceramic, as well as the use of ammonia as reactive pyrolysis atmosphere, which led to ceramics with very high specific surface areas up to several hundred m<sup>2</sup>/g. These strategies were further investigated e.g. by Schitco et al. [14, 15] who conducted an extensive study on the influence of ammonia on the microstructure and porosity of ceramics derived from three of the most popular precursor types (polysiloxanes, -carbosilanes, -silazanes). Also, the approach using metal particles was further investigated. [16-19]

Not only the stability of pores, but also a well-defined and tailorable pore size is a crucial factor for prospective applications in separation processes. Therefore, it is necessary to understand the mechanisms underlying the pore formation in PDCs. Understanding the processes occurring during the polymer-ceramic conversion led to several works focusing on the clarification of the reactions taking place during pyrolysis of different precursors. [20-25] Still, the correlation between reactions and origin of the micropores is not fully understood yet, which can also be attributed to the structural variety of precursor polymers. Still, hypotheses are made, seeing the origin of the pores in the release of gaseous species during the decomposition [26], or in the composition of micropore forming entities that can already be present in the precursor. [14]

Therefore, the aim of this work is the clarification of mechanisms responsible for the pore formation in PDCs, by detailed investigation of the effect of different processing conditions on the pore structure of ceramics derived from two commercially available precursors of different material classes, but both yielding amorphous non-oxide ceramics, a polyvinylsilazane and a polycarbosilane.

After characterization of the unaltered precursors, modification shall take place in all processing stages, from the polymeric state, over crosslinking to the pyrolysis step, which will all be dealt with in separate parts of this work, to keep a better overview. Additional chapters will focus on the stability testing of promising samples, testing the pore stability under conditions which come closer to those of prospective applications, as well as on in-situ SAXS measurements, which provide a novel method, developed in this work, to simulate the pyrolysis conditions, by both increase of temperature and constant gas flow, even of aggressive gases, up to 900 °C and therefore provide a unique possibility to in-situ observe the pore formation in PDCs under different conditions.

## 2. OBJECTIVES OF THIS WORK

This work is part of a project funded by the FWF, dedicated to the clarification of micropore formation in polymer-derived ceramics.

The specific objectives of this thesis lie on the

- **systematic investigation of the micropore formation in two commercially available precursor polymers**, a poly(vinyl)silazane PSZ (Durazane 1800, DurXtreme GmbH) and an allylhydridopolycarbosilane PCS (SMP-10, Starfire Systems)
- **...by varying parameters in all processing stages** (precursor structure, crosslinking, pyrolysis), such as the precursor composition and the modification of the precursors using different organic sidegroups, the variation of crosslinking mechanisms and introduction of other species into the crosslinked network, and change of pyrolysis temperature and atmosphere
- **...and thorough characterization of the materials** using various methods such as elemental analysis and structural investigations (NMR, ATR-IR, PDF) combined with analyses regarding the porosity (gas sorption, SAXS) and the decomposition behaviour (TGA-MS)
- **...to find correlations between processing conditions and the pore size/ pore stability in the resulting ceramics** and eventually enable tailoring of the micropore size.
- **Investigation of the stability of the materials under harsh conditions**, which are application-inspired.

### 3. SYSTEMATIC APPROACH AND STRUCTURE OF THIS WORK

There are several hypotheses about the origin of the micropores, which will be tested in this work, which are also displayed in Figure 1.

- The micropore size is predefined by the structural elements in the precursor.
- The pores are caused simply by the release of gaseous species during the polymer-ceramic conversion, independent of the structural arrangements in the material. [26]
- There are certain micropore forming entities, which, depending on the elemental composition, yield different pore sizes. [14]
- Voids that are forming during crosslinking of the polymer chains are responsible for the micropores.

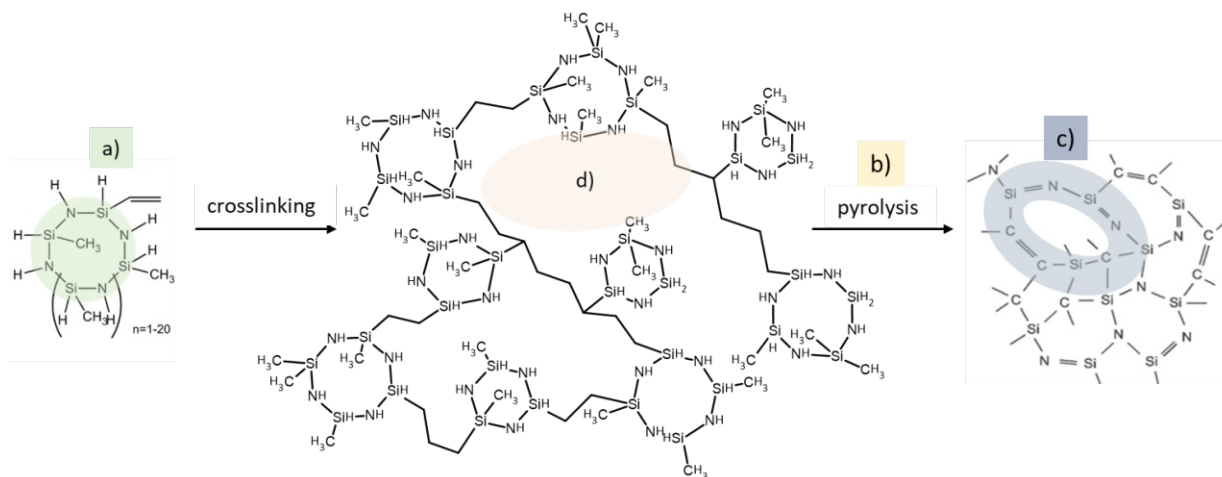


Figure 1: Schematic illustration of the processing stages from precursor polymer to PDC; the highlighted areas showing where the pores would originate from if a) they are already present in the precursor b) they were caused simply by the release of gaseous species during pyrolysis c) their size is defined by the composition of micropore forming entities d) they are caused by the voids that form during crosslinking.

The above-mentioned points will be tested by experiments in all processing stages:

**Focus I:** Detailed investigations of benchmark samples to have a base for the following investigations. Implementation of all testing methods and handling steps.

**Focus II:** Modification of the precursors before heat treatments of any kind are conducted, increase of molecular weight and copolymerization with PS. → Testing of hypotheses a) and d)

**Focus III:** Modification of the precursors by introduction of organic side groups of different size, e.g. aliphatic chains, aromatic species, ... These groups could serve as template for pores. If successful, this modification could help to custom tailor the pore size for any desired application. → Testing of hypotheses a) and d)

**Focus IV:** Modification of the precursors during the crosslinking step by a change of initiator and initiator concentration, which could lead to a different crosslinking density and therefore different composition behavior. Secondly, a change of the crosslinking mechanism to hydrosilylation is conducted. Since different bonds are forming during crosslinking, this focus tests hypotheses b),c) and d) The use of two different linker molecules causes bigger voids in the crosslinked material and therefore is a measure for the applicability of all four mentioned hypotheses.

**Focus V and Focus VI:** Pyrolysis conditions are varied by using a reactive atmosphere vs. an inert atmosphere. By checking at which temperatures the pores evolve in different materials, especially in modifications of the benchmark material, the reactions leading to the formation can possibly be revealed, together with in-situ observation of the pore formation in different atmospheres. → Testing of all four hypotheses.

**Focus VII:** Oxidation stability – The stability against oxidation of selected microporous samples will be tested in conditions close to those of prospective applications.



## 4. THEORETICAL BACKGROUND

In the following subchapters, background information about polymer-derived ceramics will be given, focusing on typical processing, from precursors to thermal conversion and applications as well as an overview on the research of PDCs since their upcome in the 1970ies. Additionally, a short introduction in characterization methods for microporous materials will be given.

### 4.1 Polymer derived ceramics

Polymer-derived ceramics (PDCs) are a new class of ceramic materials, gaining a lot of interest in the last decades. In contrast to the traditional powder based route, ceramics are produced by pyrolysis of appropriate polymeric precursors. The initial application was the production of SiC fibers, for which Yajima presented a process using polycarbosilanes as precursor in the 70ies.[1] Ever since then, intense research was performed to make this processing route suitable for various special applications, which are difficult or impossible to accomplish by the powder based route. The polymer-derived processing route has several advantages compared to the powder based route, such as:

- **Flexibility in shaping**

Since the starting compound is a polymer, processing is much easier. The precursor is usually either liquid, meltable or soluble, making the production of even complex shapes realizable. This simplifies the production of ceramic fibers or coatings, or e.g. applications in the field of micro-electro-mechanical systems MEMS. [2, 5, 6, 27-32]

- **Accessibility of new materials systems**

By changing the elements present in the precursor, the composition of the resulting ceramics is predefined and can be further influenced by the pyrolysis conditions. Additionally, it is possible to introduce metal particles into the ceramics, further influencing their properties.

- **Low processing temperatures**

Depending on the application, the pyrolysis temperature can lie drastically below the sintering temperature of comparable materials. For amorphous siliconcarbonitrides e.g. temperatures around 800 °C are used, whereas the sintering temperature for silicon nitride is around 1700 °C, not to mention the need for sintering aids, leading to a lower purity and therefore poorer properties of the ceramic. [6]

Due to drawbacks like high costs of the precursors and more complicated handling of the precursors, e.g. due to sensitivity towards hydrolysis, PDCs are rather used for special fields of applications, where the powder route doesn't lead to satisfactory results.

## 4.2 Processing of PDCs

The temperature depending steps of the PDC route are shown in Figure 2. After synthesizing or buying a precursor with the desired composition, the molecular weight is increased by polymerisation and crosslinking at rather low temperatures, before the actual polymer-ceramic conversion is performed starting at intermediate temperatures between 400 °C and ~1000 °C. In this temperature region, the ceramics are in the transition from polymers to ceramics, so called *ceramers*, with the organic groups splitting off and being released as small gaseous species, yielding amorphous ceramics in the end. These then crystallize at temperatures above 1000 °C. Shaping usually is performed in the polymer stage and the shape then fixated by crosslinking, before converting it into a ceramic.

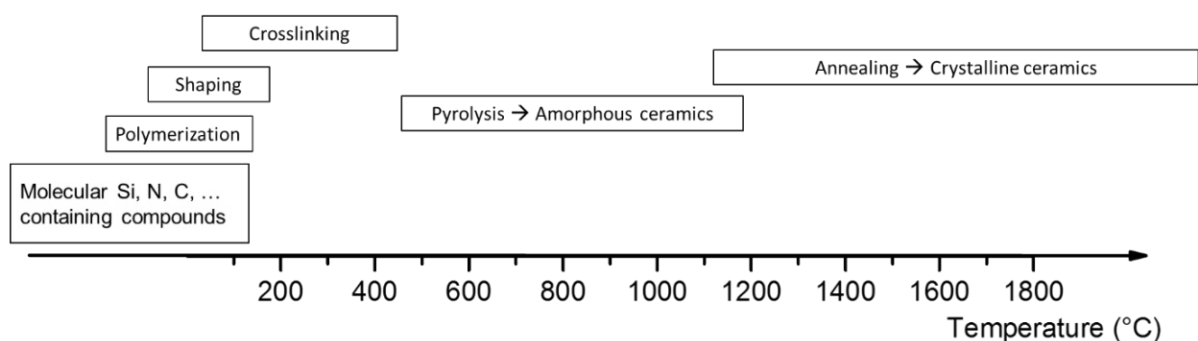


Figure 2: Processing steps of PDCs in the various temperature ranges, after [6].

## 4.3 Preceramic polymers

The most investigated precursors are silicon based, possibly containing hetero elements in the backbone or sidegroups. The classes of silicon based precursors are displayed in Figure 3, with the most popular heteroelements oxygen, carbon, nitrogen and in more special cases boron, yielding amorphous SiBCNO ceramics. The elemental composition and structural features of the precursor therefore predefine the elemental composition of the final ceramic and furthermore the phases and amounts of phases present. The design and choice of precursors therefore play a crucial role in PDCs.

The synthesis of silicon based polymers typically uses organochlorosilanes as starting compound and, by reaction with different species, leads to the classes shown in Figure 3, with some examples of the synthesis routes shown in Figure 4. The generally best investigated class of silicon-based polymers, polysiloxanes, are for example synthesized using water in reaction with organochlorosilanes with HCl as byproduct. Polysilazanes are prepared by reaction of the organochlorosilanes with ammonia and ammoniumchloride as byproduct.

Generally, preceramic polymers have to fulfil several requirements to be suitable for the PDC route. Since the ceramic yield is supposed to be as high as possible, the polymers need to have a sufficiently high molecular weight to prevent distillation of low molecular weight compounds in the lower temperature range. Still, the rheological behaviour has to be appropriate for the desired shaping process, and/or the polymer should be soluble. Furthermore, it is beneficial to have reactive side groups as some of the side chains, to enable crosslinking of the polymer once it is in the final shape and therefore retaining the shape during further processing and additionally increasing the ceramic yield by reducing the amount of low molecular weight compounds.[6]

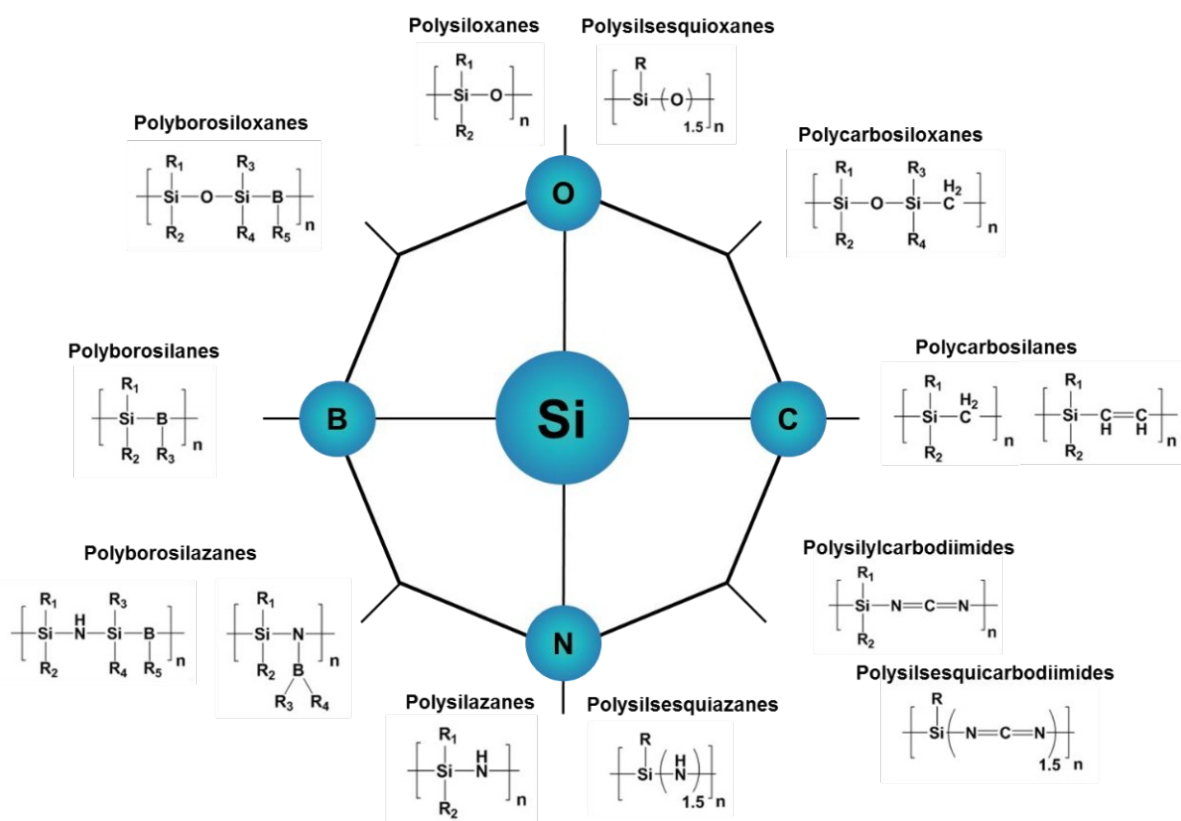


Figure 3: Scheme of silicon based precursor types and the elements present in the resulting ceramics, after [6].



#### 4.4 Crosslinking

As mentioned in the previous subchapter, crosslinking of the preceramic polymers plays a crucial role, on the one hand to fix the shape of the product and retain it during pyrolysis, and on the other hand to increase the ceramic yield by reducing the distillation of low molecular weight compounds by integrating them in the crosslinked network, which also causes less fragmentation during the polymer-ceramic conversion.

Depending on the structure of the precursor as well as the requirements on the final ceramic, various crosslinking methods are possible. An overview is listed below:

– **Oxidative crosslinking**

If oxygen is present, radical mechanisms may take place, leading to the formation of Si-O-Si, Si-OH and C=O units. The resulting ceramics exhibit high oxygen contents, which can be a drawback in several applications, since the mechanical stability at high temperatures is lower compared to pure non oxide ceramics. [27] The reactions occurring – started by the formation of a radical – are shown in Figure 5.

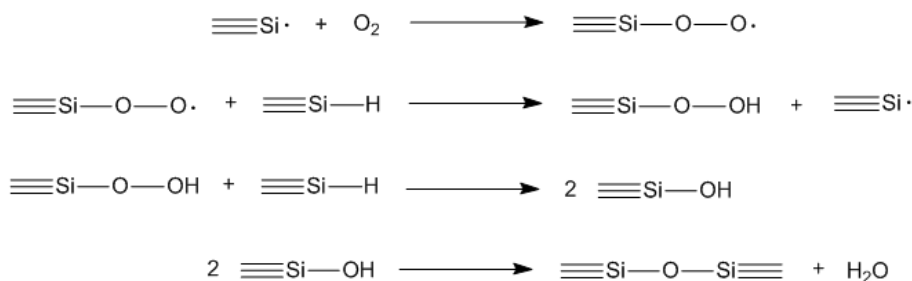


Figure 5: Oxidative crosslinking exemplarily shown for polycarbosilanes.

– **Irradiation with an E-beam**

Using irradiation with an electron-beam (or a  $\gamma$ -radiation), which usually is carried out in vacuum, the formation of radicals is initiated, leading to crosslinking of the polymers without significant oxygen contamination, e.g. in case of polycarbosilanes. The applicability of this method is limited by the size of the parts, since the penetration depth of the beam is limited. [27]

– **Thermal crosslinking**

Depending on the functional groups available in the preceramic polymer, several thermally induced reactions occur, leading to crosslinking between the polymers and formation of a stable network. Already around 100 °C, so called hydrosilylation can occur if Si-H bonds and unsaturated hydrocarbons are present. The reaction, which is also shown in Figure 6, leads to saturated Si-C bonds without any mass loss or byproducts. To promote these reactions, it is beneficial to use a catalyst, which is typically Pd-based. At temperatures up to ~400 °C, transamination reactions can take place, if polysilazanes are used. These reactions, which are shown in Figure 7, include chain scission and formation of new connections under release of ammonia. In presence of vinyl groups, their addition to saturated CH<sub>2</sub>-chains can be induced thermally around 300 °C (Figure 8). The temperature can be significantly lowered by adding a radical initiator, such as peroxides. Another type of reactions taking place at elevated temperatures are dehydrocoupling reactions under formation of Si-Si or Si-N (the latter one only if N-H groups are present in the precursor) and release of hydrogen, which are shown in Figure 9.

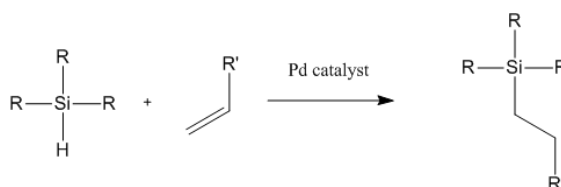


Figure 6: Schematic display of hydrosilylation reactions.

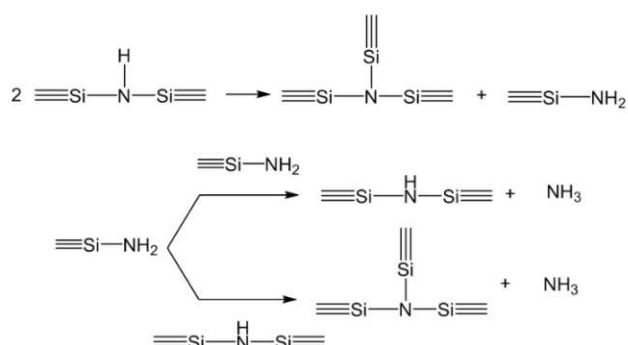


Figure 7: Schematic display of transamination reactions under release of ammonia, after [21].

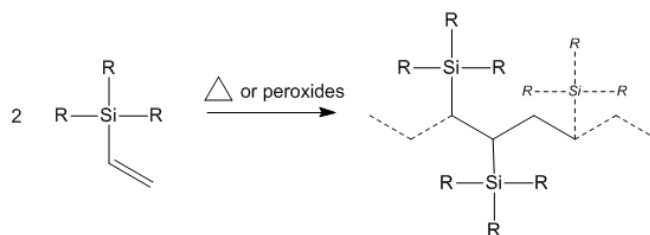


Figure 8: Polyaddition in presence of vinylgroups, thermally or radically induced.

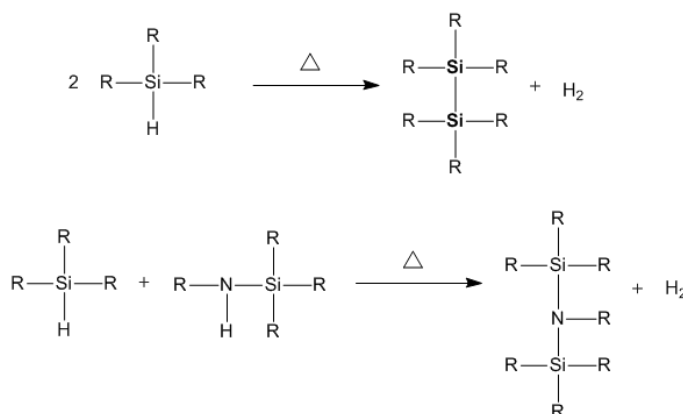


Figure 9: Dehydrocoupling reactions.

## 4.5 Polymer-ceramic conversion

While the dominant processes in the lower temperature range up to  $\sim 500$  °C are a competition between crosslinking and distillation of low molecular weight compounds, the actual ceramization of the polymers takes place at temperatures around 400-1000 °C, under release of various small gaseous species and formation of amorphous ceramics. During this conversion process, the material is somewhere inbetween a polymer and a ceramic, which is the origin of the often used term *ceramers*. Much work was done to clarify the reactions taking place during this conversion, with the different types of precursors and different structures and sidegroups making these investigations complex and difficult. [23, 26, 33, 34]

The possible reactions and therefore the released gases are strongly dependant on the precursor structure. Typically, the main evolving species during this part of the thermal decomposition are methane and hydrogen, together with other small C-containing species. Typical reactions of a polysilazane are the formation of methane and other hydrocarbons by nucleophilic substitutions between N-H and Si-R moieties or dehydrogenation between Si-H and N-H

leading to hydrogen formation. Hydrogen can also originate from the decomposition of contiguous Si-H and N-H bonds leading to hydrogen and an intermediate species, a silylimine, which then inserts into a Si-H or N-H bond. Due to the high temperatures during pyrolysis, there are most likely also radical reactions taking place. In case of methane and other hydrocarbons it is the radical cleavage of Si-CH<sub>3</sub> bonds followed by H abstraction. Hydrogen evolves through homolytic cleavage of Si-H, N-H and C-H bonds again followed by H abstraction. [20-22, 33]

A suggested mechanism for a polysilazane was proposed by Kroke et al. [26] which is shown in Figure 10. In addition a decomposition mechanism in presence of vinyl groups present in the polymer is shown in Figure 11, which leads to the formation of additional free carbon in the sample.



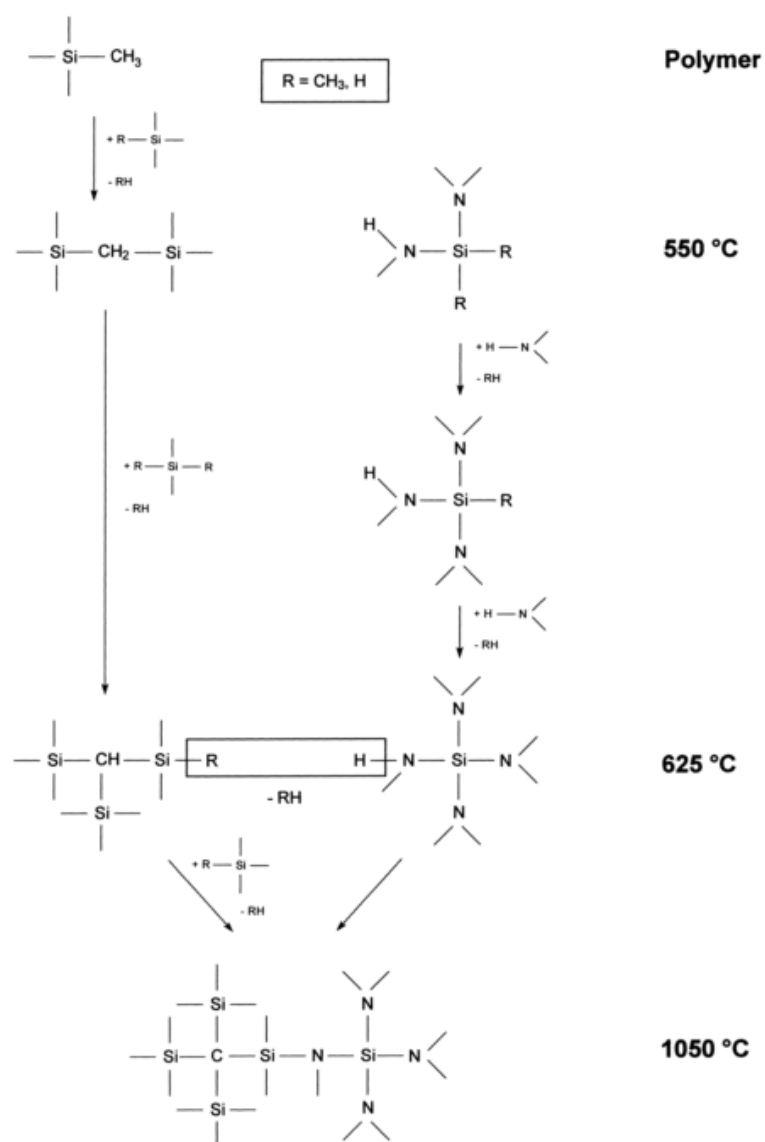


Figure 10: Reaction during decomposition of polysilazanes, reprinted with permission by the publisher [26]

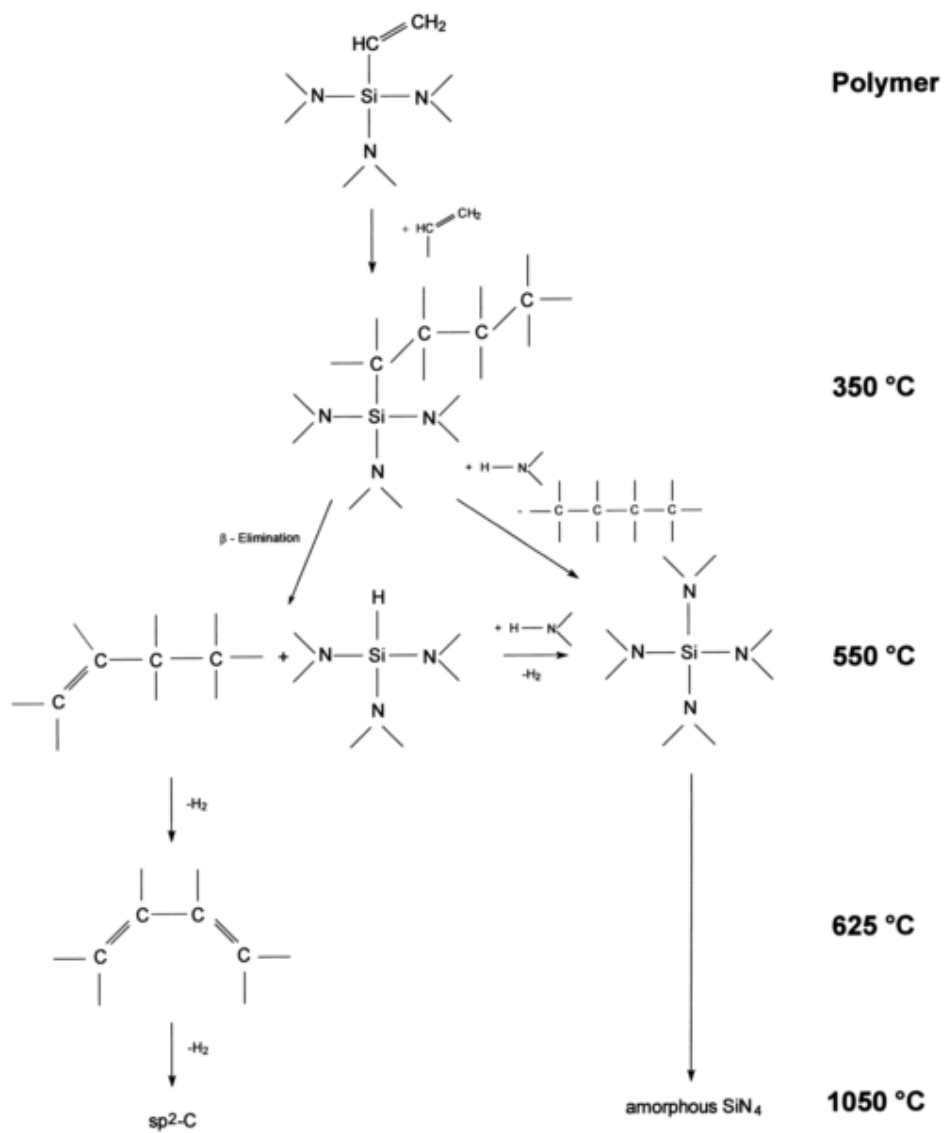


Figure 11: reactions during the decomposition of a polyvinylsilazane, reprinted with permission by the publisher [26]

## 4.6 Porosity in PDCs

During the decomposition of the organic groups and the release as gaseous species, the ceramics often exhibit (micro-)porosity, which could be useful in applications in separation processes. Unfortunately, this porosity is usually only present at intermediate pyrolysis temperatures and then seems to collapse again, which is why it is also called transient porosity and has become an important research field in polymer-derived ceramics.

This phenomenon was shown by e.g. Konegger et al. [12] for a typical precursor for SiCN ceramics, a polyvinylsilazane, which shows high specific surface areas up to temperatures of 600 °C, which then seem to collapse again, leading to nonporous ceramics, at least if pyrolyzed under nitrogen atmosphere.

The release of gaseous species during decomposition often becomes a problem, if dense ceramics shall be formed, since the evolving gases often lead to the formation of cracks. This problem can be overcome by the use of active or passive fillers, which reduce the shrinkage. [35-37]

## 4.7 Applications of PDCs

As already mentioned, PDCs provide an alternative to the traditional powder based processing of ceramics and enable the production of ceramic parts in more complex shapes, which leads to applications in many fields:

### – Fibers

(Ceramic) fibers are a versatile tool to improve mechanical properties in composite materials. CMCs, for example, are used for structural components which are used under drastic working conditions from a mechanical and chemical point of view, like turbine engines, rocket nozzles or furnaces. A driving force for the development of new ceramic fibers was the wish to replace carbon fibers, because of their instability in oxidizing environments, especially at elevated temperatures. [2] This led to the development of SiC-fibers, which were successfully prepared by Yajima et al. [1] Further improvement of the properties was then achieved using multicomponent ceramic fibers containing nitrogen and boron as additional elements (SiCBN ceramics), which can withstand temperatures as high as 1500 °C in oxidizing/corrosive atmosphere.[2]

### – **Coatings**

Using precursor polymers, it is possible to deposit ceramic coatings by liquid phase deposition, using methods like spin coating, dip coating or spray coating, which presents a convenient alternative to PVD or CVD. Ceramic coatings are typically used as thermal or environmental barrier coating to enhance the wear- and corrosion resistance of structural parts. Apart from the already beneficial ceramic properties, it is possible to relatively easy modify the elemental composition of the PDCs and tailor the properties by e.g. addition of metal particles, which in case of Fe lead to even magnetic properties, in general to an increase in corrosion resistance, which can also be achieved by adding boron. [3, 38-40]

### – **MEMS**

The PDC route enables the fabrication of MEMS/NEMS out of non-oxide ceramics, which can be used under harsh thermal or chemical conditions. Using the powder based route, it is difficult, not to say impossible to fabricate these parts with the non-oxide materials, because the dimensions are extremely small, which makes conventional processing hard or impossible, the molds too expensive or the green body shaping too complex. Using PDC, one can overcome these problems by e.g. using lithography. [5, 28-30, 32]

### – **Porous Ceramics/Foams**

Due to the already mentioned chemical and mechanical stability, combined with a low density, porous ceramics are interesting for many fields, such as liquid metal filtration, catalyst supports or membrane applications.

Porous ceramics can be produced in a variety of ways including, blowing/ foaming, the use of sacrificial templates or fugitives, freeze casting and many more. [41-49]

## 4.8 Historical overview of research fields of PDCs

The increasing interest in this research field can be demonstrated by the yearly number of publications containing the key phrase “polymer-derived ceramics” which is displayed in Figure 12, taking into account only articles and reviews (Scopus, 12/11/2019). While there were only single publications every few years until the second half of the 80ies, there was a sharp rise up to nowadays, with even 157 publications in 2019 continuing the trend that was already found by Colombo et al. in 2010. [6]

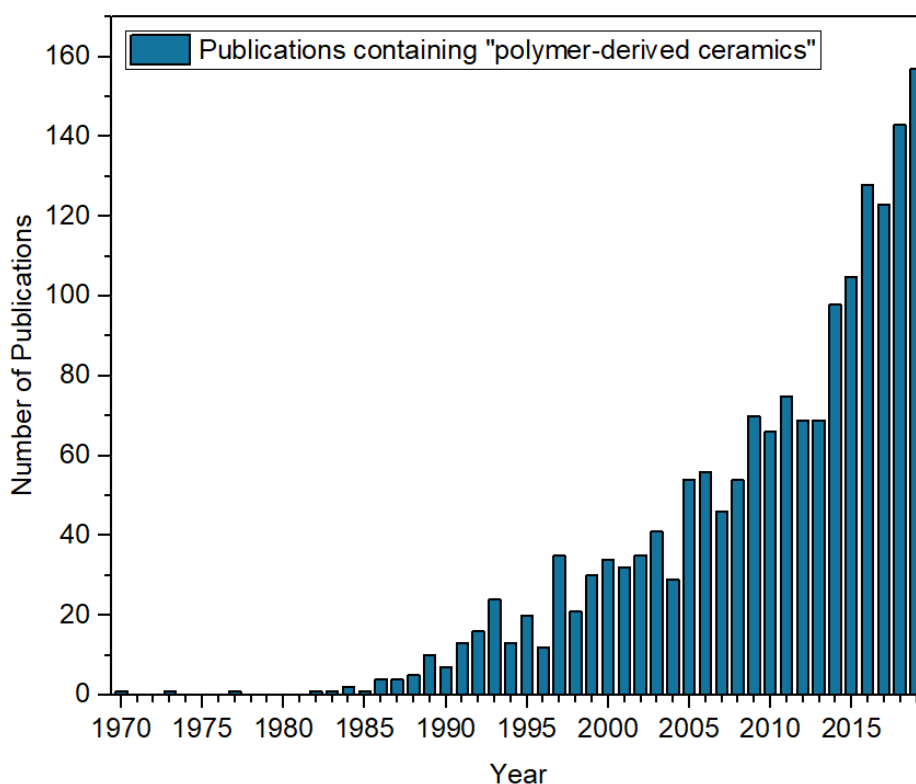


Figure 12: Yearly number of articles and reviews from 1970-2019 containing “polymer-derived ceramics” according to Scopus search, state 11/12/2019; analogous to [6].

### 4.8.1 First steps towards applications of PDCs up to and in the 1990s

While the first step in the industrial application of PDCs was the development of SiC fibers by Yajima et al. in the 1970s, the advantages of the materials, that can be produced using this processing route led to various special applications and intense research regarding different aspects of the synthesis and processing of polymer precursors.

While the publications during the first years (until the 1980s) are mainly focusing on fiber production and synthesis of precursors, the field of interest widened up in the following years (1990s) and polymer-derived ceramics became interesting also for bulk materials in structural applications. [50-52] The research group around Peter Greil made a major contribution to the fabrication of bulk PDCs due to the introduction of active-filler controlled polymer pyrolysis. By adding fillers (such as Ti or Cr) to the polymer, which react with it during its decomposition, the shrinkage can be reduced drastically, leading to a reduced formation of cracks. In addition, they also found transient porosity in the materials if pyrolyzed at intermediate temperatures, which is found as open porosity up to certain temperatures if fillers are used [35, 36, 53-58] The use of reactive fillers is an often used approach also up to nowadays, using various metals and precursor combinations. [59] Also, the group around Ralf Riedel contributed in a major way to the research field of (bulk) PDCs. They investigated the preparation of bulk PDCs resulting from polysilazanes using different processing routes, with one of them using passive fillers (ceramic powders). [37, 52, 60] First approaches towards PDC coatings were made to increase mechanical strength or enable electronical applications. [61-63] Also, polysilazane derived coatings were developed as protection against oxidation of C/C-SiC composites. [64] Petersen et al. successfully prepared ferromagnetic compounds using the PDC route in 1995. [65]

As the PDC route became more interesting, also the decomposition behaviour, microstructure and (oxidation) stability became a topic of intense research, to enable a better tailorability of the properties of the resulting ceramics.[34, 66-76] The focus in this period was set on the microstructure of the PDCs correlated with the high temperature properties and their improvement by variation of precursor composition. The microstructure of PDCs undergoes significant changes when being treated at temperatures above 1000 °C, where amorphous PDCs typically start to crystallize. An extensive study about the structural evolution during pyrolysis of polysilazanes yielding SiCN ceramics, which also give an insight in reactions occurring during heat treatment, was made by Seitz et al. [34] and further examined by Gabriel et al. [77] both showing, that there is some kind of phase separation taking place upon crystallization above  $\gg 1000^\circ\text{C}$  leading to the formation of crystalline ceramic domains and – if there is excess carbon present – domains of free  $\text{sp}^2$  carbon. Song et al. [71] prepared SiCN ceramics from a polysilazane and a polycarbosilane partially using ammonia as pyrolysis atmosphere, showing increased stability of the mixed ceramic. Also Delverdier et al. [73, 78] showed the positive influence on the stability if ceramics of mixed compositions are used retaining their amorphous

nature up to higher temperatures. A big study on the relation between microstructure and stability of SiCN ceramics was conducted by Kleebe et al. [76, 79] The presence of carbon apparently increases the onset of the crystallization of SiCN ceramics. [80]

Su et al. [67] for example investigated the effect of boron on the properties of SiCNB ceramics in an extensive study already in the early 1990ies, showing, that the presence of boron changes the crystallization behaviour in polysilazane derived ceramics, which could increase the temperature stability. In the following years, SiBCN ceramics and their positive influence on high temperature stability (even up to 1800 °C) were investigated and further improved in various studies and is explained by the strong covalent bonds and therefore poor migration possibility of the elements, which is necessary for the crystallization, and also by the formation of a protective layer by reaction of boron with oxygen. [81-83]

First approaches towards the clarification of the reactions taking place during decomposition of polysilanes, a precursor leading to SiC ceramics were made. [84]

#### **4.8.2 Detailed investigations of the decomposition behaviour of polymeric precursors**

While the first steps of the characterization of PDCs were focusing mainly on the properties of the ceramics like microstructure and thermal stability or increase of ceramic yield, the interest was then shifted to the understanding of the reactions taking place during the polymer-ceramic conversion, especially of other PDCs than SiC. This led to intense research of the decomposition behaviour of different precursor types also at relatively low temperatures.

Bahloul et al. [21, 85] investigated the pyrolysis chemistry of silazanes with varying precursors, showing that the mineralization takes place in different steps, with crosslinking of the polymers/distillation of low molecular weight compounds in the low temperature region followed by the actual mineralization at higher temperatures and eventually the phase segregation and crystallization. For example, functional groups like Si-H and Si-N groups lead to an increased ceramic yield, due to further crosslinking during the heat treatment. [86] Additionally, a good overview is given by Kroke et al. [26], reviewing silazane derived materials in general, from synthesis to processing and properties.

Similar work was done regarding polycarbosilanes [20, 25, 87] showing roughly the same behaviour. Liu et al. [88] made first approaches in this field, investigating polycarbosilanes with two H atoms at the silicon atom, proposing a decomposition mechanism.

### 4.8.3 Porous ceramics

Although nanoporosity evolving during the pyrolysis process was mentioned already in 1994 [89] and was found also by other work groups in the following years, [35, 37, 60, 90] the early work with PDCs was not focusing on that feature.

Starting mainly in the 2000s, not only fibers and bulk ceramics, but also porous ceramics formed via the PDC route got attention, since porous ceramics can serve as e.g. filter or catalyst support under conditions where metals or polymers can't be used and microporous ceramics could find an application as gas separation membrane.

Major work in this direction was done by Dismukes et al. [13] proposing several ways of preparing microporous SiCN ceramics, including the use of fillers, the introduction of metals into the ceramics or the use of ammonia as reactive atmosphere. Although already some other research groups used ammonia as reactive atmosphere during the pyrolysis [71, 91], Dismukes et al. were the first to set it in relation to the presence of microporosity in the materials. The influence of ammonia on the elemental composition, with a special focus on the carbon content, and the relation between composition and presence of microporosity were investigated in more detail in the following years up to today. [14, 15, 92] Also the strategy of using metal ions for the pore stabilization was further investigated. [16, 17] If carbon rich starting materials are used, the formation of turbostratic carbon at temperatures  $\gg 1000$  °C leads to the formation of micropores, too. [93]

The work regarding microporous ceramics resulting from polycarbosilanes was conducted e.g. by Williams et al. [94], Suda et al. [24] or Maddocks et al. [87, 95]

Not only microporous materials, but also foams, or macroporous ceramics prepared under use of fugitives were prepared for several applications. [44, 96] P.Colombo and colleagues did intense research towards macroporous and cellular ceramics produced via the PDC route. [42, 45, 97-102]



#### 4.8.4 Recent Developments

The research regarding PDCs is also driven by the recent intense developments towards additive manufacturing using all kinds of materials. Additive manufacturing processes based on photopolymerization can benefit extremely from PDCs. Instead of using a ceramic powder in combination with a photocurable polymer, polymeric precursors could be used directly. This idea led to development of (UV-)curable precursors. A fast method for the curing of PDCs in stereolithographic processing was introduced by Wang et al, who use the thiol-ene click reaction for polysilazanes, -carbosilanes, and –siloxanes. [103] Wei et al. used direct in writing to prepare cellular SiOC ceramics from UV curable polysiloxanes. [104] Li et al. prepared SiBCN/Si<sub>3</sub>N<sub>4</sub> composites by DLP. [105]

#### 4.9 Pore characterization of microporous materials

Various analysis methods are available for the characterization of pores. As shown in Figure 13, every characterization method is only applicable in a certain pore size range, leaving aside other possible material specific problems with each of the methods. For microporous materials, the number of characterization methods is limited. A common technique to obtain information about the specific surface area and the pore size distribution of porous materials is gas sorption, yielding information about pore sizes down to 0.35 nm depending on the adsorptive. Another versatile tool to get information about nanostructured samples is small angle X-ray scattering (SAXS), giving information about size shape and orientation of the structures. While scanning electron microscopy is rather limited in resolution, transmission electron spectroscopy is a good complimentary method to SAXS and physisorption investigations. When going to larger pores, in the meso- and macropore range, Hg intrusion becomes an interesting tool, applicable over a wide range of pore sizes with a lower limit of 3.6 nm.

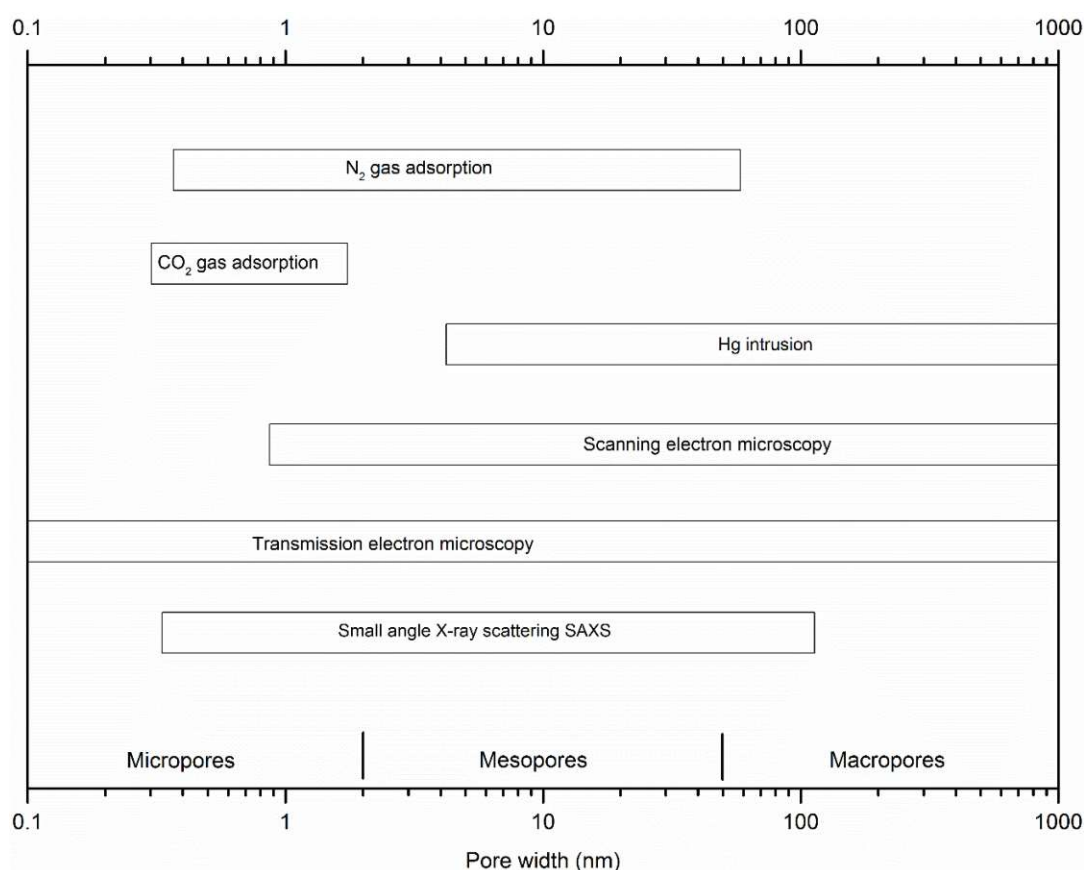


Figure 13: Selected characterization methods for various pore size ranges after [106].

## 4.9.1 Gas sorption

A popular method for the characterization of porous solids or powders is gas sorption. It can be differentiated between physical and chemical adsorption of the gases, so called physisorption and chemisorption. Knowing the properties of the adsorptive, it is possible to get information about the adsorbent, such as specific surface area and pore size distribution.

### 4.9.1.1 Terminology

As displayed in Figure 14, adsorption in general is the enrichment of species in the vicinity of an interface between a solid and a fluid phase. The adsorbed species is called adsorptive in the fluid phase and adsorbat in the adsorbed state. The solid surface is the adsorbent.

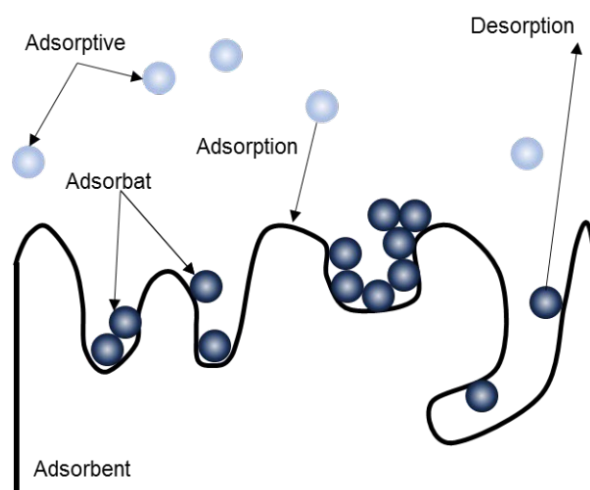


Figure 14: Schematic display of the terminology in adsorption processes

Adsorption can be caused by chemical interaction between adsorptive and adsorbent or by weaker forces like van der Waals forces, which leads to the terms chemisorption or physisorption as short version of chemical/physical adsorption. Although it is hard to clearly distinguish, there are some characteristic features for either of the two, which are listed in Table 1.

Table 1: Differences between physisorption and chemisorption [107].

<b>Physisorption</b>	<b>Chemisorption</b>
General phenomenon in solid/fluid systems	Chemical specificity
Minimal change of electronic states and chemical nature of the adsorptive	Change of electronic states and chemical nature of the adsorptive
Energy in the range of condensation of the adsorptive	Energy in the range of chemical reactions, activation energy necessary
Multilayer adsorption	Monolayer adsorption
Reversible	May not be reversible

#### 4.9.2 Methodology and primary data

Only physisorption was used to characterize the samples in this work. Therefore, the following more detailed explanations focus on physisorption, not chemisorption.

Generally, the sample is probed with an adsorptive, typically a noble gas (Kr, Ar) or N<sub>2</sub> to prevent chemical reactions, which is adsorbed on the sample surface via van der Waals forces, without significant changes in the nature and electronic states of neither the sample nor the adsorbat. Due to that fact, the process is fast and reversible.

The sample, which is placed in a defined calibrated volume under a defined temperature and evacuated thoroughly, is dosed with the adsorptive and the amount of gas that was added is recorded in relation to the relative pressure (absolute pressure in an equilibrium state vs. saturation pressure), giving adsorption isotherms, containing information about the pore filling mechanism in the sample. Since the process is reversible, also desorption isotherms can be recorded. Various models can be applied to extract information about pore size and specific surface area. The different types of isotherms are classified by IUPAC and are shown in Figure 15. Even without applying a mathematical model, the shape of the isotherm already

gives insight in the nature of the sample. If the adsorbed volume increases strongly at very low relative pressures the sample is typically microporous. Non- or macroporous samples show monolayer/multilayer adsorption, with the knee (point B) typically showing the completion of a monolayer. If there is no distinct knee, the adsorptive is typically forming clusters on the surface, without formation of continuous layers. For type VI isotherms, the multilayer adsorption on a nonporous sample can be seen from the step like increase, with each step representing the competition of a monolayer. Mesoporous samples show the same behaviour as macro- and nonporous samples in the low pressure region, because mono- and multilayers are formed on the pore walls. Reaching a certain degree of coverage, condensation occurs inside the pores, which means that a gas condenses to a liquid-like phase at pressure lower than the saturation pressure of the bulk liquid. For mesoporous samples, there is often a difference between adsorption- and desorption branch, which is caused by capillary condensation and occurs if pores exceed a specific critical value. [108]

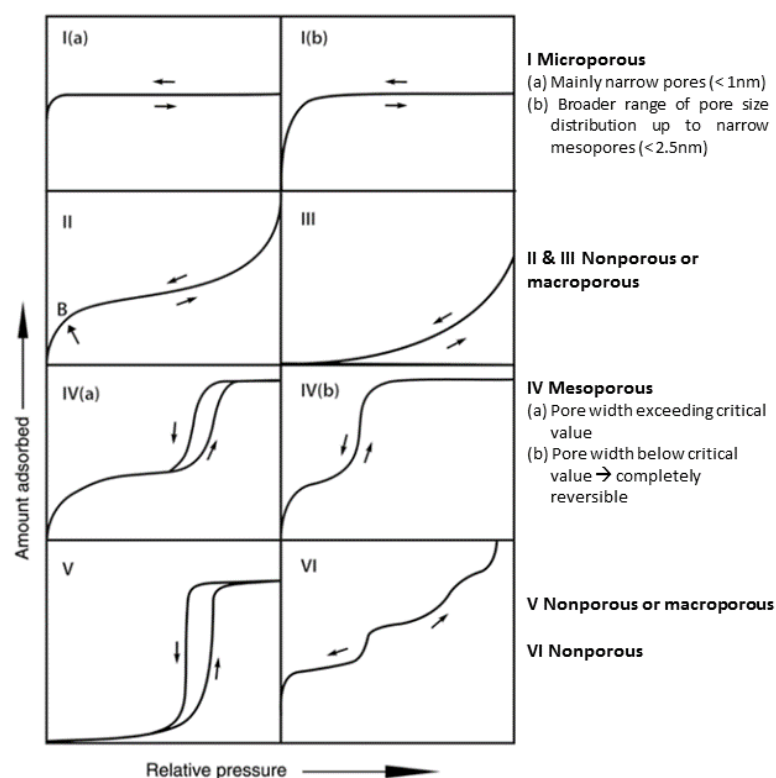


Figure 15: IUPAC classification of gas adsorption isotherms, after [108]

### 4.9.3 Assessment of specific surface area

The most popular method is the Brunauer-Emmett-Teller (BET) method, which uses a model to describe the adsorption of an unreactive gas on the specific surface of a material under formation of mono- and multilayers. [109] Since the crosssectional area of the adsorbate is known, it is possible to calculate the surface, that is accessible by the absorptive. The BET equation gives the number of gas molecules adsorbed at a certain relative pressure, taking into account the heat of adsorption by introducing the parameter C. From the BET plot, which is usually applied in a relative pressure range between 0.05 and 0.35, where the isotherm is linear, one can calculate the specific surface area using the crosssectional area of the adsorbate.[108, 110, 111]

**BET equation:**

$$\frac{\frac{p}{p^0}}{n \left(1 - \frac{p}{p^0}\right)} = \frac{1}{n_m C} + \frac{C - 1}{n_m C} \left(\frac{p}{p^0}\right)$$

To extract the specific monolayer capacity from the data, the linear relation between  $\frac{\frac{p}{p^0}}{n \left(1 - \frac{p}{p^0}\right)}$  and  $\frac{p}{p^0}$ , the BET plot, is used.

In the second step, the specific surface area  $S_{BET} = n_m L \sigma_m / m$  can be evaluated.

*p...absolute pressure*

*p<sup>0</sup>...saturation pressure*

*n...specific amount adsorbed*

*n<sub>m</sub>...specific monolayer capacity*

*C... parameter related to the energy of monolayer adsorption*

*S...specific surface area*

*m...mass of adsorbent*

### 4.9.4 Pore size distribution

There are various semi-empirical methods for the evaluation of the pore size. The Horvath-Kawazoe-method is the most popular method for microporous materials and assumes the pores

as slit shaped. The Barrett-Joyner-Halenda model (BJH) is typically used for mesoporous materials. Unfortunately, these methods tend to underestimate the pore size, but still, they are useful tools to get information about the pore size and at least compare different materials.

In the recent past, density functional theory (DFT) and other methods based on molecular simulation and statistical mechanics have become the state of the art for obtaining reliable pore size distributions over the whole micro- and mesopore range. While it was Seaton et al. [112] who first proposed applying the DFT method on adsorption isotherms, there was soon a variety of models for different adsorbent/adsorptive combinations available. They use so called DFT kernels, which are a set of theoretical isotherms for a given pair of adsorbent and adsorbate at a certain temperature with varying pore size and varying relative pressures, which are then compared to the experimental isotherms.[113] There are two advanced versions of the DFT method, non-local DFT (NL-DFT) and quenched solid DFT (QS-DFT), which are in detailed described by Landers et al. [114].

#### 4.9.5 Small angle X-ray Scattering SAXS

X-ray scattering is a non-destructive method for the investigation of solids and fluids. Depending on the angles, that are detected, one can get information about structures on an atomic level, like crystal lattices, or structures in the size of small particles/ pores or domains up to 100 nm. Since there is an inverse relation between size of the scattering center and the angle of the scattered beam, the - in comparison to interatomic distances - large structures have signals at small angles up to  $\sim 5^\circ$  ( $= \sim 10^\circ 2\Theta$ ) and are characterized using SAXS (Small angle X-ray scattering), whereas information about the crystal lattice can be found at wider angles using WAXS (Wide angle X-ray scattering). To be more precise, the effective SAXS intensity is a result from an electron density fluctuation  $\Delta\rho = \rho - \rho_0$ , which represents nanoscale regions or structures (scatterers) with a certain electron density  $\rho$ , which are distributed in a medium with another electron density  $\rho_0$ . These relations are schematically displayed in Figure 16. [115, 116]

The scattered intensity is collected as a function of the scattering angle  $2\theta$ . The scattered intensity  $I(q)$  is the Fourier Transform of  $g(r)$ , the correlation function of the electronic density  $\rho(r)$ , which corresponds to the probability to find a scatterer at position  $r$  in the sample if another scatterer is located at position  $0$ , with  $q$  being the scattering vector.

The classical and the most known parameter directly extracted from the SAXS data,  $R_g$  provides a measure of the overall size of the scattering center and can be estimated using the Guinier approximation. The  $R_g$  is the average root-mean-square distance to the centre of density in the molecule weighted by the scattering length density. [117]

The Porod law [118] describes that the slope of the plot ( $\ln I(q)$  vs  $\ln q$ ) represents the interface and fractal dimension of the scattering objects. At high  $q$ , a slope of -2 is a signature of Gaussian chain in a dilute solution, whereas a slope of -1 points to rigid rods. A slope of -4 represents a smooth interface between domains in a multiphase system. Slopes between -3 and -4 characterize rough interface of fractal dimension  $D$ .

In addition, information about agglomeration and distance between the scattering centers can be gained. These are given by the hard sphere radius  $r_{HS}$  and the hard sphere volume fraction  $\eta$ .

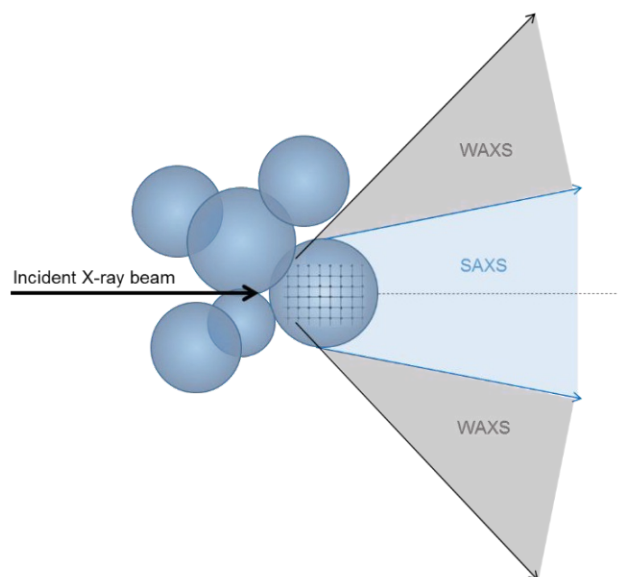


Figure 16: Schematic display of the X-ray scattering at a sample and the regions of applicability of SAXS and WAXS, after [115].



## 5. EXPERIMENTAL PROCEDURE

The used preceramic polymers as well as their storage and processing and the characterization methods for the polymers as well as pyrolyzed ceramics will be explained in the following.

Only general processing steps and characterization methods are listed in this section. There are additional experimental parts regarding the specific processing steps and materials for every focus-section.

### 5.1 Materials

Two commercially available precursors were chosen for the investigations, a poly(vinyl)silazane and a polycarbosilane, which were crosslinked using a radical initiator, dicumylperoxide:

- Poly(vinyl)silazane PSZ (**Durazane 1800, DurXtreme GmbH, Figure 17a**)
- Allylhydridopolycarbosilane PCS (**SMP-10, Starfire Systems, Figure 17b**)
- Dicumylperoxide DCP (>97 %, **Fluka, Figure 18**)

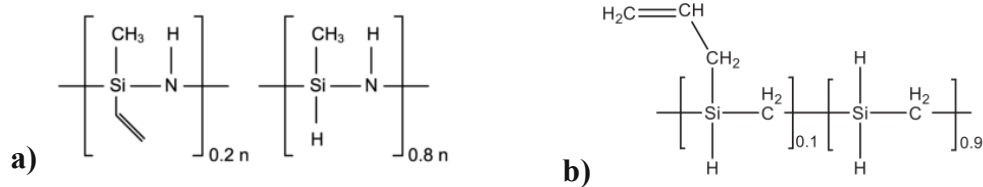


Figure 17: Structure of the preceramic polymers used in this work.

a) Durazane 1800 after [119]. b) SMP-10 according to [120].

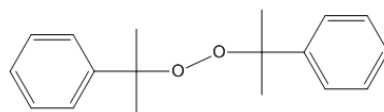


Figure 18: Structure of DCP used as radical initiator.

## 5.2 Processing

The polymer precursors undergo a heat treatment, which – through decomposition and exchange reactions – leads to an organic-inorganic-transition. During this transition, micropores form, which are called transient porosity, because they are only stable up to certain temperatures. Before the pyrolysis, the polymers are crosslinked to prevent volatilization of low molecular compounds and therefore lead to a higher ceramic yield than a non-crosslinked sample would.

The parameters which are used are based on research of Konegger et al. [12] and will be explained in detail below.

### 5.2.1 Preparation of the polymer precursors

Before use PSZ was stored in a fridge (5 °C), the PCS in a freezer (-18 °C). Only small amounts were taken out of the main storage vessel right before further usage. Since both polymers are sensitive towards moisture, all handling was done inside a glovebox under nitrogen atmosphere. To remove decomposition products, the polymers were degassed each time before they were used. As crosslinking agent, 1 wt% of DCP was added and dissolved under stirring while applying vacuum. The mixture was freshly prepared for every experiment.

### 5.2.2 Crosslinking

For crosslinking, glass vials containing approximately 2.5 g of a polymer (PSZ or PCS with 1 wt% DCP) were put into a furnace (Carbolite HZS 12/600, 1200 °C Split Tube furnace) and heated to 130°C for 12 hours with a heating rate of 1 K/min and a nitrogen flow of 0.35 l/min. The nitrogen was purified using filters for moisture and oxygen (SGT-F0101 and SGT-F0102, Scientific Glass Technology) yielding a purity of > 99.9999 % in both cases. The filling was done inside the glovebox, the vials were closed inside and not opened until being in the furnace

and vice versa. The crosslinked poly(vinyl)silazane was stored in the glove box for further investigations.

### 5.2.3 Pyrolysis

The crosslinked polymer was carefully crushed inside the glass vial using a spatula and transferred to an alumina crucible for pyrolysis (still inside the glove box). The crucible was closed with an alumina plate and sealed in a plastic bag for the transfer from glovebox to furnace. The plate was removed inside the furnace under flowing nitrogen. The temperature program is shown in Figure 19, a nitrogen flow of 0.35 l/min was used. The same furnace and atmosphere were used as for the crosslinking step.

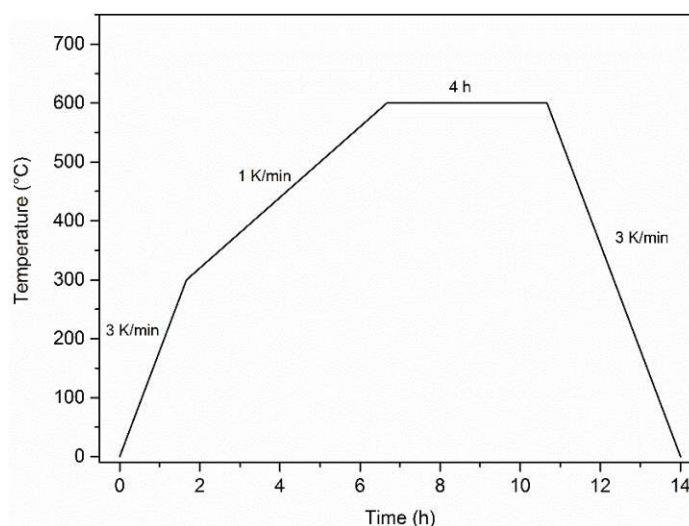


Figure 19: Standard heating program for the pyrolysis of the crosslinked samples.

## 5.3 Characterization methods

In-depth characterization of the samples in the polymer stage, after crosslinking as well as of the amorphous ceramics received after pyrolysis was carried out.

### 5.3.1 TGA-MS

The thermogravimetric measurements were carried out using a Netzsch STA 449 C (Jupiter) coupled to a quadrupole mass spectrometer (Netzsch QMS 403 C, Aëolos) under nitrogen atmosphere, with a heating rate of 5 K/min and a maximum temperature of 1500 °C. Approximately 100 mg of the sample (roughly ground) were weighed in, this was done inside a glovebox, where the crosslinked sample was stored, to prevent reaction of the sample with oxygen and moisture in the lab atmosphere. The sample was exposed to air for about one minute

during transfer of the crucible from a sealed, nitrogen filled vessel to the TGA unit and the time needed for purging the unit with nitrogen again. The  $m/z$  values analysed are given in Table 2.

Table 2:  $m/z$  values analysed using TGA-MS and corresponding species

$m/z$	species
2	H <sub>2</sub>
12	C
15	CH <sub>3</sub>
16	CH <sub>4</sub> , NH <sub>2</sub>
17	NH <sub>3</sub>
18	H <sub>2</sub> O
26; 27	Ethane, Ethene
32	O <sub>2</sub> , SiH <sub>4</sub>
41	C <sub>3</sub>
44	SiO, CO <sub>2</sub>
50-58	C <sub>4</sub>
59	H <sub>2</sub> Si(CH <sub>3</sub> ) <sub>2</sub>
73	HSi(CH <sub>3</sub> ) <sub>3</sub>
101,102	C <sub>4</sub>

### 5.3.2 Elemental Analysis

Besides investigating the oxygen contamination during each processing step, from pure polymer over crosslinking and pyrolysis, as well as handling of the pyrolyzed product, changes in elemental composition were monitored by also determining the carbon and nitrogen contents. Oxygen and nitrogen were investigated using a O/N determinator (Leco TC400). Approximately 20 mg of each sample were weighed in a tin capsule; for pure PSZ/PCS, PSZ/PCS+DCP, crosslinked PSZ/PCS and the pyrolyzed sample, weighing was carried out inside the glovebox and the capsules were taken out right before the measurement, to prevent oxygen contamination from lab atmosphere. The reference standard used for oxygen calibration was iron powder JK47, with an oxygen content of 1.09 wt%, the one for nitrogen was silicon nitride ED101. The carbon content was determined using a C/S determinator (Leco CS230). Approximately 20 mg of each samples was weighed in an alumina crucible, together with

Lecocel as ignition accelerator and an alumina lid. Silicon carbide (BAM S003) with a carbon content of 29.89 wt% was used as standard for the carbon analysis.

### 5.3.3 ATR-IR

The infrared absorption measurements were done using a platinum ATR (Tensor 37, Bruker) with a diamond. A resolution of  $4\text{ cm}^{-1}$  was chosen and 10 scans were done. The liquid polymers were measured directly, the powder samples were finely ground and then measured.

### 5.3.4 NMR

$^1\text{H}$  and  $^{13}\text{C}$  (DEPT-135) spectra were recorded using a Bruker Advance III HD spectrometer (Bruker BioSpin GmbH) at 600.15 MHz for  $^1\text{H}$  and 150.90 MHz for  $^{13}\text{C}$ . For the measurement, approximately 10 mg of the samples was dissolved in D-chloroform ( $\sim 500\ \mu\text{l}$ ). The received data was then evaluated using TopSpin4.0.2 (Bruker BioSpin GmbH).

### 5.3.5 Solid State NMR

$^{29}\text{Si}$  and  $^{13}\text{C}$  NMR spectra were recorded to further clarify the structural features in all processing stages. Solid-state nuclear magnetic resonance spectra were recorded with a Bruker spectrometer model AVANCE 300 equipped with a 4 mm broadband probe head ( $^{13}\text{C} = 75.40\text{ MHz}$ ,  $^{29}\text{Si} = 59.57\text{ MHz}$ ). All NMR measurements were conducted in CP/MAS mode with a rotational speed of 4 kHz.

### 5.3.6 $\text{N}_2$ -Physisorption

The nitrogen adsorption and desorption isotherms of the pyrolyzed PSZ and PCS were measured at 77 K using an ASAP2020 (Micromeritics). Approximately 80 mg of each sample were used. After degassing at 250 °C for 12 h, the analysis was carried out in a pressure range from  $5\text{E-}06$  bar to saturation pressure. The specific surface area was estimated using the Brunauer Emmett Teller method (BET) with five values located in the linear range of the isotherm. The pore size distribution was calculated using the non-local density functional theory NLDFT (model: *Carbon-N2*, *2D-NLDFT Heterogeneous Surface*, SAIEUS or *N2-Cylindrical Pores – Oxide Surface*, Micromeritics). The exact parameters are given in Table 3 and Table 4 for the degassing step and the actual analysis.

## EXPERIMENTAL PROCEDURE

Table 3: Parameters for the degassing step prior to the N<sub>2</sub>-physisorption.

Evacuation Phase		Heating Phase	
Temperature ramp rate	10.0 °C/min	Ramp rate	10.0 °C/min
Target temperature	100 °C	Hold temperature	250 °C
Evacuation rate	6.7 mbar/s	Hold time	720 min
Unrestricted evacuation from	6.7 mbar	<b>Evacuation and Heating Phases</b>	
Vacuum setpoint	13 μbar		
Evacuation time	30 min		
		Hold pressure	133 mbar

Table 4: Parameters for the N<sub>2</sub>-physisorption measurement.

<b>Free Space</b>	Enter			
<b>P° and temperature options</b>	Measure p° at intervals during analysis. Calculate the Analysis Bath Temperature from these values			
	Measurement interval: 120 min			
<b>Equilibration</b>	Relative pressure p/p°: 1.0			
	Equilibration interval: 10 s			
	Maximum equilibration delay at p/p° >= 0.995: 600 s			
<b>Sample Backfill Options</b>	Backfill sample at end of analysis; Backfill gas: N <sub>2</sub>			
<b>Pressure table</b>				
	Adsorption	0.000005385	Desorption	
		0.000008203		0.990000000
		0.000012496		0.942500000
		0.000019035		0.895000000
		0.000028997		0.847500000
		0.000044172		0.800000000
		0.000067289		0.5- steps down to 0.15
		0.000102503		
		0.000156146		
		0.000237961		
		0.000362341		
		0.000551966		
		0.000840826		
		0.001951167		
		0.002972272		
		0.004527753		
		0.006897265		
		0.010506814		
		0.016005350		
		0.024381437		
		0.037140987		
		0.056577999		
		0.086186991		
		0.131291273		
		0.200000000		
		0.05-steps up to 0.85		
		0.897206258		
		0.929556311		
		0.951725531		
		0.966917911		
		0.977329122		
		0.984463837		
	0.989353198			
	0.992703836			
	0.995000000			

### 5.3.7 Small angle X-ray scattering

SAXS investigations were carried out, using a Bruker Nanostar equipped with a microfocus source (Incoatec High Brilliance, Germany) and a 2D position sensitive detector (Vantec 2000, Bruker AXS).

For ex-situ SAXS, the samples were placed between two Scotch tapes. Collected X-ray data were radially integrated and background corrected to obtain scattering intensities in dependence on the scattering vector  $q$ . For evaluation, the same model as in a previous work [12] was used, describing slightly agglomerated pores with a unified fit function [121] and a structure factor from a hard sphere model [122].

For the experimental part of the in-situ SAXS investigations see section 11.2

## 6. FOCUS I – CHARACTERIZATION OF THE UNALTERED PRECURSORS

This work focuses on the understanding of mechanisms responsible for the pore formation and their stability. Taking into account every step in the processing chain, from precursor composition and structure over crosslinking agents to pyrolysis conditions (atmosphere, temperature), critical parameters shall be identified. In the first part of this project, the unaltered precursors (polyvinylsilazane, polycarbosilane) undergo a standard treatment that was already used in the work of Konegger et al. [12] and are characterized using N<sub>2</sub>-Physisorption, element analysis (O, N, C), thermal gravimetric analysis (TGA-MS) and infrared spectroscopy (ATR-IR), as well as NMR and SAXS. These results will provide the basis for the interpretation of the influence of the previously mentioned parameters.

### 6.1 Experimental Procedure – Focus I

The starting materials and the experimental procedure were described in section 5.

### 6.2 Results and Discussion – Focus I

In the following sections, the results of the in-depth characterization of the two precursors in all processing steps will be described, including the changes during decomposition, regarding optical appearance as well as the change in elemental composition and structural entities present in the material, and eventually, the pore characteristics using gas sorption.

#### 6.2.1 Optical appearance

The samples in each processing step are shown in Figure 20. PSZ is a colorless liquid as pure compound, which becomes a soft, yet slightly brittle, solid after crosslinking. In the pyrolyzed state, the color changes to a dark brown in case of the roughly ground material and yellowish if it is finely ground. The change in color is probably caused by a free carbon phase, that forms during pyrolysis. PCS is a yellow liquid as pure compound. In the crosslinked stage, the color of the now brittle solid becomes slightly lighter. Like PSZ, also PCS undergoes a change of color during pyrolysis, becoming a dark brown material. Even finely ground, PCS keeps the dark brown color, indicating a higher amount of free carbon in the material.



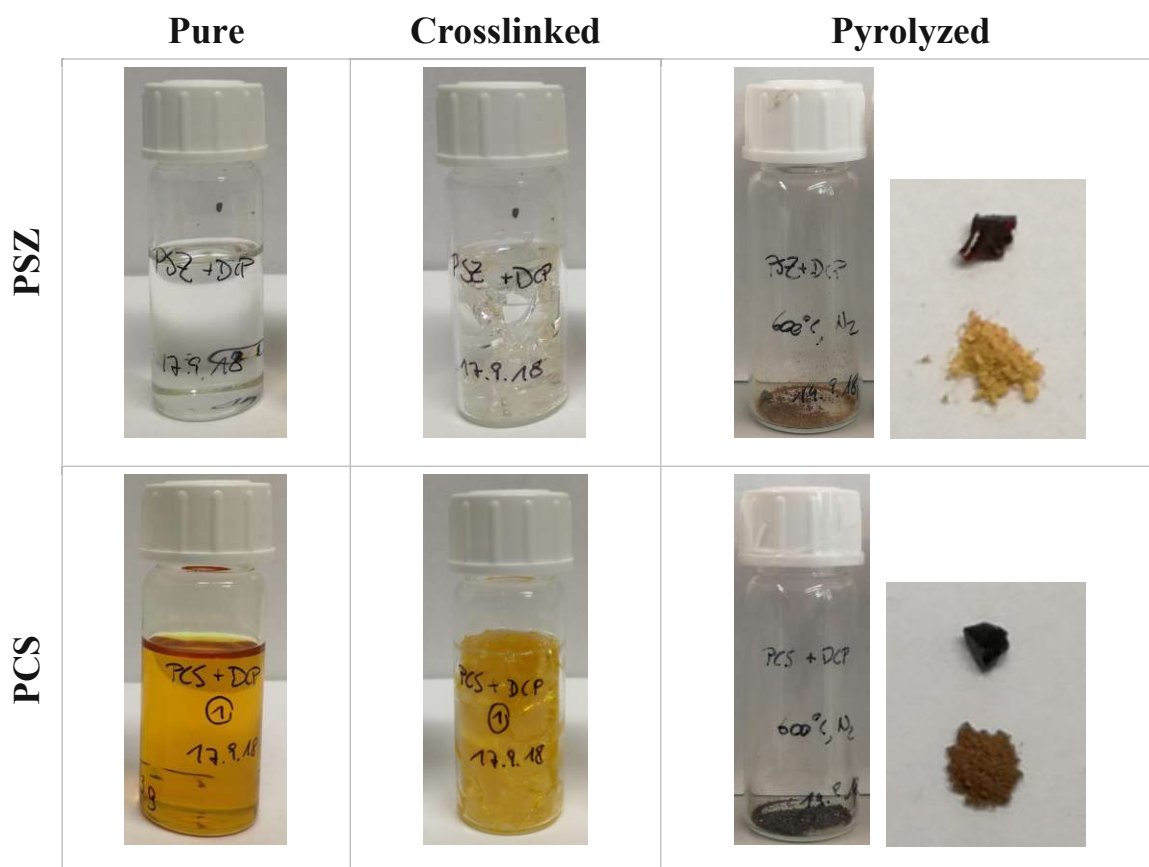


Figure 20: Pictures of the samples taken before and after crosslinking as well as in the pyrolyzed state. The pyrolyzed samples are shown in the storage vial, as well as one bulk piece (~2 mm) and finely ground sample, to get a better impression of the actual color.

## 6.2.2 Ceramic yield and decomposition behaviour

The ceramic yield was evaluated by weighing the sample after each processing step and by TGA measurements. By combining the latter method with MS, also information about reactions taking place during the pyrolysis can be gathered.

## 6.2.3 Mass change

The mass change determined by simply weighing the samples before and after each processing step is shown in Table 5. The values for both preceramic polymers are in a similar range, with around 3 % during crosslinking and ~ 26 % during pyrolysis. Both values are slightly higher for PCS, which, especially in the crosslinking step, indicates, that there is a higher fraction of low molecular weight compounds, which are distilled before they can react during the crosslinking process. The ceramic yield, which is the remaining part of the material after

pyrolysis is therefore (when using the crosslinked materials as starting compounds) 74 % for PSZ and 73 % for PCS.

Table 5: Mass change of PSZ and PCS during crosslinking (130 °C) and pyrolysis (600 °C).

	$\Delta m_{\text{pure-crossl.}}, \%$	$\Delta m_{\text{crossl.-pyro}}, \%$
PSZ	-2.2	-26.0
PCS	-3.6	-26.6

### 6.2.3.1 TGA-MS investigations

A useful tool for the evaluation of the decomposition behaviour of a material is TGA coupled with MS, because the weight loss during certain temperature regions combined with the released species can give information about the reactions taking place in that temperature region.

### 6.2.3.2 PSZ

The TGA results are shown in Figure 22 to Figure 24. There are two major temperature regions, one starting at 250 °C and ending at 500 °C, yielding a mass loss of 12,37 %; the other going from 500 to 900 °C with a mass loss of 12,62 %. This gives a total mass loss of 25 % which corresponds to a **ceramic yield of 75 %**. Usually, the first step corresponds to the loss of volatile compounds, whereas the second step is due to the polymer-ceramic-conversion.[21] Since in the first step, there is a competition between distillation of low molecular volatile compounds and crosslinking, a crosslinking step prior to pyrolysis increases the ceramic yield. Low molecular species can also be formed by exchange reactions between Si-N and Si-H bonds.[33] In this investigation, a crosslinked sample was used; only low amounts of oligomer-fragments ( $m/z$  41, 58, 59) are detected. The dominant species at temperatures from 250-500 °C is  $\text{NH}_3$  ( $m/z$  17), which is formed through transamination-condensation reactions (Figure 21). In addition, methane and other C-containing species evolve ( $m/z$  12, 15, 16, 26, 27, 41, 58, 59).  $\text{H}_2$  is released due to dehydrocoupling reactions. [17], [21]

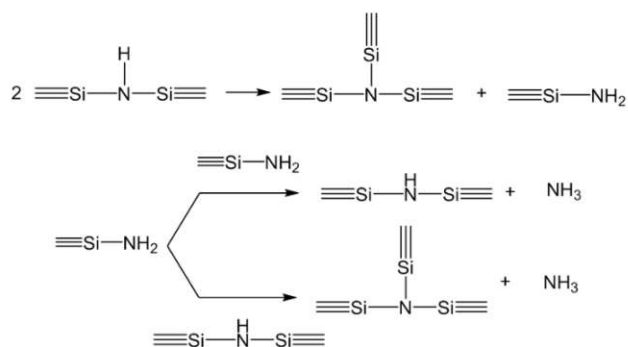


Figure 21: Transamination reactions during crosslinking of a polysilazane, after[21]

At 300 °C and from 500 – 700 °C, a slight oxygen signal ( $m/z$  32) and water signal ( $m/z$  18) occur, accompanied by a signal with  $m/z$  44, which represents either SiO or CO<sub>2</sub>. A  $m/z$  value of 32 could also result from SiH<sub>4</sub>, which in this temperature range is the most reasonable explanation. Breunig et al. [22] observed water formation by oxygen consumption of the evolving hydrogen, but only for a non-crosslinked sample, which could be the origin of the  $m/z$  value of 18.

When reaching temperatures of 1400 °C and higher during the pyrolysis, these  $m/z$  values (18, 32, 44) are found again, which is now most likely due to oxygen contamination during preparation (grinding etc.). This leads to SiO<sub>2</sub> formation during pyrolysis, which then reacts with the free carbon (equation 1), forming SiO and CO (which is not detected, because of the nitrogen atmosphere).



The second step starting at 500 °C is dominated by the formation of methane ( $m/z$  12, 15, 16) and hydrogen ( $m/z$  2), caused by the mineralization of the polymer. The formation of methane and other hydrocarbons can be explained by nucleophilic substitutions between N-H and Si-R moieties. Dehydrogenation between Si-H and N-H leads to hydrogen formation, as in the previous step. Hydrogen can also originate from the decomposition of contiguous Si-H and N-H bonds leading to hydrogen and an intermediate species, a silylimine, which then inserts into a Si-H or N-H bond. But also radical mechanisms can explain the reactions, which is likely due to the high temperature. In case of methane and other hydrocarbons it is the radical cleavage of Si-CH<sub>3</sub> bonds followed by H abstraction. Hydrogen evolves through homolytic cleavage of Si-H, N-H and C-H bonds again followed by H abstraction. [20-22, 33]

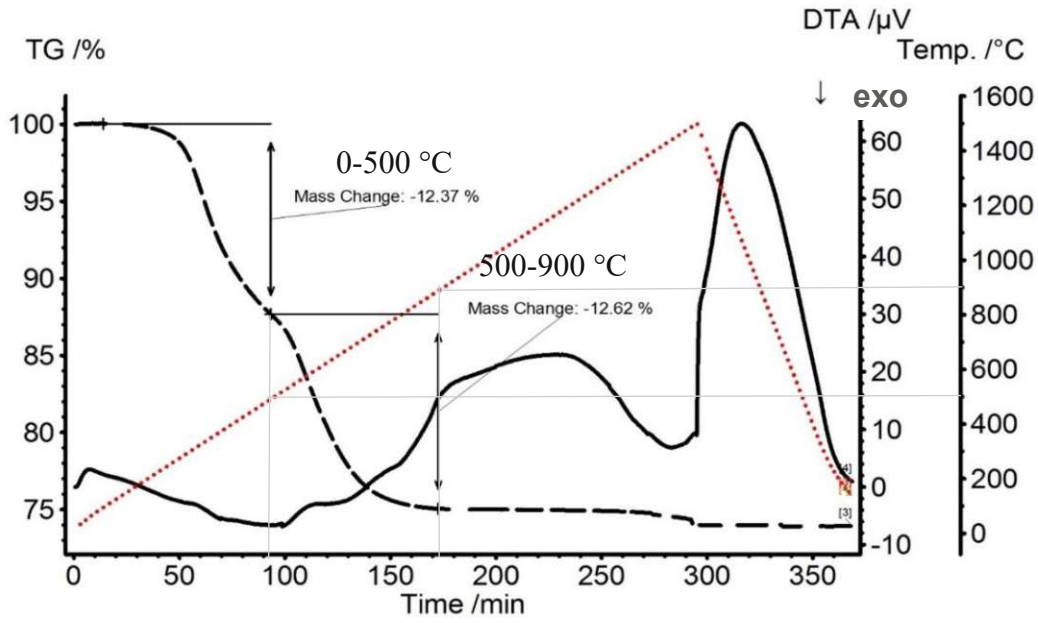


Figure 22: Thermal gravimetric analysis of the HTT1800 polysilazane crosslinked with 1wt% DCP (5 K/min, N<sub>2</sub>, T<sub>max</sub>=1500 °C, 89 mg sample)

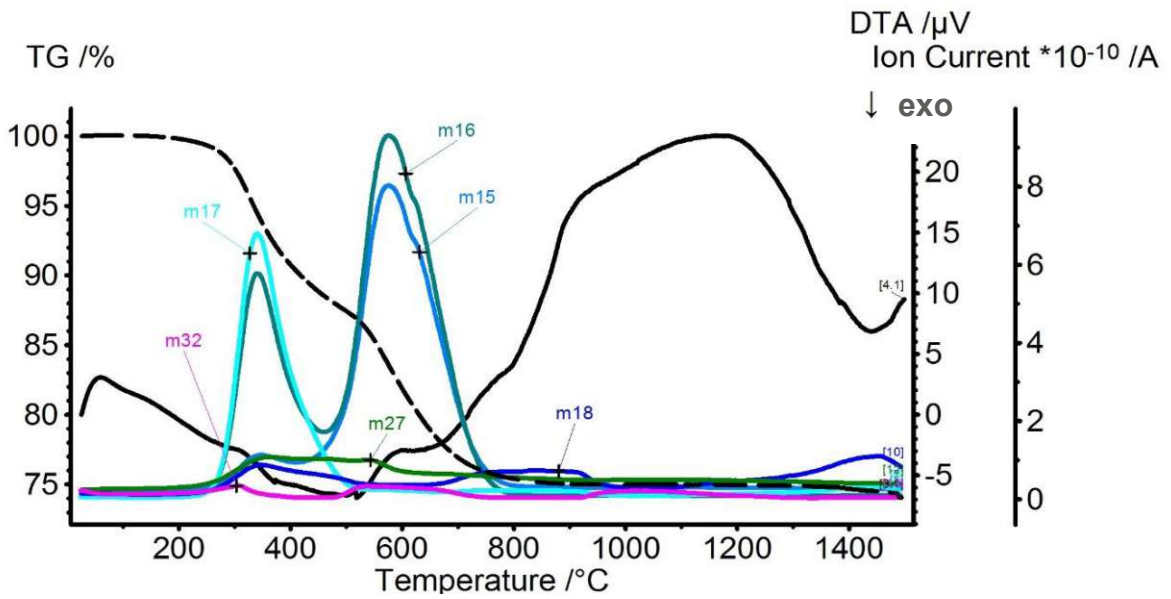


Figure 23: Intense m/z signals during TGA-MS of the crosslinked HTT 1800

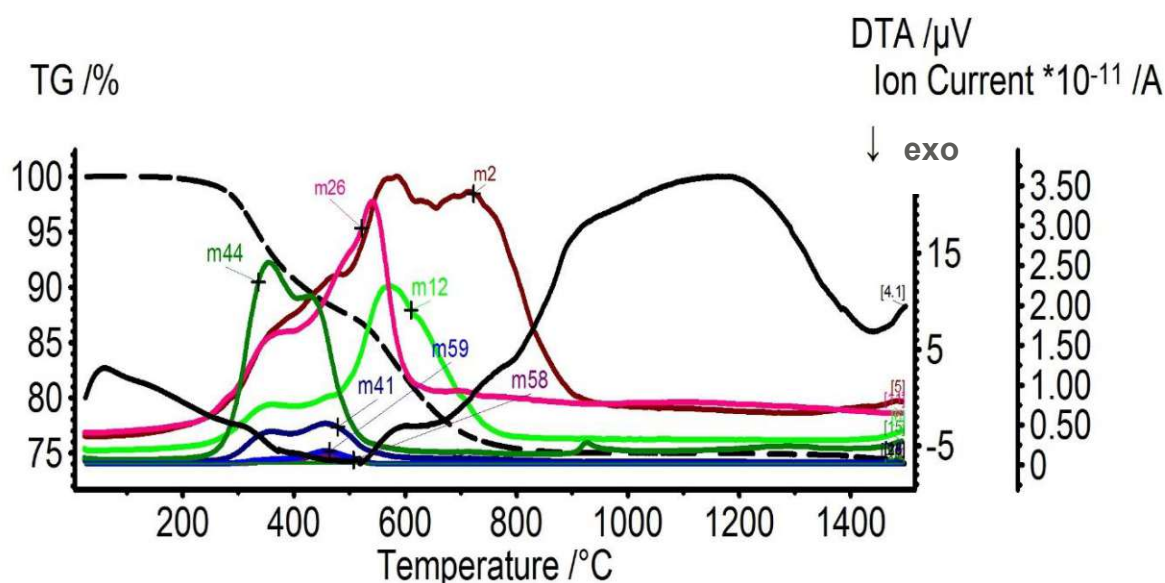


Figure 24: Low intensity  $m/z$  signals during TGA-MS of the crosslinked HTT 1800

### 6.2.3.3 PCS

The TGA results are shown in Figure 25 to Figure 27. There are three steps, in which the mass loss takes place. The major one (-18.44 %) is between 200 °C and 500 °C, correlated to the loss of volatile compounds, the second one (-4.74 %) up to 900 °C due to the polymer-ceramic-conversion and a third very small loss of 0.99 % between 900 °C and 1400 °C caused by dehydrogenation. This gives a total mass loss of 24.17 % which corresponds to a **ceramic yield of 75.83 %**.

The first mass loss is caused mainly by C-containing low molecular weight compounds, all with a maximum at 300 °C, especially by C<sub>2</sub>-species with  $m/z$  values of 26 and 27, accompanied by  $m/z$  values of 15 and 16 (CH<sub>3</sub>, CH<sub>4</sub>) as well as 41 (C<sub>3</sub>-species) and 50-58 (C<sub>4</sub>-species). Correlated to the C-containing species, there is also a signal at a  $m/z$  value of 12 (C). With a maximum at the same temperature, hydrogen ( $m/z$  2) and water ( $m/z$  18) as well as CO<sub>2</sub> or SiO ( $m/z$  44) and dimethylsilane ( $m/z$  59) evolve.

Starting at approximately 400 °C, hydrogen and methane dominate the MS spectrum, which indicates the starting polymer-ceramic-conversion. There is also a second but significantly lower maximum of C<sub>2</sub> species, probably due to decomposition of sidechains. Whereas the methane formation finishes after two equal maxima at 500 °C and 600 °C, hydrogen formation starts a little earlier and lasts longer with the first higher and sharper maximum at 480 °C and a broad signal from 550 °C to almost 800 °C. This may be due to dehydrogenation, which is also responsible for the maximum at 1100 °C.

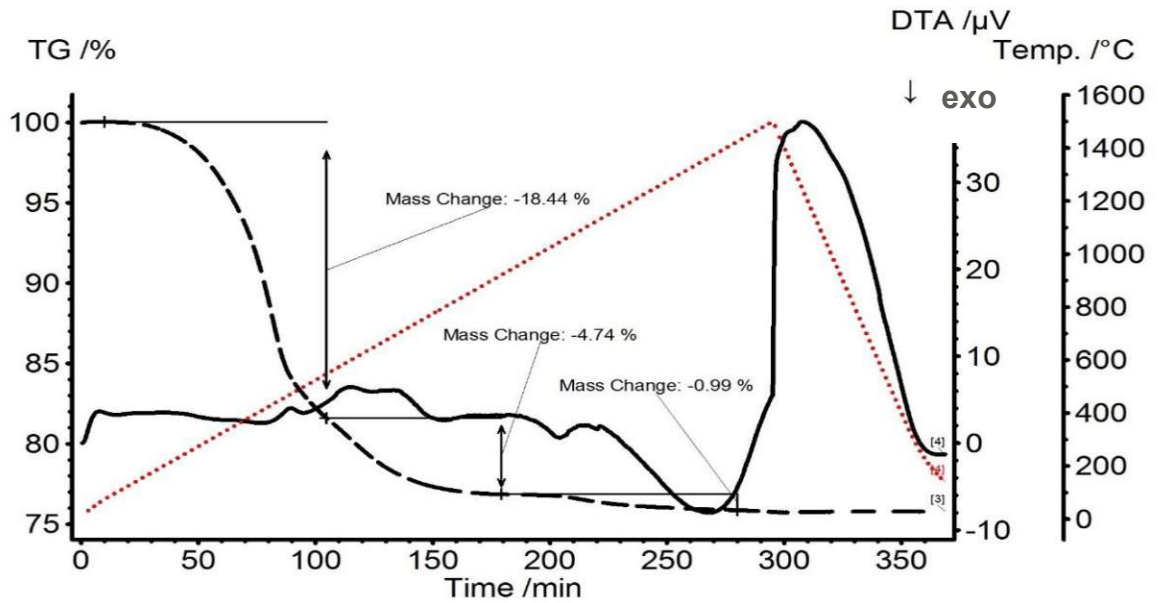


Figure 25: TGA of the SMP-10 PCS crosslinked with 1 wt% DCP (5 K/min, N<sub>2</sub>, T<sub>max</sub>=1500 °C, 93 mg sample)

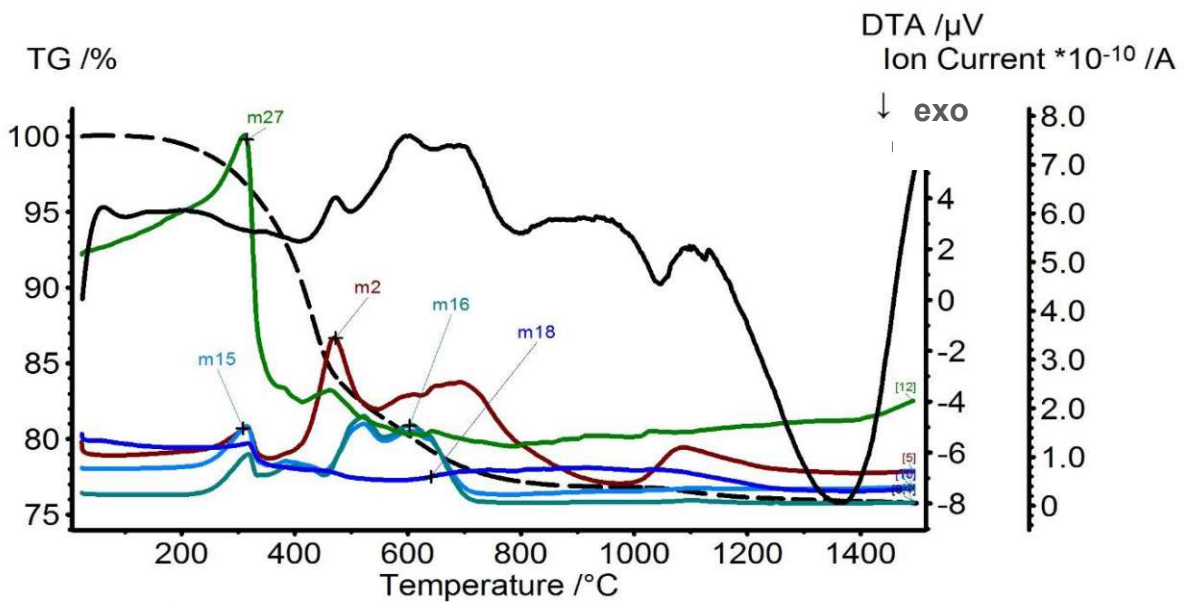


Figure 26: Intense *m/z* signals during TGA-MS of crosslinked PCS



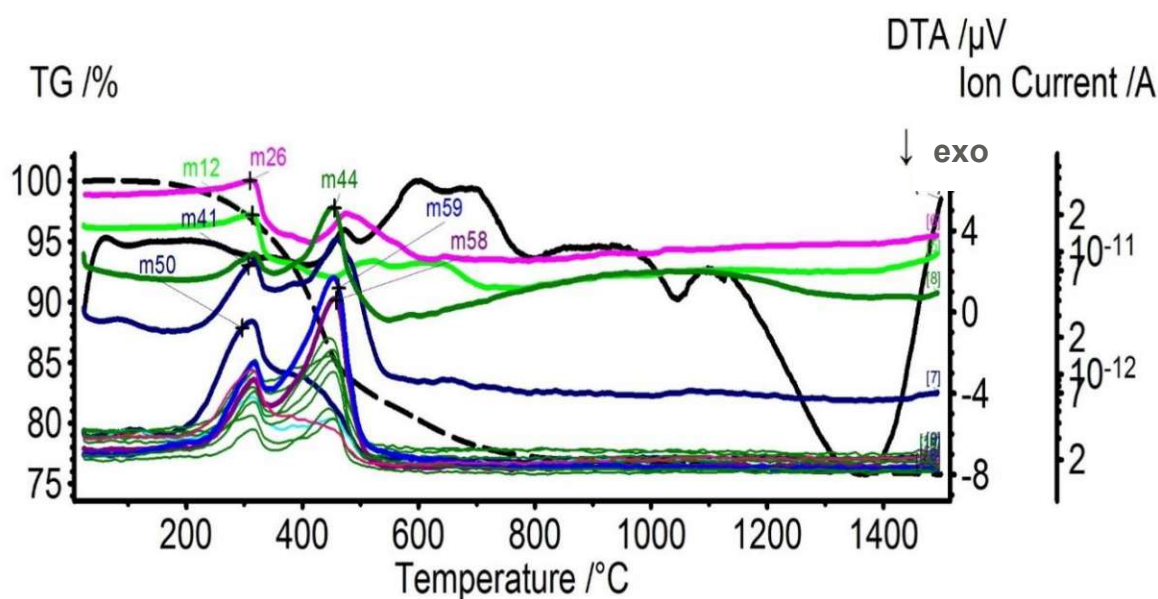


Figure 27: Logarithmic presentation of the low intensity  $m/z$  signals during TGA-MS of crosslinked PCS

## 6.2.4 Elemental composition

The elemental composition of the precursor polymers was determined – oxygen-, nitrogen- and carbon content were measured, the silicon content was calculated.

For orientation, the theoretical compositions of precursor polymers, calculated from the structural formula, and of the ceramics silicon nitride and silicon carbide are given in Table 6. Since the composition should not change significantly by adding the initiator, the values for the polymer-initiator-mixture and the crosslinked polymer should be similar to those of the pure polymer. The experimental data is given in Table 7 and Table 8 and shown in Figure 28 and Figure 29.

Table 6: Composition of the precursor polymers and pure ceramics according to their theoretical structural formula.

	Si, wt%	N, wt%	C, wt%	H, wt%
<b>PSZ</b>	43.65	21.77	26.13	8.46
<b>PCS</b>	58.35	-	32.44	9.21
<b>Si<sub>3</sub>N<sub>4</sub></b>	60.06	39.94	-	-
<b>SiC</b>	70.05	-	29.95	-

## Oxygen

For **PSZ**, the oxygen content slightly increases when adding DCP, there's no significant change during crosslinking. Pyrolysis even leads to a decrease in oxygen content.

The oxygen content in the **PCS** samples is always around 3 wt%, except for the crosslinked sample, being slightly higher with approximately 4 wt%. The values for the pyrolyzed samples tend to be smaller than in the polymer stage, as it can be observed for the PSZ samples too.

## Nitrogen

Due to the liquid state and the moisture sensitivity of the precursor polymers, the nitrogen measurement is delicate. The preparation, which means filling and folding of the tin capsule, is done inside the glove box, which leads to two problems. Due to the liquid state, the capsule can't be folded from the bottom to the top, as it is done for powders to prevent air entrapment. Hence, some nitrogen of the glove box atmosphere is most likely entrapped in the capsule. The second problem is, that if the capsule is not closed completely by folding, the liquid can leak. Whereas nitrogen entrapment leads to an apparently higher nitrogen content of the sample, a leakage functions in the opposite way.

The nitrogen content of the first three stages, **PSZ/PSZ+DCP/PSZcrosslinked**, should be roughly the same with around 22 wt% (Table 6). According to the measurement, this is only the case for the latter two, which are similar with ~18 wt% and 19 wt%. of nitrogen. For an unknown reason, the pure PSZ differs much with only ~11 wt% nitrogen. After pyrolysis, the nitrogen content decreases, which can probably be explained by transamination reactions, that can also be found in the TGA-MS measurements by NH<sub>3</sub> formation.

Since there is no nitrogen present in the structure of **PCS**, the content should be 0 wt% (Table 6). Nevertheless, values around 1.3 wt% were measured for the first three stages (PCS, PCS+DCP, PCScrosslinked) and 0.4 wt% for the pyrolyzed PCS. This could be explained by nitrogen entrapment during preparation as mentioned above, dissolving of the nitrogen atmosphere during storage in the liquid polymer and potentially by the nitrogen atmosphere during pyrolysis.

## Carbon

According to the structural formula, the carbon content of **PSZ** in the first three stages should be around 26 wt%. The measured value for the pure PSZ is low with only 15 wt% and increases unexpectedly much with the addition of the initiator: 21 wt% for PSZ+DCP. The initiator itself



cannot be the reason for an increase of 5 wt%, because only 1 wt% of it was added. There is also a strong increase during the crosslinking step from 21 wt% to 25 wt%. The carbon content decreases after pyrolysis, since during the polymer-ceramic-conversion, decomposition products such as methane, ethane etc. are released.

In case of **PCS**, the carbon content should be around 32 wt%. As for the PSZ, the content is low for the pure polymer with 22 wt% but increases strongly through addition of the initiator (26 wt%) without a plausible reason and again also during the crosslinking process (30 wt%). The pyrolyzed PCS has a composition close to that of silicon carbide and is therefore reasonable.

### Silicon

The main elements present in the samples are silicon, carbon, nitrogen and hydrogen together with low impurities of oxygen. Since the carbon, nitrogen and oxygen contents are measured, the difference to 100 % can be roughly attributed to silicon and hydrogen. During pyrolysis, hydrogen is released. But according to the TGA-MS results, hydrogen formation is finished at ~900 °C, which means that after pyrolysis at 600 °C, there should be some hydrogen left.

Also, for the pure **PSZ**, a N/Si-ratio of 1 was expected due to the backbone of the polymer. Therefore, a value for the Si-content can be calculated using the molar ratio of 1 and the molecular weights of nitrogen and silicon. This was only done for the samples in the polymer state, which means the first three processing stages. For the pure PSZ the two values for the silicon content differ much. The one calculated using the assumed structure would leave approximately 40 wt% open for additional elements, which is not realistic. Since, for the PSZ+DCP and the crosslinked PSZ, the values fit well, it seems as if something went wrong during nitrogen measurement of the pure polymer.

For **PCS** the silicon contents are close to the theoretical value, especially when taking into account that no oxygen impurities are considered in the theoretical formula. The composition of the pyrolyzed sample is close to that of silicon carbide and therefore reasonable.

### Comparison with literature

In Table 9 there are literature values for the same polymer precursors that were used in this work in some of the processing steps. The pure PSZ was investigated by Bazarjani et al. [17]; except for the eye catching high oxygen content of 13 wt% the composition is similar. The pyrolyzed PSZ was investigated by Schitco et al. [14] and Prasad [9], but both used higher

temperatures and argon atmosphere. The carbon content is similar to the experimental results in this work, the nitrogen content is higher in both cases, but they are also differing much compared to each other. The composition of the pyrolyzed PCS differs from the composition measured by Schitco et al., but it is close to that of silicon carbide and therefore reasonable.

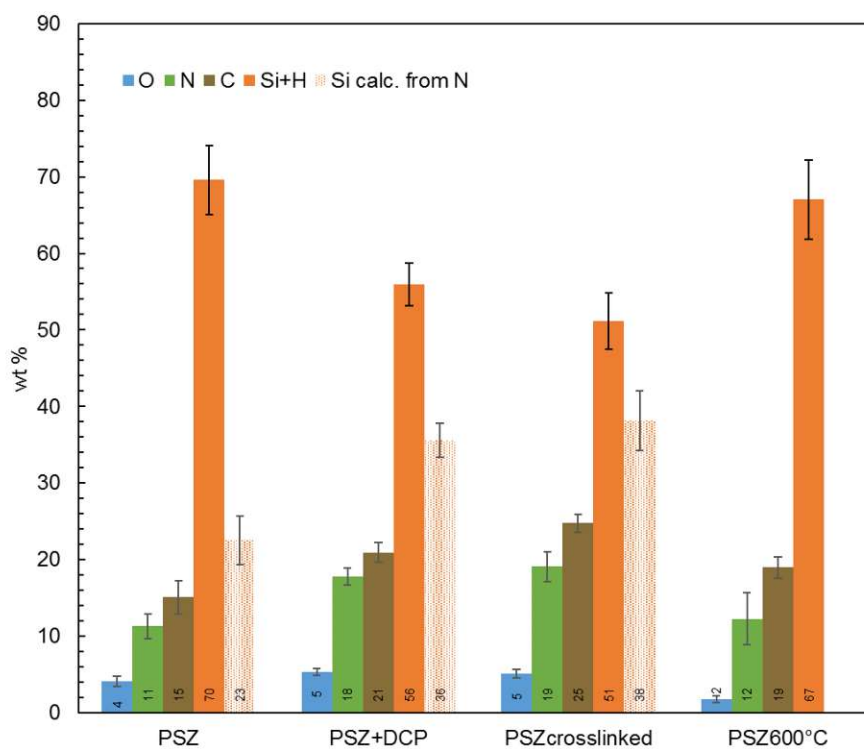


Figure 28: Elemental composition of PSZ in all processing stages; O, N, and C content are measured, Si+H is calculated as remainder to 100 wt%, Sicalc is calculated based on the nitrogen content.

Table 7: Elemental composition of PSZ in all processing stages, O, N, and C content are measured, Si+H is calculated as remainder to 100 wt%, Sicalc is calculated based on the nitrogen content.

	O, wt%	N, wt%	C, wt%	Si+H, wt%	Si calc., wt%
<b>PSZ</b>	4 ± 1	11 ± 2	15 ± 2	70 ± 5	22 ± 3
<b>PSZ+DCP</b>	5 ± 1	18 ± 1	21 ± 1	56 ± 3	36 ± 2
<b>PSZcrosslinked</b>	5 ± 1	19 ± 2	25 ± 1	51 ± 4	38 ± 4
<b>PSZ600°C</b>	2 ± 1	14 ± 2	18 ± 1	66 ± 4	-

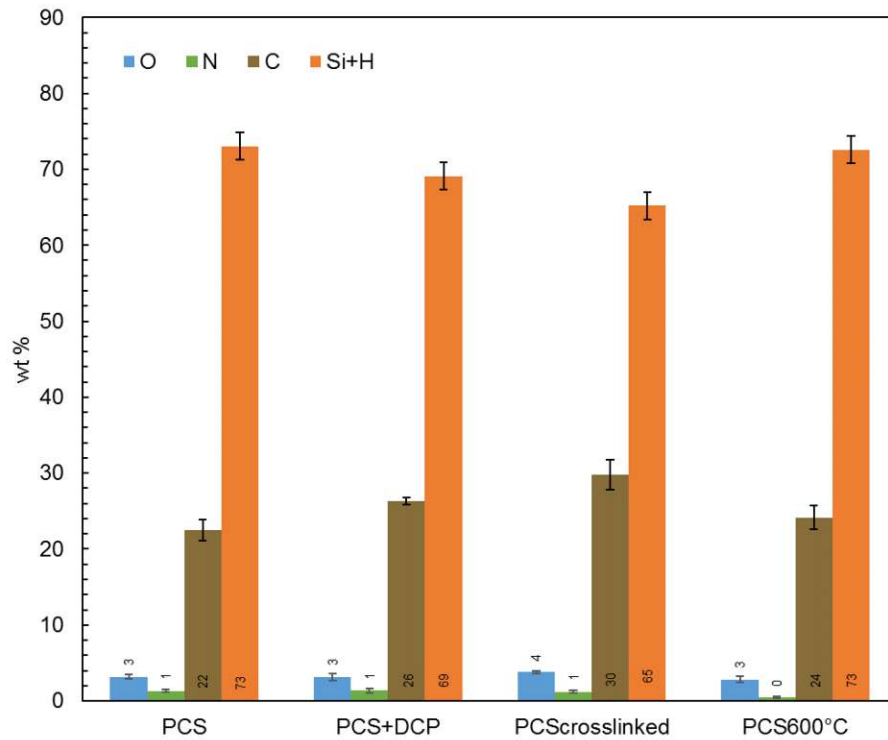


Figure 29: Elemental composition of PCS in all processing stages, O, N, and C content are measured, Si+H is calculated as remainder to 100 wt%,.

Table 8: Elemental composition of PCS in all processing stages, O, N, and C content are measured, Si+H is calculated as remainder to 100 wt%, Sicalc is calculated based on the nitrogen content.

	O, wt%	N, wt%	C, wt%	Si+H, wt%
<b>PCS</b>	3 ± 1	1 ± 0.5	23 ± 2	73 ± 4
<b>PCS+DCP</b>	3 ± 1	1 ± 0.5	26 ± 1	70 ± 3
<b>PCScrosslinked</b>	4 ± 1	0 ± 0.5	24 ± 2	72 ± 4
<b>PCS600°C</b>	3 ± 1	0 ± 0.5	27 ± 4	70 ± 6

Table 9: Elemental composition in literature for comparison

reference	material	conditions	Si, wt%	N, wt%	C, wt%	H, wt%	O, wt%
<b>Bazarjani et al. [17]</b>	PSZ	pure	45	16	19	3.5	13
<b>Schitco et al. [14]</b>	PSZ	Pyrolysis, 750 °C, Ar	53	22	16	0.4	5
<b>Prasad [9]</b>	PSZ	Pyrolysis, 800 °C, Ar	54	26	21	0.6	2
<b>Schitco et al. [14]</b>	PCS	Pyrolysis, 750 °C, Ar	60	0	34	0.7	5

### 6.2.5 Structural investigations

To get information about the bonds present in the ceramics in every processing stage, infrared spectroscopy measurements were conducted. In addition, solid state NMRs,  $^{13}\text{C}$  and  $^{29}\text{Si}$ , were measured to learn about the chemical environment of the elements.

### 6.2.6 ATR-IR

The infrared absorption spectra of the PSZ and PCS samples were recorded for every processing step. The results can be seen in Figure 30 for PSZ and in Figure 31 for PCS, the absorption bands are assigned in the spectrum itself. To facilitate comparison, the spectra are all displayed together with a shift in y-direction. Therefore, the intensity scale isn't numbered. Since none of the bands can be assumed to stay constant, it wasn't possible to normalize the spectra, but the overall intensity was kept in the same range when displaying the spectra.

The functional groups in PSZ can be clearly seen in the spectrum of the pure compound: The N-H band is visible at  $3360\text{ cm}^{-1}$  and  $1180\text{ cm}^{-1}$  and the Si-H group gives a clear signal at  $2150\text{ cm}^{-1}$ . Aromatic C-H vibrations, as originating from the vinyl group, are found at  $3200\text{--}3000\text{ cm}^{-1}$  and at  $1600\text{ cm}^{-1}$ . Aliphatic C-H vibrations can be seen at wavenumbers of  $3000\text{--}2800\text{ cm}^{-1}$  and  $1400\text{--}1250\text{ cm}^{-1}$ . In the fingerprint region, below  $1500\text{ cm}^{-1}$ , there are two main signals, besides the already mentioned ones, caused by Si-N and Si-C vibrations at  $880\text{ cm}^{-1}$  and  $700\text{ cm}^{-1}$  respectively, together with a sharp signal caused by the Si-CH<sub>3</sub> group at

1200  $\text{cm}^{-1}$ . The addition of DCP leads to no change in the spectrum, probably due to the low concentration of only 1 wt% DCP in PSZ. After crosslinking, most bands are staying the same, but the vinyl group, which is supposed to react during crosslinking, can't be found in the spectrum anymore. This confirms that the crosslinking process must have been complete. Also, the other signals, although still present, seem to broaden.

The pyrolyzed sample shows one main broad band with at least two maxima, caused by at least two overlapping bands, most likely  $\nu(\text{Si-N})$  and  $\nu(\text{Si-C})$ . In addition, aliphatic C-H signals around 1300  $\text{cm}^{-1}$  and the Si-CH<sub>3</sub> band can still be found, which shows, that not all organic groups have split off at this pyrolysis temperature. At  $\sim 1100 \text{ cm}^{-1}$ , Si-O- bonds can be seen in all the three stages. The low intensity is confirmed by the elemental analysis.

For PCS, the main peak apart from the fingerprint region is the Si-H band, as for PSZ at 2150  $\text{cm}^{-1}$ . Again, the vinyl group can be found due to peaks in the aromatic C-H region at  $\sim 3200\text{-}3000 \text{ cm}^{-1}$  and at 1650  $\text{cm}^{-1}$ , with the latter band being shifted when compared to the spectra of PSZ (1600  $\text{cm}^{-1}$ ), showing the influence of the chemical environment on the band. Analogous to PSZ, the aliphatic C-H vibrations can be found at wavenumbers of 3000-2800  $\text{cm}^{-1}$  and 1400-1250  $\text{cm}^{-1}$ . In the fingerprint region, there are four main bands, originating from various Si-CH<sub>2</sub> and Si-H vibrations. Again, the addition of DCP doesn't lead to any changes in the spectrum and crosslinking only affects the vinyl group, which disappears, showing that also for PCS, crosslinking was successful and complete. After pyrolysis at 600 °C, there is a broad band with two maxima in the fingerprint region, which is caused by Si-C-H-containing bonds. That there is still hydrogen present in the sample at that stage was already indicated by the TGA-MS measurements and can be seen in the aliphatic C-H vibrations still present after pyrolysis at that temperature. Like for PSZ, there are slight oxygen contaminations visible in all processing stages, which is in accordance with the results of the elemental composition.

The bands are comparable to IR-measurements conducted for the same precursors used in this work, for PSZ for example by Bazarjani et al. [17] or Prasad [9], the bands of the pure PCS to Kaur et al. [120]

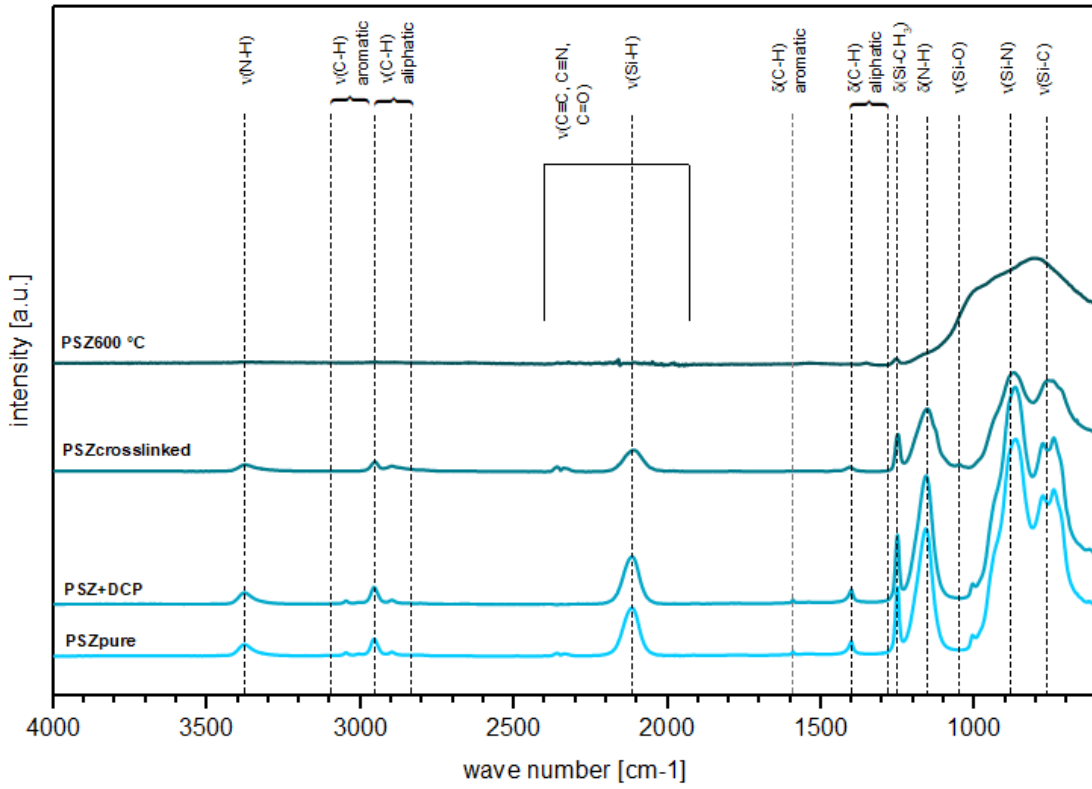


Figure 30: ATR-IR spectra of PSZ in all processing stages.

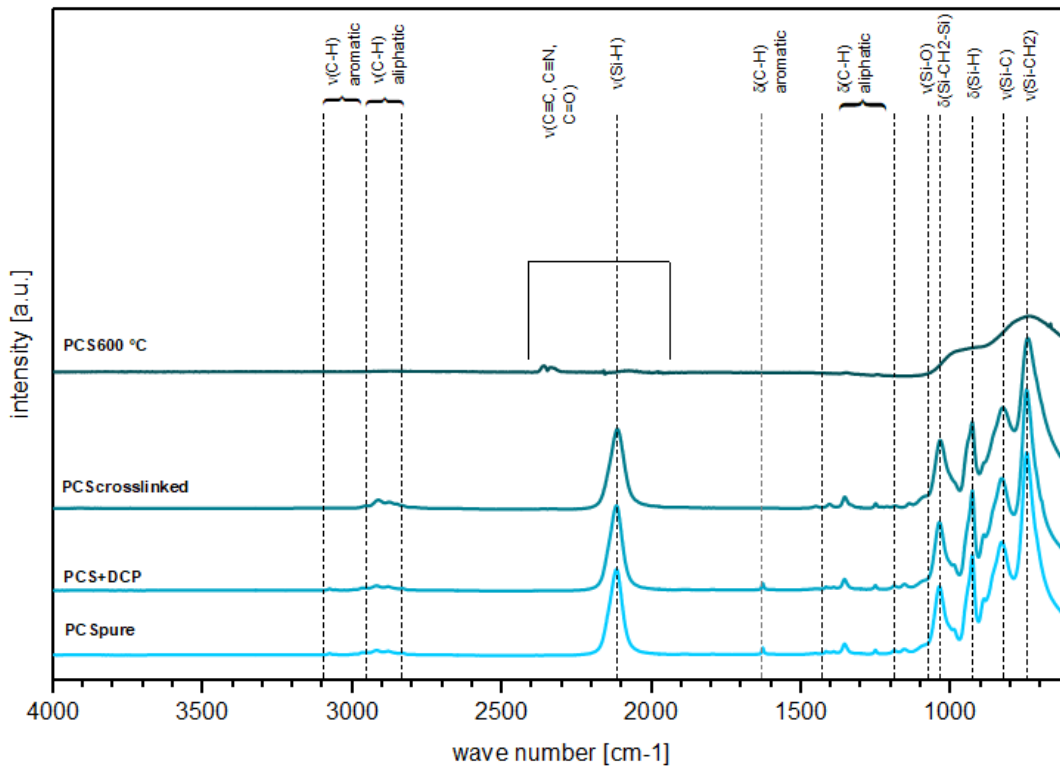


Figure 31: ATR-IR spectra of PCS in all processing stages.

## 6.2.7 Solid state NMR

To get more information about the structural elements present as well as the chemical environment of the elements present in each preceramic polymer and in the amorphous ceramics after pyrolysis, solid state NMRs were recorded ( $^{13}\text{C}$  and  $^{29}\text{Si}$ ).

### 6.2.7.1 PSZ

The  $^{13}\text{C}$ -NMR spectrum, which is shown in Figure 32 in all processing stages of the pure PSZ shows two regions of signals, one around 0 ppm, which is caused by the Si-CH<sub>3</sub> group. This peak is split up, which is due to the different chemical environment, whether a hydrogen or a vinyl group is attached to the silicon. The second region of chemical shift is around 120-140 ppm, originating from the C-atoms of the vinyl group – therefore also split up in two peaks (which each are split up, too) at 125 ppm and 135 ppm. When comparing the  $^{13}\text{C}$ -NMR spectra of the pure and the crosslinked PSZ, the main difference is the vanishing of the peaks correlated with the vinyl groups at 120-140 ppm. Since the crosslinking is achieved via the vinyl groups using a radical initiator, NMR results confirm that crosslinking was successful and complete. In the spectrum of the pyrolyzed sample, there is not just the peak around 0 ppm anymore, but also a broad peak around 135 ppm, which can be attributed to amorphous carbon, together with spinning side bands (marked by an asterisk) originating from chemical shift anisotropy. [15]

The  $^{29}\text{Si}$ -NMR spectrum (cf. Figure 33) of the pure PSZ consists of one big peak at -17 to -25 ppm and a small one with a maximum at 32 ppm. The big one can be attributed to the typical Si-environment in the pure poly(vinyl)silazane –SiCH<sub>3</sub>H-NH- [9], the smaller peak could be caused by SiHC(sp<sup>2</sup>)N<sub>2</sub> according to Gérardin et al. [85], which is in accordance with the literature. [9] In the crosslinked stage, two new peaks appear. The bigger one at 0 to -10 ppm which, according to Gérardin et al. [85] and Riedel et al. [23], can be attributed to SiC(sp<sup>3</sup>)<sub>2</sub>N<sub>2</sub>, could be due to the double bonds in the vinyl groups opening up during crosslinking. After pyrolysis at 600 °C there is one broad peak with several shoulders, which indicates overlapping bands. Therefore, deconvolution using Gaussian approximation was done with three maxima at -10, -24 and -37 ppm. These fitted the data best. Si<sub>3</sub>N<sub>4</sub> with the tetrahedral SiN<sub>4</sub> structure occurs typically at -47 ppm. Since there is only a minor part of the signal in this region, SiN<sub>4</sub> tetrahedra are not the main structural element. The more N-atoms are replaced by C-atoms, the further the shift towards 0 ppm, whereas oxygen substitution shifts to more negative values. So, according to literature, SiN<sub>3</sub>C typically shows at -25 to -40 ppm, SiC<sub>2</sub>N<sub>2</sub> at -5 to -25 ppm, SiC<sub>3</sub>N at 30 to -5 ppm and SiC<sub>4</sub> tetrahedra at -10 to -25 ppm. [123] According to these values, the PSZ

pyrolyzed at 600 °C consists mainly of mixed silicon carbon and nitrogen bonds,  $\text{SiN}_3\text{C}$ ,  $\text{SiN}_2\text{C}_2$  and  $\text{SiNC}_2$ . Although the curve fitting doesn't include silicon carbide and silicon nitride (tetrahedra), it is likely that at least a small amount of these structural elements are also present.

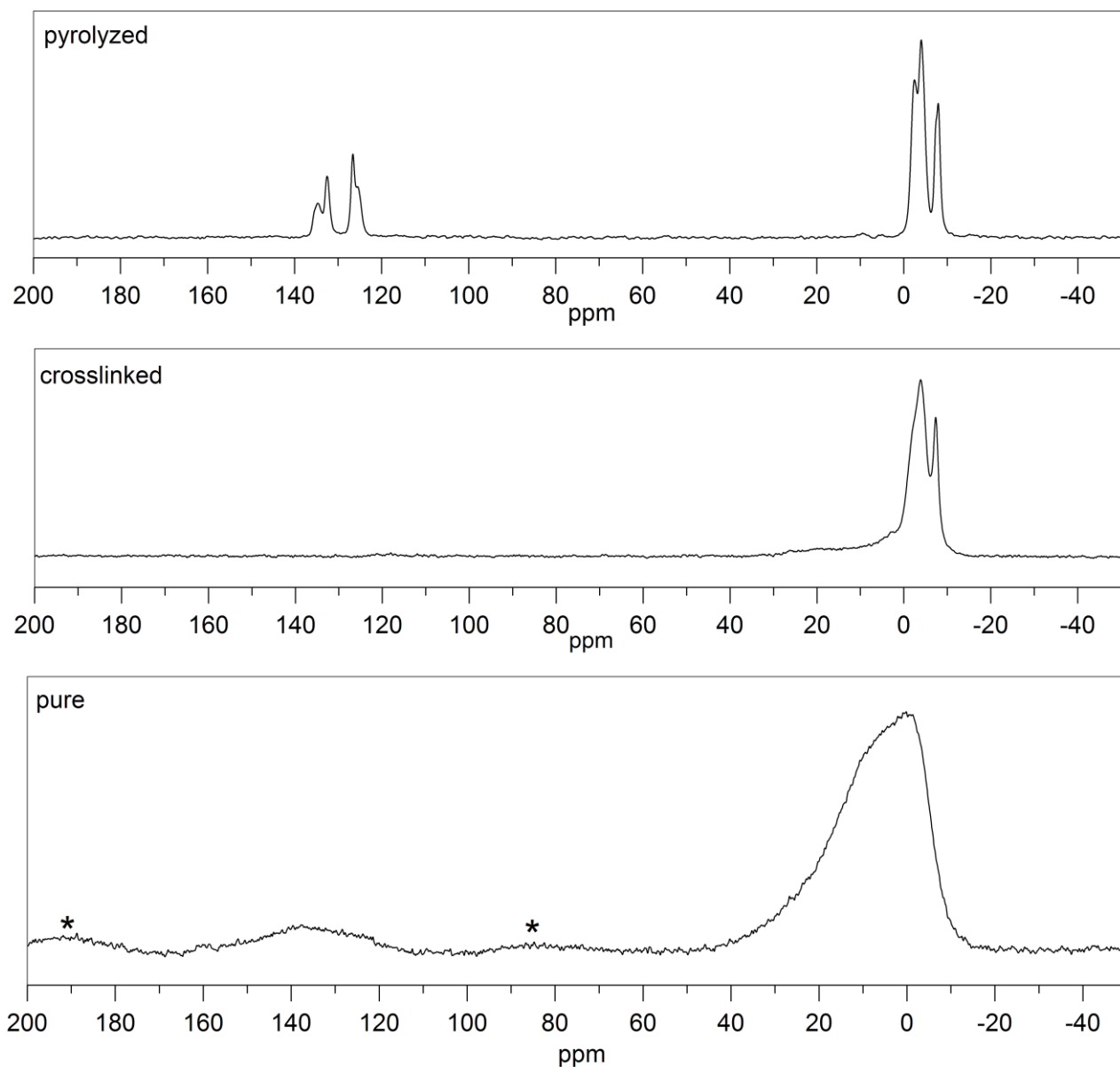


Figure 32:  $^{13}\text{C}$  solid state NMR of PSZ in all three processing stages. Spinning side bands are marked with an asterisk.



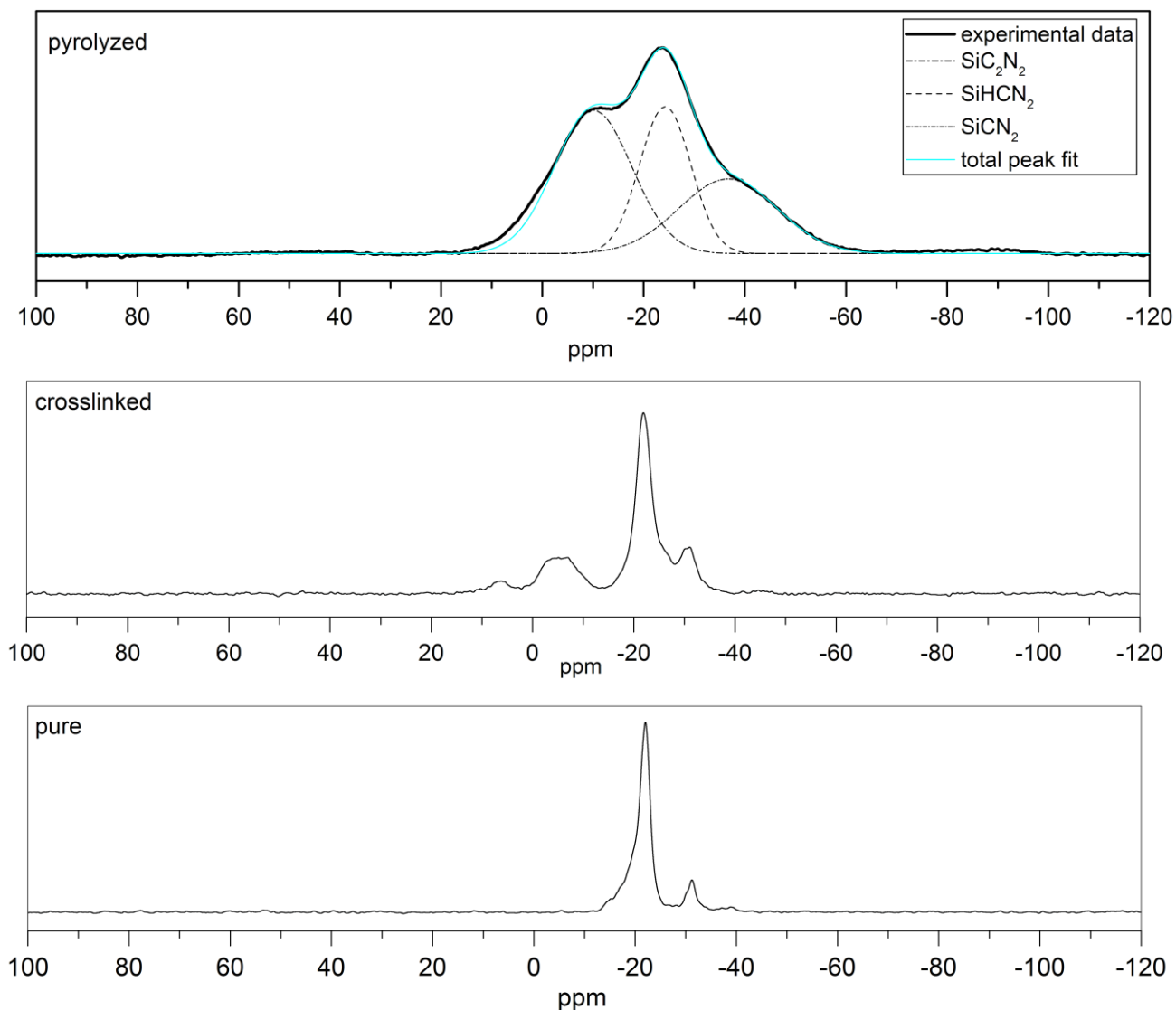


Figure 33:  $^{29}\text{Si}$  solid state NMR of PSZ in all three processing stages.

### 6.2.7.2 PCS

The NMR spectra of PCS in the three processing stages can be seen in Figure 34 and Figure 35.

In the  $^{13}\text{C}$  NMR spectrum of the pure PCS, the vinyl groups can be found at 108 and 128 ppm, the backbone of the polymer consisting of  $-\text{Si}-\text{CH}_2-\text{Si}-$  units shows at 0 to -20 ppm. The additional peaks might be due to oxygen contamination. During crosslinking, the signals of the vinyl-group vanish, which shows that crosslinking is complete. The pyrolyzed PCS shows only one very broad signal from 30 to -15 with a maximum at 8 ppm, which originates most likely from C-atoms in Si-based networks.  $\text{SiC}_4$  tetrahedra, which build silicon carbide, give signals

from 13-23 ppm, which is close to the value of our sample. The differences might be caused by the slightly different surrounding due to nitrogen and oxygen contaminations and the presence of residual hydrogen. In contrast to the large amount of amorphous carbon in the sample prepared by Schitco et al. [15], there is no  $sp^2$  hybridized C present in the sample prepared in this work, which means that all of the C-atoms are bonded to Si, N, H or O. This could be caused by lower processing temperatures in our case, which lead to incomplete decomposition of the organic parts of the polymer resulting in less amounts of free C.

The  $^{29}\text{Si}$  NMR spectrum of the pure PCS is similar to the one Wen et al. [19] measured of the same precursor polymer (SMP-10, Starfire Systems). It consists mainly of three peaks, the one at -11 ppm originates from  $\text{SiC}_3\text{H}$ -moieties, the biggest one at -34 ppm from  $\text{SiC}_2\text{H}_2$ -units and the third one at -60 and -62 ppm from  $\text{CSiH}_3$  groups. In the crosslinked sample, the signals are the same as in the pure PCS. The spectrum of the PCS sample pyrolyzed at 600 °C shows only one very broad signal from 25 to -25 ppm with a maximum at -1.5 ppm, which would according to [123] be the range of  $\text{SiC}_3\text{N}$ . Since there are only ~0.5 wt% N in the pyrolyzed PCS according to elemental analysis, the  $\text{SiC}_3\text{N}$  moieties can't make up the whole sample. It is more likely that the signal is caused by  $\text{SiC}_4$  tetrahedra, which according to Williams et al. [94] can occur at 0 ppm (in contrast to [123]) and just a small contribution by nitrogen containing units. Schitco et al. [15] investigated the same polycarbosilane, but used 750 °C as pyrolysis temperature in argon atmosphere. Still, they got a spectrum similar to that of the sample sample prepared in this work, with just one broad signal ranging from 50 ppm to -50 ppm with the maximum at -6 ppm, which they attribute to mainly  $\text{SiC}_4$  and low amounts of  $\text{SiC}_3\text{O}$ .

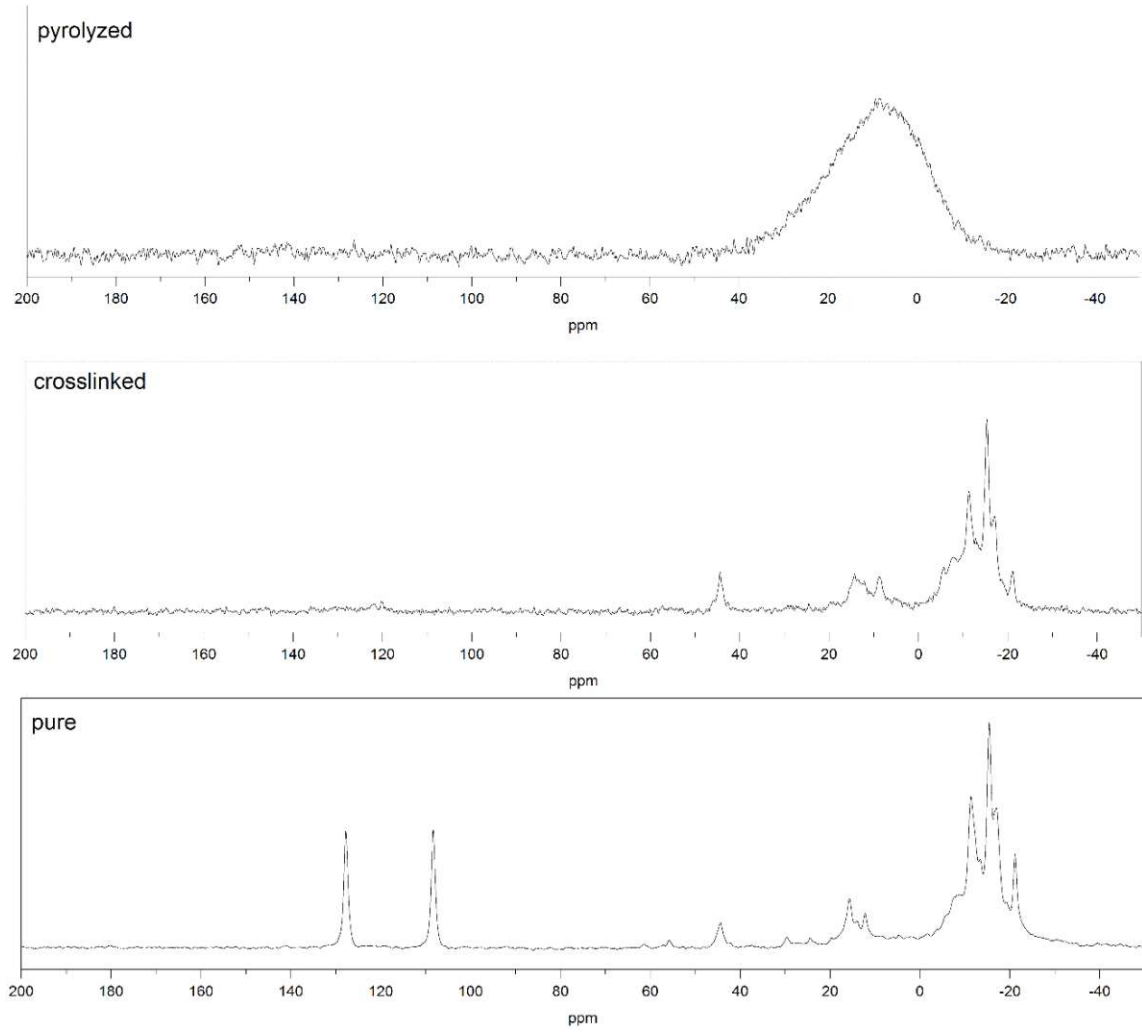


Figure 34:  $^{13}\text{C}$  solid state NMR of PCS in all three processing stages.

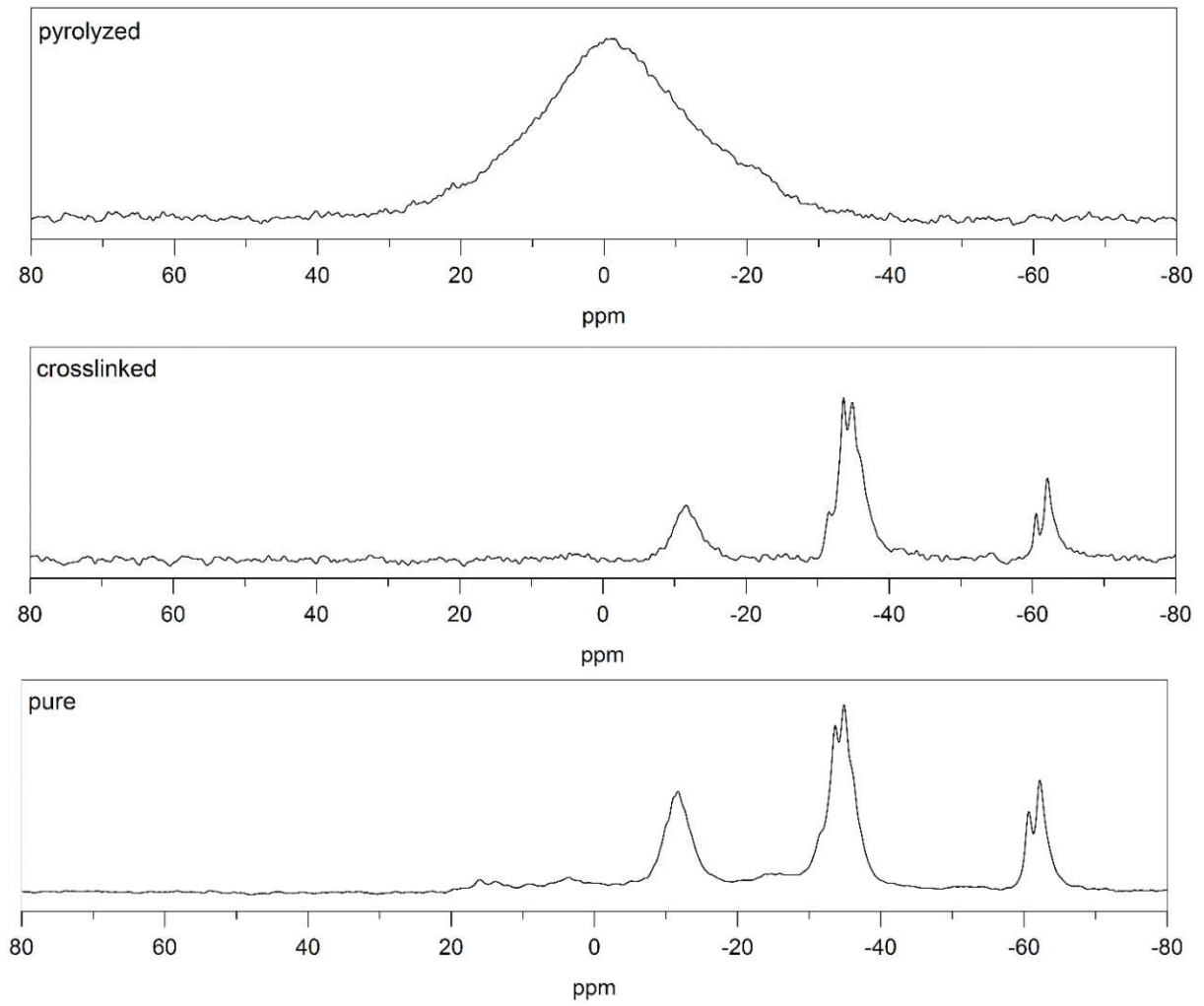


Figure 35:  $^{29}\text{Si}$  solid state NMR of PCS in all three processing stages.

## 6.2.8 Porosity in the amorphous ceramics

The pore characteristics were investigated using gas sorption with nitrogen at 77 K as well as CO<sub>2</sub> at 273.15 K, the latter one only for PSZ.

### 6.2.8.1 N<sub>2</sub> physisorption

The isotherm of PSZ600°C, which can be seen in Figure 36, has a sharp rise at very low relative pressures before reaching a plateau and is completely reversible, which is a typical type I isotherm. Type I isotherms are originating from microporous materials, which is therefore showing that the SiCN ceramic at these pyrolysis conditions has pores in the micropore range. From the linear range in the low pressure region, it is possible to estimate the specific surface area using the BET-method. The BET specific surface area of PSZ600°C is satisfactory with  $195 \pm 6 \text{ m}^2/\text{g}$ , which is also in accordance with the literature. [12] Using different methods, in this case, an NLDFT-model, it is possible to calculate the pore size distribution from the isotherm. The resulting pore size distribution as well as the cumulative pore volume are displayed in Figure 37, for the micropore range up to 2 nm. The maximum of the PSD is with a value of 0.86 nm in the micropore range. The micropore volume (cumulative volume in the graph) is around  $0.85 \text{ cm}^3/\text{g}$ .

The isotherm of PCS after pyrolysis at 600 °C, which is shown in Figure 38, in contrast, is a type II isotherm, caused by macro- or nonporous materials. This can be seen from the rather continuous increase of the adsorbed quantity with increasing relative pressure, as well as the low overall quantity adsorbed per gram of the sample. This is confirmed by the PSD (cf. Figure 39), which shows no pores below 2 nm, and only a minor volume in the mesoporous range with a maximum at 3.3 nm. The cumulative volume over the whole range of 0.36-50 nm yields only  $0.01 \text{ cm}^3/\text{g}$ , so one magnitude lower than the micropore volume of PSZ.

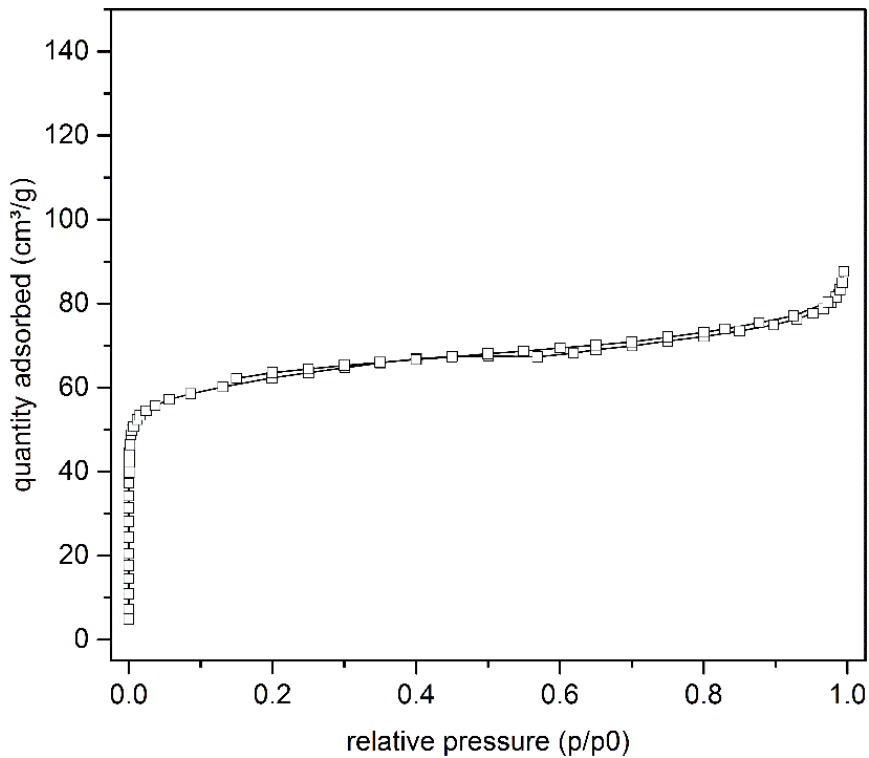


Figure 36: N<sub>2</sub> physisorption isotherm of PSZ600°C.

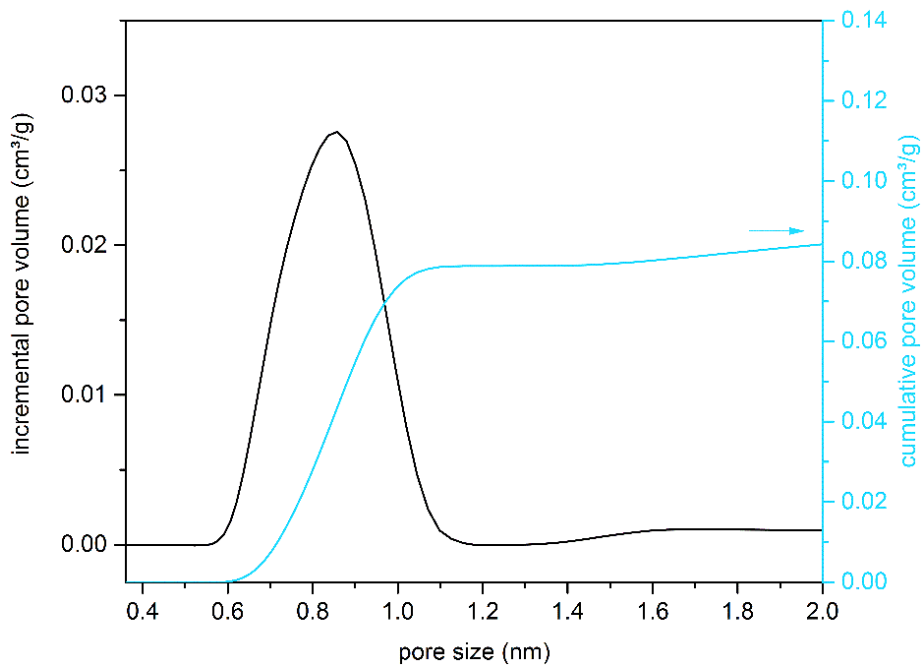


Figure 37: PSD and cumulative pore volume for PSZ600°C.

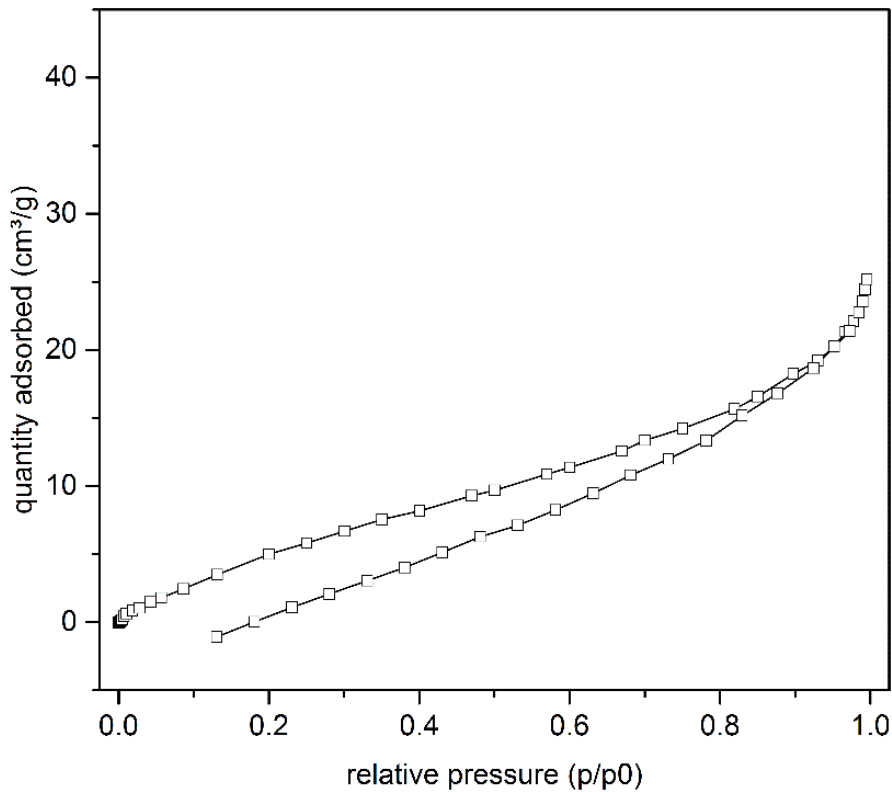


Figure 38: N<sub>2</sub> physisorption isotherm of PCS600°C.

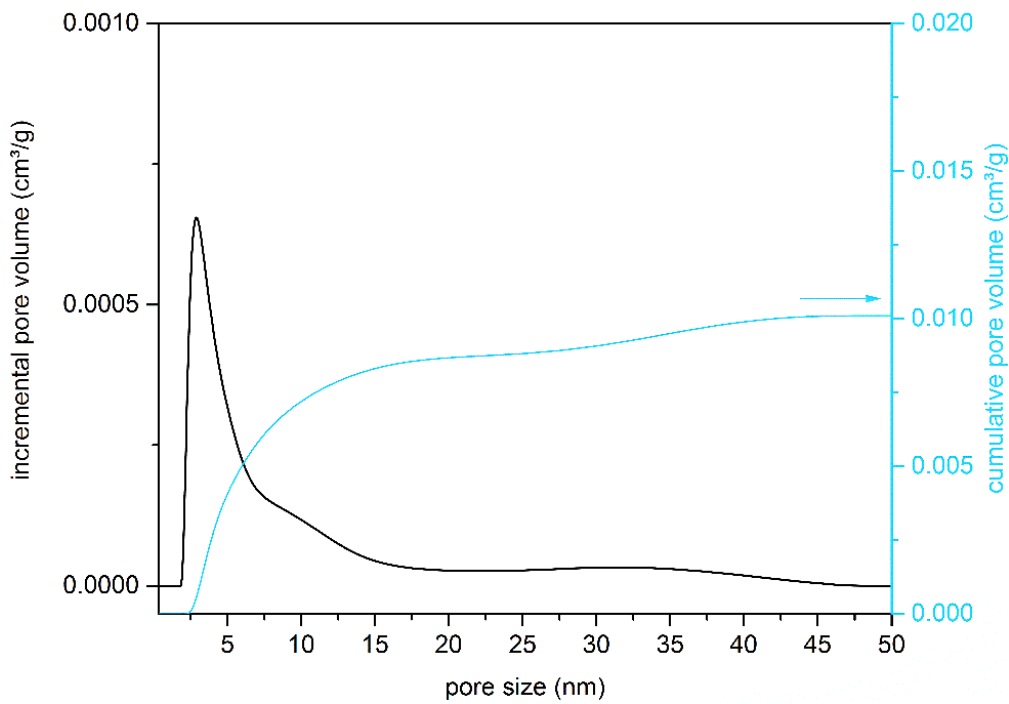


Figure 39: PSD and cumulative pore volume for PCS600°C.

### 6.2.8.2 CO<sub>2</sub> physisorption

Since physisorption can also be carried out using different gases than N<sub>2</sub> such as Ar, Kr, CO<sub>2</sub> reaching other pore size ranges or suiting materials better, the benchmark sample PSZ600°C was also investigated using CO<sub>2</sub>-physisorption. These measurements are carried out at 0 °C, using an ice bath. Since there is no additional pressure applied during the measurement, only relative pressures of  $p/p_0=0.03$  can be reached due to the saturation pressure of CO<sub>2</sub>. This limits the pore size that can be investigated to approximately 1 nm as upper limit. But the great benefit of CO<sub>2</sub> measurements is that due to the higher temperatures during the measurement, they take less time. Since these measurements focus on the ultramicropore range, they are a good complimentary method for the N<sub>2</sub>-measurements.

The same sample was used for both measurements, the degassing step was carried out in the same way. A pressure table for CO<sub>2</sub> given by the ASAP2020 software was used for the CO<sub>2</sub> measurement. The adsorption isotherm for CO<sub>2</sub> can be seen in Figure 40. In Figure 41 is the pore size distribution of PSZ600°C is shown for both gases. The model that was used was either *N<sub>2</sub>@77 on Carbon Slit Pores* or *CO<sub>2</sub>@273 on Carbon, Slit Pores* by Micromeritics. The pore size maximum is only slightly shifted to a smaller value for the measurement with CO<sub>2</sub>, the lack of the other higher maxima that can be found with N<sub>2</sub> as analysis gas is due to the limited pressure range of CO<sub>2</sub>. Regarding the overall micropore volume, there is not really a difference, since both samples yield micropore volumes of 0.06 cm<sup>3</sup>/g.

Overall it can be stated that there is not much of a benefit when using CO<sub>2</sub> in this case. It could become more interesting if the pore size could be shifted to even lower values.



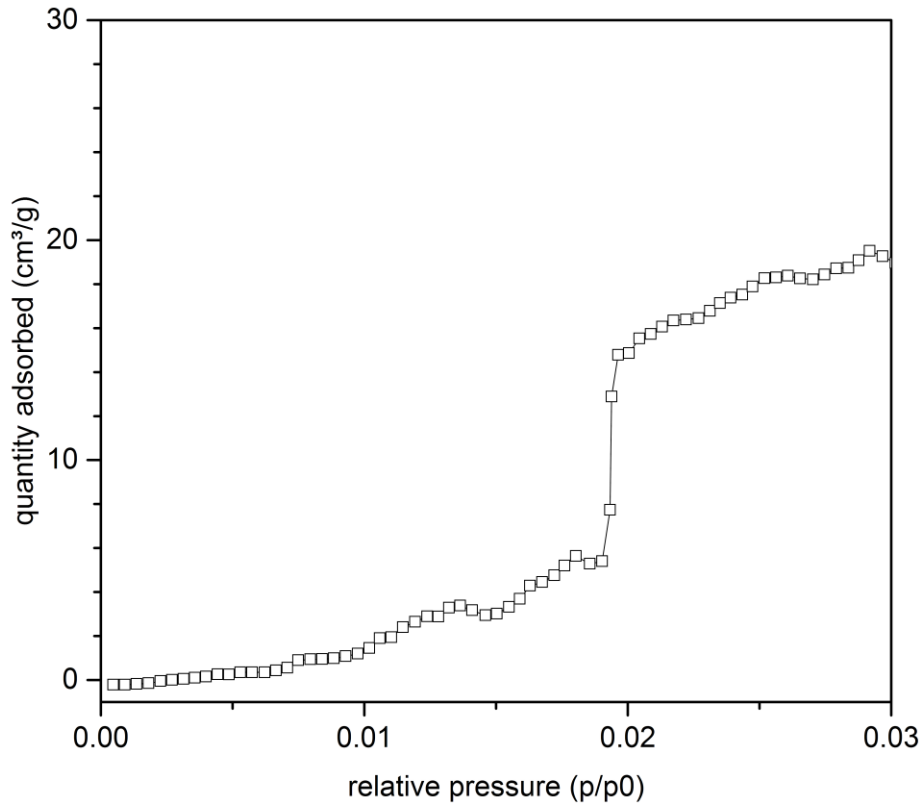


Figure 40: CO<sub>2</sub> physisorption isotherm of PSZ600°C.

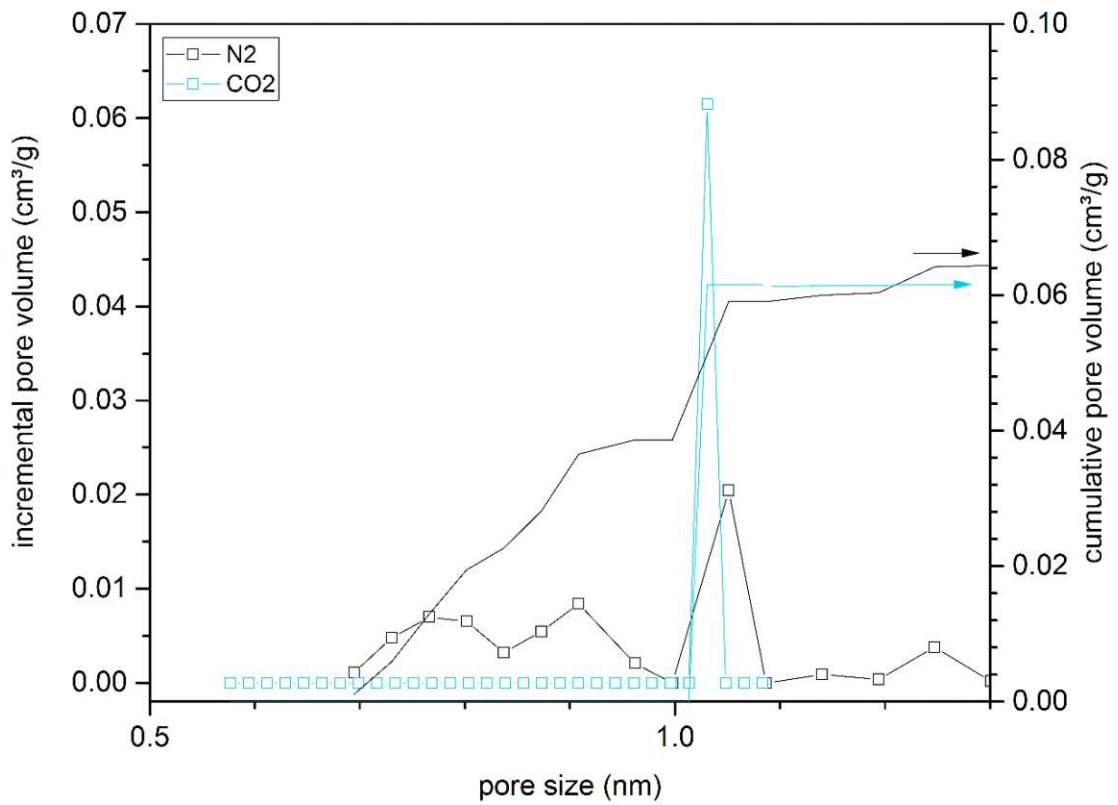


Figure 41: Comparison of the PSD of PSZ600inert using CO<sub>2</sub> and N<sub>2</sub> as adsorption gas.

### 6.3 Summary and conclusions – Focus I

A full characterization of the two polymer precursors and their products if undergoing a standard procedure was done using various characterization methods.

According to TGA, the ceramic yield is around 75 % for both polymers. The polymer-ceramic-conversion takes place between 500-800 °C for PSZ and 450-700 °C for PCS if methane formation is used as indicator.

The elemental analysis gives reasonable results for both of the polymers in the pyrolyzed stage. Also, the composition of the pure polymer is similar to literature, except for the nitrogen value in case of PSZ.

Results of the ATR-IR measurements are comparable to results reported in the literature. The disappearance of vinyl-related bands after crosslinking proves that crosslinking was successful and complete. The low oxygen content measured during element analysis is confirmed by the IR measurements.

Solid state NMR investigations showed that PSZ600°C consists of mixed Si-C-N-(H) tetrahedra. Surprisingly, there is also a free carbon phase present, already at these pyrolysis temperatures. PCS600°C consists most likely of SiC<sub>4</sub> tetrahedra at this pyrolysis temperature; there was no free C phase found.

The N<sub>2</sub>-physisorption investigations showed the expected type I isotherm for the pyrolyzed PSZ600°C handled in inert atmosphere with a main pore size around 0.86 nm. The BET specific surface area of PSZ600°C is satisfactorily high at 195 ± 6 m<sup>2</sup>/g, which is also in accordance with the literature. [12] CO<sub>2</sub> physisorption showed no benefits in comparison to the nitrogen measurements, which is why N<sub>2</sub> is preferred as adsorbate, since it gives information about a wider pore size range.

PCS in contrast follows a type II isotherm and according to this is non- or macroporous. The BET surface area is low; the pore size is in the mesoporous range.

According to the results so far, only PSZ could possibly be used as membrane material if prepared under these conditions.

## 7. FOCUS II – MODIFICATION IN THE PRECURSOR STAGE BY INCREASE OF MOLECULAR WEIGHT AND COPOLYMERISATION

In a first step, the influence of the precursor structure on the properties of the pyrolyzed ceramics was investigated. Therefore, the structure of the commercially available polyvinylsilazane PSZ was modified in various ways. The experiments were limited to PSZ, to check, whether there is an influence or not.

It was shown that the molecular weight of a polymer precursor has an influence on ceramic yield since there is a competition between crosslinking reactions and distillation of low molecular weight components in the low temperature range. [13, 24]

During the Bachelor thesis of Toni Bakovic [124], copolymers of PSZ and PS were prepared. Also, to have a bigger variety of materials, the copolymers were also prepared with two higher molecular weight versions of PSZ instead of the as received one. Two different approaches were used to increase the molecular weight of Durazane HTT1800, one using RAFT polymerization as described by Nguyen [125]. Selective cross-linking via the N–H and Si–H groups with tetra-n-butylammoniumfluoride (TBAF) as a catalyst was done as described by Flores et al. [126]

Since, as mentioned above, molecular weight has an influence on ceramic yield and possibly on pore size, six of the materials prepared during the Bachelor thesis were also investigated on their applicability for the membrane preparation.

### 7.1 Experimental Procedure – Focus II

#### 7.1.1 Materials

The following materials were used for the experiments:

- Poly(vinyl)silazane PSZ  
(Durazane HTT 1800, durXtreme GmbH)  
as polymer precursor
- High molecular weight PSZ prepared after Nguyen (PSZhm-N) or Flores (PSZhm-F)  
as polymer precursor
- Copolymers of PSZ, PSZhm-N and PSZhm-F with 2 equivalents of styrene (CoH,  
CoN and CoF respectively) as polymer precursor
- Dicumylperoxide DCP (>97,0%, Fluka) as initiator

### 7.1.2 Molecular weight of the materials

The molecular weight of the six materials was measured via gel permeation chromatography (GPC). GPC is an analytical technique that separates molecules in polymers by size and provides the molecular weight distribution of a material. GPC is also sometimes known as size exclusion chromatography (SEC). The results are taken from the bachelor thesis of Toni Bakovic [124] and are listed in Table 10.

Table 10: Molecular weight of the six materials, PSZ, PSZhmN, PSZhmF, and the copolymers CoPSZ, CoN, CoF; average molecular weight ( $M_n$ ), weight average molecular weight ( $M_w$ ), z average molecular weight ( $M_z$ ).

	sample	$M_n$ , Da	$M_w$ , Da	$M_z$ , Da
unaltered	PSZ	801	1179	1822
high molecular weight PSZ	PSZhmN	1284	3010	6910
	PSZhmF	953	1667	2955
copolymers with styrene	CoPSZ	10108	80207	256949
	CoPSZ-N	8631	34847	107647
	CoPSZ-F	425005	466807	518304

### 7.1.3 Crosslinking and pyrolysis

Since the hm-versions as well as the copolymers were highly viscous, they were dissolved in toluene and 1 wt% DCP was added. The solvent was then carefully evaporated in the furnace with a low temperature heating step. The further processes are following the standard procedure described in section 5.2.2 and 5.2.3

## 7.2 Results – Focus II

### 7.2.1 Optical appearance

After crosslinking, the polymers are solid and brittle (Figure 42). Whereas the pure polysilazanes were clear, foaming occurred in case of the copolymers. The reason for that is most likely the use of a solvent and the high viscosity of the solution. Although a solvent was used for the PSZhm-N too, the lower viscosity might be a reason for the lack of foaming. After pyrolysis, all ceramics were dark brown in colour. An example is given in Figure 43.

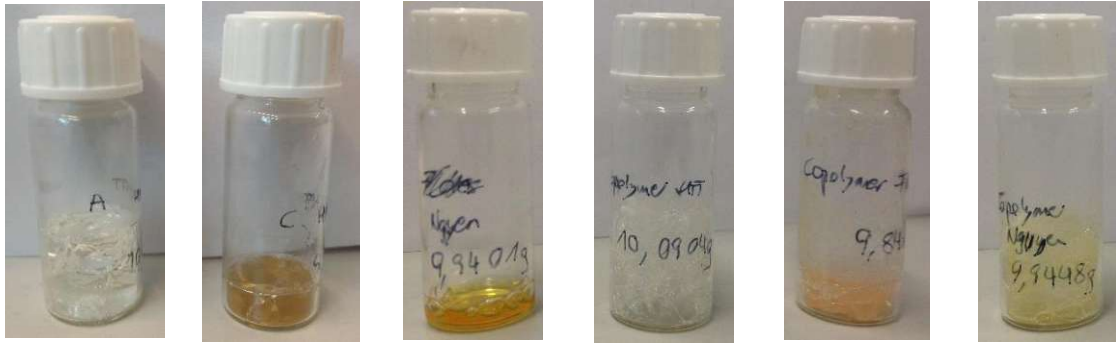


Figure 42: Crosslinked polymers; f.l.t.r.: PSZ, PSZ-hmF, PSZ-hmN, CoPSZ; CoPSZ-F, CoPSZ-N.



Figure 43: Exemplary picture of the samples after pyrolysis.

### 7.2.2 Mass change

When compared to the PSZ used as received, the high molecular versions show a similar mass loss in both stages (see Table 11). In contrast to that, the mass loss of the copolymers is much higher, with 5 to 13 % already during crosslinking and another ~90 % during pyrolysis. The mass loss during crosslinking might be due to residual solvent or maybe residual trapped monomer (styrene). Two thirds by weight are supposed to be polystyrene parts in the copolymer. If a complete decomposition of these parts is assumed, it would lead to a weight loss of 66.6 %. Since the PSZ itself has a ceramic yield of 75%, this adds an additional loss of 8 % ( $33.3 \% \text{ PSZ} \times 0.25$ ). The therefrom expected loss of 74 % during pyrolysis is even exceeded during experiments.

Table 11: Mass change of PSZ, the high molecular weight compounds and their copolymers with styrene during crosslinking and pyrolysis.

	sample	$\Delta m_{\text{pure-crossl.}}, \%$	$\Delta m_{\text{crossl.-pyro}}, \%$
unaltered	PSZ	-2.2	-26.0
high molecular weight PSZ	PSZhmN	-2.1	-25.0
	PSZhmF	-0.9	-20.0
copolymers with styrene	CoPSZ	-12.5	-94.0
	CoPSZ-N	-7.9	-87.8
	CoPSZ-F	-5.0	-91.1

### 7.2.3 Elemental analysis

The elemental composition of the precursor polymers was determined. The oxygen-, nitrogen- and carbon content were measured, the remaining part to 100% was assumed as Si+H content.

The results of the elemental analysis are given in

Table 13 and shown in Figure 44. The theoretical composition of PSZ, styrene and the 1:2 copolymer is given in Table 12.

Table 12: Calculated elemental composition of PSZ, styrene and copolymer.

	Si, wt%	N, wt%	C, wt%	H, wt%
<b>PSZ</b>	43.65	21.77	26.13	8.46
<b>Styrene</b>	-	-	92.26	7.74
<b>PSZ:Styrene; 1:2</b>	14.55	7.26	70.22	8.04

### **Oxygen**

The oxygen content of the high molecular weight PSZ is initially higher than the one of the as received PSZ, which is due to handling during the molecular weight increasing step. For the copolymers, the oxygen content is lowered when compared to the related PSZ species, which can be explained by the addition of two equivalents styrene, which dilute the oxygen that is present in the precursor. After pyrolysis, most of the polystyrene component has decomposed, which leads again to high oxygen values. After pyrolysis it's above 10 wt%, which is partly due to decomposition of the styrene parts and therefore reduction of the C-content in the remaining SiCN. Also, the handling before and after pyrolysis can contribute to the high oxygen content.

### **Nitrogen**

The samples with increased molecular weight only show minor differences when compared to the as received PSZ. The nitrogen content of the pure and crosslinked copolymer samples is low with just 2 wt% for the same reason as the oxygen content – the added styrene consists only of carbon and hydrogen and therefore “dilutes” the nitrogen present in PSZ. The nitrogen content of the pyrolyzed copolymer samples is comparable to that of PSZ, which confirms the assumption that the polystyrene parts are completely burnt out.

### **Carbon**

Especially in the pure polymer stage, the C-content of the high molecular weight samples is higher than the one of the as-received PSZ. In the crosslinked and pyrolyzed state, the differences are minor. For the copolymers the C-content is higher than expected. This could be due to inhomogeneities in the copolymer itself, higher deviation of the measurement due to the extremely high contents (the highest calibration standard is SiC) or weighing errors due to the low sample weight. Although it's ca. 5-10% higher than expected, it is in a reasonable range for 2 equivalents styrene. After pyrolysis, the C-content is similar to the ones of PSZ and high-molecular weight compounds, which leads to the assumption that the polystyrene parts are decomposed during pyrolysis.

Table 13: Elemental composition of PSZ, the high molecular weight compounds and their copolymers after various processing stages.

	O, wt%	N, wt%	C, wt%	Si+H, wt%
<b>PSZ</b>	4 ± 1	11 ± 2	15 ± 2	70 ± 5
<b>PSZcrosslinked</b>	5 ± 1	19 ± 2	25 ± 1	51 ± 4
<b>PSZ600°C</b>	2 ± 1	14 ± 2	18 ± 1	66 ± 4
<b>PSZhmF</b>	11 ± 1	15 ± 1	25 ± 1	49 ± 3
<b>PSZhmFcrosslinked</b>	6 ± 1	20 ± 1	25 ± 1	49 ± 3
<b>PSZhmF600°C</b>	12 ± 1	18 ± 2	17 ± 2	53 ± 5
<b>PSZhmN</b>	6 ± 1	15 ± 1	28 ± 3	49 ± 5
<b>PSZhmNcrosslinked</b>	4 ± 1	14 ± 1	27 ± 2	55 ± 4
<b>PSZhmN600°C</b>	3 ± 1	11 ± 1	21 ± 2	65 ± 4
<b>CoPSZ</b>	2 ± 1	2 ± 1	82 ± 2	14 ± 4
<b>CoPSZcrosslinked</b>	2 ± 1	2 ± 1	87 ± 2	8 ± 4
<b>CoPSZ600°C</b>	12 ± 2	10 ± 1	32 ± 3	46 ± 6
<b>CoPSZ-F</b>	2 ± 1	3 ± 1	79 ± 2	16 ± 4
<b>CoPSZ-Fcrosslinked</b>	3 ± 1	3 ± 1	83 ± 2	11 ± 4
<b>CoPSZ-F600°C</b>	10 ± 1	9 ± 1	23 ± 4	58 ± 6
<b>CoPSZ-N</b>	2 ± 1	3 ± 1	76 ± 4	19 ± 6
<b>CoPSZ-Ncrosslinked</b>	3 ± 1	3 ± 1	86 ± 3	8 ± 5
<b>CoPSZ-N600°C</b>	11 ± 2	12 ± 2	23 ± 3	54 ± 7



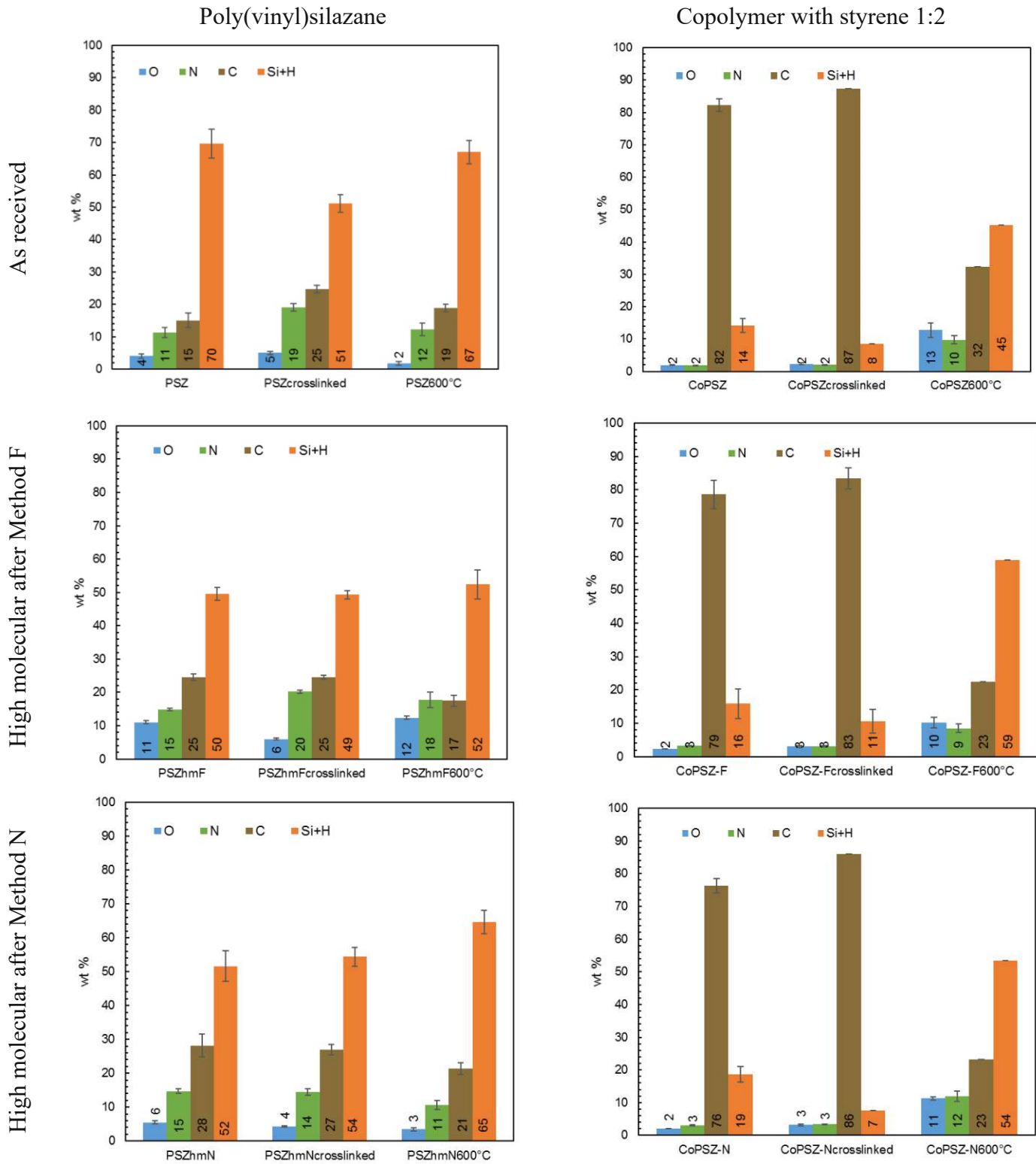


Figure 44: Elemental analysis in the three stages of processing; O, N, and C content are measured, Si+H is calculated as remainder to 100 wt%.

## 7.2.4 ATR-IR

The infrared absorption spectra of the polymers were recorded for every processing step (pure, crosslinked, pyrolyzed) and are shown with a shift on the y-axis in Figure 45. The PSZ-species are shown in intense colours, the corresponding copolymers in the lighter versions of the same colour. The samples with increased molecular weight (purple and green) show almost the same bands as the as received PSZ (blue) does, but with a slightly higher signal in the range of the oxygen bands. Also, the vinyl group is still visible at  $1600\text{ cm}^{-1}$ , which means that it isn't affected by the reactions during the increase of the molecular weight and can be used during the standard crosslinking step using DCP. The remaining functional groups, like Si-H and N-H are not affected either. For the copolymers, there are the additional bands of polystyrene, which are aromatic C-H vibrations around  $3000\text{ cm}^{-1}$ , the bending of a benzene ring from  $2000$  to  $1700\text{ cm}^{-1}$ , the so called "benzene fingers", and aromatic C=C vibration around  $1500\text{ cm}^{-1}$  as well as some additional signals in the fingerprint region.

For the crosslinked samples, the vinyl band around  $1600\text{ cm}^{-1}$  vanishes for all samples except for PSZhm-N. This shows that crosslinking, even of the high molecular weight compounds, is possible and all vinyl groups are used during the reaction, with PSZhm-N as exception, which can indicate a sterical hindrance of the radical crosslinking due to the high molecular weight.

The pyrolyzed samples show all similar spectra with one broad band between  $1100$  and  $700\text{ cm}^{-1}$ . For the copolymers, the shoulder closer to the oxygen related bands is higher. For all samples, there are still signals present in the aliphatic C-H region around  $1200\text{ cm}^{-1}$ , showing that at this pyrolysis temperature, the conversion to a ceramic is not complete yet and there is still hydrogen present in the sample. But, aromatic signals vanish completely during the pyrolysis step. The styrene domains therefore seem to decompose completely during the pyrolysis already up to the maximum temperature of  $600\text{ °C}$ . This is in accordance with the findings regarding the elemental composition, since the carbon content of the pyrolyzed copolymers is similar to that of the corresponding polysilazanes. Hence, their possible use as porogen looks promising and has to be evaluated using e.g. gas sorption.

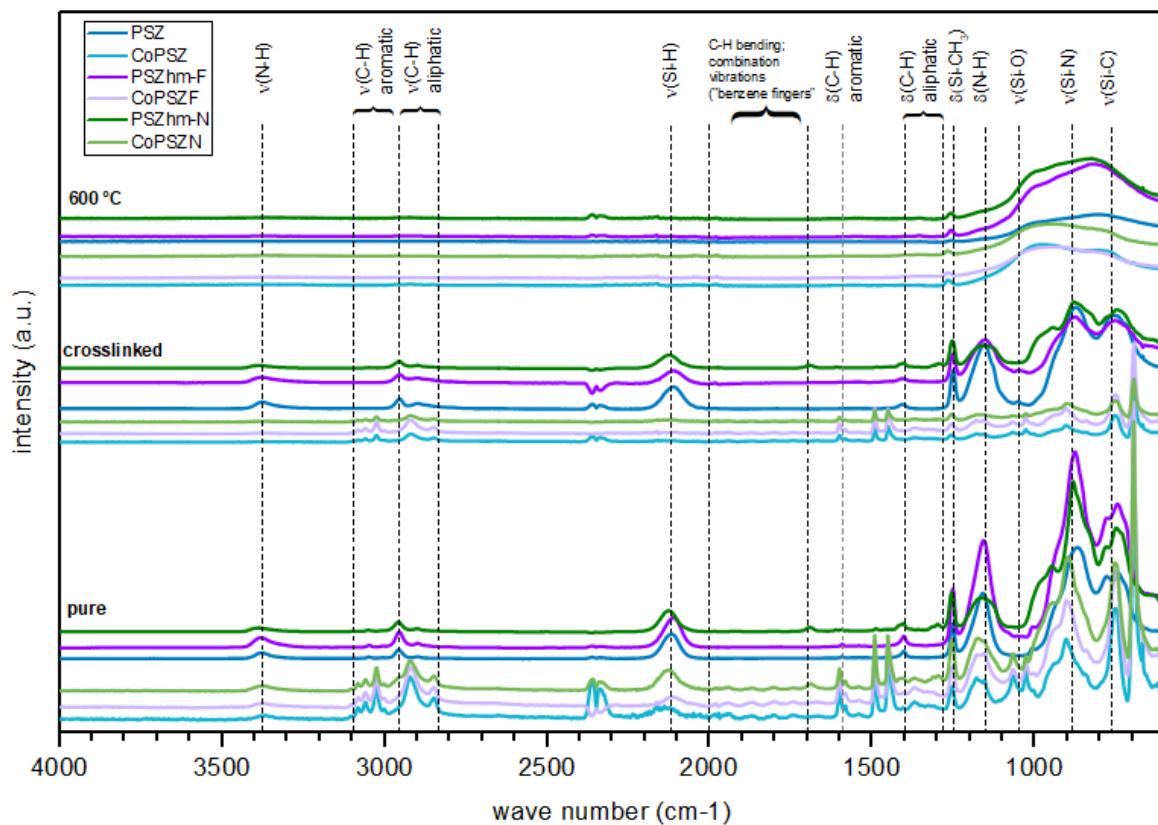


Figure 45: ATR-IR spectra of PSZ, the high molecular weight compounds and copolymers in the pure, the crosslinked and the pyrolyzed (600°C) state.

### 7.2.5 Porosity in the amorphous SiCN ceramics

A fast screening of the samples was done using BET measurements. A 5-point BET program (with 20-point BHJ desorption) was chosen to evaluate the specific surface area of the samples. The results can be found in Table 14. Whereas the samples with increased molecular weight showed very low specific surface areas of  $\sim 20$  m<sup>2</sup>/g or below, indicating a nonporous sample, the copolymers increased the surface area of their corresponding PSZ compounds significantly, yielding values around 400 m<sup>2</sup>/g, which could be explained by the decomposition of the styrene domains acting as porogens.

Table 14: BET specific surface area of PSZ, the high molecular weight compounds, and copolymers.

sample	BET surface area, m <sup>2</sup> /g
PSZ600°C	195
PSZhm-F600°C	22
PSZhm-N600°C	8
CoPSZ600°C	386
CoPSZ-F600°C	406
CoPSZ-N600°C	352

For the copolymers, which showed a significantly higher specific surface area, a second physisorption measurement was conducted over the whole pressure range, including the micropore range, to get further information about the pore size. The recorded isotherms are shown in Figure 46. The shape of the isotherms of the three copolymers differs slightly. CoPSZN yields a type I isotherm with almost no hysteresis, typical for a microporous sample, which is similar to that of PSZ. CoPSZF is a mixture between type I and type IV, so a mixture between a microporous and a mesoporous sample, with the latter one being confirmed by a hysteresis loop, that is typical for mesopores exceeding a critical size and therefore causing capillary condensation. Although the BET surface area of CoPSZ is high, the isotherm is of type II, which refers to non- or macroporous samples. The results are found in the PSDs calculated from the physisorption data (Figure 47), showing the same maximum for PSZ and CoN, which also had a similar isotherm. CoF indeed has its main maximum in the micropore range, combined with a relatively broad distribution of pore sizes in the mesopore range. CoPSZ in contrast has no pores in the micropore range and only a minor amount of pores in the mesopore range. Also, the BET areas of the newly conducted measurements were calculated

and are listed in Table 15 together with the other characteristics received by the physisorption measurements.

Table 15: Type of isotherm, BET specific surface area ( $S_{BET}$ ), maximum of the pore size distribution ( $PSD_{max}$ ) and micropore volume ( $V_{micro}$ ) of PSZ and the copolymers.

	Isotherm	$S_{BET}$ (m <sup>2</sup> /g)	$PSD_{max}$ (nm)	$V_{micro}$ (cm <sup>3</sup> /g)	Comment
<b>PSZ600 °C</b>	Type I	195 ± 6	0.84	0.10	Microporous
<b>CoPSZ600°C</b>	Type II	213 ± 6	3.0	-	Non- or macroporous
<b>CoPSZ-F600°C</b>	Type I/IV	355 ± 13	0.78, 1.1-2.1, 5	0.08	Micro- and mesoporous
<b>CoPSZ-N600°C</b>	Type I	145 ± 6	0.86	0.08	Microporous

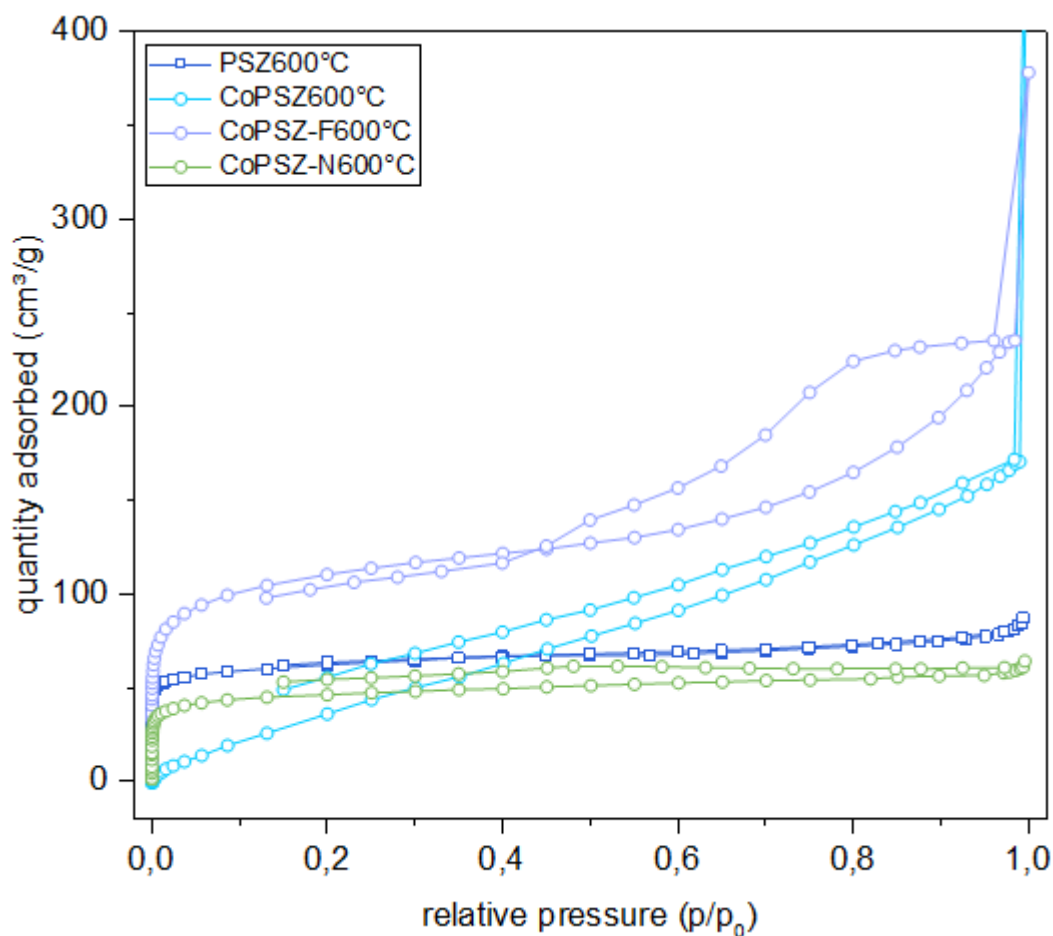


Figure 46: N<sub>2</sub> physisorption isotherms of PSZ and the three copolymers CoPSZ, CoPSZ-F and CoPSZ-N after pyrolysis (600 °C).

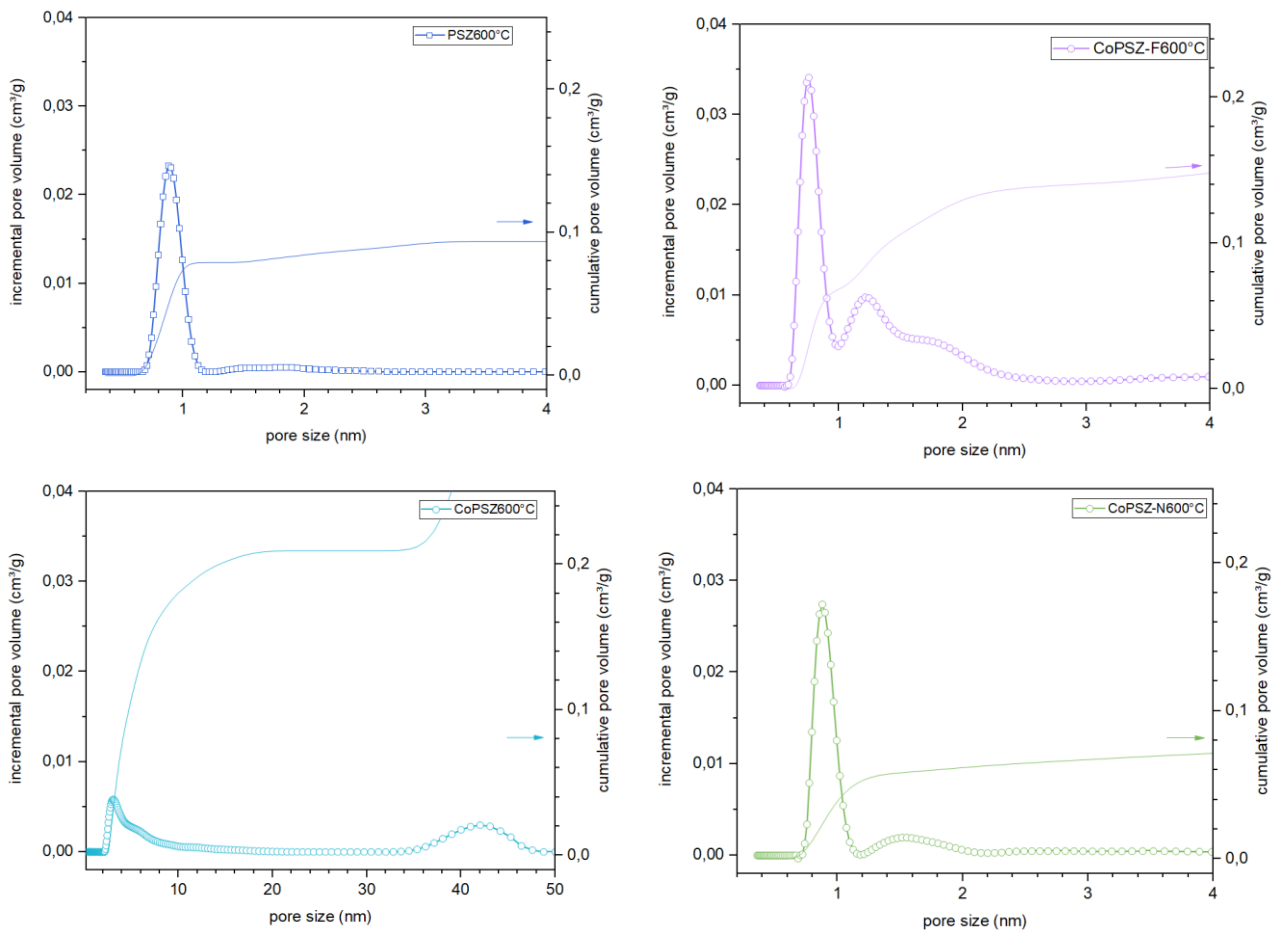


Figure 47: PSDs of PSZ and the copolymers after pyrolysis at 600 °C, calculated from the N<sub>2</sub> physisorption data using NL-DFT.

### 7.3 Conclusions – Focus II

Two high molecular weight versions of PSZ and copolymers of those with styrene were investigated on their microporosity.

The styrene doesn't seem to stay integrated in the final ceramic network but rather decomposes during pyrolysis and therefore leading to very high surface areas when compared to the PSZ versions without styrene. This assumption is confirmed by the elemental analysis during the three processing stages showing the expected composition for a mixture or copolymer with styrene in pure and crosslinked stage but a similar composition after pyrolysis to that of pyrolyzed as received PSZ. The pore size is only slightly influenced.

The copolymers offer a possibility to increase the surface area significantly, but since the mass loss during pyrolysis is very high with ~90 %, it is most likely not possible to form a crackfree, thin membrane layer.

## 8. FOCUS III – MODIFICATIONS OF THE PRECURSOR BY INCORPORATION OF ORGANIC SIDEGROUPS

Crosslinking of preceramic polymers before the pyrolysis step develops a network that can work as template for the final pore structure in the ceramic. The approach therefore is, to attach different organic groups to the backbone of the polymer which could influence the pore size when decomposing during pyrolysis. Since they aren't supposed to be in the network, but just serve as "space-holder", the groups shall substitute the H atom in the N-H-bond as it is displayed in Figure 48, by using up more space in the crosslinked network than an H atom would and leading to a change in pore size since the amount of gaseous species is changes during pyrolysis.

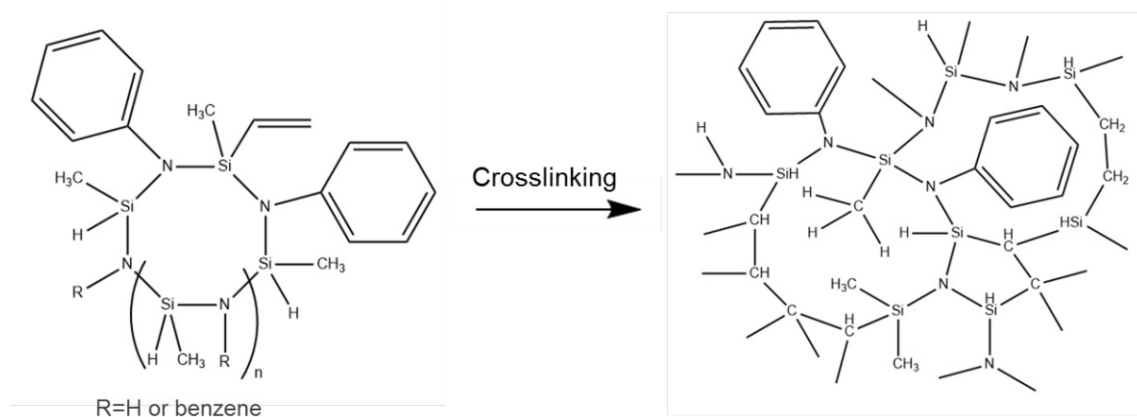


Figure 48: Schematic display of the crosslinking process of a modified PSZ, showing how a N-benzyl group in the crosslinked network could work as template for pores in the PDC.

### 8.1 Experimental Procedure – Focus III

In the following subsections, the materials that were used for the modification of the preceramic polymer as well as the experimental parameters will be discussed, first for the methodological development, then for the final parameter set.

Two methods were tested to substitute the N-H-group by an alkyl-group, for first trials a C4-group. Li et al. [127] modified the same poly(vinyl)silazane as used here, while Moore et al. [128] provide a general method for the alkylation of secondary amines. Both use a halide to introduce organic groups. The free electron pair at the nitrogen atom attacks the C-chain of the 1-bromobutane in  $\alpha$ -position. HBr evolves, which further forms a quaternary salt with the tertiary amine, which was added to prevent the salt formation with the alkylated polymer, as it is shown schematically in Figure 49.



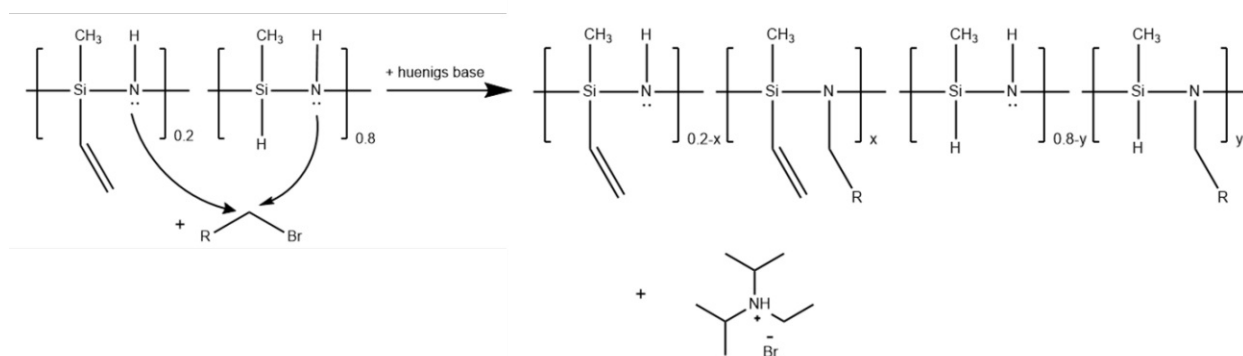


Figure 49: Reaction scheme during the substitution reaction of the N-H group by halides.

### 8.1.1 Materials

The following materials were used for the experiments for modification of the PSZ at the nitrogen atoms:

- Poly(vinyl)silazane PSZ  
(Durazane HTT 1800, durXtreme GmbH)  
as polymer precursor
- 1-Bromobutane (ReagentPlus®, 99%, Sigma Aldrich)
- Benzylbromide (ReagentPlus®, 99%, Sigma Aldrich)
- N,N-diisopropylethylamine (Huenigs Base,  $\geq 99.5\%$ , Sigma Aldrich)
- Triethylamine ( $\geq 99\%$ , Sigma Aldrich)

### 8.1.2 Crosslinking and pyrolysis

Because of the samples being highly viscous or solid, the crosslinking step was chosen to be conducted without an initiator. Hence, the samples were heated to higher temperatures than the 130 °C that were typically used in combination with DCP. The samples were heated to 250 °C at a heating rate of 1 K/min and held at that temperature for 2.5 h before cooling to room temperature at 3K/min. The same furnace and atmosphere were used as for the pyrolysis, which is described in 5.2.3.



### 8.1.3 Methodological screening using 1-bromobutane

The first trials were carried out after Li et al. [127], since the same polymer as in this project is used. The difference in procedure is the additional use of a tertiary amine, to prevent salt formation with the modified polymer, and the use of an alkylhalide instead of the more complex Methyl-2-(bromo-methyl)acrylate. In a typical batch, 1 g PSZ, 4.15 g bromobutane and 4 g of triethylamine and 20 ml of solvent (toluene) were used. The reaction was carried out in nitrogen atmosphere in a round bottom flask and under constant stirring. The other parameters and molecular ratios (with respect to the nitrogen atoms) are listed in Table 16.

Table 16: Reactions parameters for the C4-modification of PSZ, molar ratios with respect to nitrogen, after Li et al. [127]

sample name	Halide (mol.equ.)	Tertiary amine (mol.equ.)	Temperature, °C	Duration, h
<b>PSZC4rt</b>	1-Bromobutane (1.1)	Triethylamine (2)	room temperature	72
<b>PSZC460°</b>	1-Bromobutane (1.1)	Triethylamine (2)	60 °C	72
<b>PSZC460°1.5</b>	1-Bromobutane (1.5)	Triethylamine (2)	60 °C	72
<b>PSZC470°1.5</b>	1-Bromobutane (1.5)	Triethylamine (2)	70 °C	72

The reaction mixtures for the various parameter combinations are shown in Figure 50. The formation of the precipitate, which is expected to form due to the addition of the tertiary amine, can be seen clearly for the three reaction procedures at elevated temperatures. The sample PSZC4rt was not further investigated.

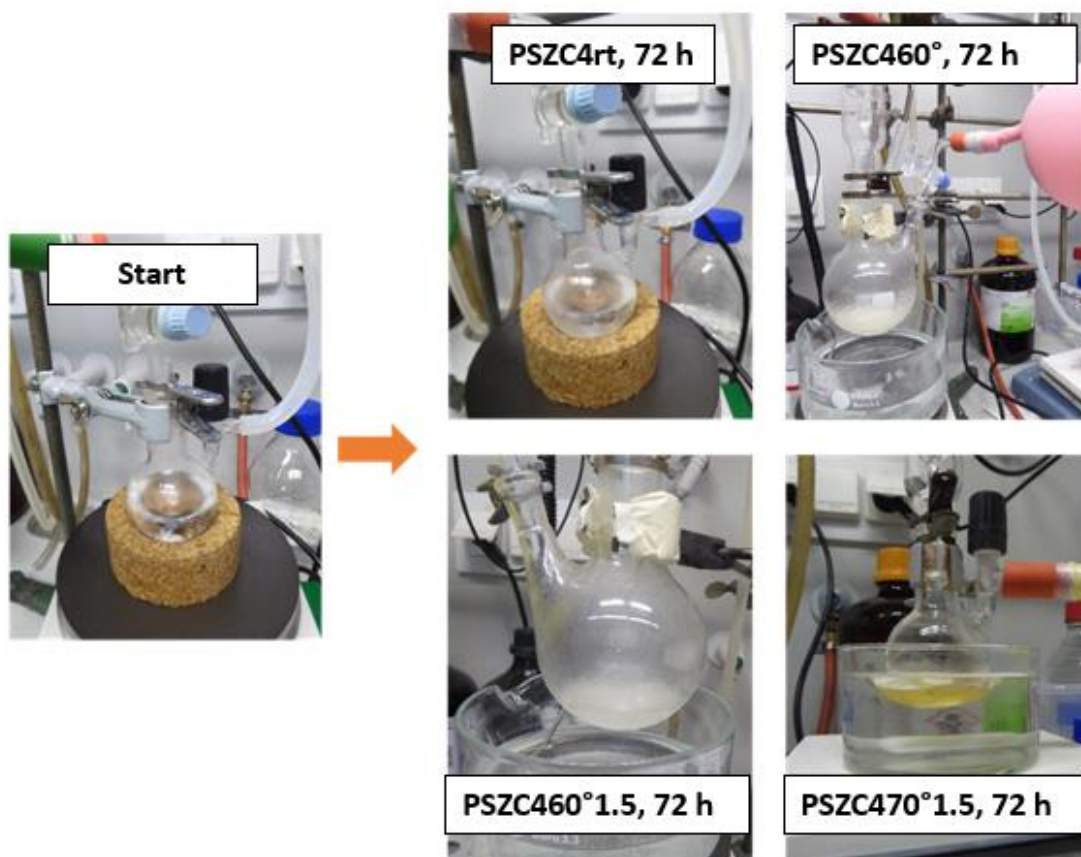


Figure 50: Reaction mixture during C4-modification using various parameter combinations.

## 8.2 Results – Focus III

### 8.2.1 NMR spectroscopy

$^1\text{H}$ - and  $^{13}\text{C}$ -NMR spectra were recorded. Figure 51 shows the  $^1\text{H}$ -NMR spectrum of as received PSZ, with the peaks correlated to the different H-atoms in the polymer. The vinyl group yields peaks around 6 ppm, Si-H at 4.2-4.8 ppm, Si-CH<sub>3</sub> around 0 ppm and the N-H (that is supposed to be substituted) from 0.6 to 0.8 ppm. The area of the integrated peaks also confirms the structure shown before (Figure 17): When using the Si-CH<sub>3</sub> group as reference the area of the integrated N-H peak should be one third, resembling the single H-atom compared to three H-atoms. The vinyl group, that should be present on 20 % of the silicon atoms, has a value of 0.55, which matches the theoretical value of 0.60 (3 H-atoms x 0.2), and the Si-H group with 0.70 instead of the theoretical value of 0.80. The small variations can be explained by inaccuracy in

setting the integration limits or oxygen impurities, which aren't taken into account in the theoretical values.

The  $^1\text{H}$  spectra of the modified PSZs are shown in Figure 52 with differences compared to PSZ highlighted in light blue. The signals around 7 ppm and at 2.1 ppm originate from  $\text{CDCl}_3$  and residual solvent (toluene). In addition to those and the signals of pure PSZ, there are some multiplets in the region between 1 and 3.5 ppm. Typically, this is the region in which alkyl groups show and the shift up to 3 ppm indicates them being attached to nitrogen. Also, the signal of the N-H atom (around 0.8 ppm) decreases, although it is hard to quantify that, because of the multiplet overlapping. Still, the grade of substitution is very low.

In Figure 53 the DEPT  $^{13}\text{C}$  spectra of the modified PSZ can be found. In this type of spectra,  $\text{CH}_2$ -groups show as negative peaks,  $\text{CH}$ - and  $\text{CH}_3$ -groups as positive peaks and C atoms without an H attached, don't give a signal at all. The signal around 0 ppm is originating from the Si- $\text{CH}_3$  group, those at 135 and 140 ppm are showing the vinyl group.  $\text{CDCl}_3$  shows at 77.36 ppm, the signals at 125-130 ppm as well as the one at 20 ppm are caused by residual solvent (toluene). As for the  $^1\text{H}$  NMR, there are several small signals in a region that can be correlated with alkyl groups in the region from 13 to 60 ppm. But as for the  $^1\text{H}$  spectra, only a low grade of substitution can be found.

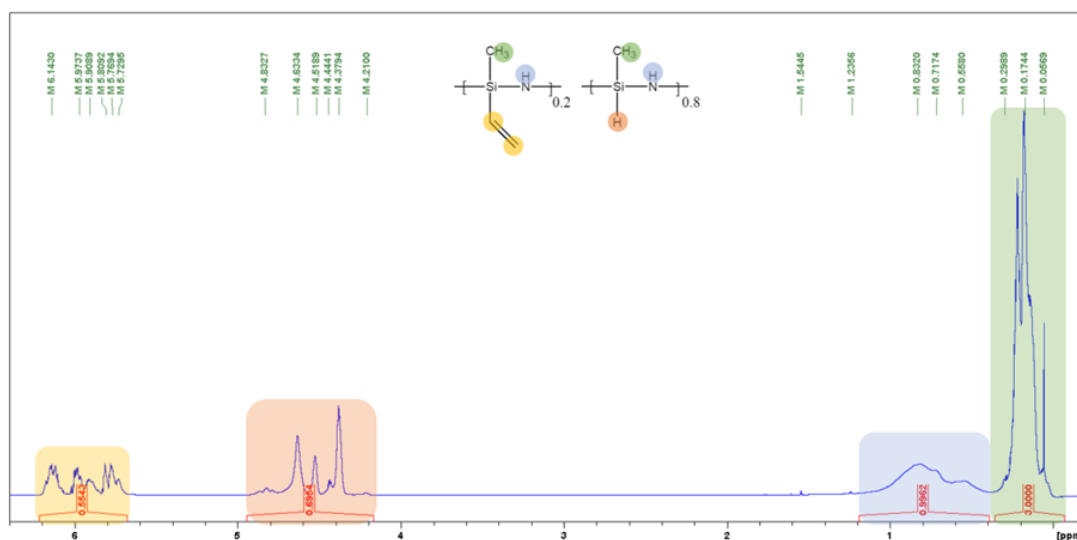


Figure 51:  $^1\text{H}$  NMR of as-received PSZ; peaks are correlated to the structure.

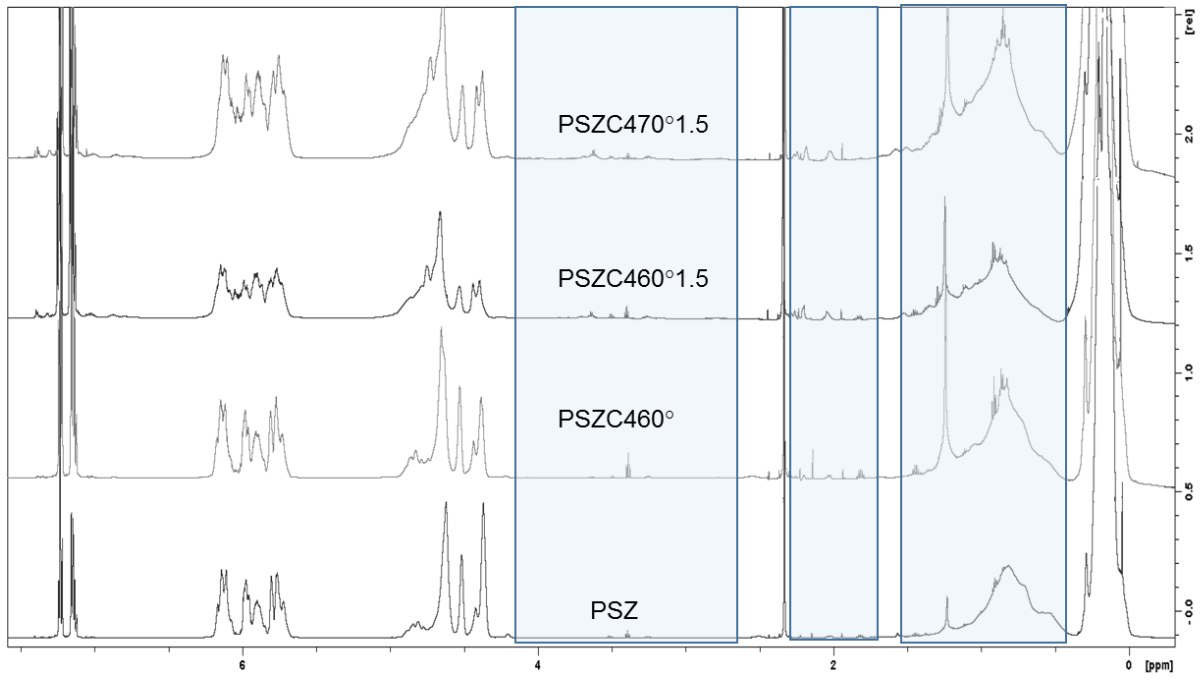


Figure 52:  $^1\text{H}$  NMR of the C4 modified PSZ using different reaction parameters.

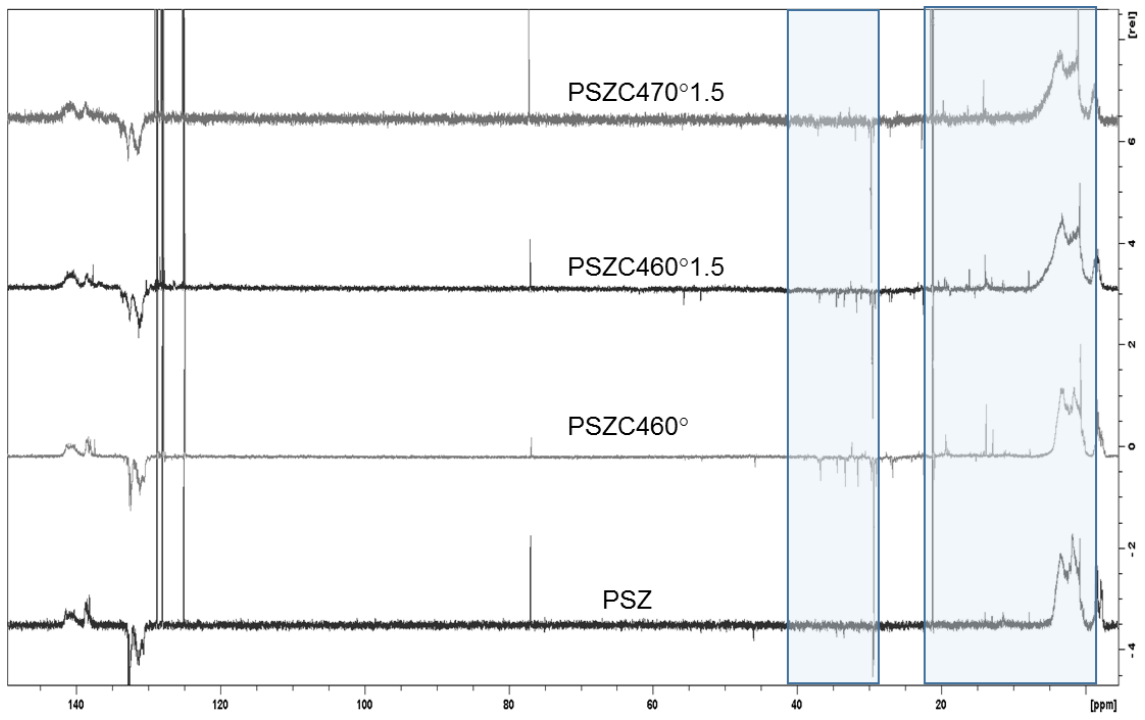


Figure 53:  $^{13}\text{C}$  -NMR of the C4 modified PSZ using different reaction parameters.

## 8.2.2 Mass change and optical appearance

The mass change during processing is given in Table 17. During crosslinking, it is significantly higher for the C4 modified versions of PSZ with 10 % or even 16 % compared to 2 %. This could be due to remaining solvent or educt that wasn't removed during vacuum distillation. That is supported by the pictures taken of the samples before and after crosslinking (Figure 54) which show foaming of PSZC460°1.5. The mass change during pyrolysis is lower for the three modified polymers, which is surprising since the C4 group is expected to decompose and would therefore lead to a higher mass loss. A different decomposition mechanism due to hindering of certain reactions such as transamination reactions due to substitution of the N-H group by N-C<sub>4</sub> could explain the lower mass change.

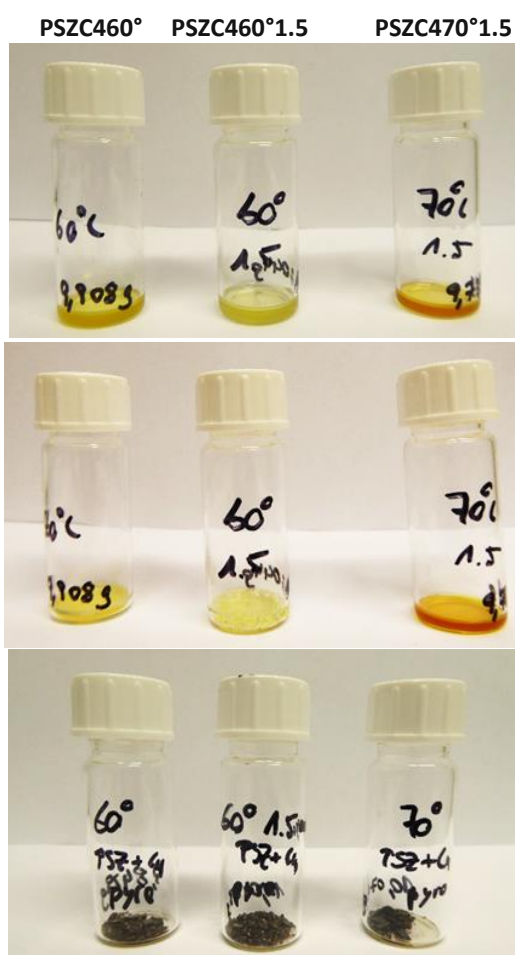


Figure 54: C4 modified PSZ before crosslinking (top), after crosslinking (middle), and after pyrolysis (bottom)

Table 17: Mass change of the C4 modified samples during crosslinking and pyrolysis.

	sample	$\Delta m$ pure-crossl., %	$\Delta m$ crossl.-pyro,%
<b>unaltered</b>	PSZ	<b>-2.2</b>	<b>-26.0</b>
<b>C4 modification</b>	60 °C	<b>-10.8</b>	<b>-21.0</b>
	60 °C 1.5	<b>-16.1</b>	<b>-20.3</b>
	70 °C 1.5	<b>-11.7</b>	<b>-17.7</b>

### 8.2.3 Elemental composition

The elemental composition for these first experiments in the three processing stages is given in Table 18 with pure PSZ for comparability. The **oxygen** content of the pure materials is approximately the same for all three with 4-5 wt% and also similar to that of PSZ. Whereas the oxygen content decreases during pyrolysis for the as received PSZ, it increases for the modified compounds. The overall mass loss is equal for all four versions of PSZ, so it seems as if the oxygen is more integrated in the network formed during crosslinking and not just in a side group that is released during pyrolysis or open for reactions for the modified samples than for the as received PSZ. The **nitrogen** content doesn't differ much from that of as received PSZ, especially when taking into account the deviation of the measurement. The **carbon** content is 5 wt% higher for all three modified samples than for the as-received PSZ in the pure and crosslinked stage. Therefore, the substitution of the N-H group with an organic group was successful to a certain degree, but the reaction procedure has to be further optimized to get higher yields. After pyrolysis, the difference in carbon content is smaller with only 2 wt%. This indicates decomposition of the C4 chains and release of the decomposition products. This decomposition of the organic groups during pyrolysis is supposed to cause increased porosity and was the purpose of the precursor modification. The effect on the porosity will be controlled using gas physisorption.

Table 18: Elemental composition of the C4 modified PSZ for different parameter combinations in the pure, crosslinked and pyrolyzed state; O, N, and C content are measured, Si+H is calculated as remainder to 100 wt%.

	O, wt%	N, wt%	C, wt%	Si+H, wt%
<b>PSZ</b>	4 ± 1	11 ± 2	15 ± 2	70 ± 5
<b>PSZcrosslinked</b>	5 ± 1	19 ± 2	25 ± 1	51 ± 4
<b>PSZ600°C</b>	2 ± 1	14 ± 2	18 ± 1	66 ± 4
<b>PSZC460°</b>	5 ± 1	12 ± 1	26 ± 1	57 ± 3
<b>PSZC460°_crosslinked</b>	7 ± 1	18 ± 1	30 ± 2	45 ± 4
<b>PSZC460°_600°C</b>	8 ± 1	15 ± 2	21 ± 1	56 ± 4
<b>PSZC460°1.5</b>	5 ± 1	12 ± 1	24 ± 4	59 ± 6
<b>PSZC460°1.5_crosslinked</b>	7 ± 1	18 ± 1	30 ± 2	45 ± 4
<b>PSZC460°1.5_600°C</b>	8 ± 1	16 ± 2	21 ± 1	55 ± 4
<b>PSZC470°1.5</b>	5 ± 1	12 ± 2	28 ± 3	55 ± 6
<b>PSZC470°1.5_crosslinked</b>	6 ± 1	17 ± 2	31 ± 2	46 ± 5
<b>PSZC470°1.5_600°C</b>	8 ± 1	13 ± 1	22 ± 1	57 ± 3

## 8.2.4 ATR-IR

ATR-IR spectra of the products were recorded and compared to the spectrum of pure PSZ. These are shown in Figure 55, with the relevant wavenumber regions highlighted. The spectra are displayed without shift on the y-axis, to show the change of intensity of some bands. Therefore, all the spectra were also normalized using the Si-CH<sub>3</sub> band from 1300-1230 cm<sup>-1</sup>, since this band is not expected to change. In comparison to the pure PSZ, a decrease in signal of the N-H bands at 3400 cm<sup>-1</sup> and 1180 cm<sup>-1</sup> can be seen, which is stronger the higher the temperature and the higher the excess of bromobutane is. The Si-H band decreases too, which indicates that the substitution is not selective for the N-H band. In both regions of alkyl-signals (around 3000 cm<sup>-1</sup> and around 1500 cm<sup>-1</sup>), there are new signals visible, confirming that the substitution took place.



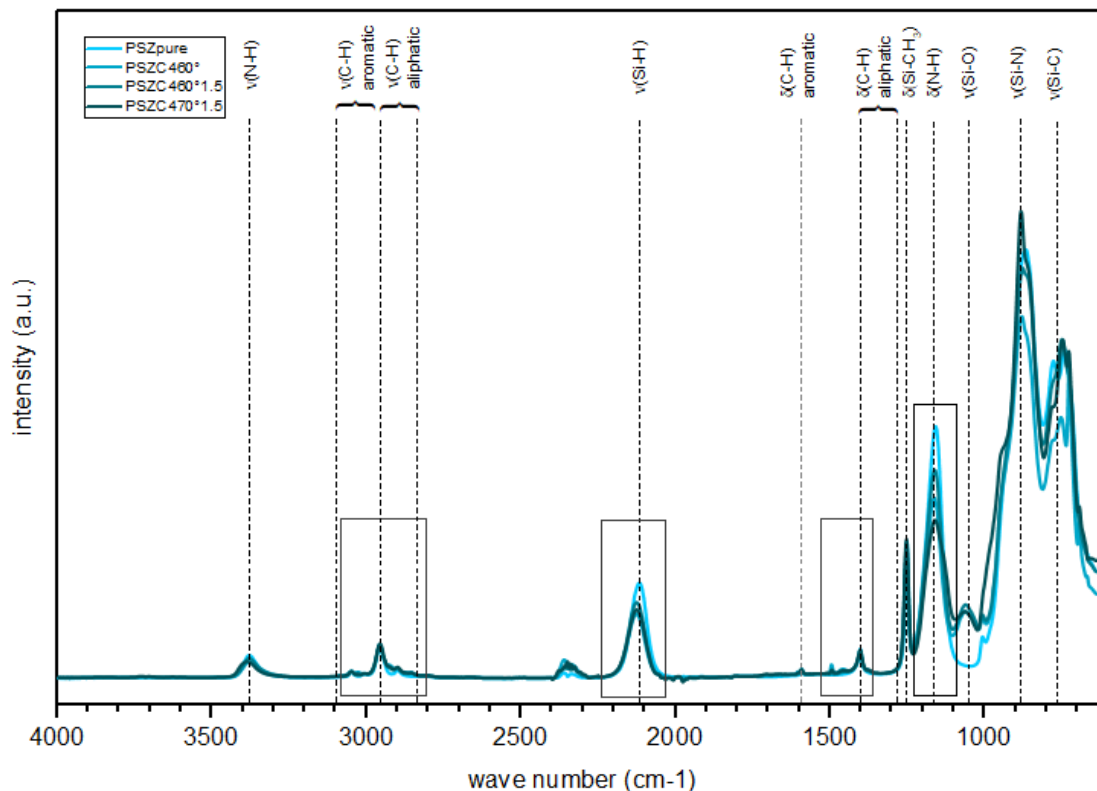


Figure 55: ATR-IR spectra of the C4 modified PSZ after different parameter combinations; in the pure, crosslinked and pyrolyzed state; the spectra are normalized on the Si-CH<sub>3</sub> band from 1230-1300 cm<sup>-1</sup>.

### 8.2.5 Interim conclusions

None of the samples showed significant differences in elemental composition or major differences in the ATR-IR spectra, which is why the reaction parameters are changed to the procedure proposed by Moore et al. [128], which will be described in more detail in the following sections.

### 8.2.6 Final parameters for the N-H substitution

Since the substitution reaction took place only in a minor degree, the method was changed and following the procedure that was proposed by Moore et al. [128].

The reaction parameters were therefore fixed on 3-4 days at 60 °C with 2 molequ. huenigsbase as tertiary amine (instead of triethanolamine) and 1.5 molequ. (with respect to the nitrogen atoms in PSZ) of bromobutane/benzylbromide in 20 ml acetonitrile per g PSZ in nitrogen atmosphere and under constant stirring. Since the quaternary salt seems to be soluble in acetonitrile to a certain degree, the extraction step with toluene or n-hexane was added to the procedure. The steps of the procedure are shown in Figure 56. Using this procedure, two



different samples were produced, using two different halides and therefore two different organic groups, which can serve as template for pores.

Table 19: Reactions parameters for the modification of PSZ, molar ratios with respect to nitrogen in PSZ; acetonitrile as solvent.

sample name	Halide (mol.equ.)	Tertiary amine (mol.equ.)	Temperature, °C	Duration, h
<b>PSZbutyl</b>	1-Bromobutane (1.5)	huenigsbase (2)	60 °C	72
<b>PSZbenzyl</b>	Benzylbromide (1.5)	huenigsbase (2)	60 °C	72

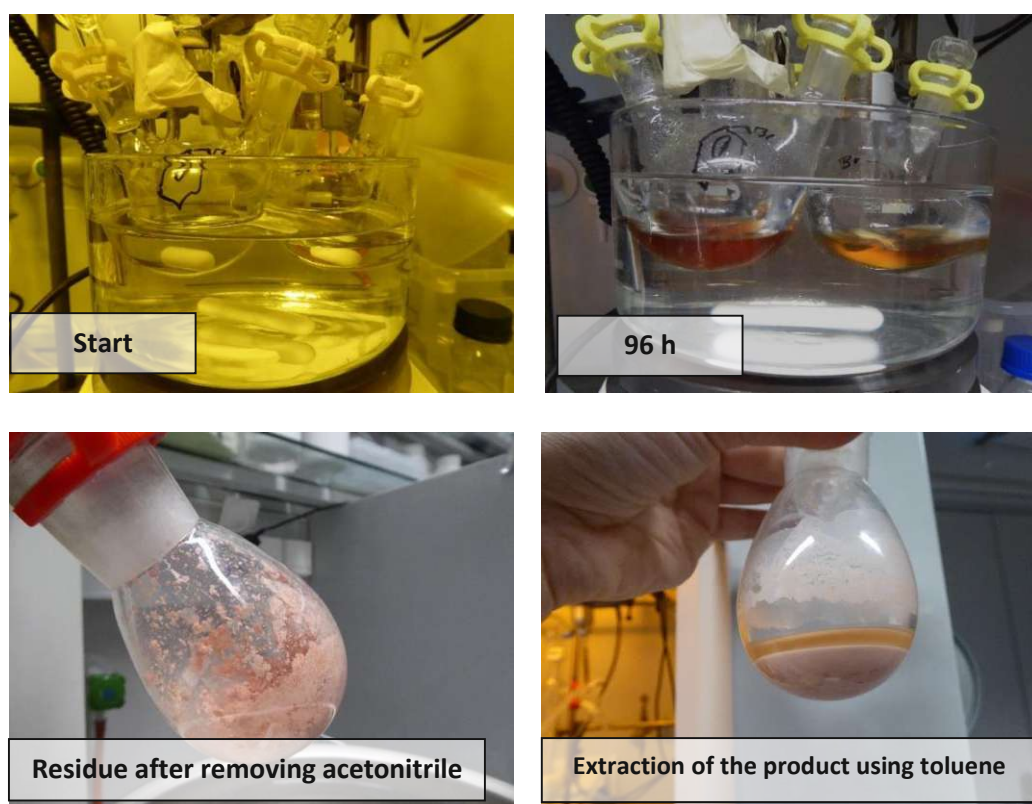


Figure 56: Reaction mixtures of PSZ modifications using benzylbromide (left flask) or 1-bromobutane (right flask) at start and end of the reaction as well as during further processing.

### 8.2.7 Mass change

The mass change of the samples modified using either a benzyl or a butyl group is listed in Table 20. Since the modified samples were just thermally crosslinked without adding the initiator, there is also the value for the thermally crosslinked pure PSZ. The values of PSZbutyl are similar to those of the thermally crosslinked PSZ, those of PSZbenzyl are higher in both steps, indicating that most of the groups decomposed during pyrolysis.

Table 20: Mass change of PSZ and the versions modified using a benzyl or a butyl group; the thermally crosslinked sample is shown as additional reference, since the modified versions were crosslinked without initiator.

	$\Delta m_{\text{pure-crossl.}}, \%$	$\Delta m_{\text{crossl.-pyro600}^\circ\text{C}}, \%$
PSZ+DCP	-2.2	-26.0
PSZ_ crosslinked without initiator	-15.9	-19.0
PSZbenzyl	-19.8	-59.3
PSZbutyl	-16.0	-16.6

### 8.2.8 NMR

The products were also investigated using NMR techniques,  $^1\text{H}$  NMR spectra and  $^{13}\text{C}$  spectra were recorded and are shown in Figure 57 to Figure 60. The C-spectra were recorded in DEPT mode, so a difference between C-atoms with 1,2 or 3 H-atoms attached can be seen, with 1 and 3 H atoms yielding positive peaks, and 2 H atoms yielding negative peaks. The PSZ modified with benzylbromide shows the signals of pure PSZ combined with those of a benzene ring at 7 ppm and the  $\text{CH}_2$ -group at 3.5 ppm. The peaks that are not marked are most likely due to residual educt or solvent that couldn't be removed completely. There is almost no signal of the N-H group (up to 0.8 ppm) visible anymore. In the  $^{13}\text{C}$  spectrum, the benzene ring overlaps with residual toluene (125-129 ppm), the  $\text{CH}_2$  group can be seen at 58 ppm. The substitution seems to be complete, the integral of the  $\text{CH}_2$ -peak even exceeds the expected value a little, which is probably due to overlapping with side bands. For the C4 modified PSZ, there are four additional peaks in both spectra, correlated to the alkyl chain. Again, the peaks that are not marked are due to toluene or unreacted halide. The grade of substitution is around 20 % for the C4 modified sample.

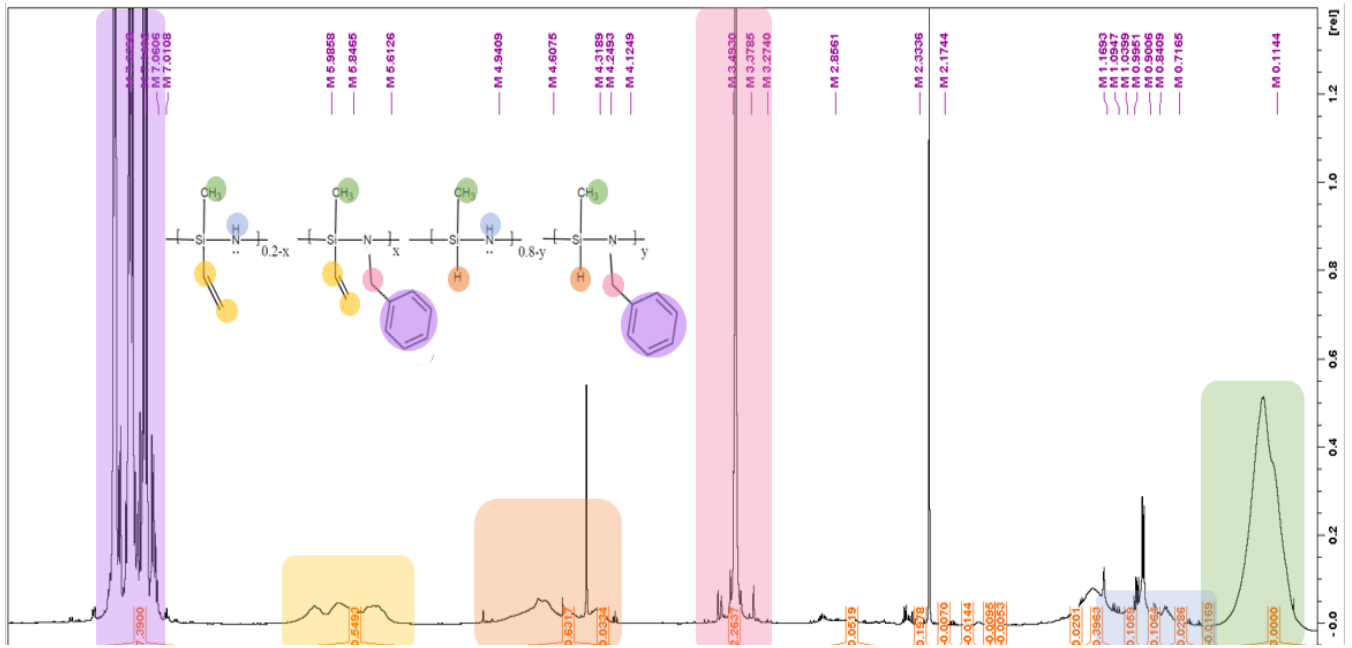


Figure 57:  $^1\text{H}$  NMR of PSZbenzyl (acetonitrile, huenigsbase, 60 °C).

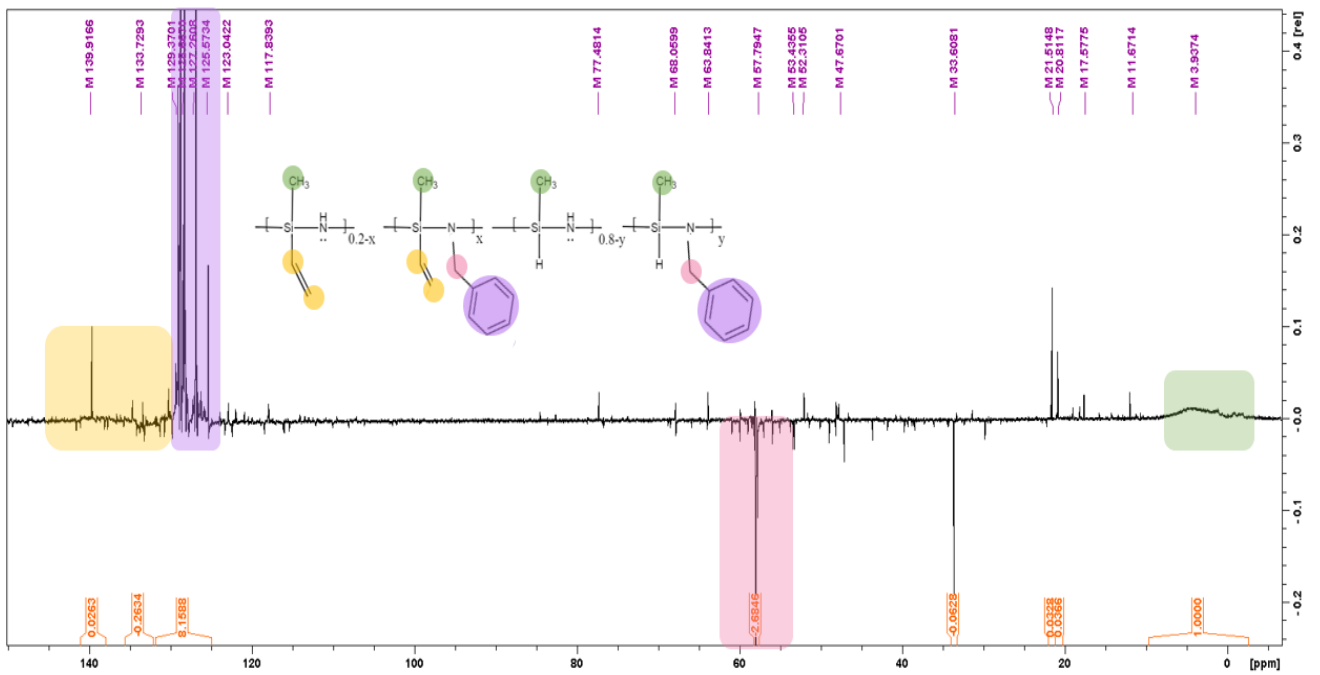


Figure 58 :  $^{13}\text{C}$  NMR of PSZbenzyl (acetonitrile, huenigsbase, 60 °C).

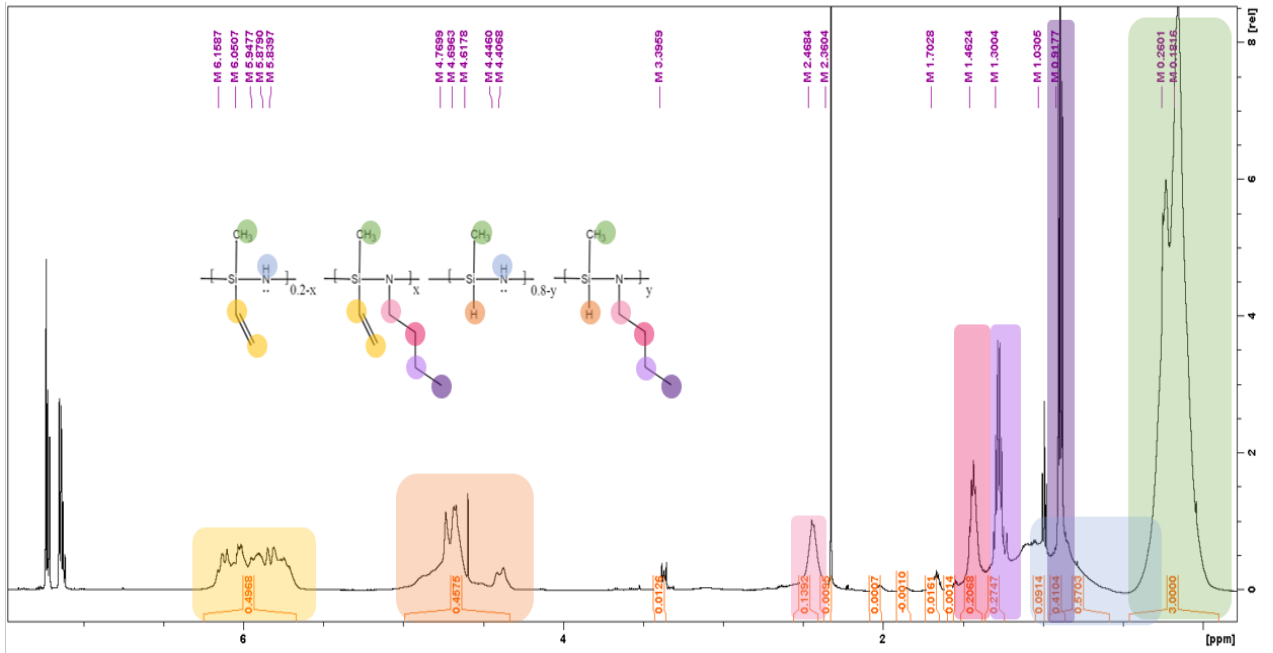


Figure 59 : <sup>1</sup>H NMR of PSZbutyl (acetonitrile, huenigsbase, 60 °C).

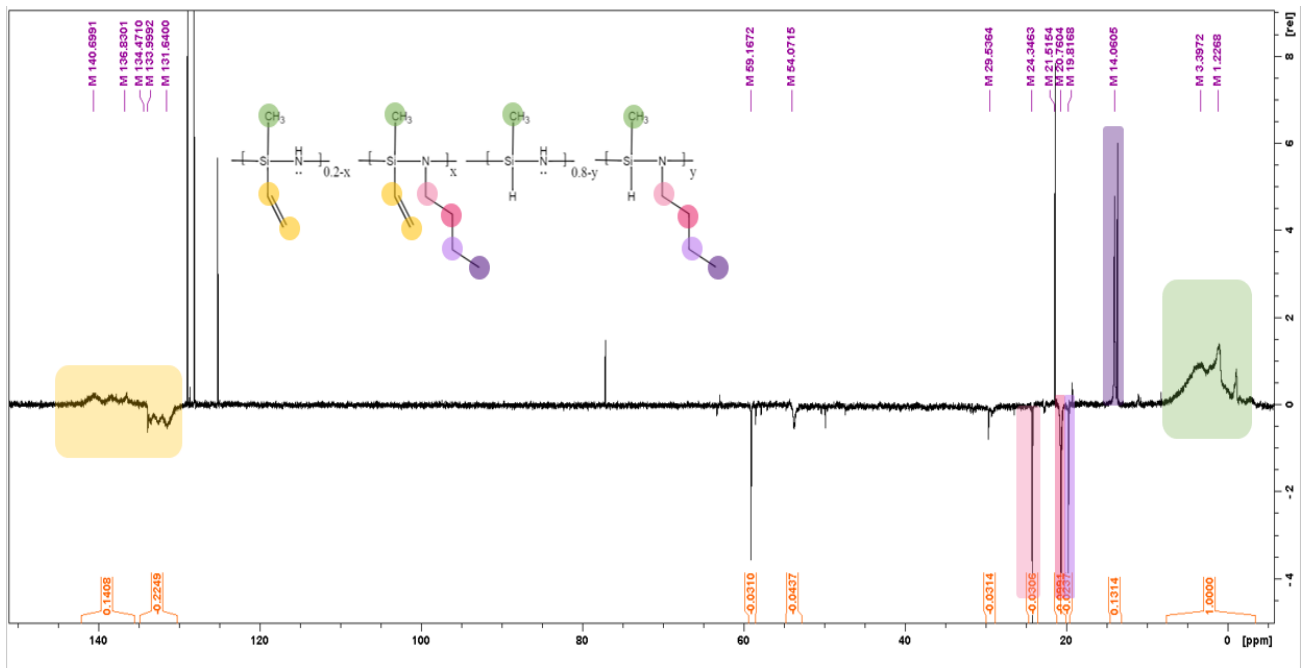


Figure 60 : <sup>13</sup>C NMR of PSZbutyl (acetonitrile, huenigsbase, 60 °C).

### 8.2.9 Elemental composition

The elemental composition of the modified polymers was measured and is given in Table 22. Also, the theoretical composition was calculated assuming a 100% substitution of the N-H group by a C4-group or a benzyl-group, which is given in Table 21. When comparing the theoretical and the experimental composition, they fit quite well for the benzyl modified PSZ, especially when taking into account that there are oxygen contaminations in the actual sample, with a relatively high percentage of 6.5 wt%. For the C4 modified sample, the results differ more from the theoretical ones, which indicates an incomplete substitution. If a substitution of 25 % is assumed, the results fit the theoretical values much better. This is in accordance with the IR-spectra and also with the NMR spectra. A reason for the higher grade of substitution could be the activation of the C-atom by the benzyl group. After pyrolysis, the compositions of the modified versions are very close to that of the unmodified version, except for the significantly higher oxygen content, which had already been present before pyrolysis. Slightly higher carbon contents are a leftover of the modification, but most of the side groups seem to decompose during the pyrolysis, as desired.

Table 21: Theoretical composition of the modified PSZ.

	Si, wt%	N, wt%	C, wt%	H, wt%
<b>PSZ</b>	43.7	21.8	26.1	8.5
<b>PSZ+butyl</b>	23.3	11.6	53.9	11.3
<b>PSZ+benzyl</b>	18.2	9.1	65.3	7.4

Table 22: Elemental composition of PSZ, PSZbenzyl and PSZbutyl in the processing stages; O, N, and C content are measured, Si+H is calculated as remainder to 100 wt%.

	O, wt%	N, wt%	C, wt%	Si+H, wt%
<b>PSZ</b>	4 ± 1	11 ± 2	15 ± 2	70 ± 5
<b>PSZcrosslinked</b>	5 ± 1	19 ± 2	25 ± 1	51 ± 4
<b>PSZ600°C</b>	2 ± 1	14 ± 2	18 ± 1	66 ± 4
<b>PSZbutyl</b>	11 ± 1	7 ± 1	33 ± 1	48 ± 3
<b>PSZbutyl_600°C</b>	12 ± 1	12 ± 2	15 ± 2	61 ± 5
<b>PSZbenzyl</b>	7 ± 1	9 ± 1	70 ± 2	15 ± 4
<b>PSZbenzyl_600°C</b>	10 ± 1	10 ± 2	21 ± 1	59 ± 4

### 8.2.10 ATR-IR

The ATR-IR spectra of PSZ and the two modified versions are shown in Figure 61. Although there is a slight difference regarding the baseline, it can be clearly seen that the spectra change for both organic groups.

For both samples, the N-H bands at wavenumbers of 1180 cm<sup>-1</sup> and 3300 cm<sup>-1</sup> decrease significantly. Also, the Si-H signal at 2200 cm<sup>-1</sup> decreases in the same extent, indicating that the reaction isn't selective for the N-H group. There are also changes in region of aliphatic and aromatic C-H vibrations. New signals appear and the intensity increases for both modified versions, which can be seen around 3000 cm<sup>-1</sup> and from 1400-1600 cm<sup>-1</sup>. In case of PSZbenzyl, the so called "benzene fingers" between 1600-1900 cm<sup>-1</sup> can be found.

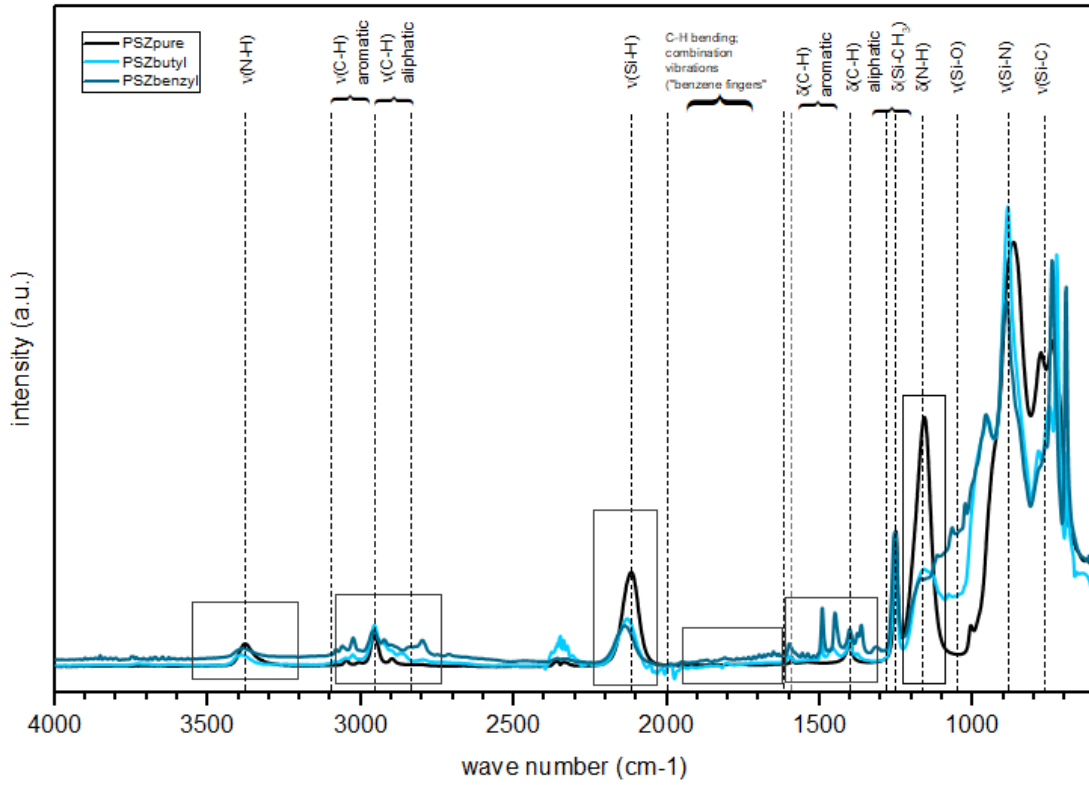


Figure 61: ATR-IR spectra of PSZbenzyl and PSZbutyl in comparison to the PSZ crosslinked using DCP; the spectra are normalized with respect to the Si-CH<sub>3</sub> band from 1230-1300 cm<sup>-1</sup>.

### 8.2.11 TGA-MS

Unfortunately, there were problems with the analysis of the modified samples using TGA-MS. Apparently, the decomposition occurred abruptly which led to the loss of parts of the sample, which were shot out of the crucible. Consequently, the decomposition led to a blocked capillary in the measurement set up and MS measurements were not possible anymore.

The part of the analysis where the MS signals were still detected is displayed in Figure 62. One can already see the abrupt decomposition by the jagged line in some temperature regions, e.g. at around 350 °C or 460 °C and especially above 600 °C, and the resulting complete loss of signal above 700 °C.

Still, some information can be extracted from these spectra. The jagged parts always go along with an increase of aromatic signals, like the  $m/z$  value of a benzene ring (78) and fragments (e.g. 73), caused by the decomposition and release of the benzyl groups that were added. This decomposition starts around 300 °C and reaches its maximum around 500 °C. Comparing these results to the results of PSZ, which are shown in Figure 63 (c.f. 6.2.3.2), one can see, that the actual polymer-ceramic conversion indicated by the methane formation is taking place with a maximum slightly below 600 °C. The main decomposition of the benzyl group therefore occurs below this conversion.

An additional TGA measurement was performed without the MS unit which showed no abrupt mass changes. The results are displayed in Figure 64, showing the higher mass loss of PSZbenzyl, which is in accordance with the one calculated by weighing. Since the introduced organic groups decompose at relatively low temperatures, it is questionable whether they can influence the pores in the final ceramic or if further rearrangements at higher temperatures nullify the effect.



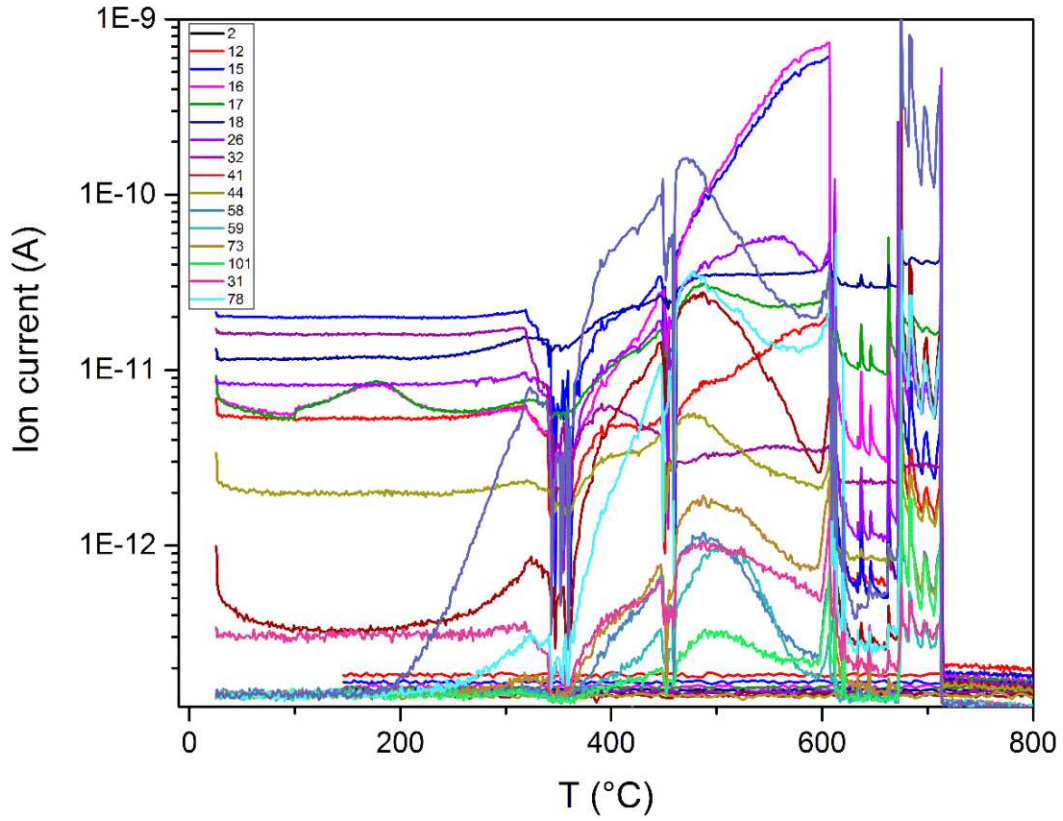


Figure 62: (TGA-)MS results of PSZbenzyl before the transfer capillary to the MS set up was blocked by a piece of the sample, leading to the loss of the remaining data.

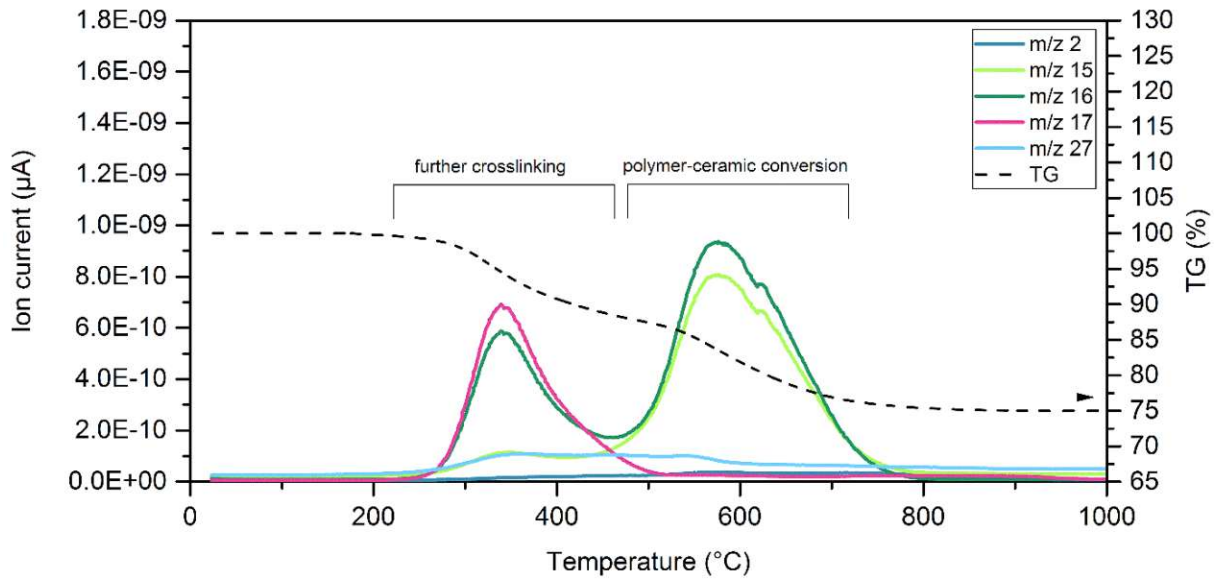


Figure 63: Simplified TGA-MS results of PSZ crosslinked with DCP.

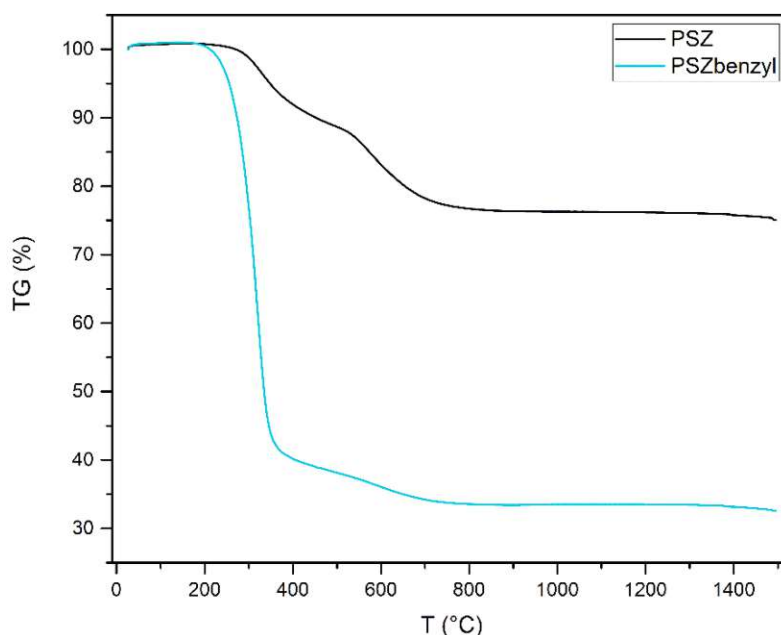


Figure 64: TGA curve of PSZ+DCP and PSZbenzyl after crosslinking.

## 8.2.12 Pore characteristics

### 8.2.12.1 N<sub>2</sub>-Physisorption

The integration of organic sidegroups at the nitrogen atom doesn't lead to significant changes in the pore characteristics of the ceramics after pyrolysis at 600 °C. The isotherms (Figure 65) are still of type I, which means that the samples are microporous. The overall adsorbed gas quantity lies in the same range for all samples. The calculated PSDs show small differences in the pore volume but no significant changes in the position of the pore size maximum. This is also clearly visible from the pore characteristics derived from the isotherm, which are summarized in Table 23. There is only a slight increase in specific surface area, but no significant change in pore size or micropore volume.

Table 23: Type of isotherm, BET specific surface area ( $S_{BET}$ ), maximum of the pore size distribution ( $PSD_{max}$ ) and micropore volume ( $V_{micro}$ ) of PSZ and modified versions with organic sidegroups.

	Isotherm	$S_{BET}$ (m <sup>2</sup> /g)	$PSD_{max}$ (nm)	$V_{micro}$ (cm <sup>3</sup> /g)	Comment
<b>PSZ600 °C</b>	Type I	195 ± 6	0.86	0.10	Microporous
<b>PSZbenzyl_600°C</b>	Type I	212 ± 7	0.88	0.10	Microporous
<b>PSZbutyl_600°C</b>	Type I	222 ± 12	0.86	0.10	Microporous

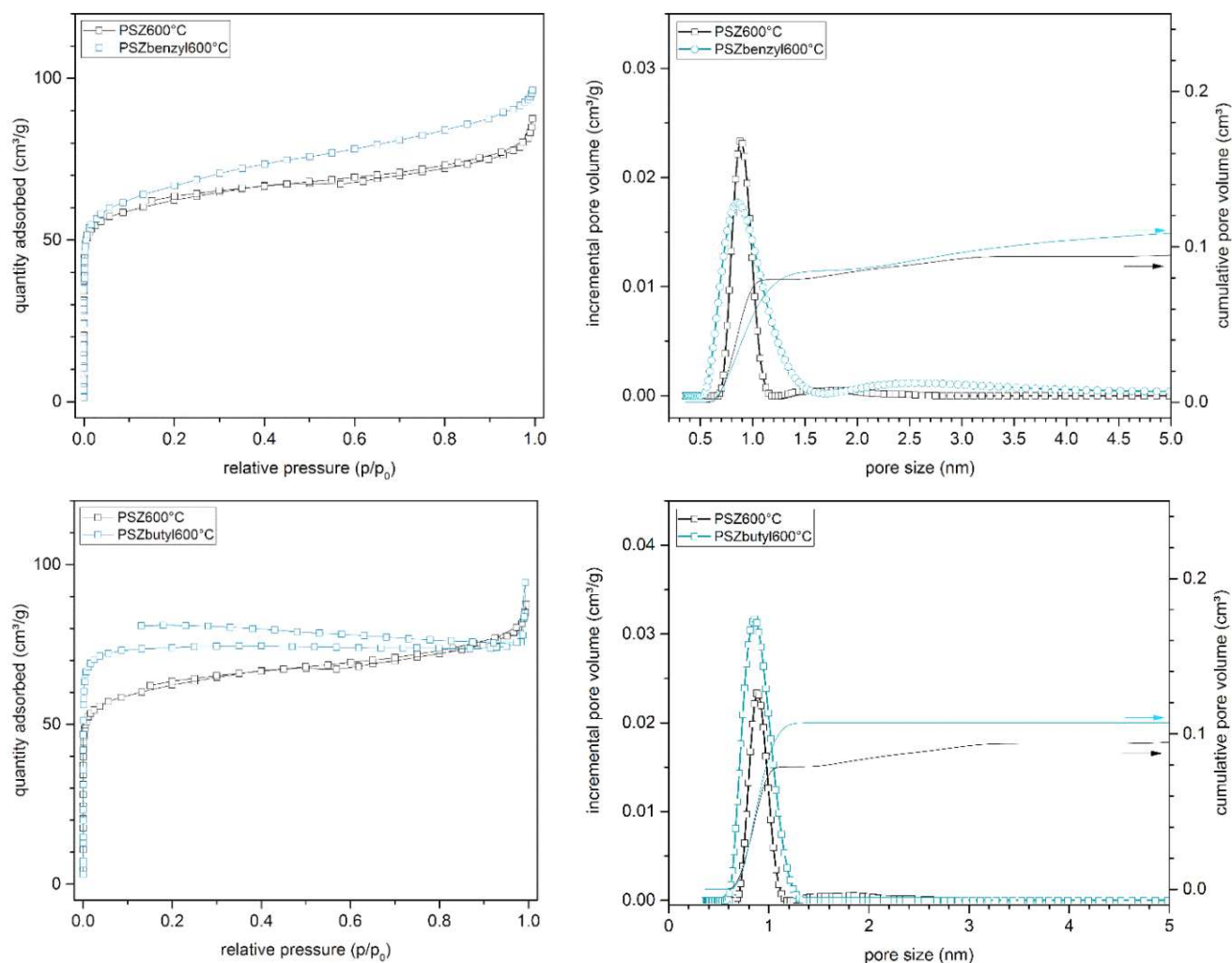


Figure 65:  $N_2$  physisorption isotherms of PSZ, PSZbenzyl and PSZbutyl after pyrolysis (600 °C) on the left; PSDs calculated from the  $N_2$  physisorption data using NL-DFT on the right.

### 8.2.13 SAXS investigations

In addition to the physisorption measurements, SAXS measurements were carried out, to double check on the results. In addition to the two different organic groups used in this work, several other organic groups were used by Matthias Nebel during his master's thesis [129]. The SAXS measurements of these modified PSZ types were carried out in this work.

The experimental SAXS curves with the corresponding fits are shown in Figure 66 and the most interesting section is shown on a linear scale in Figure 67. The data calculated from the fits is summarized in Table 24.

The values for  $2R_g$ , which resemble the pore size, increase with an increase in organic group – the butyl group leads to almost no change, the aromatic groups and the longer aliphatic octyl-

group lead to bigger values. These values have to be seen critically though, because the fit doesn't match the experimental data perfectly in all regions. The other values that can be calculated from the fit are similar for all the modifications. The fractal dimension  $D$  is close to 4 for all the samples, indicating a sharp interface between bulk and pores. The hard sphere radius, which resembles the distance between the pores and the hard sphere volume fraction which is a measure for the agglomeration of the pores don't show significant differences between the samples.

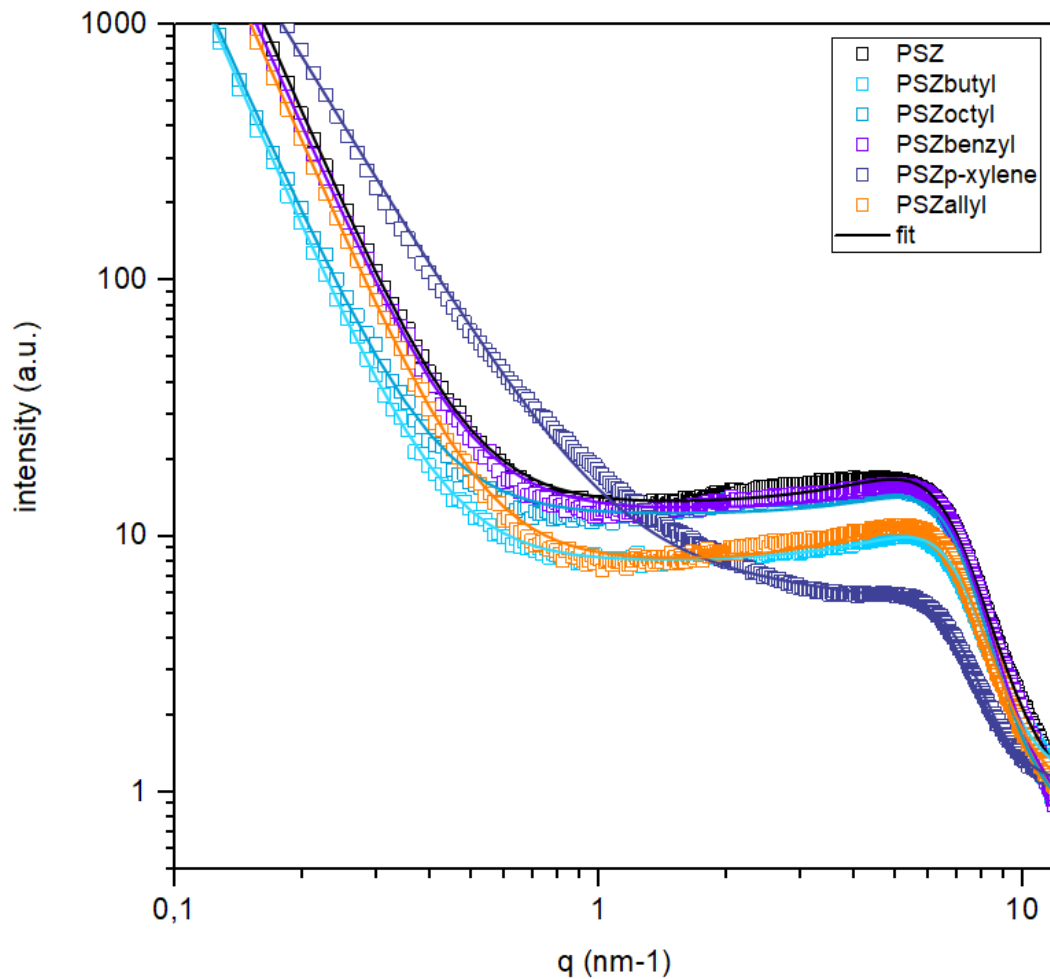


Figure 66: Experimental SAXS curves and the corresponding fits of the different modifications of PSZ.

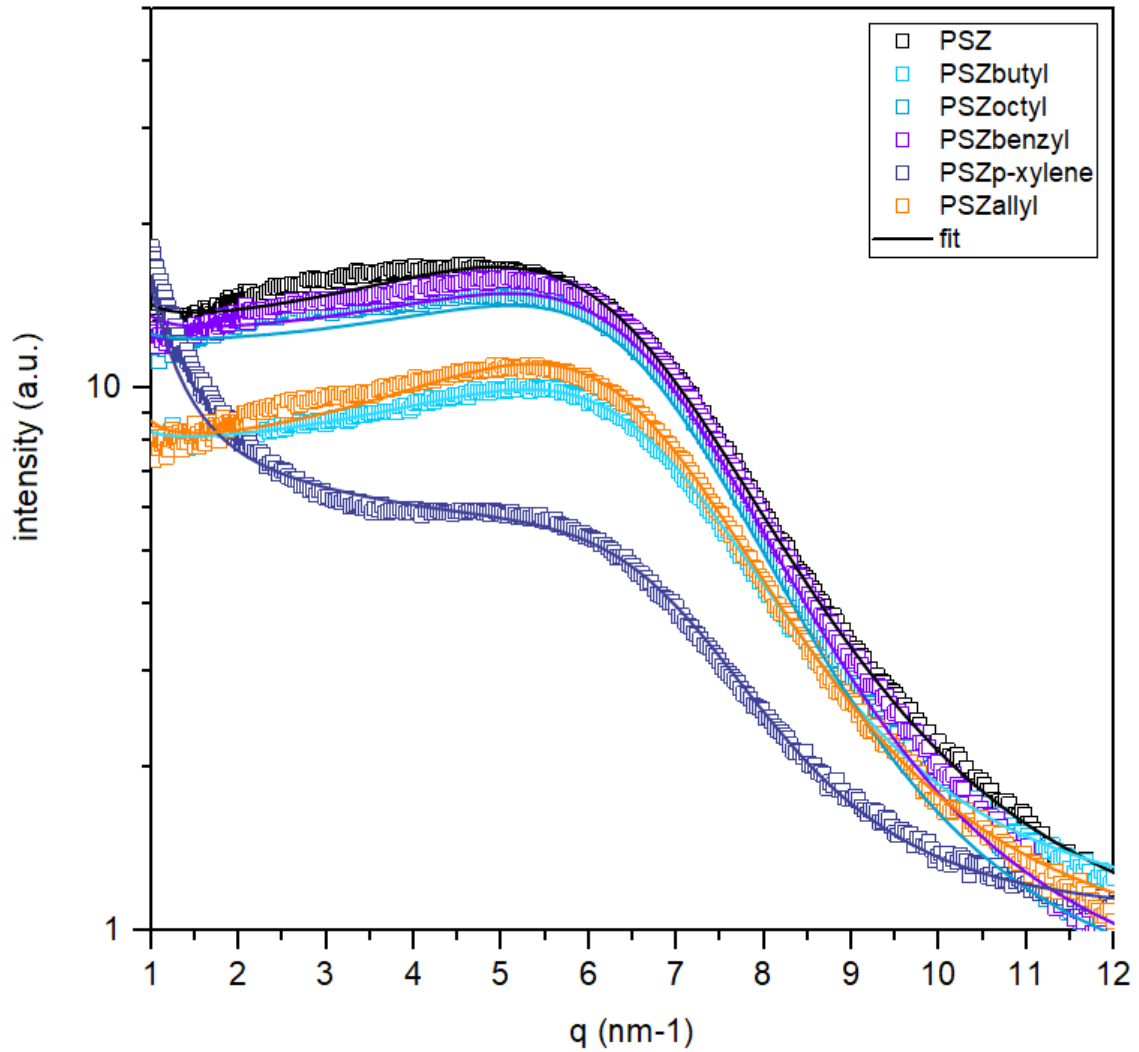


Figure 67: Section of the SAXS curves on a linear scale.

Table 24: Parameters obtained from applying a model fit to the SAXS data: Radius of gyration ( $R_g$ ), fractal dimension ( $D$ ), hard sphere radius ( $R_{hs}$ ), and hard sphere volume fraction ( $\eta$ ).

	$2R_g$ (nm)	$D$	$2R_{hs}$ (nm)	$\eta$
<b>PSZ</b>	0.71	3.85	0.89	0.19
<b>PSZbutyl</b>	0.72	3.82	0.86	0.21
<b>PSZoctyl</b>	0.77	3.73	0.87	0.22
<b>PSZbenzyl</b>	0.75	3.76	0.87	0.21
<b>PSZp-xylene</b>	0.84	2.80	0.84	0.23
<b>PSZallyl</b>	0.72	3.83	0.89	0.22

### 8.3 Conclusions – Focus III

Two different organic groups, a butyl and a benzyl group, were successfully incorporated in the crosslinked network by modifying the preceramic polymer using halides before thermal treatment. The use of an aromatic compound yielded better results, which could be due to an activation of the C-atom due to the aromatic nature of the benzene ring. NMR spectroscopy and elemental analysis indicated a complete substitution in case of the benzyl group and approximately one third of the N-H groups were substituted by the butyl group. TGA-MS analysis – despite problems with the measurements – showed release of aromatic compounds in a temperature range between 300-500 °C, which is below the maximum of the polymer-ceramic conversion of the pure PSZ.

The pore characterization showed no significant differences between PSZ, PSZbenzyl and PSZbutyl (after pyrolysis), neither in specific surface area nor in pore size maximum. So although an H-atom was substituted by a much bigger organic group, which was actually released during the pyrolysis and didn't stay integrated, there was no effect on the pores. This indicates that the reactions relevant for the micropore formation in PSZ are taking place above the decomposition temperature of the benzyl group.

Overall, it can be said that although the substitution of the N-H group by organic groups was successful, there was no profound effect on the pore characteristics of the resulting ceramic visible.

## 9. FOCUS IV – MODIFICATIONS DURING THE CROSSLINKING STEP

Since there are many possible ways of crosslinking polymers, some parameters were changed in this processing step and the influence on the resulting ceramics was investigated. These changes include the change of type and amount of initiator as well as changing the crosslinking mechanism to thermally induced crosslinking or hydrosilylation with or without the use of different linker molecules.

### 9.1 Experimental procedure – Focus IV

#### 9.1.1 Materials

The following materials were used for the experiments:

- Poly(vinyl)silazane PSZ (Durazane HTT 1800, durXtreme GmbH) as polymer precursor
- Dicumylperoxide DCP (Fluka, >97,0%) as initiator
- Azobis(isobutyronitril) (Sigma Aldrich, 98%) AIBN as initiator
- Divinylbenzene DVB (Sigma Aldrich, 80 %, isomer mixture)
- 1,5-Hexadiene (Sigma Aldrich, 97%)
- Karstedt catalyst (Sigma Aldrich, Platin(0)-1,3-divinyl-1,1,3,3-tetramethyldisiloxan in xylene, ~ 2% Pt)

#### 9.1.2 Thermal crosslinking without initiator addition

The used polysilazane crosslinks without initiator if heated above 200 °C. Therefore, a sample was prepared by heating PSZ (degassed before use) up to 250 °C with a dwell time of 2.5 hours and a heating rate of 1 K/min. A nitrogen flow of 0.35 l/min was used. The sample will be referred to as “PSZthermally” in the following chapters.

#### 9.1.3 Variation of the DCP concentration

As described in the previous chapters, the polysilazane was degassed in vacuum before every use. Different amounts of DCP as radical initiator were dissolved in the polysilazane and then degassed again. Mixtures with 0.5, 1.0, 1.5, 2.5, 5 wt% of DCP in relation to PSZ were prepared and then crosslinked using the standard heating program with 1 K/min up to 130 °C (12 h dwell time) under N<sub>2</sub>-flow (0.35 l/min).



### 9.1.4 Changing the radical initiator

To check if changing the initiator used has an influence on the resulting ceramic, AIBN was used instead of DCP. The processing was kept the same, meaning 1 wt% of AIBN was dissolved in PSZ and the mixture was – after degassing – heated up to 130 °C under flowing N<sub>2</sub>.

### 9.1.5 Changing the crosslinking mechanism using hydrosilylation

According to the literature, hydrosilylation is a common way to crosslink especially polycarbosilanes using the Si-H-groups in the backbone of the polymer and a linker molecule, often DVB, containing at least two unsaturated bonds. Using a catalyst, a saturated Si-hydrocarbon-bond forms. Since the polysilazane that is used in these investigations contains both groups that are necessary for the reaction, experiments were conducted with the pure polymer as well as with linker molecules. Preliminary experiments were conducted to find out which amount of catalyst, which temperature and dwell time are necessary to get a solid as result. The parameters chosen for the final experiments are listed in Table 25.

Table 25: Parameters of the hydrosilylation experiments.

	PSZ	DVB or HDE, molequ.	Temperature	Time	Catalyst (Karstedt's catalyst)
<b>PSZ20µl</b>	1 g	0	120 °C	12 h	50 ppm (with respect to the SiH groups of PSZ) = 0.044g=20µl of 2% solution
<b>PSZ+HDE</b>	1 g	0.8	120 °C	12 h	20 µl
<b>10DVB</b>	0.5g	0.1	120 °C	12 h	50 ppm (with respect to the SiH groups of PSZ) = 0.022g=10µl of 2% solution
<b>20DVB</b>	0.5 g	0.2	120 °C	12 h	10 µl
<b>40DVB</b>	0.5 g	0.4	120 °C	12 h	10 µl
<b>80DVB</b>	0.5 g	0.8	120 °C	12 h	10 µl

### 9.1.6 Pyrolysis

All of the samples were pyrolyzed using the standard heating program up to 600 °C (5.2.3).



## 9.2 Results – Focus IV

The results of the different characterization methods are given in the following sub-chapters.

### 9.2.1 Sample without initiator addition

#### 9.2.1.1 Optical appearance

The sample that was thermally crosslinked without initiator addition (PSZ<sub>thermally</sub>) is shown in Figure 68 before and after crosslinking as well as after pyrolysis. In the first two stages it is colorless, after crosslinking solid with signs of foaming, which can be explained by volatilization of low molecular weight compounds since the crosslinking starts at higher temperature than when an initiator is used and is therefore a competitive reaction to the distillation. After pyrolysis, it is dark brown, as the benchmark sample.

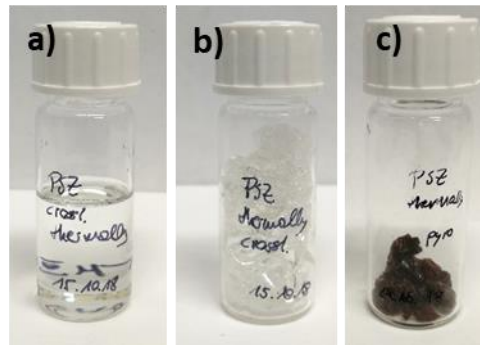


Figure 68: Sample images of PSZ<sub>thermally</sub> different processing steps. a) before crosslinking b) after crosslinking at 250°C c) after pyrolysis at 600 °C.

#### 9.2.1.2 Mass Change

The thermally crosslinked sample is expected to have a higher mass loss since a higher crosslinking temperature is necessary than for the samples crosslinked using an initiator and low molecular weight compounds can therefore be distilled. According to the results in Table 26, the mass loss is indeed higher for the thermally crosslinked sample than for a sample crosslinked by DCP addition. During pyrolysis on the other hand, the mass loss is lower for PSZ<sub>thermally</sub>. This can be explained by the temperature used for crosslinking, 250 °C, at which first reactions of the polymer-ceramic-conversion could already take place. That part of the mass loss would therefore be missing in the value for the pyrolysis step. Overall, the mass loss for the two steps is higher for the thermally crosslinked sample with 34 %, compared to 28 % observed for a DCP-crosslinked sample, which confirms the assumption that, in this case, volatile compounds are distilled off before they can be included in the crosslinked network.

Table 26: Mass change of the benchmark-sample crosslinked with DCP compared to PSZ crosslinked without initiator addition.

	$\Delta m_{\text{pure-crossl.}}, \%$	$\Delta m_{\text{crossl.-pyro}}, \%$
PSZ+DCP	-2.2	-26.0
PSZ <sub>thermally</sub>	-15.9	-19.0

### 9.2.1.3 Elemental composition

The elemental composition is shown for the crosslinked samples in Figure 69 and the pyrolyzed ones in Figure 70. There are barely any differences between samples crosslinked without initiator addition and the benchmark sample with 1 wt% DCP. The oxygen content is slightly higher in all processing stages. Small differences in carbon and nitrogen content can be found, but they are not significant.

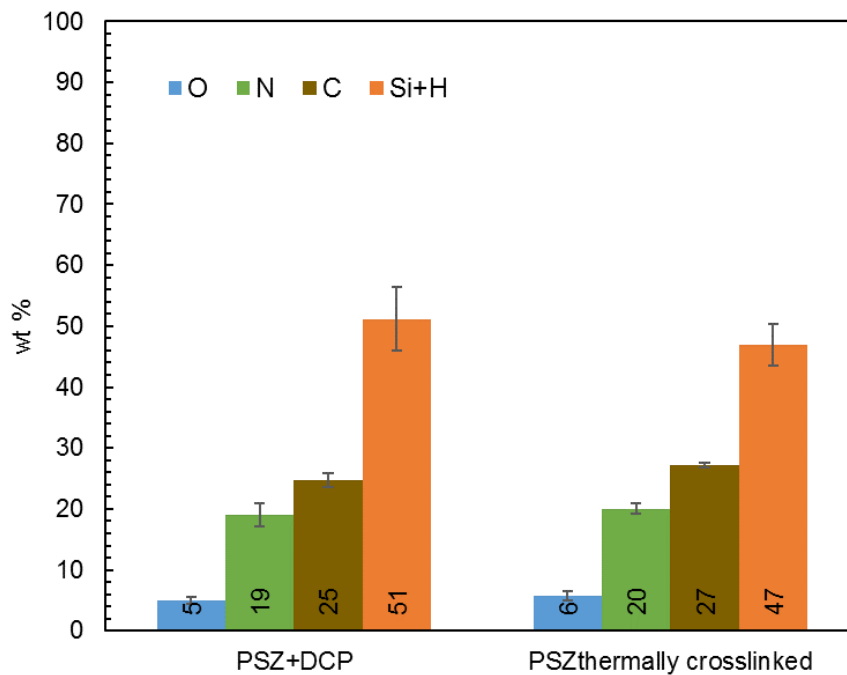


Figure 69: Elemental composition of PSZ crosslinked using DCP as initiator or without initiator addition; O, N, and C content are measured, Si+H is calculated as remainder to 100 wt%.

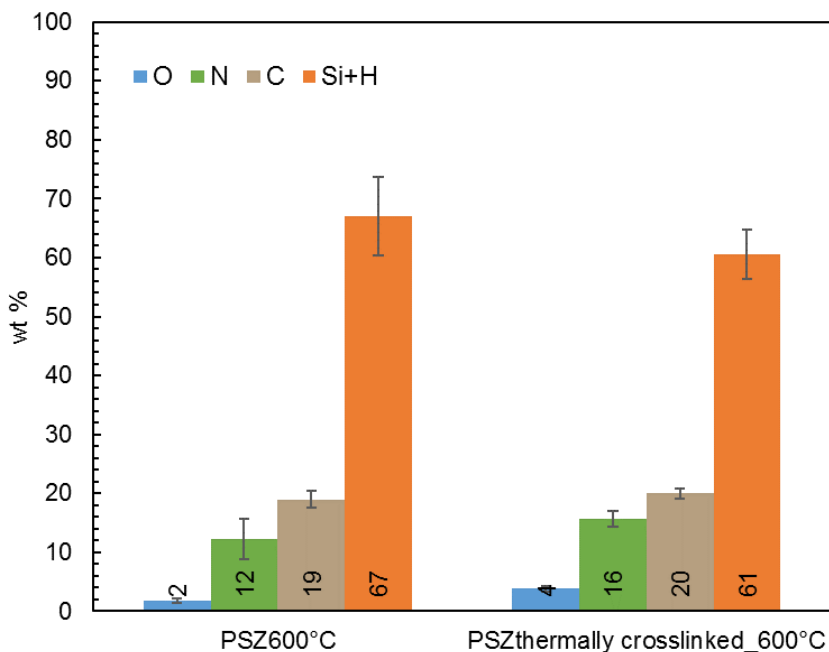


Figure 70: Elemental composition of PSZ crosslinked using DCP as initiator or without initiator addition after pyrolysis at 600 °C; O, N, and C content are measured, Si+H is calculated as remainder to 100 wt%.

#### 9.2.1.4 ATR-IR

The ATR-IR spectrum of the thermally crosslinked sample in comparison to the benchmark sample that was crosslinked using DCP as radical initiator is shown in Figure 71, normalized on the Si-CH<sub>3</sub> band. An interesting difference between the two spectra is that after the thermal crosslinking, there are still vinyl groups visible in the spectrum at wavenumbers of 1600 cm<sup>-1</sup> and 3050 cm<sup>-1</sup>, indicating that the radical crosslinking mechanism leading to the polyaddition of vinyl groups is less important than reactions between e.g. Si-H and N-H groups, which both decrease. In addition, the Si-H and N-H signals shift slightly to higher wave numbers, which originates from a slight decrease in bond length, probably caused by a change of the neighboring atoms. Around 1050 cm<sup>-1</sup>, there is a big difference between the two spectra, which could on the one hand be caused by a higher oxygen content since this wave number region is the region of Si-O vibrations, but since the elemental composition shows no significant difference, this is unlikely. Another explanation could be the formation of C-N bonds which also leads to bands in this region and which might form during the crosslinking process. This would also explain the relatively strong decrease of the N-H band at 1200 cm<sup>-1</sup>.

In Figure 72, there are the corresponding spectra after pyrolysis. The intensities of the main bands were adjusted to be approximately the same, since normalization is not possible, as none of the bands can be assumed to remain unchanged. There is no significant difference between the two spectra, the Si-CH<sub>3</sub> signal at ~1230 cm<sup>-1</sup> can be found in both spectra, together with the corresponding C-H vibrations at ~1320 cm<sup>-1</sup>. The other signals present in the spectrum of the thermally crosslinked sample are background signals resulting from air.

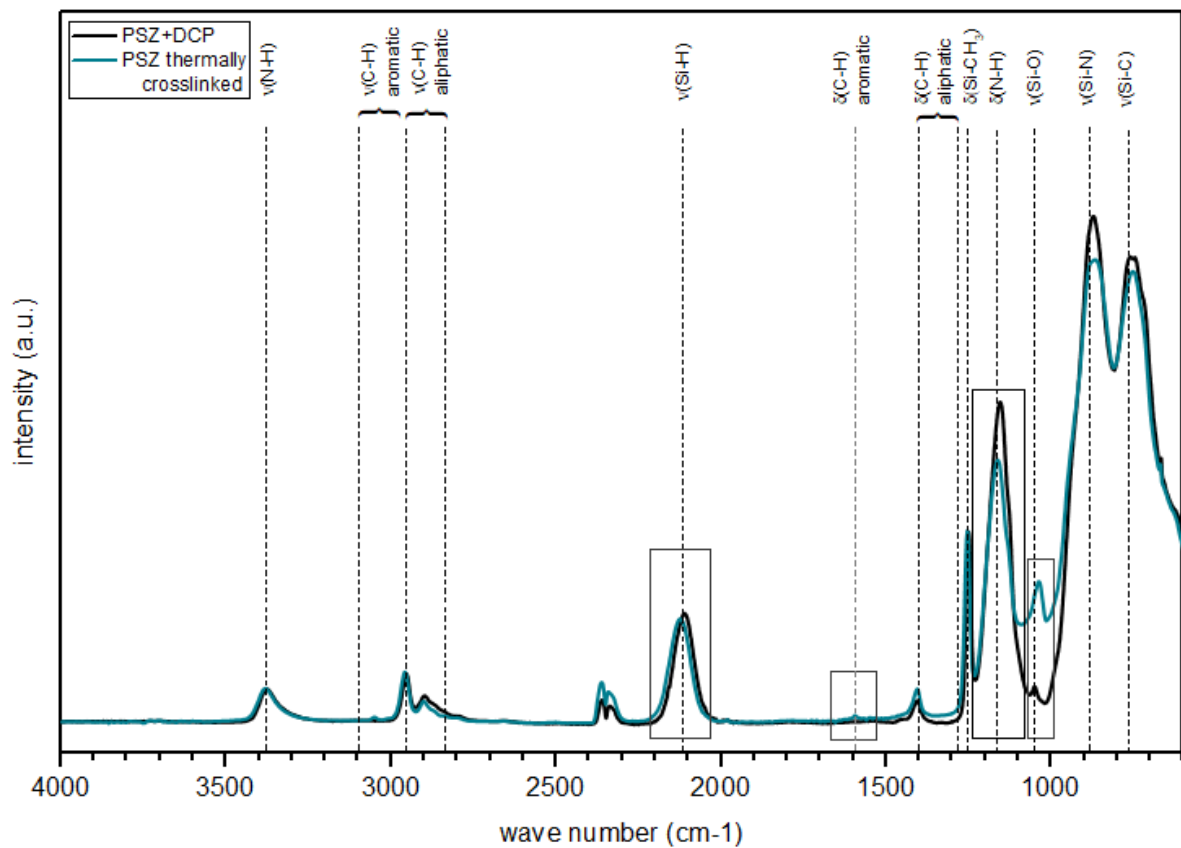


Figure 71: ATR-IR spectra of the thermally crosslinked pure PSZ in comparison to the PSZ crosslinked using DCP; the spectra are normalized on the Si-CH<sub>3</sub> band from 1230-1300 cm<sup>-1</sup>.

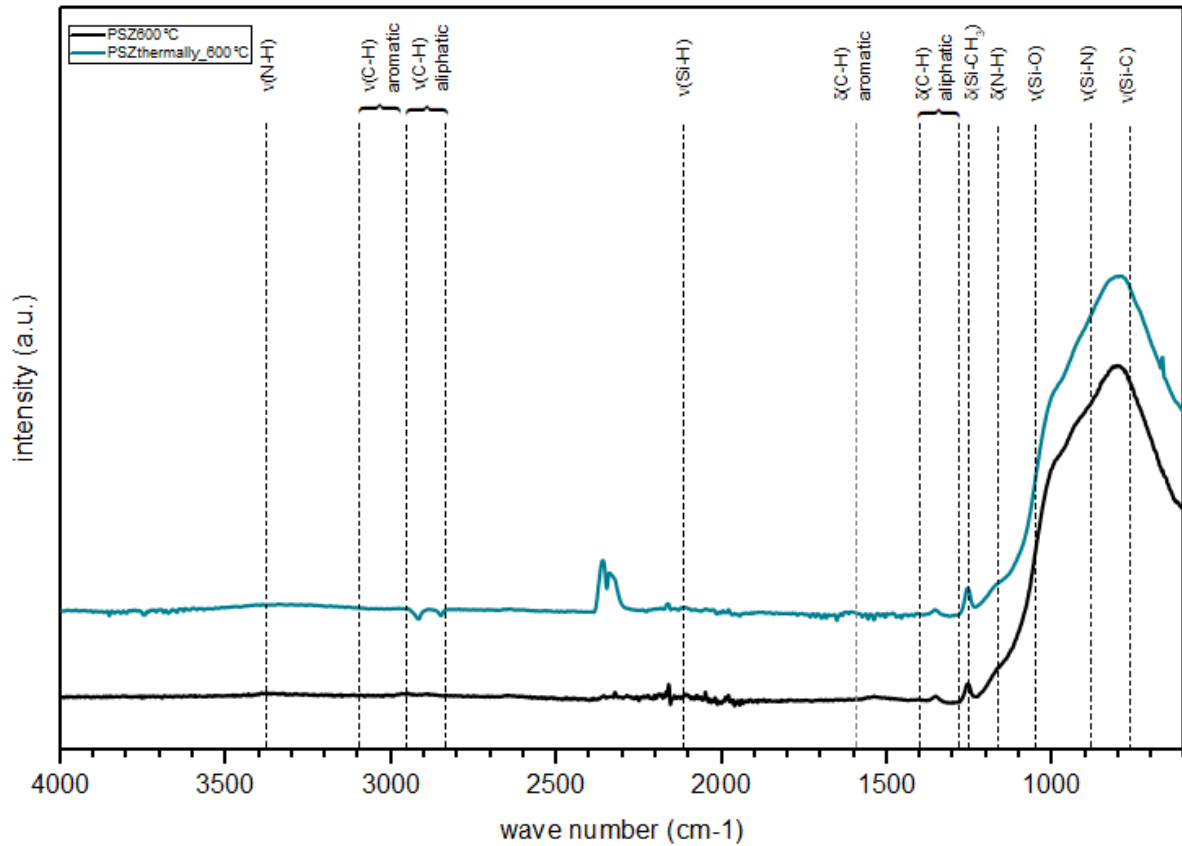


Figure 72: ATR-IR spectra of the thermally crosslinked pure PSZ in comparison to the PSZ crosslinked using DCP after pyrolysis at 600 °C.

### 9.2.1.5 N<sub>2</sub>-Physisorption

The isotherm of the thermally crosslinked pure PSZ after pyrolysis was recorded using N<sub>2</sub>-physisorption and is shown in Figure 73 together with that of PSZ crosslinked using DCP (benchmark sample). The isotherm is of type I which means the sample is microporous. The PSD (Figure 74) shows only one maximum at 0.84 nm, which is almost the same value as for the benchmark sample (0.86 nm). This indicates that the pore size is either predefined by the cyclic moieties of the starting polymer or by the elemental composition of the resulting ceramic, since the main maximum doesn't change by changing the crosslinking mechanism. In contrast to the benchmark sample, there is only one maximum in the microporous region; the benchmark sample has a second smaller maximum around 2 nm. That could lead to the assumption that this second maximum is caused by the structures forming through bridging at the crosslinking spots.

As can be seen in Table 27, the BET surface area of the thermally crosslinked sample is  $213 \pm 11 \text{ m}^2/\text{g}$ , which is in the region of PSZ+DCP pyrolyzed at the same temperature ( $195 \pm 11 \text{ m}^2/\text{g}$ ). Also the micropore volume is comparable, with  $\sim 0.10 \text{ cm}^3/\text{g}$  for both samples. Since all the parameters calculated from the isotherms are similar, the absence of the initiator doesn't influence the porosity of the resulting ceramic drastically. Still, the lack of the second maximum around 2 nm could indicate that the crosslinking mechanism leads to the formation of a second pore type formed by the polyaddition of the vinyl groups when DCP is used as radical initiator.

Table 27: Type of isotherm, BET specific surface area ( $S_{\text{BET}}$ ), maximum of the pore size distribution ( $\text{PSD}_{\text{max}}$ ) and micropore volume ( $V_{\text{micro}}$ ) of PSZ crosslinked thermally or using DCP.

	Isotherm	$S_{\text{BET}}$ ( $\text{m}^2/\text{g}$ )	$\text{PSD}_{\text{max}}$ (nm)	$V_{\text{micro}}$ ( $\text{cm}^3/\text{g}$ )	Comment
<b>PSZ600 °C</b>	Type I	$195 \pm 6$	0.86	0.10	Microporous
<b>PSZthermally crosslinked600°C</b>	Type I	$213 \pm 11$	0.84	0.10	Microporous

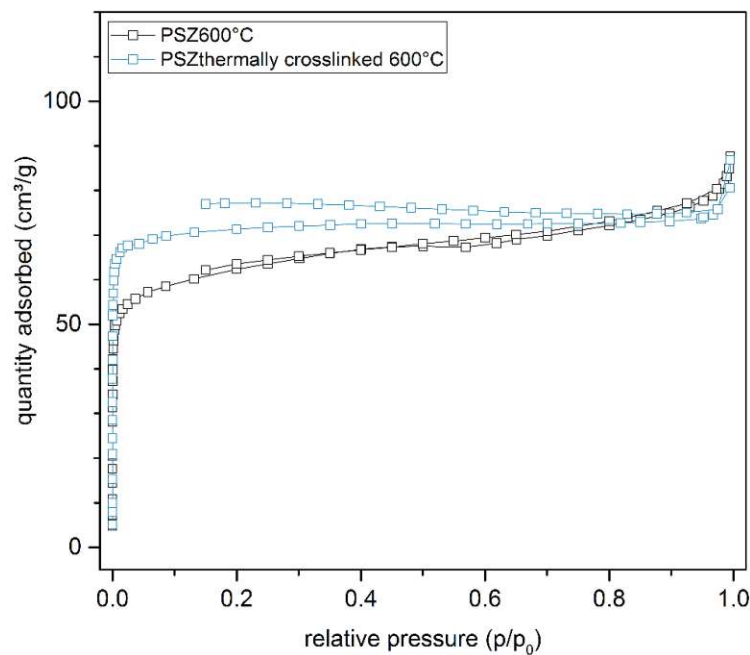


Figure 73:  $\text{N}_2$  physisorption isotherms of the thermally crosslinked PSZ and the one using DCP after pyrolysis ( $600 \text{ }^\circ\text{C}$ ).

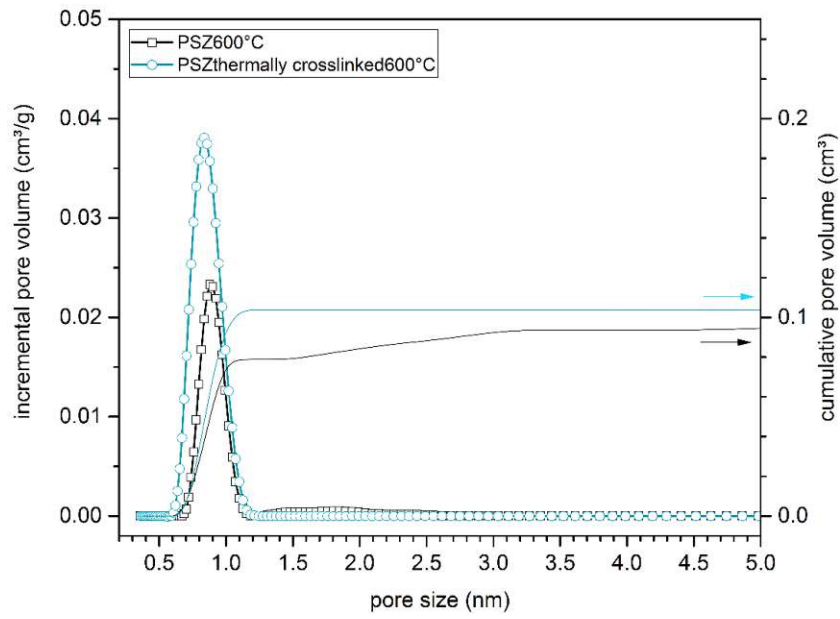


Figure 74: PSDs of PSZ crosslinked thermally and PSZ using DCP after pyrolysis (600 °C), calculated from the  $N_2$  physisorption data using NL-DFT.

## 9.2.2 Change of the amount of initiator

To check whether different amounts of the same initiator influence the crosslinking behaviour, experiments were conducted using different amounts of DCP.

### 9.2.2.1 Optical appearance

As can be seen in Figure 75, there is no difference between the samples with varied amounts of DCP. All of them are colorless before and after crosslinking and dark brown in after pyrolysis.

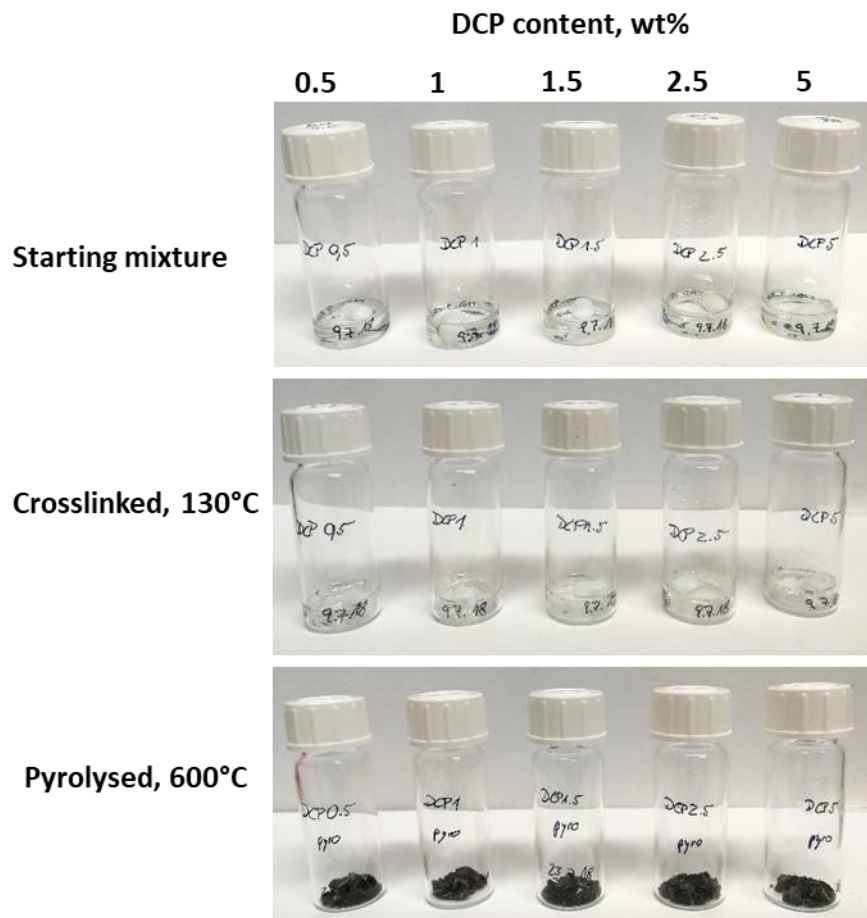


Figure 75: Sample images of the DCP variation before (top) and after (middle) crosslinking and in the pyrolysed stage (bottom).



### 9.2.2.2 Mass change

The mass loss of the samples with varied DCP amount is given in Table 28. Although there is a slight trend showing higher mass loss with higher DCP amount, the differences are small and - when taking the weighing error into account - not significant.

Table 28: Mass change of the sample crosslinked with different amounts of DCP as initiator.

	$\Delta m_{\text{pure-crossl.}}, \%$	$\Delta m_{\text{crossl.-pyro.}}, \%$
DCP0.5	-3.3	-22.7
DCP1	-3.2	-22.9
DCP1.5	-3.4	-23.1
DCP2.5	-3.4	-23.1
DCP5	-4.1	-23.9

### 9.2.2.3 Elemental analysis

The elemental composition of the samples with varied amounts of the radical initiator DCP is shown in Figure 76. The samples with 1, 2.5 and 5 wt% DCP have nearly the same composition, the other two have higher oxygen and lower nitrogen values, but since there is no obvious trend with increasing amount of initiator, this may be attributed to mistakes in storage.

The composition of the samples after pyrolysis was measured too and is shown in Figure 77. As for the crosslinked samples, no significant differences can be found except for varying oxygen contents which were already present after crosslinking, and which result in variations in nitrogen content too.

FOCUS IV – MODIFICATIONS DURING THE CROSSLINKING STEP

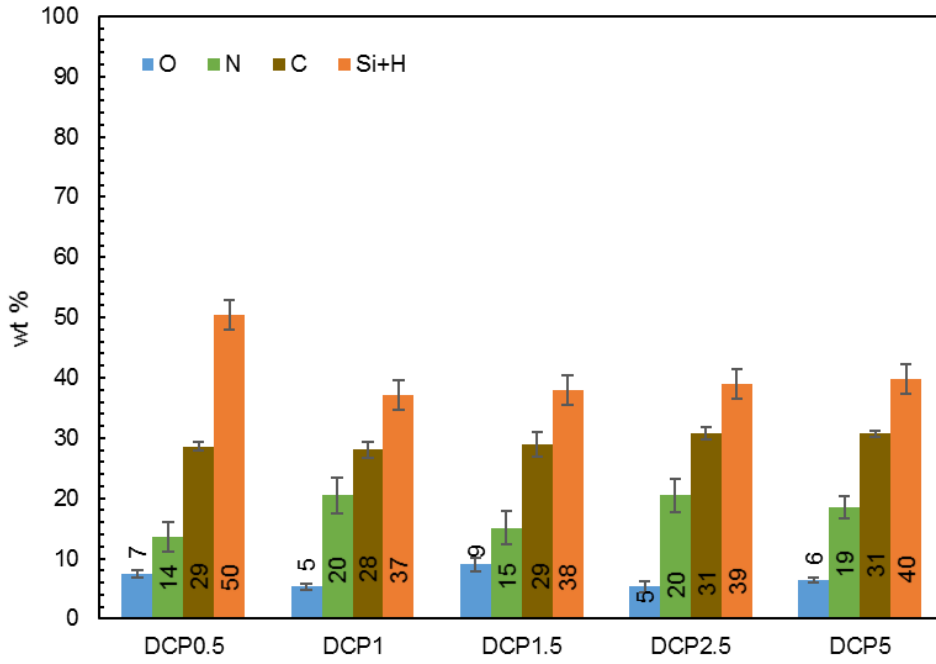


Figure 76: Elemental composition of PSZ crosslinked using different amounts of DCP as initiator; O, N, and C content are measured, Si+H is calculated as remainder to 100 wt%.

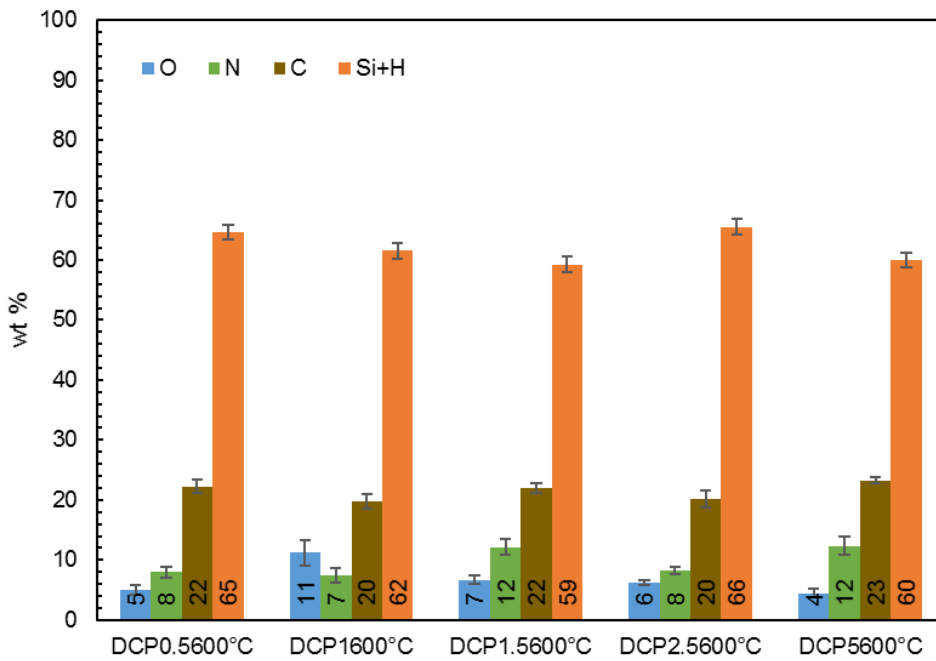


Figure 77: Elemental composition of PSZ crosslinked using different amounts of DCP as initiator after pyrolysis at 600 °C; O, N, and C content are measured, Si+H is calculated as remainder to 100 wt%.

### 9.2.2.4 ATR-IR

The ATR-IR spectra of the samples crosslinked with different amounts of DCP are shown in Figure 78, normalized on the Si-CH<sub>3</sub> band. Apart from the sample with 1.5 wt% DCP, which shows strong oxidation (Si-O vibrations at 1090 cm<sup>-1</sup>) and therefore a decrease in intensity for the N-H and Si-H bands, all the spectra look similar and no trend with increasing amount of DCP can be found. The oxidation of DCP1.5 was already visible in the results of the elemental composition.

The spectra of the pyrolyzed samples are shown in Figure 79; except for the sample with 5 wt% DCP, all the spectra almost completely overlap. The sample with 5 wt% is shifted to higher wavenumbers, which could be due to a higher oxygen content and therefore bigger contribution of the Si-O vibrations to the broad signal.

Since no correlation between DCP content and changes in mass loss, IR spectra or elemental composition was found, no further analyses were performed

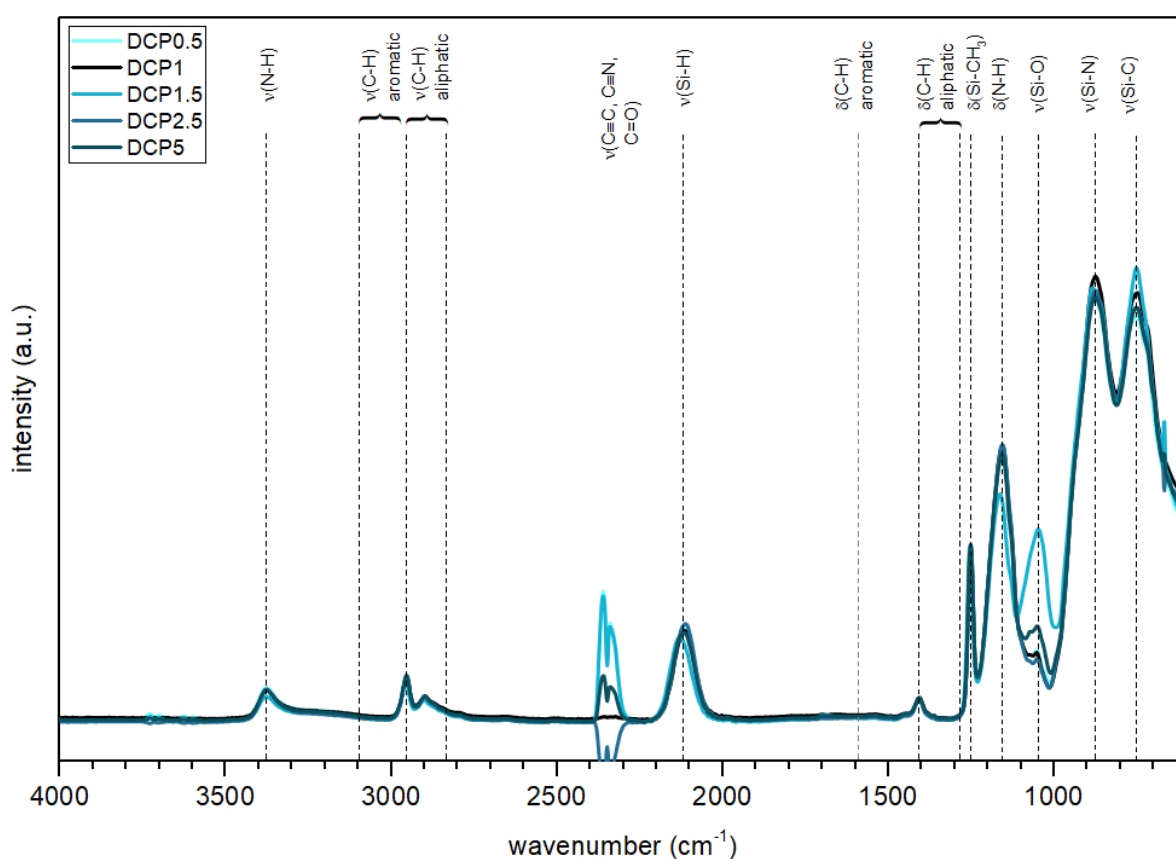


Figure 78: ATR-IR spectra of PSZ crosslinked using different amounts of DCP; the spectra are normalized on the Si-CH<sub>3</sub> band from 1230-1300 cm<sup>-1</sup>.

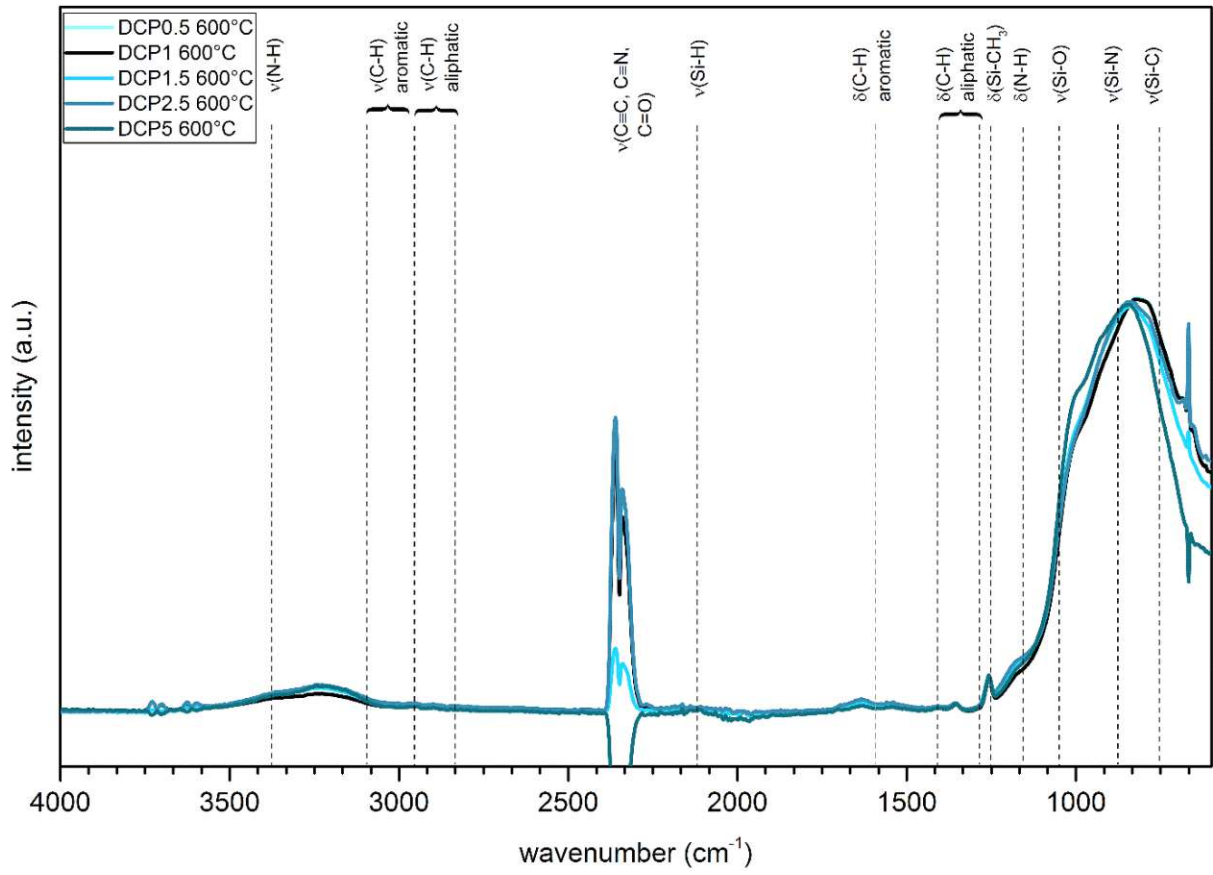


Figure 79: ATR-IR spectra of PSZ crosslinked using different amounts of DCP after pyrolysis (600 °C).

### 9.2.3 Change of the radical initiator from DCP to AIBN

The radical initiator was changed from DCP to AIBN (each 1 wt%) to check the influence of the initiator itself on the properties of the crosslinked PSZ and the resulting pyrolyzed sample.

#### 9.2.3.1 Optical appearance

As can be seen in Figure 80, the release of nitrogen during decomposition of AIBN leads to foaming of the sample and is therefore rather not applicable for the membrane layer. The pyrolyzed sample is dark brown and looks like the benchmark sample.



Figure 80: Sample images of the sample after crosslinking at 130°C with AIBN as initiator (left) and after pyrolysis at 600°C (right)

#### 9.2.3.2 Mass change

The mass change for both processing steps can be found in Table 29. During the crosslinking step, the mass loss is higher if AIBN is used instead of DCP, which can partly be attributed to the decomposition of the initiator releasing nitrogen. The mass loss during the pyrolysis step is slightly lower than for the benchmark sample, yet in the same range as for the DCP experiments, that can be found in the previous section 9.2.2.2.

Table 29: Mass change of the sample crosslinked with AIBN (1 wt%).

	$\Delta m_{\text{pure-crossl.}}, \%$	$\Delta m_{\text{crossl.-pyro}}, \%$
PSZ+DCP	-2.2	-26.0
PSZ+AIBN	-5.0	-23.9

### 9.2.3.3 Elemental composition

The elemental composition of the sample prepared using AIBN as initiator is shown in Figure 81 for the crosslinked stage and in Figure 82 for the samples after pyrolysis. The oxygen content is in both cases higher for the sample prepared using AIBN when compared to that with DCP. This could be caused by the foaming of the samples as soon as AIBN starts to decompose and forms nitrogen, leading to a higher specific surface area of the samples making them more susceptible for oxidation. But the same trend of decreasing oxygen content through pyrolysis can be observed for both samples. In the crosslinked stage, the carbon and nitrogen content are slightly higher, which could result from the nitrogen forming when AIBN decomposes.

In the pyrolyzed stage, the oxygen content of the AIBN sample is three times higher than for the DCP sample, showing the influence of the higher surface due to the foaming. The carbon content is the same as for the sample with DCP while the nitrogen content is higher for AIBN.

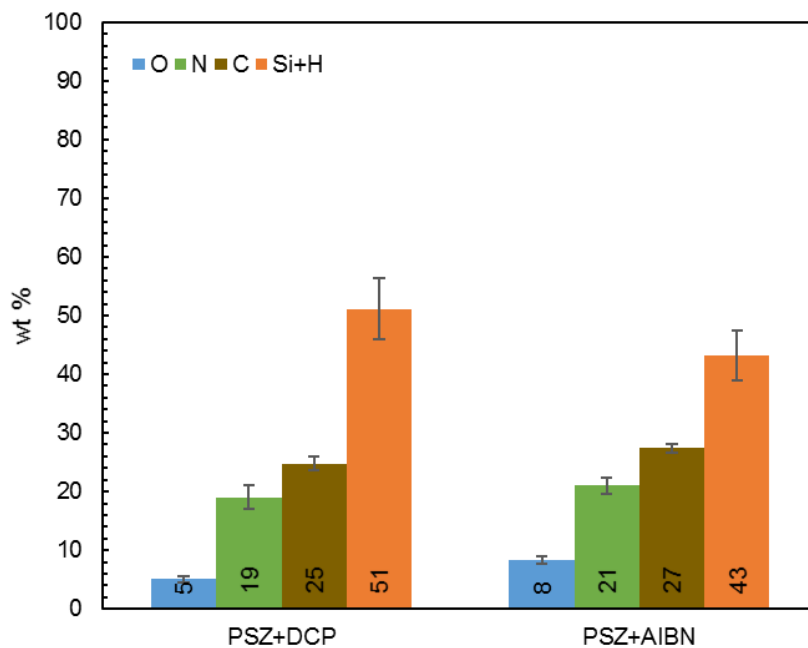


Figure 81: Elemental composition of PSZ using AIBN or DCP as initiator; O, N, and C content are measured, Si+H is calculated as remainder to 100 wt%.

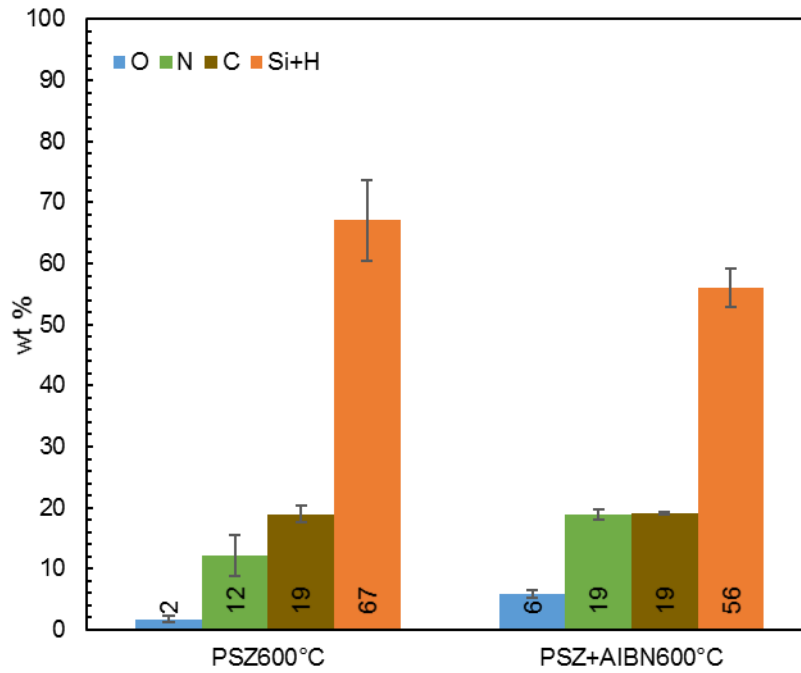


Figure 82: Elemental composition of PSZ using AIBN or DCP as initiator after pyrolysis at 600 °C; O, N, and C content are measured, Si+H is calculated as remainder to 100 wt%.

#### 9.2.3.4 ATR-IR

The ATR-IR spectra of PSZ+AIBN in the crosslinked and in the pyrolyzed stage can be found in Figure 83 and Figure 84, respectively. Apart from oxidation of the AIBN samples visible at  $1090\text{ cm}^{-1}$  and around  $3300\text{ cm}^{-1}$ , and subsequent decrease of the Si-N and Si-C bands, there is no significant difference between the spectra.

No further analyses were performed for this sample.

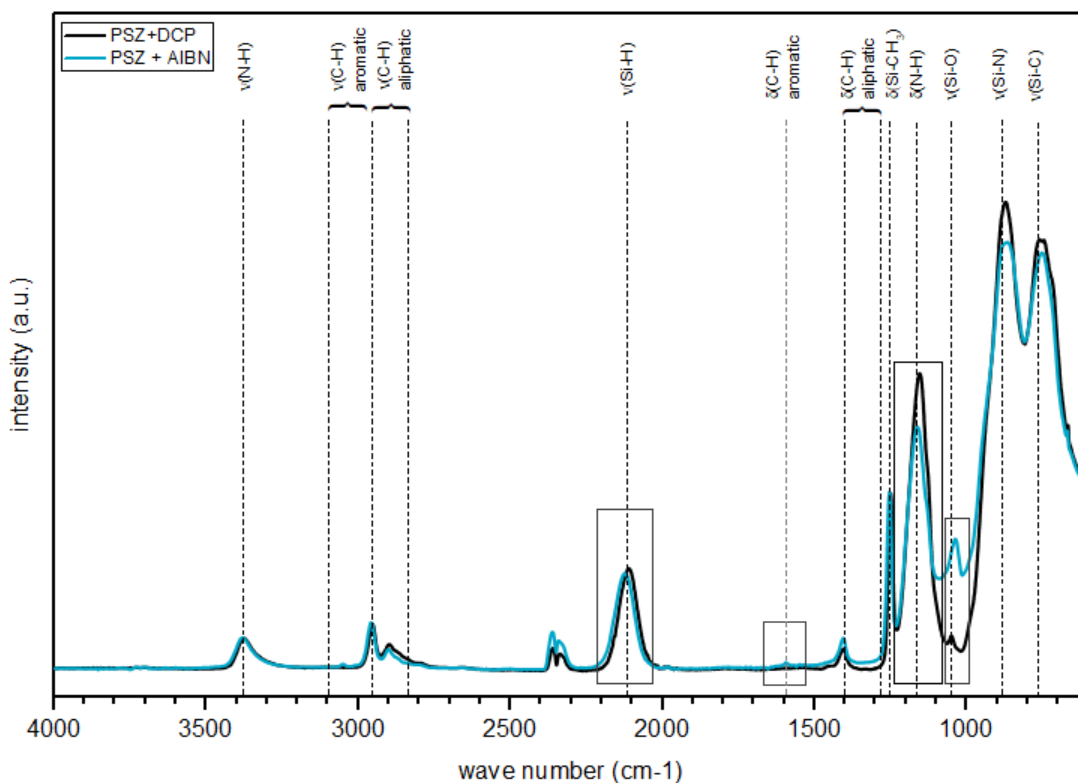


Figure 83: ATR-IR spectra of PSZ crosslinked using AIBN or DCP as initiator; the spectra are normalized on the Si-CH<sub>3</sub> band from 1230-1300 cm<sup>-1</sup>.

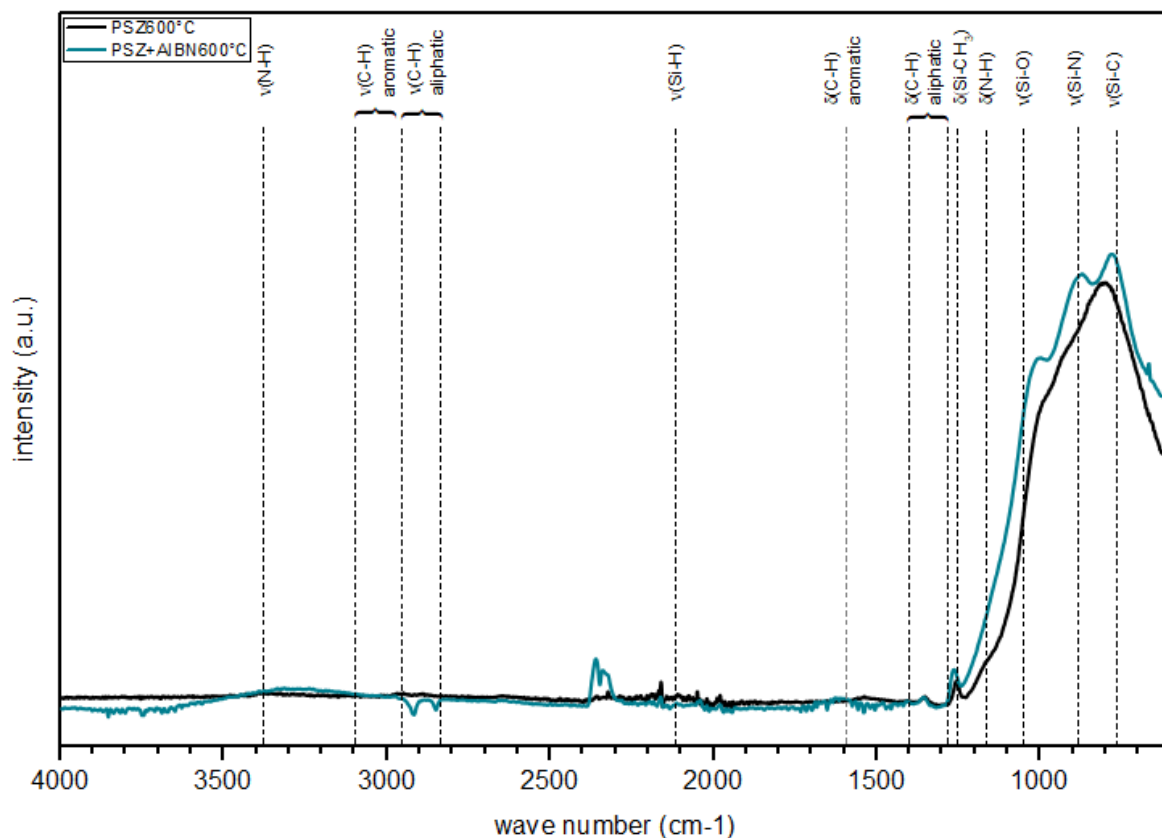


Figure 84: ATR-IR spectra of PSZ crosslinked using AIBN or DCP as initiator after pyrolysis (600 °C).



## 9.2.4 Hydrosilylation without linker

Since PSZ already contains both the groups involved in hydrosilylation experiments without addition of a linker molecule were performed.

### 9.2.4.1 Optical appearance

The sample images of the hydrosilylation without linker molecule are shown in Figure 85. The crosslinked sample is yellowish – the color change originates from addition of Karstedts catalyst and the sample remained colored while crosslinking. The pyrolyzed sample is dark brown like the benchmark sample.

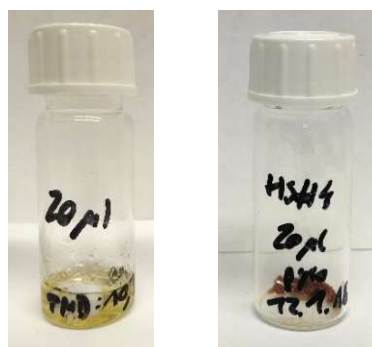


Figure 85: Sample images of the hydrosilylation without linker (PSZ20 $\mu$ l) in the crosslinked (left) and the pyrolyzed stage (right)

### 9.2.4.2 Mass change

The mass change (Table 30) of the sample during crosslinking is higher than for the benchmark sample crosslinked with 1 wt% DCP. This is partly due to distillation of the solvent of the catalyst. If the mass of the catalyst (0.04 g) is subtracted from the absolute mass loss, the relative value would change to 3.7 %. Surprisingly, the mass loss during pyrolysis is lower than for the benchmark sample. Actually, the expected result was a higher mass loss due to a lower degree of crosslinking and therefore distillation of low molecular weight compounds.

Table 30: Mass change of the sample crosslinked via hydrosilylation compared to the benchmark sample crosslinked using DCP.

	$\Delta m_{\text{pure-crossl.}}, \%$	$\Delta m_{\text{crossl.-pyro}}, \%$
PSZ+DCP	-2.2	-26.0
PSZ20 $\mu$ l	-5.9	-16.4

### 9.2.4.3 Elemental composition

In the crosslinked stage, the elemental composition is expected to be the same for the sample crosslinked using hydrosilylation as for the one using the radical initiator DCP, since in both cases only very small amounts of DCP or Karstedts catalyst are added. The results are shown in Figure 86; the only difference between the two is the higher oxygen content for the hydrosilylation sample. Oxygen is probably introduced partially by the catalyst solution itself as well as the mixing process.

The results for the pyrolyzed stage are shown in Figure 87. The main difference is again the oxygen content. Not only the absolute value is higher, but it is also constant from crosslinked to pyrolyzed stage, which could indicate that it is built into the network differently.

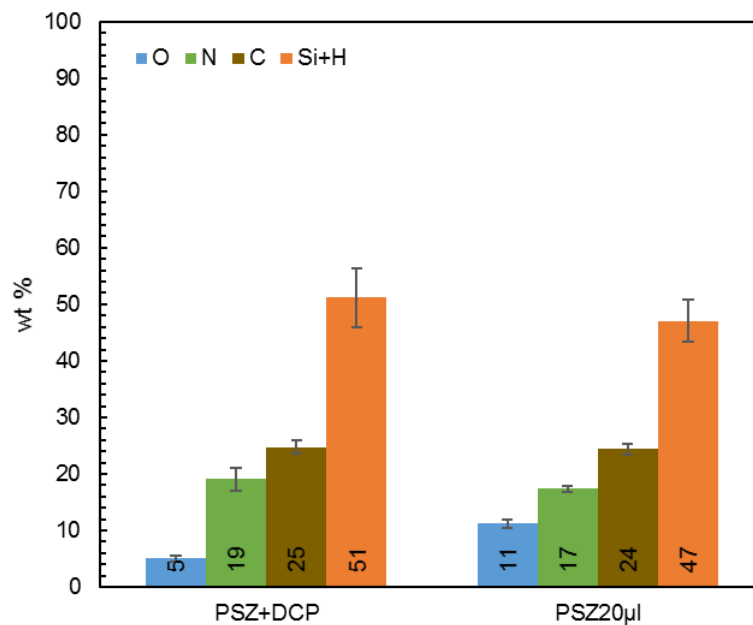


Figure 86: Elemental composition of PSZ using hydrosilylation for crosslinking or DCP as initiator in the crosslinked stage; O, N, and C content are measured, Si+H is calculated as remainder to 100 wt%.

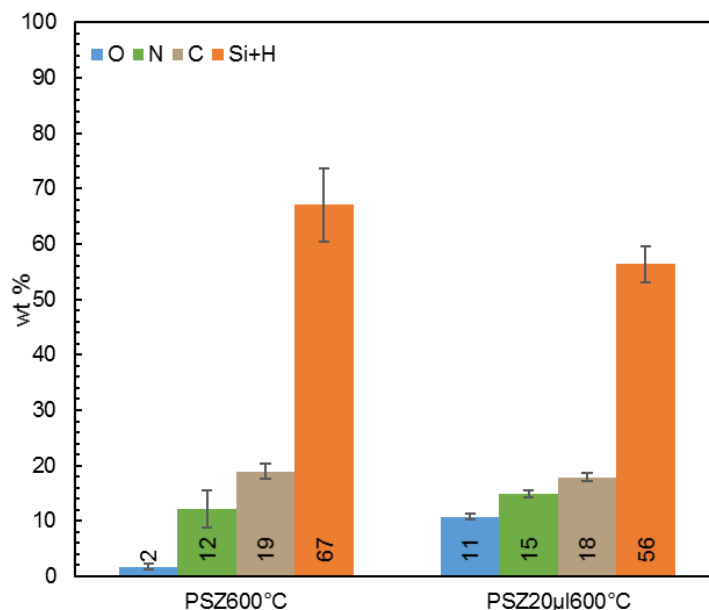


Figure 87: Elemental composition of PSZ using hydrosilylation for crosslinking or DCP as initiator after pyrolysis (600 °C); O, N, and C content are measured, Si+H is calculated as remainder to 100 wt%.

#### 9.2.4.4 ATR-IR

The spectrum of the sample crosslinked without a linker using hydrosilylation is shown in Figure 88, compared to PSZ+DCP. Only minor differences can be seen in the spectra, like a slight increase in the Si-H signal, which is surprising, because this functional group is supposed to react during the hydrosilylation process. Also, there is still the signal of the vinyl groups visible at  $1600\text{ cm}^{-1}$ . Therefore, it is unlikely that the hydrosilylation reactions took place.

The spectra of the samples after pyrolysis, which are shown in Figure 89, are nearly the same, which is an indication that the changes in crosslinking influenced the decomposition behaviour only in a minor way.

Since it is unclear whether the hydrosilylation actually took place, no further analyses were made.

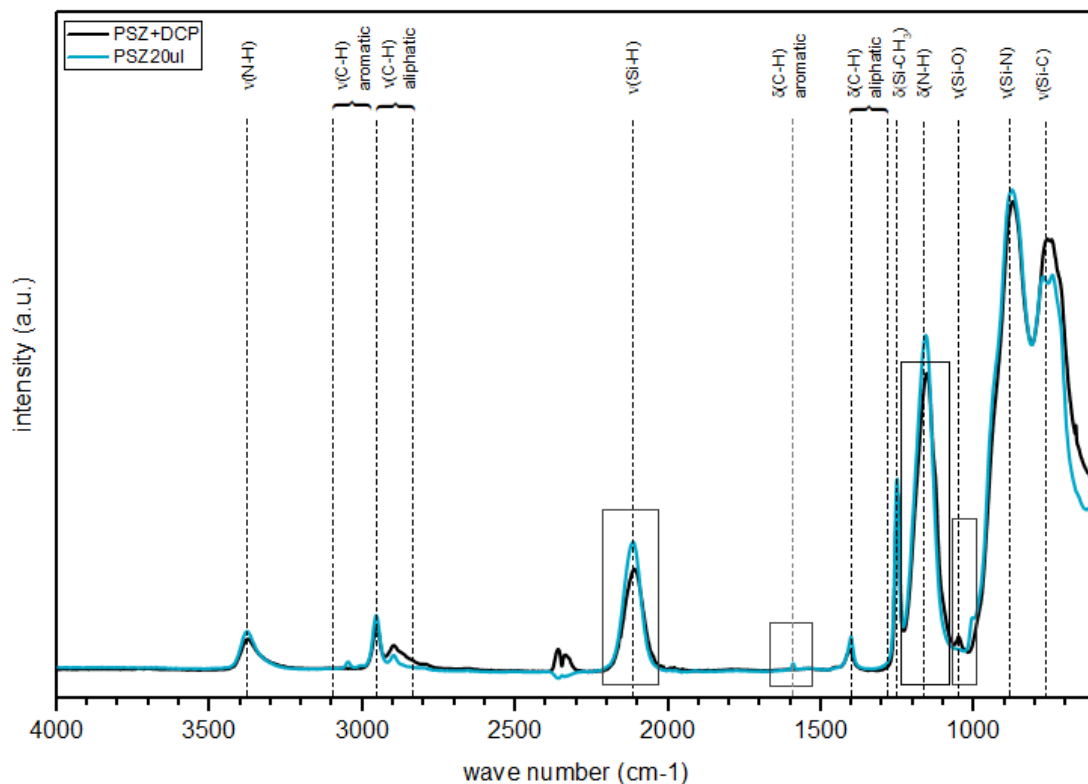


Figure 88: ATR-IR spectra of PSZ crosslinked using hydrosilylation (PSZ20 $\mu$ l) or DCP as initiator; the spectra are normalized with respect to the Si-CH<sub>3</sub> band from 1230-1300 cm<sup>-1</sup>.

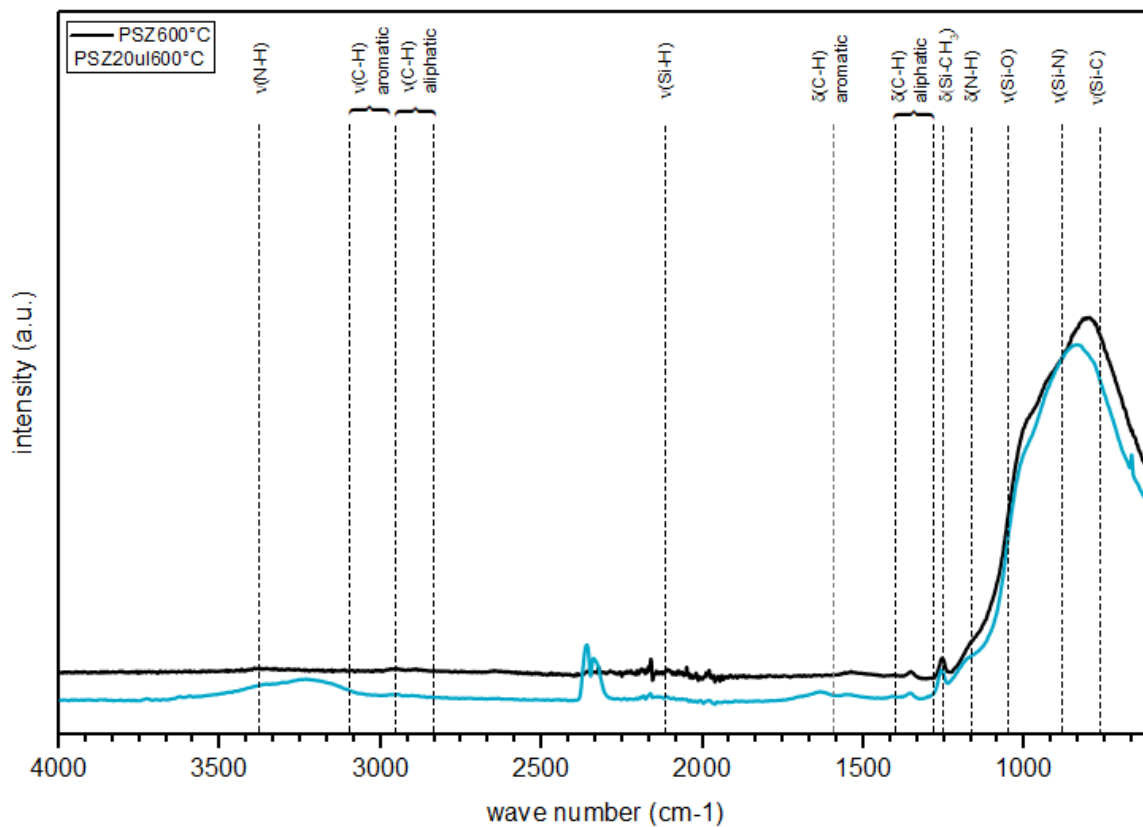


Figure 89: ATR-IR spectra of PSZ20 $\mu$ l and PSZ+DCP after pyrolysis at 600°C.

## 9.2.5 Hydrosilylation with HDE as linker molecule

1,5-hexadiene was used as linker molecule, which contains two double bonds which can react with two Si-H bonds of PSZ. By generating these longer bridges between the PSZ chains, the pore size in the resulting amorphous ceramic could be influenced.

### 9.2.5.1 Optical appearance

The sample images in Figure 90 show that the sample in the crosslinked stage is gel-like and slightly yellowish. The crosslinking apparently yields another network than when a radical initiator is used. In the pyrolyzed stage, the sample is dark brown, like the benchmark sample.

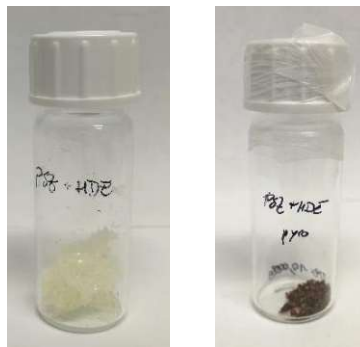


Figure 90: Sample images of the sample crosslinked with HDE as linker molecule in the crosslinked (left) and pyrolyzed (right) stage.

### 9.2.5.2 Mass change

The mass change of the sample crosslinked using hydrosilylation with HDE as linker is given in Table 31 in comparison to the benchmark sample crosslinked using DCP.

During both processing steps, the crosslinking and the pyrolysis, the mass loss is higher for the HDE sample. The higher mass loss in the crosslinking step can be attributed to the high vapour pressure (223 hPa, 20 °C) and low boiling point (bp=60 °C) of HDE.

The mass loss during pyrolysis is 7 % higher than for the benchmark sample, which indicates that the HDE included in the network decomposes during pyrolysis.

Table 31: Mass change of the sample using HDE as linker

	$\Delta m_{\text{pure-crossl.}}, \%$	$\Delta m_{\text{crossl.-pyro}}, \%$
PSZ+DCP	-2.2	-26.0
PSZ+HDE	-6.7	-33.3

### 9.2.5.3 Elemental composition

The elemental composition of the sample prepared with HDE as linker molecule is shown in Figure 91 together with the calculated composition for complete integration of all the starting compounds in the network forming during crosslinking. Also, the benchmark sample crosslinked with DCP is shown for better comparability. The theoretical compositions are given in Table 32.

The oxygen content is slightly higher which can be explained by handling. Also, the carbon content is higher for the sample with HDE as linker, which can be explained by integration of HDE into the network, since the molecule consists only of carbon and hydrogen. If compared to the theoretical composition, 50% of the HDE was actually introduced in the network based on the carbon content.

The elemental composition of the pyrolyzed sample is shown in Figure 92. Apart from the oxygen content, the composition is almost the same which leads to the assumption that HDE linkers are thermally decomposed during pyrolysis.

*Table 32: Theoretical elemental composition of the sample crosslinked using HDE as linker*

	Si, wt%	N, wt%	C, wt%	H, wt%
<b>PSZ+DCP</b>	43.7	21.8	26.1	8.5
<b>PSZ+HDE</b>	35.0	17.5	38.6	9.2

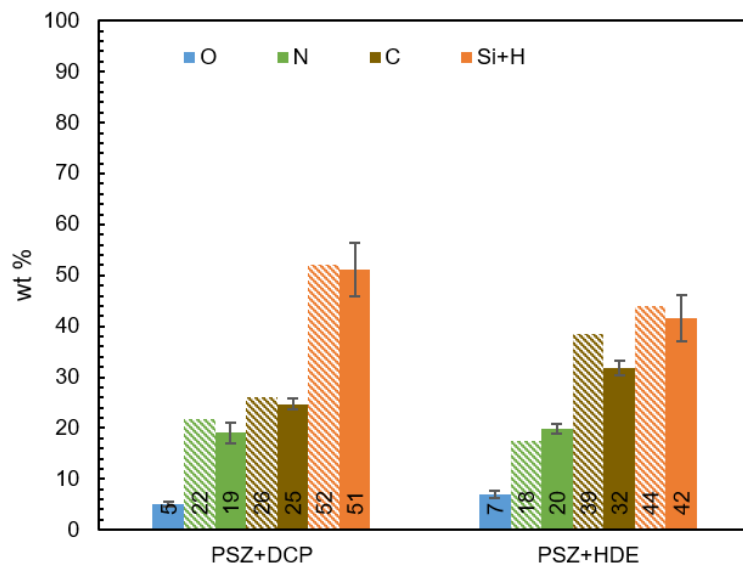


Figure 91: Elemental composition of PSZ+DCP and PSZ+HDE after crosslinking at 130°C/120°C; O, N, and C content are measured, Si+H is calculated as remainder to 100 wt%; the theoretical composition is shown by the patterned bars.

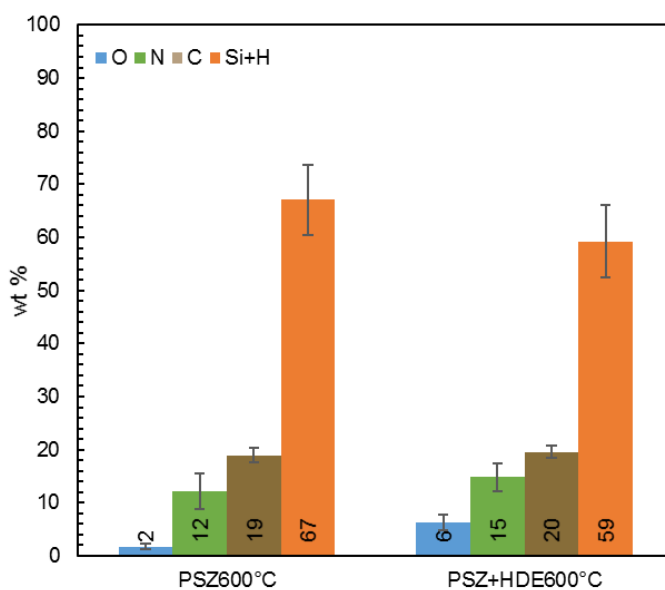


Figure 92: Elemental composition of PSZ+DCP and PSZ+HDE after pyrolysis (600 °C); O, N, and C content are measured, Si+H is calculated as remainder to 100 wt%.

#### 9.2.5.4 ATR-IR

The ATR-IR spectrum of PSZ crosslinked using HDE as linker molecule is very similar to that of the benchmark sample, as can be seen in Figure 93. The spectra were normalized with respect to the Si-CH<sub>3</sub> band. There are slight differences in the area of aliphatic C-H vibrations around 3000 cm<sup>-1</sup>. Also, it looks as if there were signals of vinyl groups slightly above 3000 cm<sup>-1</sup> and 1650 cm<sup>-1</sup>. The latter one is shifted when compared to the vinyl groups of pure PSZ, which are

still indicated by the dashed line at  $1600\text{ cm}^{-1}$ . The Si-H band doesn't decrease significantly, the N-H band slightly decreases.

Altogether, this leads to the assumption that HDE did not react with PSZ, but got entrapped in the network formed during crosslinking.

For the pyrolyzed samples (Figure 94), the spectra look quite different. The main broad peak is split up in three clearly visible maxima for the sample crosslinked with HDE. While two of them can be attributed to Si-N and Si-C, the third one is most likely caused by Si-O vibrations. This is due to a delayed measurement of the pyrolyzed sample and oxidation, which is strengthened by the broad peak around  $3300\text{ cm}^{-1}$ , typical for OH-groups. The Si-CH<sub>3</sub> group can still be found for the samples at these pyrolysis temperatures.

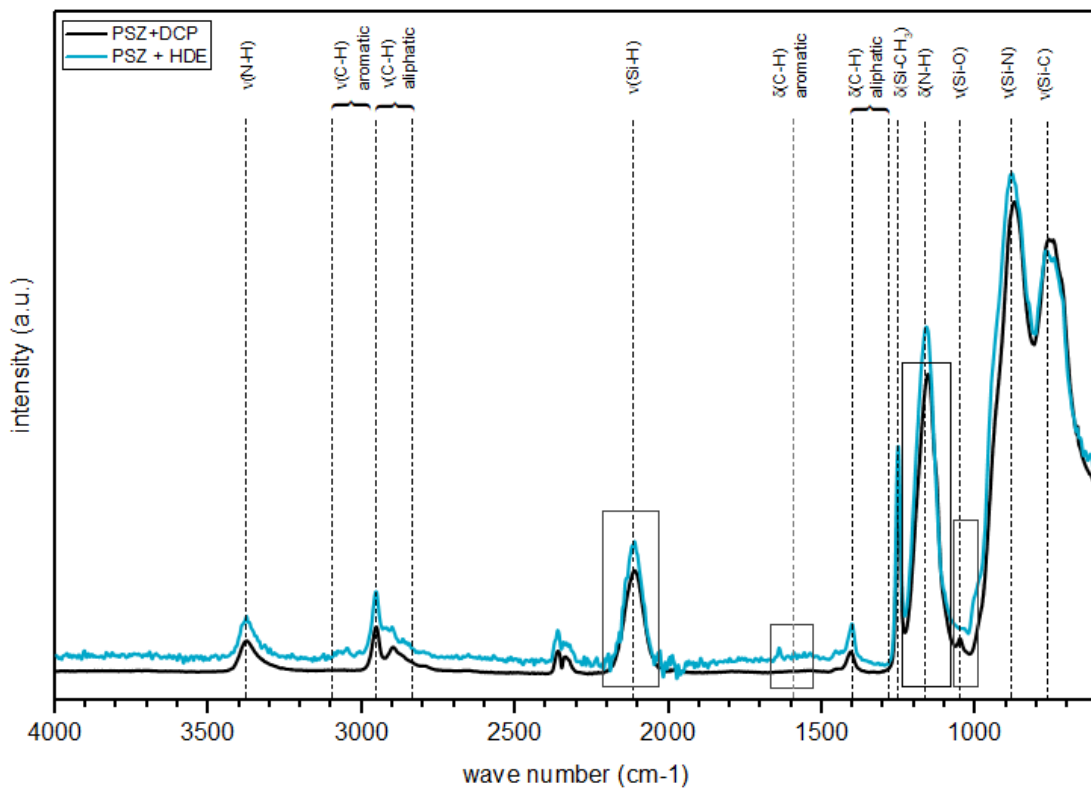


Figure 93: ATR-IR spectra of PSZ+HDE and PSZ+DCP after crosslinking at  $120^{\circ}\text{C}/130^{\circ}\text{C}$ ; the spectra are normalized with respect to the Si-CH<sub>3</sub> band from  $1230\text{-}1300\text{ cm}^{-1}$ .



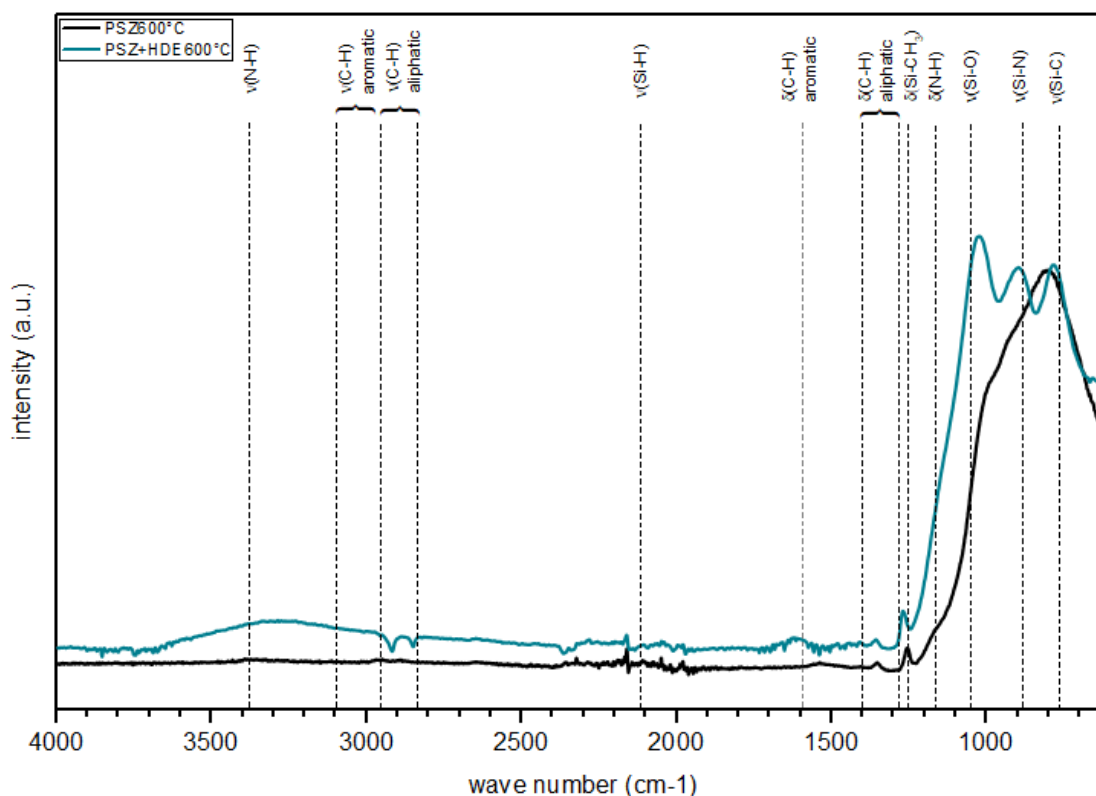


Figure 94: ATR-IR spectra of PSZ using hydrosilylation with HDE as linker for crosslinking or DCP as initiator after pyrolysis (600 °C).

### 9.2.5.5 N<sub>2</sub>-Physisorption

The adsorption-/desorption- isotherms of PSZ+HDE as linker after pyrolysis was recorded using N<sub>2</sub>-physisorption and is shown in Figure 95 together with that of PSZ crosslinked using DCP. The isotherms are almost identical with those of the benchmark sample and therefore of type I which means the sample is microporous. The PSD (Figure 96) shows only one maximum at 0.85 nm, which is almost the same value as for the benchmark sample (0.86 nm). This linker molecule therefore doesn't seem to have an impact on the porosity characteristics of the polymer-derived ceramic. As can be seen in Table 33, the BET surface area of PSZ+HDE is – when taking into account the standard deviation – the same as for the benchmark sample. Also the micropore volume is similar with ~ 0.10 cm<sup>3</sup>/g for both samples. Since all the parameters calculated from the isotherms are similar, the change of the crosslinking process by introducing HDE as linker molecule doesn't appear to influence the porosity of the resulting ceramic.

Table 33: Type of isotherm, BET specific surface area ( $S_{BET}$ ), maximum of the pore size distribution ( $PSD_{max}$ ) and micropore volume ( $V_{micro}$ ) of PSZ crosslinked thermally or using DCP.

	Isotherm	$S_{BET}$ (m <sup>2</sup> /g)	$PSD_{max}$ (nm)	$V_{micro}$ (cm <sup>3</sup> /g)	Comment
<b>PSZ600 °C</b>	Type I	195 ± 6	0.86	0.10	Microporous
<b>PSZ+HDE600°C</b>	Type I	192 ± 8	0.85	0.10	Microporous

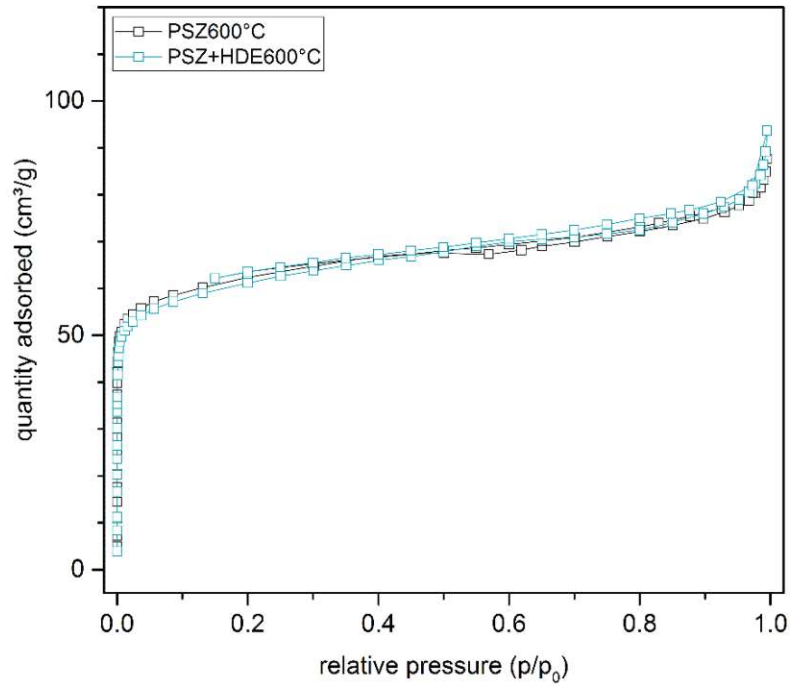


Figure 95:  $N_2$  physisorption isotherms of PSZ using hydrosilylation with HDE as linker for crosslinking or DCP as initiator after pyrolysis (600 °C).

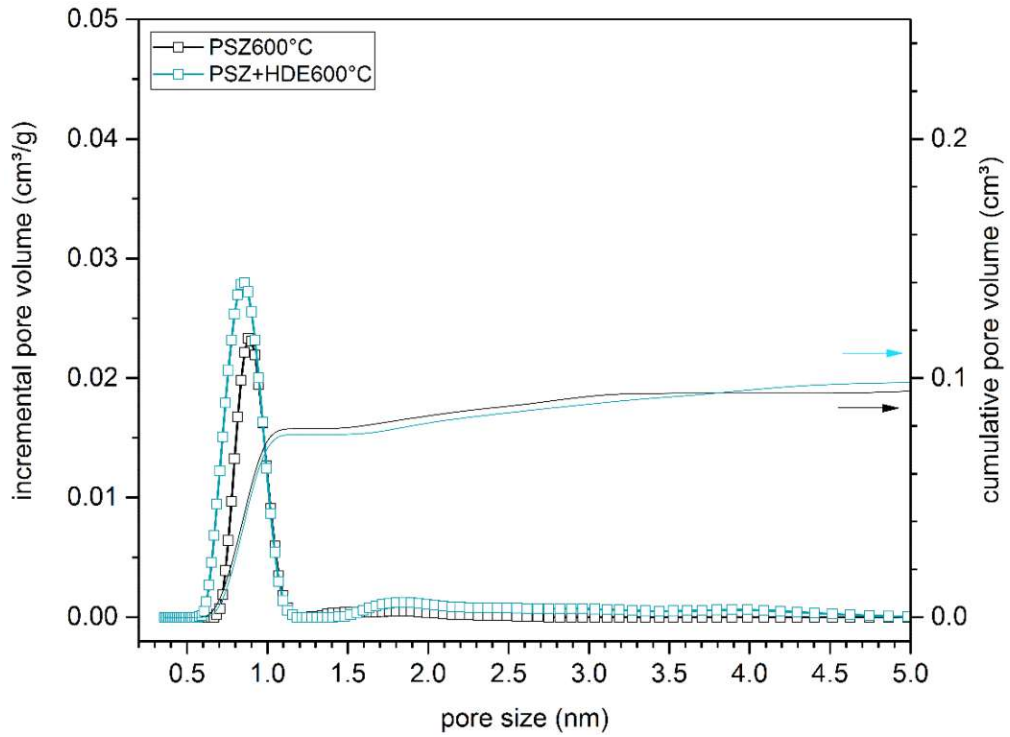


Figure 96: PSDs of PSZ using hydrosilylation with HDE as linker for crosslinking or DCP as initiator after pyrolysis (600 °C), calculated from the N<sub>2</sub> physisorption data using NL-DFT.

## 9.2.6 Hydrosilylation with DVB as linker molecule

Divinylbenzene was used as linker molecule in the second series of hydrosilylation experiments. Due to its two double bonds it can serve as crosslinking agent. By creating larger distances between the PSZ chains in the crosslinked network, an influence regarding reaction mechanisms during pyrolysis and resulting pore size could be generated. The simplified reaction scheme is shown in Figure 97. To get more detailed information about the influence of DVB on the pyrolysis behaviour, different DVB contents were used.

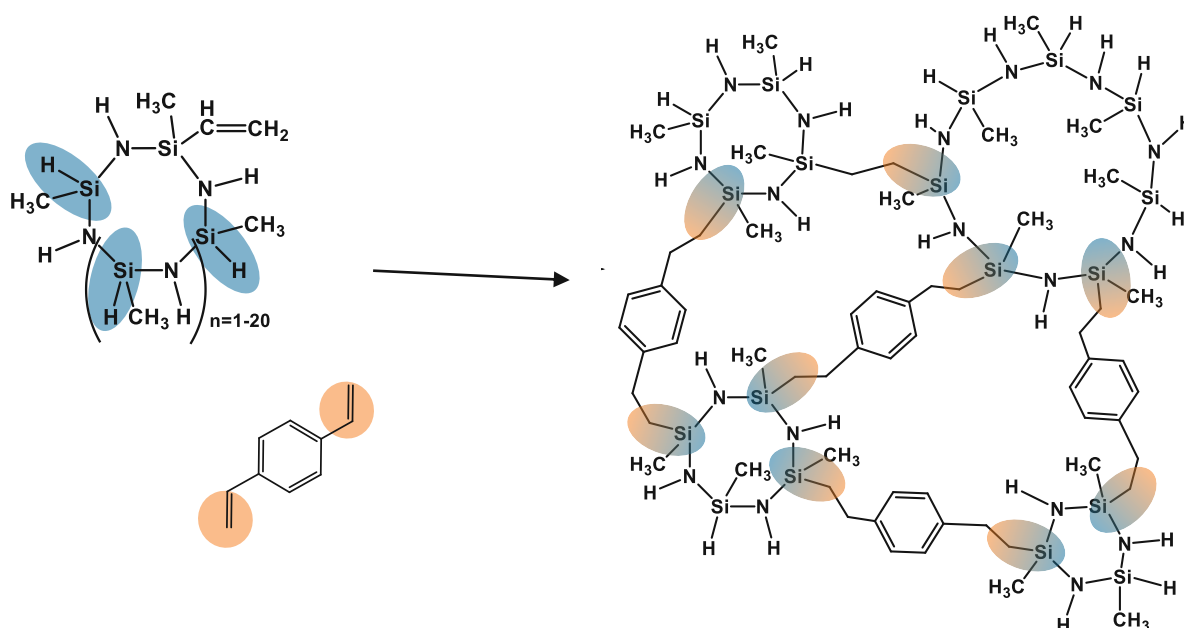


Figure 97: Simplified reaction scheme of the hydrosilylation reaction between PSZ and DVB.

### 9.2.6.1 Optical appearance

The appearance of samples crosslinked with DVB as linker molecule after every processing step are shown in Figure 98. Before crosslinking, the mixture is transparent and yellowish. After crosslinking it turns opaque and colorless for the two higher DVB contents, 40DVB and 80DVB. For the two lower DVB contents, the sample was still gel-like and yellowish, but not transparent anymore.

After pyrolysis, all samples are dark brown/black.

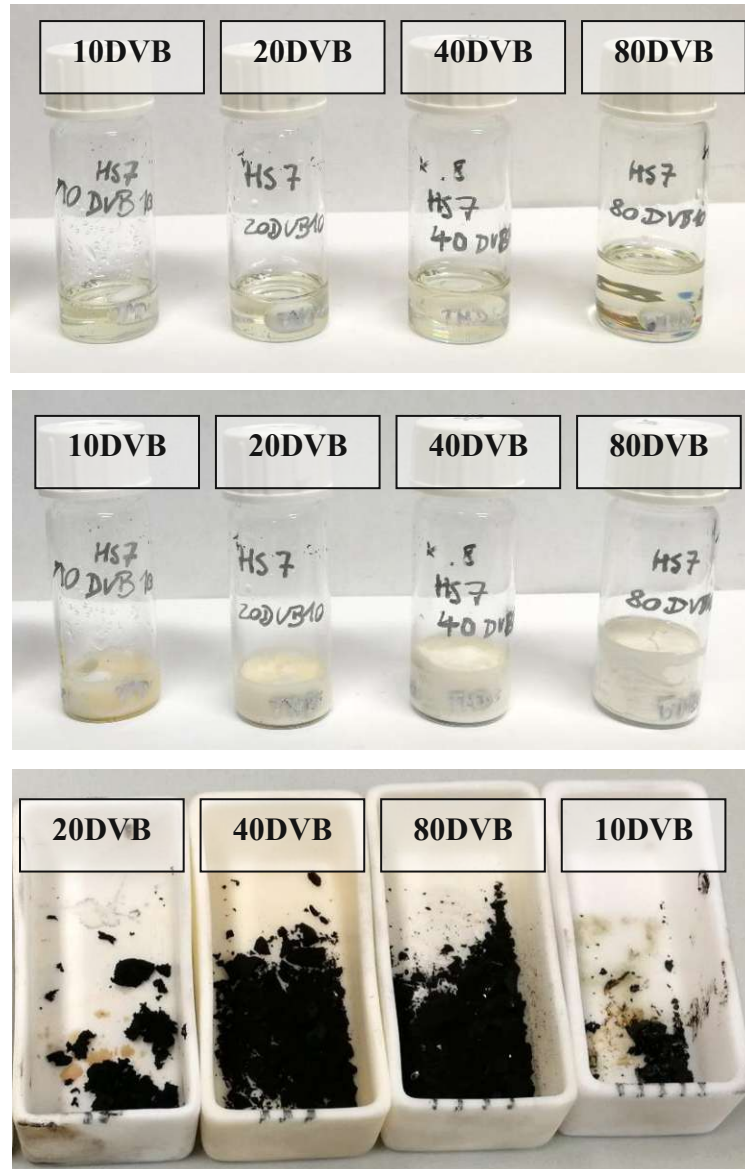


Figure 98: Sample images of the samples crosslinked with DVB as linker before (top) and after (middle) crosslinking as well as after pyrolysis at 600 °C (bottom)

### 9.2.6.2 Mass change

The mass change of the samples prepared using DVB as linker given in Table 34 for both the crosslinking and the pyrolysis step. The values after crosslinking are much higher than for the sample crosslinked using DCP. A possible explanation could be distillation of parts of the DVB, although the actual boiling point is at 198 °C. Also, the increase is not proportional to the DVB content (cf. 40DVB and 80DVB).

According to the mass loss during pyrolysis, part of the DVB decomposes during the heating process.

Table 34: Mass change of the samples crosslinked with DVB as linker molecule.

	$\Delta m_{\text{pure-crossl.}}, \%$	$\Delta m_{\text{crossl.-pyro}}, \%$
PSZ+DCP	-2.2	-26.0
10DVB	-13.2	-27.8
20DVB	-16.6	-32.0
40DVB	-19.3	-38.0
80DVB	-15.8	-50.2

### 9.2.6.3 Elemental composition

The elemental composition was measured in the crosslinked and pyrolyzed stage, and the results are shown in Figure 99 and Figure 100, respectively. The theoretical composition for the samples was calculated by assuming that the whole amount of starting compounds is part of the formed network, and is given in Table 35.

The **oxygen** content is approximately the same for all the samples crosslinked using DVB as linker molecule and is in the range of the polymer precursor, which shows that neither the catalyst nor the DVB contaminate the mixture with oxygen or moisture. The **nitrogen** content as well as the **Si+H** content decrease with increasing amount of DVB. The experimental composition is similar to the calculated composition, which leads to the assumption that all of the starting compound is included in the network somehow. The **carbon** content increases with increasing amount of DVB, again, the values are very close to the theoretical ones.

Overall, it can be stated that apart from the oxygen content (which is not included in the calculations of the theoretical values) the elemental composition confirms a complete reaction.

For the pyrolyzed samples, the **oxygen** content shows bigger differences between the samples. The benchmark sample shows a decrease in **oxygen** content during pyrolysis from ~5 wt% to 2 wt%. The samples crosslinked with DVB show no decrease or even an increase in oxygen with up to 9 wt% for the 40DVB sample. A possible explanation could be that the carbon rich domains decompose, while the oxygen containing species stay in the network.

The **nitrogen** content on the other hand shows almost no change with DVB ratio, which is in contrast to the crosslinked samples, and lies always around 14 wt%. The **carbon** content still increases with higher initial DVB ratio, and therefore shows the same trend as the crosslinked samples. Due to these trends, the **Si+H** part decreases with increasing DVB amount.

Since the nitrogen content is independent of the DVB amount and the carbon content of the pyrolyzed samples, it seems as if the nitrogen is either stabilized by the linker molecules or the decomposition of other units is facilitated by the less dense network created by the long bridges formed by the linker molecules.

Table 35: Theoretical composition based on a complete reaction between all of the starting compounds for the samples crosslinked using different amounts of DVB.

	Si, wt%	N, wt%	C, wt%	H, wt%
<b>PSZ+DCP</b>	43.7	21.8	26.1	8.5
<b>10DVB</b>	36.6	18.4	36.6	8.4
<b>20DVB</b>	31.3	15.7	44.2	8.3
<b>40DVB</b>	24.3	12.2	54.3	8.2
<b>80DVB</b>	16.9	8.5	66.5	8.1

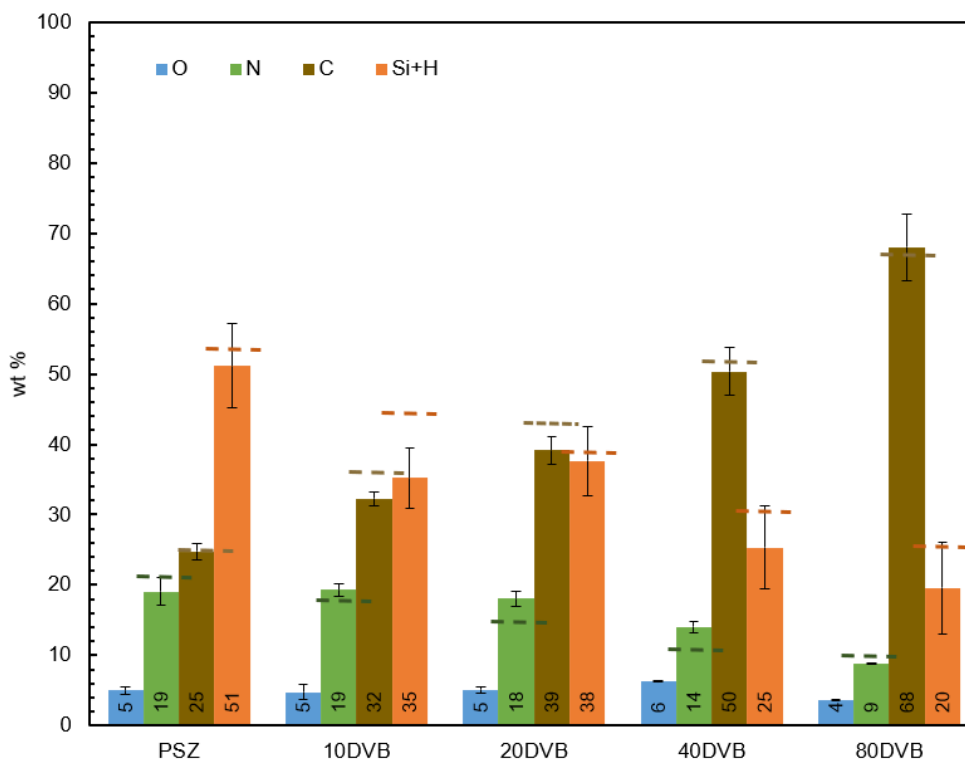


Figure 99: Elemental composition of PSZ using hydrosilylation with different amounts of DVB as linker for crosslinking or DCP as initiator; O, N, and C content are measured, Si+H is calculated as remainder to 100 wt%; the theoretical compositions are displayed by the dashed lines.

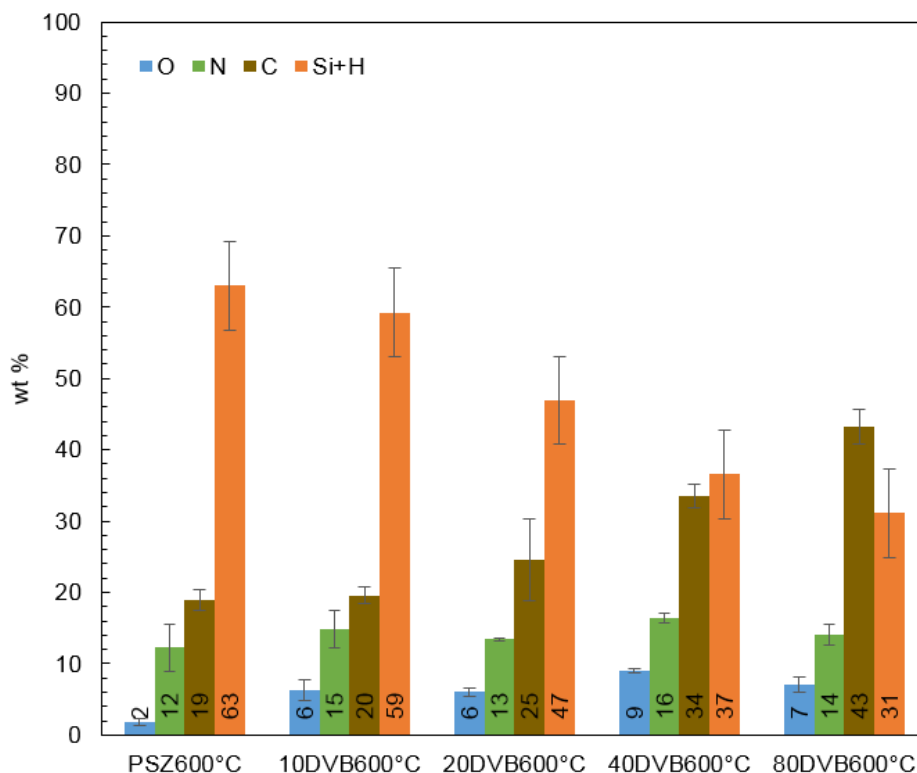


Figure 100: Elemental composition of PSZ using hydrosilylation with different amounts of DVB as linker for crosslinking or DCP as initiator after pyrolysis (600 °C); O, N, and C content are measured, Si+H is calculated as remainder to 100 wt%.

#### 9.2.6.4 ATR-IR

Since hydrosilylation is a reaction between Si-H bonds and unsaturated hydrocarbons, the reaction should be visible in the IR spectrum by a decrease of Si-H signals (at 2200  $\text{cm}^{-1}$ ) and increase of aromatic and aliphatic C-H signals (around 1500  $\text{cm}^{-1}$  and 3000  $\text{cm}^{-1}$ ). The IR-spectra of the samples prepared with different amounts of DVB are shown in Figure 101 in comparison to that of the standard sample crosslinked with 1 wt% DCP. The spectra were normalized on the Si-CH<sub>3</sub> signal at 1200-1230  $\text{cm}^{-1}$  to make a comparison of the spectra possible.

The amount of DVB that was added should consume all the Si-H-groups for 40DVB and 80DVB and the signal should vanish. Although there is a decrease, that is stronger with higher amount of DVB, the signal only decreases by approximately one third. The same behaviour was found by Liu et al. [130], where similar amounts of DVB were added and even if over-stoichiometric amounts were used, not all Si-H groups were consumed. There is also a slight decrease of the N-H signals.



The benzene ring can be seen in different areas of the spectra, around 1550-1620  $\text{cm}^{-1}$  and 3000-3100  $\text{cm}^{-1}$  due to CH-vibrations and the C-H-bending (“benzene-fingers”) from 1650-2000  $\text{cm}^{-1}$ . In addition, there is also a rise in aliphatic C-H signals, which is due to the opening of the double bonds during the reaction. These signals can be seen between 1400-1530  $\text{cm}^{-1}$ . Since both the DVB and the PSZ contain vinyl groups, it is also possible that crosslinking isn’t just performed via hydrosilylation but also via reaction between the double bonds. However, the vinyl groups are visible at 1600  $\text{cm}^{-1}$ , which overlaps with the region of aromatic signals, and the assumption can therefore not be validated.

In Figure 102 the spectra of the pyrolyzed samples are displayed with a shift in y-direction. A normalization wasn’t performed this time. The main signal is – as for the benchmark sample – from 1000 – 600  $\text{cm}^{-1}$  for all the DVB samples. In addition, there are signals of the Si-CH<sub>3</sub> group that are still left in the sample, which shows that the polymer-ceramic-conversion is not complete at 600 °C. The Si-CH<sub>3</sub> group can also be seen at 1400  $\text{cm}^{-1}$  due to aliphatic C-H-deformation vibrations.

For the DVB samples, there are even more bands visible, on the one hand in the range of aromatic groups from 2000 – 1600  $\text{cm}^{-1}$  and on the other hand in the two regions of N-H vibrations (around 3400  $\text{cm}^{-1}$  and 1190  $\text{cm}^{-1}$ ). This could indicate a hindrance of reactions of the N-H group by the DVB.

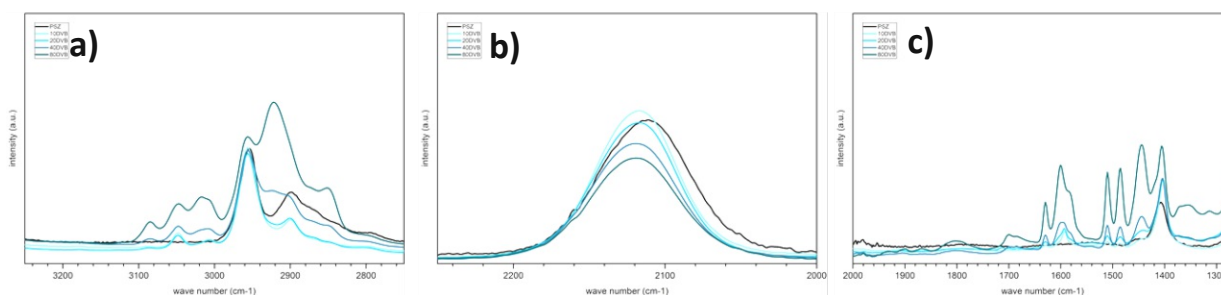
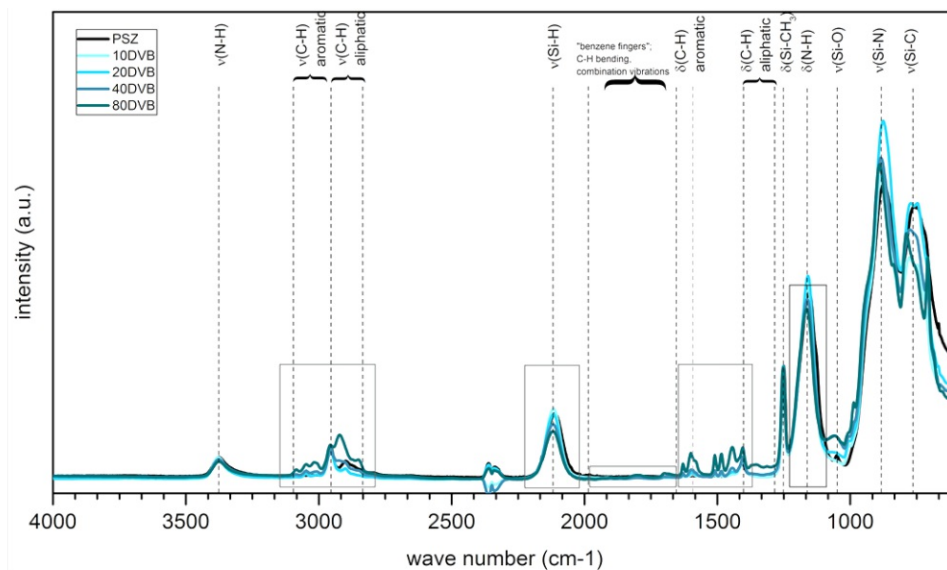


Figure 101: ATR-IR spectra of PSZ using hydrosilylation with different amounts of DVB as linker for crosslinking or DCP as initiator; the spectra are normalized with respect to the Si-CH<sub>3</sub> band from 1230-1300 cm<sup>-1</sup>. a)&c) CH-vibrations b) Si-H band.

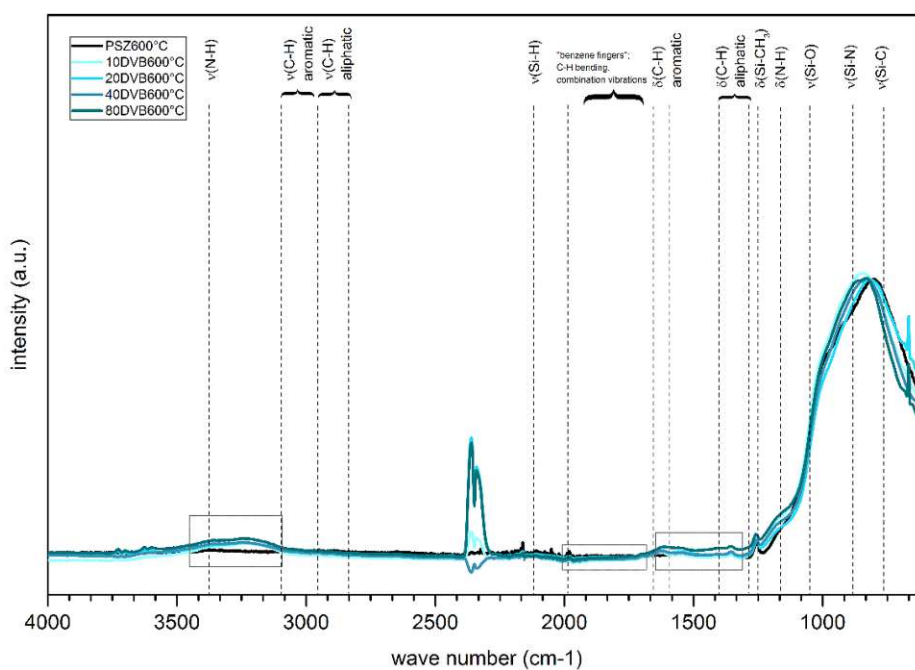


Figure 102: ATR-IR spectra of PSZ using hydrosilylation with different amounts of DVB as linker for crosslinking or DCP as initiator after pyrolysis (600 °C).

### 9.2.6.5 TGA-MS

To get more information about the influence of the linker molecules on the pyrolysis process, TGA-MS investigations were conducted. The decomposition products detected by MS give an insight in reactions that are favoured or hindered when compared to PSZ without linker and additional reactions including the decomposition of the linker molecule itself.

Two samples were investigated, 20DVB and 80DVB, using the program that was used for PSZ already with additional m/z values for the linker molecule, with the results shown in Figure 103 and Figure 104. Interesting changes in MS spectra are summarized in Table 36.

Whereas the TGA curve for PSZ+DCP shows several steps starting at 250 °C and ending at 900 °C, the DVB-containing samples already show mass loss below 250 °C, then the major step starting at 450 °C up to approximately 720 °C and, in contrast to PSZ+DCP, a second big mass loss step at 1500 °C.

The first loss of about 1.4 % could be attributed to distillation of remaining DVB, probably entrapped in the crosslinked network. The boiling point of DVB at ambient pressure is at 195 °C, which is in accordance with the temperature range of the mass loss. The species found by MS are C<sub>2</sub> species as well as CH<sub>3</sub> and small amounts of hydrogen with m/z values of 27, 15 and 2, respectively. The values for ring containing compounds are missing, which is weakening the theory of entrapped DVB. Another explanation could be that DVB is not used in a pure form, but as mixture of p- and m-DVB with ethylvinylbenzene. The latter one could only bond with PSZ or DVB with one side (the vinyl group), therefore leaving the ethyl group open for possible decomposition in the low temperature range.

The major step from 450 °C to 720 °C can be further split up in two regions according to the species evolving, which are mainly DVB related species up to 500 °C and species typical for the polymer-ceramic-conversion of PSZ. For DVB, m/z values of 130, 105, 78, 76 are found, which correspond to complete DVB molecules (C<sub>6</sub>H<sub>4</sub>(CH<sub>2</sub>CH<sub>2</sub>)<sub>2</sub>), monosubstituted benzene rings (C<sub>6</sub>H<sub>4</sub>CH<sub>2</sub>CH<sub>2</sub>), benzene rings and further fragmented DVB molecules (C<sub>6</sub>H<sub>4</sub>), respectively. The dominant species in the exact same temperature window is m/z 27 followed by 15. The double bonds of DVB form C<sub>4</sub>- or C<sub>2</sub>-bridges when reacting with the vinyl groups of PSZ or Si-H if the desired hydrosilylation mechanism is assumed. According to the mass spectra found in the NIST Webbook [131], butane undergoes strong fragmentation, with C<sub>2</sub>-fragments being the main product. This would explain the strong occurrence of m/z 27. The

corresponding  $C_3$  ( $m/z$  41) and  $C_4$  ( $m/z$  50-58) values can be found too, having the same sharp peak shape.

Although methane is already detected in this temperature range, it becomes dominant at 600-800 °C, which can be seen from  $m/z$  values 16 and 15. The same behaviour is found for hydrogen ( $m/z$  2) but with an additional peak from 800-900 °C. The maximum is shifted to higher temperatures when compared to PSZ without linker. It seems as if part of the DVB has to decompose before it is possible for PSZ to undergo the polymer-ceramic-transformation in the usual way.

For PSZ, the dominant reaction below 500 °C is the formation of  $NH_3$  by transamination reactions. The  $m/z$  value 17 is the main signal detected by MS for PSZ in that temperature range and isn't present above 500 °C anymore. For the 80DVB sample, the value is detected starting at 430 °C, so slightly delayed to the DVB related species, and detected up to almost 600 °C. So again, the typical reactions of PSZ during pyrolysis are shifted to higher temperatures in presence of DVB. One possible explanation could be that the excess of DVB leads to the stiff separation of PSZ oligomers by DVB domains and therefore prevents reactions between the oligomers in the lower temperature range.

Another reason for the decreased ammonia formation could be that DVB partially bonds to N-H instead of Si-H, which is strengthened by the ATR-IR spectra that show a decrease in intensity of the N-H band at  $1180\text{ cm}^{-1}$  for the DVB containing samples. If hydrogen of the N-H group is substituted by an organic rest, transamination reactions are hindered, too.

For the 20DVB sample, the effect isn't that strong. The TGA curve as well as the MS data are similar to that of PSZ, yet with clear contributions of the linker molecule. Like for the 80DVB sample, there is mass loss below 250 °C, in this case of 0.58 % and with  $m/z$  27 as only MS signal. In contrast to 80DVB, but similar to PSZ, ammonia and methane are detected already at 300 °C up to 450 °C, but to a lower degree compared to the methane signal found at temperatures around 600 °C. From 400-500 °C, the previously described  $m/z$  values of DVB related species can be found, but in a lower extent than for 80DVB. With a second maximum, that is shifted to the DVB species, ammonia can be found from 430-550 °C. Above 500 °C, it's the typical pyrolysis behaviour of PSZ, with methane and hydrogen as well as  $m/z$  27 as major signals. Still, the temperature range is shifted when compared to solely PSZ, with methane ending at 850 °C and hydrogen evolving even up to 1200 °C.

## FOCUS IV – MODIFICATIONS DURING THE CROSSLINKING STEP

Summing up these measurements, an increasing DVB amount seems to inhibit the reactions leading to the polymer-ceramic-conversion of PSZ, which can be seen from a shift of MS signals to higher temperatures and different ratios of e.g. methane in two temperature ranges or ammonia compared to methane.

Table 36: TGA-MS results of PSZ, 20DVB and 80DVB; main temperature regions of the decomposition products in bold font.

	PSZ+DCP	20DVB	80DVB
$\Delta m_{TGA1500^{\circ}C, \%}$	-24	-45	-65
$\Delta m_{TGA600^{\circ}C, \%}$	-18	-19	-45
$\Delta m_{furnace600^{\circ}C, \%}$	-26	-32	-50
<b>NH<sub>3</sub></b>	280-500 °C <i>major signal below 500 °C</i>	300-550 °C <i>intensity compared to methane drastically reduced</i>	430-580 °C <i>signal hardly visible below 400 °C, maximum at 450 °C together with DVB decomposition</i>
<b>H<sub>2</sub></b>	300-900 °C	400-1200 °C	600-1000 °C
<b>CH<sub>4</sub></b>	250-450 °C, <b>450-800 °C</b>	300-450 °C, <b>500-850 °C</b>	450-500 °C, 450-550 °C, <b>550-800 °C</b>
<b>CH<sub>3</sub></b>	250-450 °C, <b>450-800 °C</b>	300-450 °C, <b>500-850 °C</b>	450-500 °C, <200 °C, <b>400-500 °C</b> , 500-900 °C
<b>C<sub>2</sub>-species</b>	300-800 °C (m/z 27) 280-600 °C (m/z 26)	~ 200 °C, 450-500 °C, <b>500-600 °C</b> , 600-1500 °C (m/z 27) 450-650 °C (m/z 26)	~200 °C, <b>400-480 °C</b> , 480-600 °C, 600-800 °C, 800-1500 °C (m/z 27) <b>450- 500 °C</b> , 500-650 °C (m/z 26)
<b>DVB related species</b>	-	400-500 °C	400-500 °C

# FOCUS IV – MODIFICATIONS DURING THE CROSSLINKING STEP

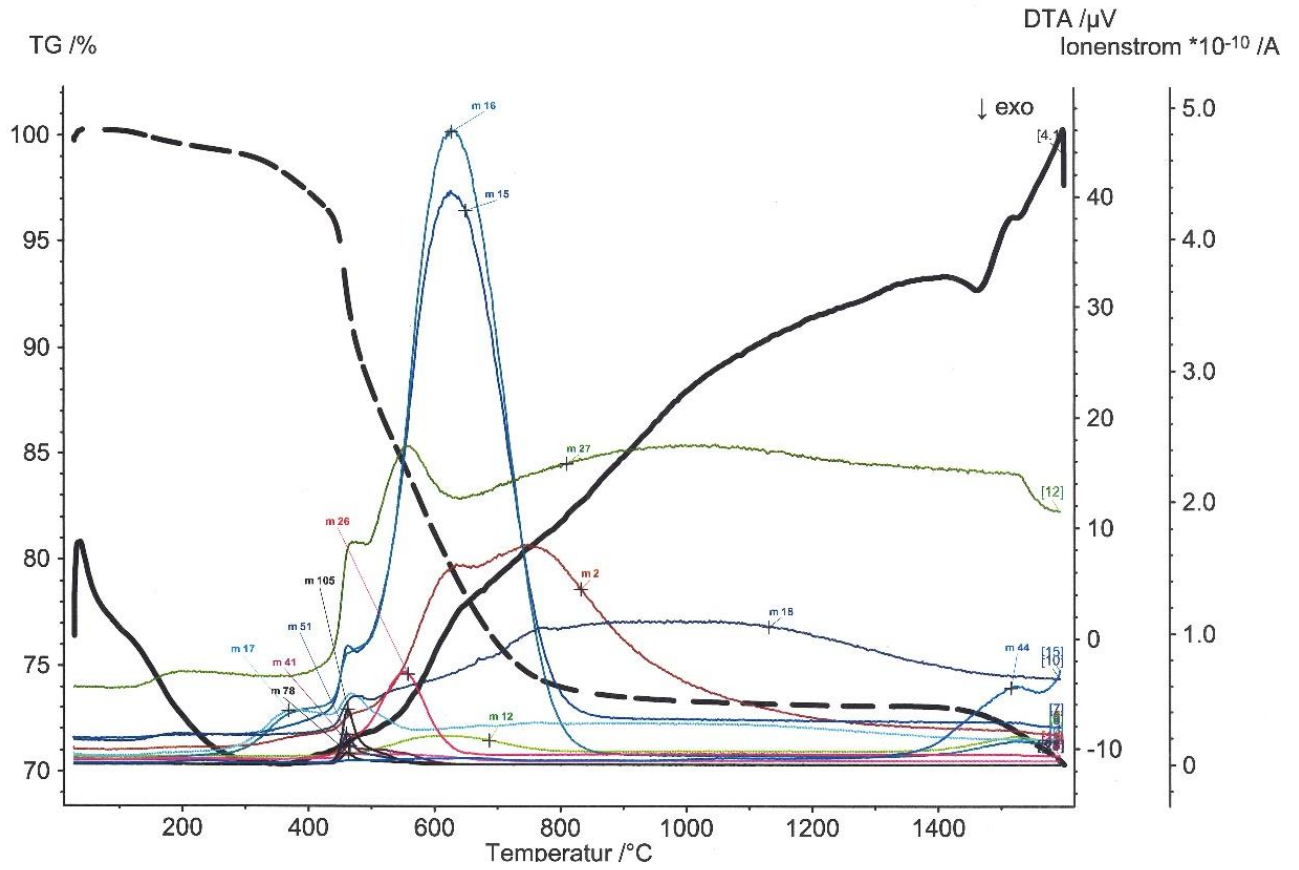


Figure 103: TGA-MS results of 20DVB pyrolyzed under nitrogen up to 1500 °C.

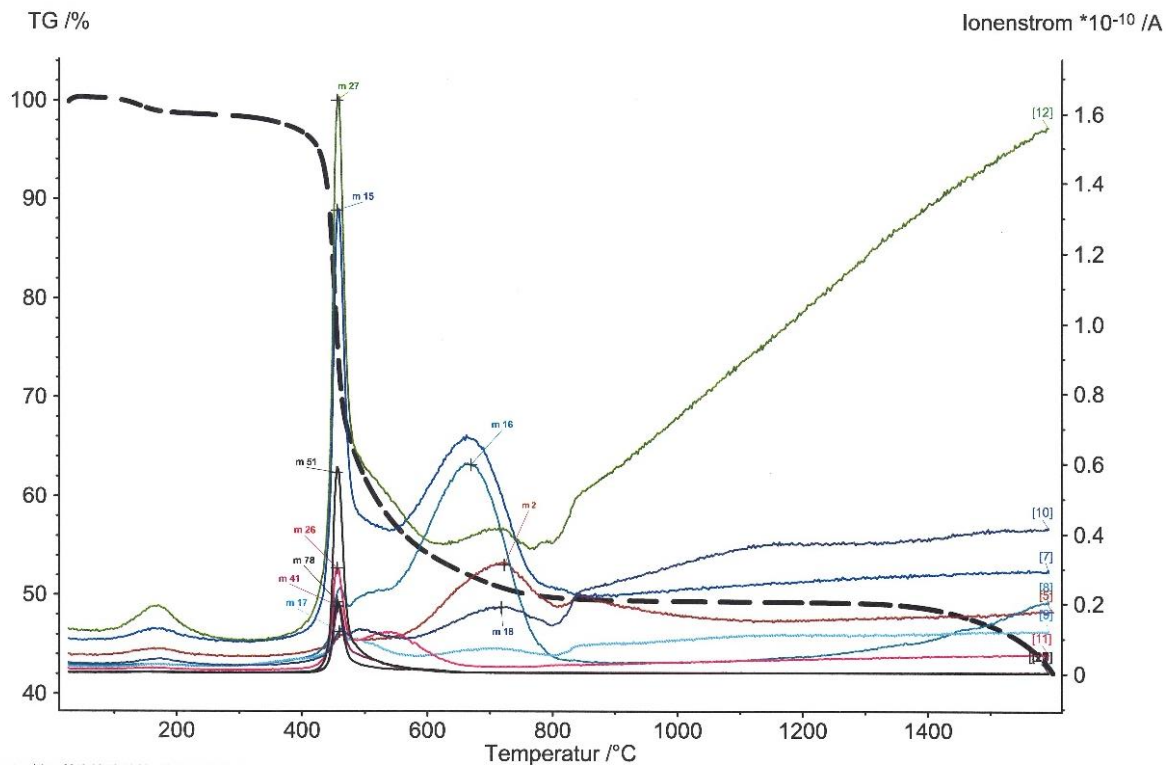


Figure 104: TGA-MS results of 80DVB pyrolyzed under nitrogen up to 1500 °C.



### 9.2.6.6 Solid state NMR

$^{13}\text{C}$  and  $^{29}\text{Si}$  solid state NMRs were recorded for the sample with the highest DVB content (80DVB) after pyrolysis at  $600\text{ }^\circ\text{C}$ , which are shown in Figure 105 and Figure 106. The  $^{13}\text{C}$  NMR shows a peak around 0 ppm resulting from Si-C bonds of carbon ( $\text{sp}^3$ ) in a silicon network, which was already present in the spectrum of PSZ600 $^\circ\text{C}$  (cf. 6.2.7). In addition, there is the main maximum at  $\sim 140$  ppm, which lies in a region that is typical for  $\text{sp}^2$  carbon, accompanied by two peaks similar in shape and arranged more or less symmetrical around it at  $\sim 45$  ppm and  $\sim 210$  ppm. These two peaks are marked by asterisks in the spectrum, because they are most likely spinning sidebands caused by chemical shift anisotropy. [15] The high amount of  $\text{sp}^2$  carbon in the sample can be explained by the high DVB content of that sample, which seems to form domains which are only partially removed during pyrolysis and form a free carbon phase.

The  $^{29}\text{Si}$  spectrum of 80DVB – like PSZ600  $^\circ\text{C}$  – shows a very broad peak that consists of several overlapping peaks, which were deconvoluted using a Gaussian approximation (Figure 106). Three maxima were found at -12, -28 and -34 ppm, with increasing intensity in this order. According to the TGA-MS results shown above, hydrogen is still present in the ceramic at  $600\text{ }^\circ\text{C}$  since hydrogen evolution can be observed up to  $900\text{ }^\circ\text{C}$ . Therefore, the material most likely consists of mixed Si-C-N-O-H tetrahedra. This assumption is strengthened by the chemical shift of the peak which lies between or is overlapping with the values of pure  $\text{Si}_3\text{N}_4$  or SiC. Pure  $\text{Si}_3\text{N}_4$  consists of  $\text{SiN}_4$  tetrahedra that appear at -47 ppm ( $\pm 1$  ppm),  $\text{SiC}_4$  tetrahedra appear from -10 to -25 ppm [15, 123], or even up to 0 ppm, according to Williams et al. [94] Literature also provides values for different types of mixed tetrahedra: According to Kenneth et al. [123],  $\text{SiCN}_3$  tetrahedra,  $\text{SiC}_2\text{N}_2$  tetrahedra and  $\text{SiC}_3\text{N}$  tetrahedra range from -35 to -25 ppm, from -25 to 0 ppm, and from 0 to 30 ppm, respectively. According to Williams et al. [94],  $\text{SiHC}_3$  and  $\text{SiH}_2\text{C}_2$  moieties can be found at -17 ppm and -38 ppm, respectively, and  $\text{SiH}_3\text{C}$  tetrahedra are located at around -67 ppm. Mixed Si-H-C-N moieties are likely to be present, too, which are located at -19 ppm for  $\text{SiHC}_2\text{N}$  and at -24 ppm for  $\text{SiHCN}_2$  [132].

The deconvoluted peaks of 80DVB can be described best by the presence of  $\text{SiC}_2\text{N}_2$ ,  $\text{SiHCN}_2$  and  $\text{SiCN}_3/\text{SiH}_2\text{C}_2$  tetrahedra, taking into account the chemical shifts found in literature. As can be seen in Figure 106 from the curves of the peak fit, the contribution of more nitrogen-rich tetrahedra is dominant. These findings go along with the results of the elemental analysis, indicating that more nitrogen remains in the DVB containing samples, due to the hindrance of reactions leading to the loss of nitrogen.

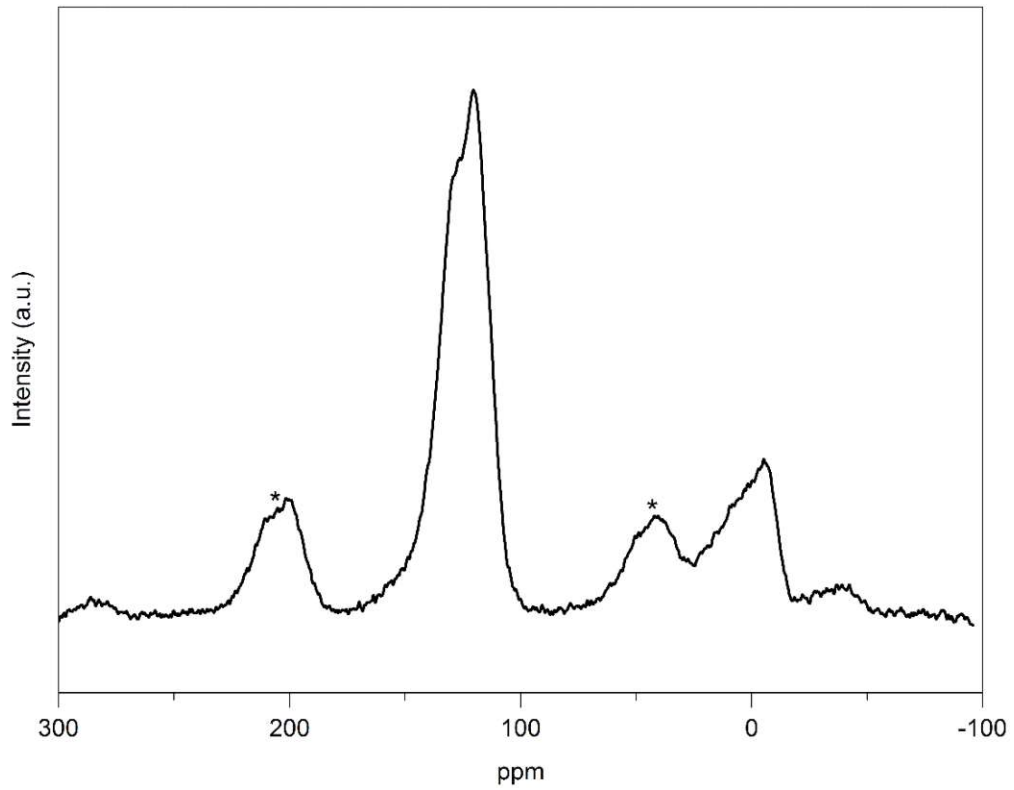


Figure 105:  $^{13}\text{C}$  solid state NMR of 80DVB pyrolyzed at 600 °C; spinning side bands are marked by an asterisk.

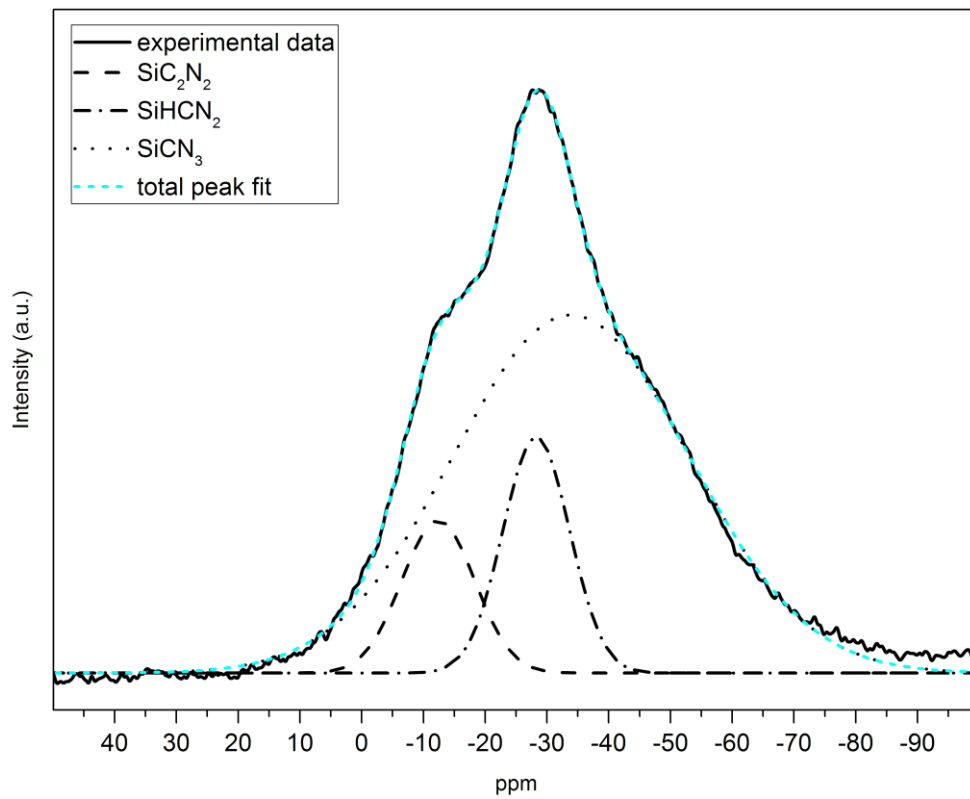


Figure 106:  $^{29}\text{Si}$  solid state NMR for 80DVB pyrolyzed at 600 °C; the deconvoluted peaks are displayed using dashed lines.



### 9.2.6.7 N<sub>2</sub>-Physisorption

The isotherms of the PSZ samples with different concentrations of DVB after pyrolysis were recorded using N<sub>2</sub>-physisorption and are shown in Figure 107. All of the isotherms are of type I, which means that the samples are microporous, which is confirmed by the results of the PSD, where the samples have their main maxima below 2 nm. In Figure 108 the PSDs of the samples are displayed together in one diagram in a pore size range from 0.36 nm (lower limit of N<sub>2</sub> as adsorption gas) to 2 nm, the micropore range. All four have in common that there is one main maximum around 0.8 nm and some smaller ones at higher pore sizes. The main maximum shifts to lower values the higher the DVB content. Together with the even lower BET specific surface area (cf. Table 37), it is indicated that the pores formed through DVB have a minor contribution to the overall porosity, but that the presence of DVB influences the size of the pores formed by decomposition of PSZ. A reason could be the electronegativity of the benzene ring, which influences the strength of neighbouring bonds, because the presence of DVB hinders certain reactions, e.g. transamination reactions (which was shown during the TGA-MS investigations), which leads to a higher nitrogen content left in the PSZ domains. That was already shown by the elemental composition and the solid state NMRs. Therefore, the elemental composition of the micropore forming entities is influenced and could result in a different pore size.

The theory that the network formed during crosslinking is responsible for the pore size in the resulting ceramic becomes less likely based on the results. The linker molecules form longer bridges than those formed by crosslinking without the linkers. Therefore, the voids in the network become bigger and, consequently, the pore size should increase. The opposite is the case, as the pore size decreases with increasing DVB-amount.

The correlation between initial DVB amount added (as molar ratio) and the resulting pore size maximum calculated from the physisorption results is displayed in Figure 109. An actual effect on the pore size is only visible above a certain amount of DVB present in the sample.

Table 37: Type of isotherm, BET specific surface area ( $S_{BET}$ ), maximum of the pore size distribution ( $PSD_{max}$ ) and micropore volume ( $V_{micro}$ ) of PSZ crosslinked with different amounts of DVB as linker or using DCP.

	Isotherm	$S_{BET}$ (m <sup>2</sup> /g)	$PSD_{max}$ (nm)	$V_{micro}$ (cm <sup>3</sup> /g)	Comment
<b>PSZ600 °C</b>	Type I	195 ± 6	0.84	0.10	Microporous
<b>20DVB600°C</b>	Type I/ IV	153 ± 7	0.84	0.08	Micro- and mesoporous
<b>40DVB600°C</b>	Type I/ IV	147 ± 7	0.76	0.08	Micro- and mesoporous
<b>80DVB600°C</b>	Type I/ IV	164 ± 9	0.70	0.09	Micro- and mesoporous

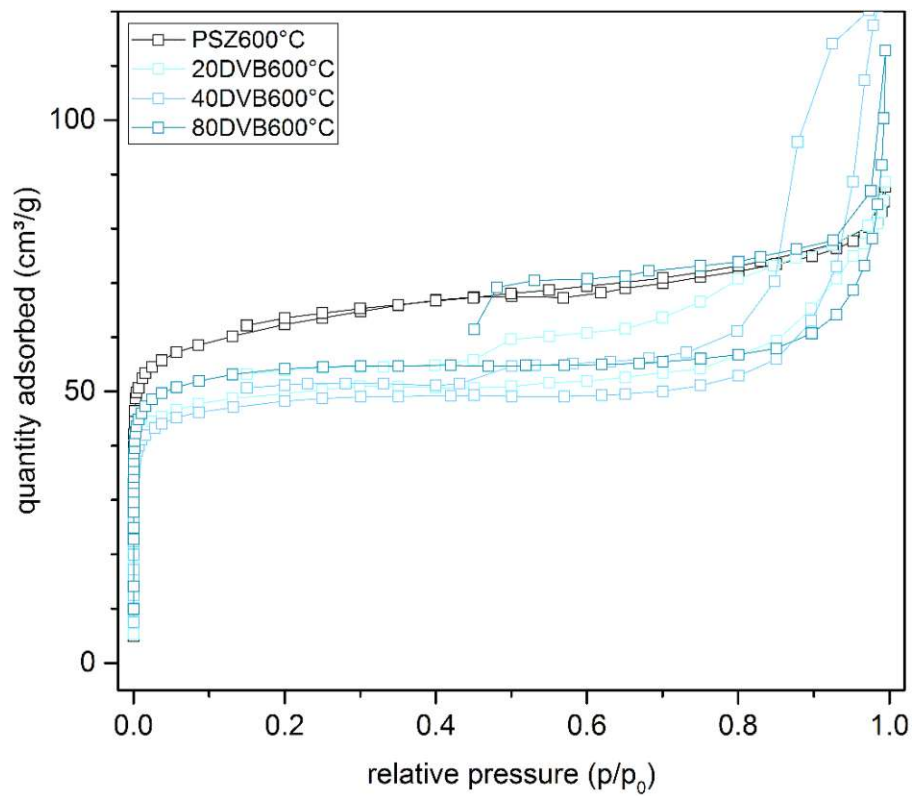


Figure 107: N<sub>2</sub> physisorption isotherms of PSZ using hydrosilylation with different amounts of DVB as linker for crosslinking or DCP as initiator after pyrolysis (600 °C).

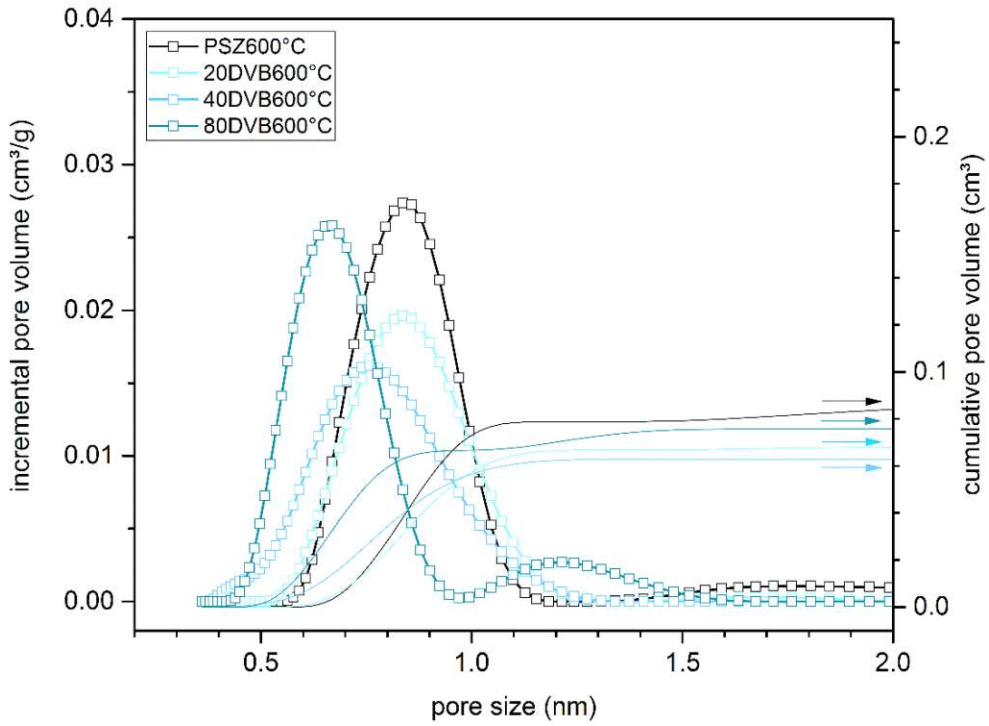


Figure 108: PSDs of PSZ using hydrosilylation with different amounts of DVB as linker for crosslinking or DCP as initiator after pyrolysis (600 °C), calculated from the  $N_2$  physisorption data using NL-DFT.

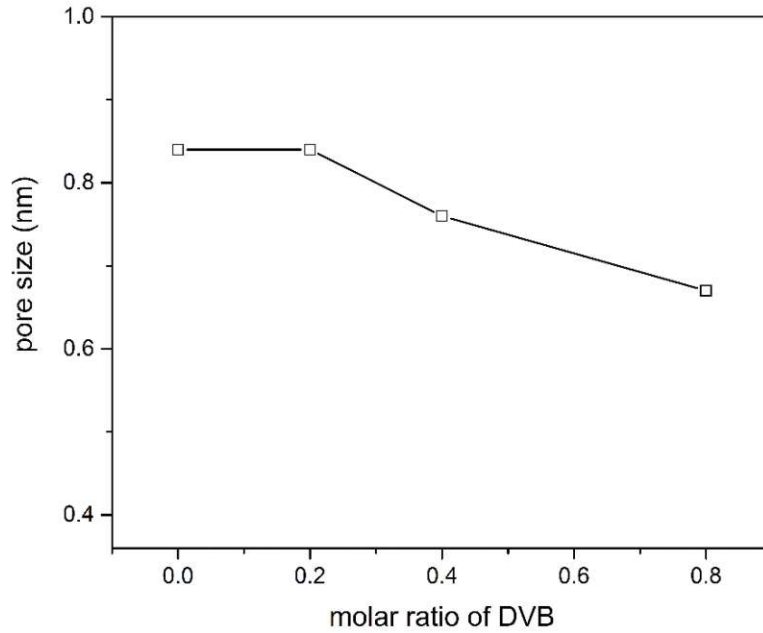


Figure 109: Correlation between the molar ratio of DVB in relation to PSZ added during the crosslinking process and the pore size maximum evaluated using  $N_2$  physisorption.

### 9.2.7 SAXS investigations of the samples prepared via hydrosilylation

To double check the results obtained by physisorption experiments, some selected samples were investigated using SAXS. The experimental SAXS curves are shown in Figure 110, the parameters obtained from the fitted data are summarized in Table 38. As it was already shown by the other characterization methods, the only major changes were obtained by the sample prepared with DVB as linker molecule. The two other samples have almost identical parameters when compared to the benchmark sample PSZ600°C. The trends found by physisorption were confirmed by SAXS in case of 80DVB; although the absolute values differ, the shift of the micropore maximum to lower values is also shown by this analysis method.

Table 38: Parameters obtained from applying a model fit to the SAXS data: Radius of gyration ( $R_g$ ), fractal dimension ( $D$ ), hard sphere radius ( $R_{hs}$ ), and hard sphere volume fraction ( $\eta$ ).

	$2R_g$ (nm)	$D$	$2R_{hs}$ (nm)	$\eta$
<b>PSZ600 °C</b>	0.71	3.85	0.89	0.19
<b>PSZ20<math>\mu</math>l600°C</b>	0.72	3.70	0.88	0.23
<b>PSZ+HDE600°C</b>	0.72	3.72	0.86	0.18
<b>80DVB600°C</b>	0.48	4	-	-

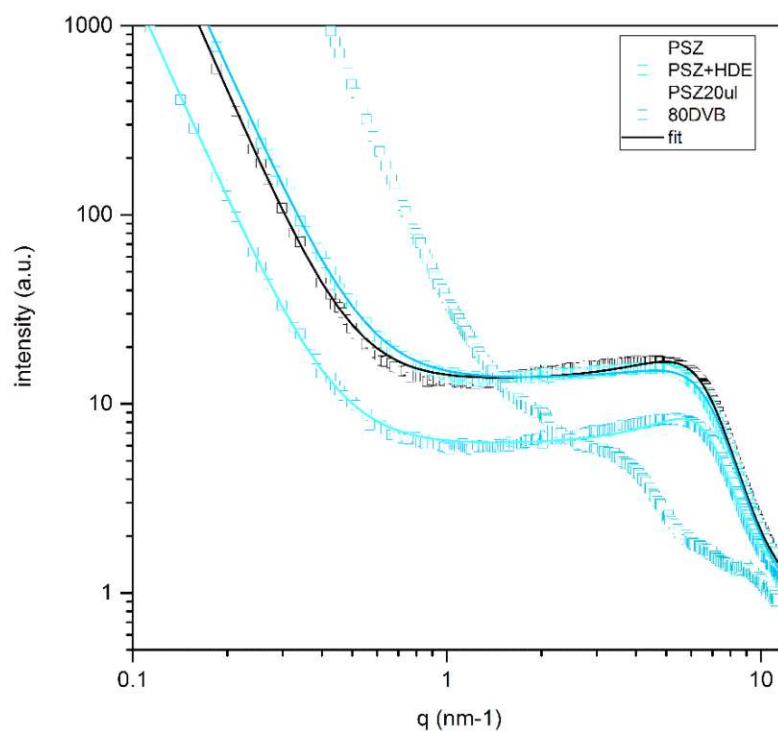


Figure 110: Experimental SAXS curves of samples prepared using hydrosilylation after pyrolysis at 600 °C.

### 9.3 Conclusions – Focus IV

The majority of crosslinking experiments showed only minor effects on the properties of the resulting amorphous ceramics.

The only exception is the use of DVB as linker molecule and hydrosilylation as crosslinking mechanism. TGA-MS investigations revealed the hindrance of certain reactions and delay of the typical reactions occurring during the polymer-ceramic conversion in presence, especially of an overstoichiometric amount of DVB. DVB directly influences the elemental composition by increasing the carbon content under formation of carbon rich domains, but also indirectly, because reactions between the PSZ oligomers are hindered, e.g. transamination reactions, which leads to a relatively taken higher amount of nitrogen present in the PSZ domains. Both findings were confirmed by solid state NMR investigations, showing a high amount of free carbon present in the samples, which results from decomposition of DVB domains and also the presence of more nitrogen rich tetrahedral in the PSZ domains. The changes in decomposition behaviour resulted in a shift of the pore size maximum in the micropore range to lower values compared to PSZ, to 0.70 nm compared to 0.86 in the most extreme case, although already understoichiometric amounts of DVB led to slight shifts.

Since it looks as if the micropores are formed primarily in the former PSZ domains, because the maximum is only shifted, an explanation could be that transamination reactions, which are hindered by the presence of DVB, are playing a crucial role in the formation of microporosity in PSZ-derived ceramics. Another reason could be the higher amount of nitrogen remaining in the PSZ domains, which could cause a different composition of the entities forming the pores and therefore a different size and stability of the pores.

To get more information about the effect of DVB on the pore formation in PSZ, further pyrolysis experiments were conducted and will be discussed in the following chapters (cf. chapter 10.8).

## 10. FOCUS V – EFFECT OF PYROLYSIS CONDITIONS ON MICROPORE FORMATION IN POLYMER-DERIVED CERAMICS

### 10.1 Experimental Procedure – Focus V

The starting compounds for the pyrolysis experiments were crosslinked PSZ and PCS. A mixture of 50 wt% PSZ and PCS was tested too, to check whether the precursors interact with each other during pyrolysis. Crosslinking was achieved using 1 wt% DCP as radical initiator and heat treatment in a tube furnace under flowing nitrogen (0.35 l/min, purity > 99.999 %), with a dwell time of 12 h at the maximum temperature of 130 °C and a heating rate of 1 K/min.

The crosslinked compounds were ground and stored in a glove box under nitrogen atmosphere until further use.

#### 10.1.1 Pyrolysis in nitrogen atmosphere

The temperature programs for pyrolysis under nitrogen are shown in Figure 111 and are similar to the standard heating program described in section 5.2.3. After a first heating step up to 300 °C with a heating rate of 3 K/min, the heating rate was changed to 1 K/min up to the maximum temperature, where it was held for 4 h and then cooled down to room temperature with 3 K/min. The pyrolysis was carried out under flowing purified nitrogen (0.35 l/min).

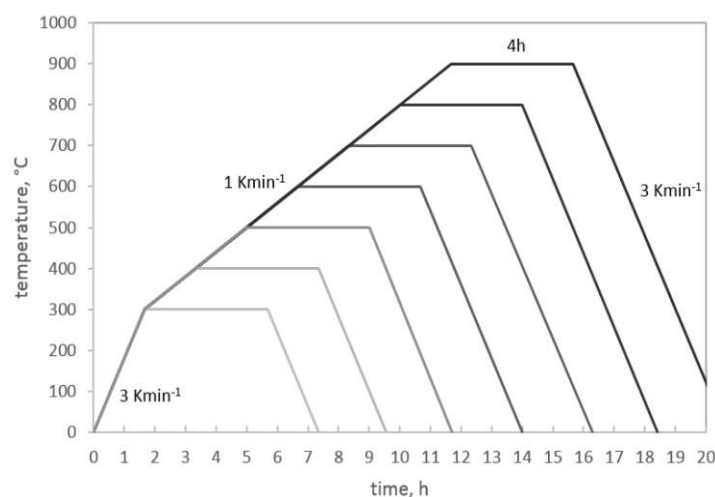


Figure 111: Temperature profiles for pyrolysis experiments under nitrogen

### 10.1.2 Pyrolysis in diluted ammonia

The experiments using diluted ammonia were carried out at Clemson University (SC, USA) at the Department of Materials Science and Engineering.

The experiments were carried out using 10 % ammonia in nitrogen with a flow of 0.25-0.3 l/min in a quartz tube furnace (Lindberg, Hevy Duty; controlling unit: Omega CN8600) that is shown in Figure 112 and was kept inside a fume hood.

First experiments were done changing the atmosphere when reaching the maximum temperature and then holding the temperature for one hour. Then, up to temperatures of 600, 700 and 800 °C, the whole heating process was done under reactive atmosphere. Two experiments using the diluted ammonia only during a specific temperature window were carried out with a maximum temperature of 800 °C and the use of ammonia from either 500-700 °C or 500-800 °C.

Parts of the samples prepared with diluted ammonia as atmosphere during the whole heating period were heat treated again under nitrogen at 800 °C using the standard heating program that was described previously (section 5.2.3).

The samples were then kept in sealed vials filled with nitrogen and sent to Vienna for analysis.



Figure 112: Furnace set up for the experiments using diluted ammonia.



### 10.1.3 Pyrolysis in concentrated ammonia

Experiments with partial use of the reactive atmosphere during a certain temperature range, as well as experiments with reactive atmosphere during the whole heating period were carried out. After a first heating step up to 300 °C with a heating rate of 3 K/min, the heating rate was changed to 1 K/min up to the maximum temperature and then cooled down to room temperature with 3 K/min. The experiments were carried out without dwell time, because the experiments would have become too long to observe them constantly (safety reasons) and it was already critical to neutralize all of the ammonia for the experiment with a maximum temperature of 900 °C without dwell time. The pyrolysis was carried out under flowing ammonia (purity 3.8, Messer) with a flow of 0.2 l/min during the heating period, the cooling period was performed in nitrogen.

Maximum temperatures of 500 °C, 600 °C, 700 °C, 800 °C and 900 °C were used. Additional experiments were carried out by varying the heating program with 700 °C as maximum temperature: the dwell time at maximum temperature was increased to 1 or 4 hours; the ammonia atmosphere was used during heating and cooling period; ammonia was only used from 300-700 °C or 500-700 °C. Also, an experiment with changing the atmosphere to ammonia solely during the dwell time was carried out at a maximum temperature of 600 °C and a dwell time of 1 h. In addition, the influence of grain size of the crosslinked powder on the resulting ceramics was investigated using 4 different sieving fractions and a maximum temperature of 600 °C.

## 10.2 Results - Pyrolysis in nitrogen atmosphere

All experiments for the focus sections I to IV were conducted under flowing nitrogen to examine the properties for the whole temperature range from 300-900 °C to have benchmark samples for the experiments with different atmospheres in the following chapters for PSZ, PCS and a 50/50 mixture.

### 10.2.1 Optical appearance

The sample images of the pyrolysis experiments under nitrogen are shown in Figure 113. During pyrolysis, the samples color changes from colorless or yellow in the crosslinked stage and at lower pyrolysis temperatures to brown around 600 °C and dark brown/black at higher temperatures. Interestingly, the samples pyrolyzed at 900 °C were all covered with a silvery layer (including the crucibles). This could be due to a graphite layer forming.





Figure 113: Sample images of PSZ (top), PCS (middle) and PSZPCS (bottom) after pyrolysis from 300-900 °C under nitrogen.

### 10.2.2 Mass change

The samples were weighed before and after the pyrolysis step and the mass change was calculated. The results are shown in Figure 114. As expected, the curves look like the mass loss curves recorded via TGA for PSZ and PCS (cf. section 6.2.3.1), except for the slight increase of PCS at 900 °C. After pyrolysis at 900 °C, the samples as well as the crucibles were completely coated with a shiny silvery layer, probably graphite. Surprisingly, the mass loss of the mixture doesn't lie in between the other two during the whole temperature range. Starting at 600 °C, the curve reaches a plateau and the final mass loss at 900 °C is 23 %, whereas both of the other were above 25 %. This shows that PSZ and PCS rather seem to react with each other than solely with themselves during the crosslinking step.

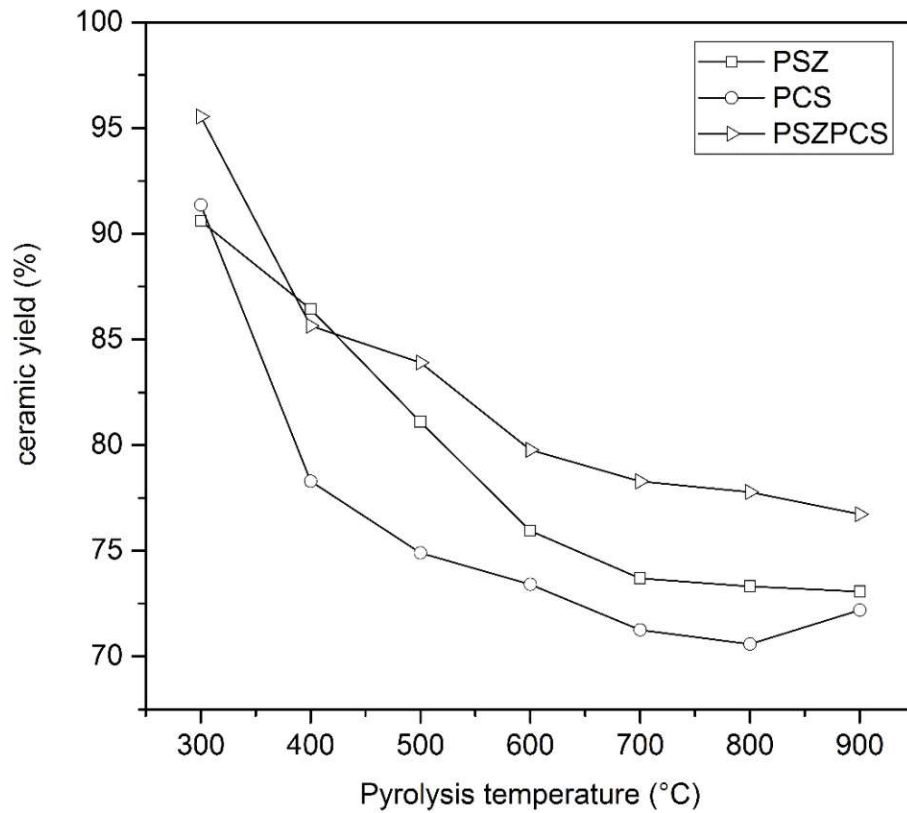


Figure 114: Ceramic yield of PSZ, PCS and PSZPCS after pyrolysis under nitrogen in a temperature range from 300-900°C

### 10.2.3 Elemental composition

The elemental composition of the samples at each temperature was measured. The change in content of each element with increasing temperature is shown for PSZ, PCS and PSZPCS in Figure 115, Figure 116 and Figure 117, respectively. The Si+H content wasn't measured, but symbolizes the amount missing to get a full 100 %. Therefore, the Si+H trend is only the result of the trends for the other elements.

For **PSZ**, the oxygen content decreases with increasing temperature, which indicates the consumption of oxygen by the hydrogen forming during decomposition or its release as other decomposition product. The first assumption is strengthened by the TGA-MS investigations that were described in detail in Focus I (see section 6.2.3.1). They show that simultaneously with oxygen and hydrogen evolution, there is a water signal. The nitrogen content decreases

slightly starting at 400 °C, which is the region of ammonia formation ( $m/z$  17) due to transamination reactions. Apart from slight deviations, the nitrogen content stays constant after that. The carbon content decreases more profoundly up to a temperature of 600 °C. The temperatures aren't completely in accordance with the TGA-MS results, because the release of carbon containing groups continues up to 800 °C according to TGA-MS but the carbon content doesn't change significantly after 600 °C according to the elemental analysis. A reason for that could be the much higher heating rate during the TGA-investigations (5 to 10 K/min vs. 1 K/min) and the lack of dwell time (0 h vs. 4 h) and therefore shifting of the signals. The same shift in temperature can also be found for the ammonia formation.

For **PCS**, the oxygen content shows the same trend as for the PSZ and slightly decreases with increasing pyrolysis temperature. Again, a water signal can be found in the TGA-MS results. The nitrogen content of ~ 1 wt% also decreases with increasing pyrolysis temperature. The carbon content decreases constantly up to 900 °C.

For the mixture **PSZPCS**, the oxygen content is approximately twice as high as that of the pure versions of PSZ and PCS over the whole temperature range and doesn't decrease significantly at higher temperatures. There is an increase in oxygen at temperatures from 500-700 °C. The so called transient porosity that forms during polymer-ceramic-conversion typically reaches its maximum at temperatures between 400 and 600 °C. When transferring the samples from the furnace to the glovebox, they get in touch with a bit of air for a short time. Oxygen uptake is expected to be higher for higher surface areas, which could explain the increase in oxygen for these samples. Zera et al. [133] found extreme oxidation of SiCNO-aerogels when taking them out of the furnace, due to the extremely high surface area of the aerogels, the oxidation was so severe, that the samples even started to glow.

A similar trend but not as remarkable was found for the pure versions too. Also, the nitrogen content doesn't vary significantly with pyrolysis temperature. The carbon content shows the most change as it decreases up to a pyrolysis temperature of 600 °C and then increases again. The decrease is due to release of decomposition products like methane and other small hydrocarbons. The increase is probably due to a release of hydrogen and therefore a higher carbon content.

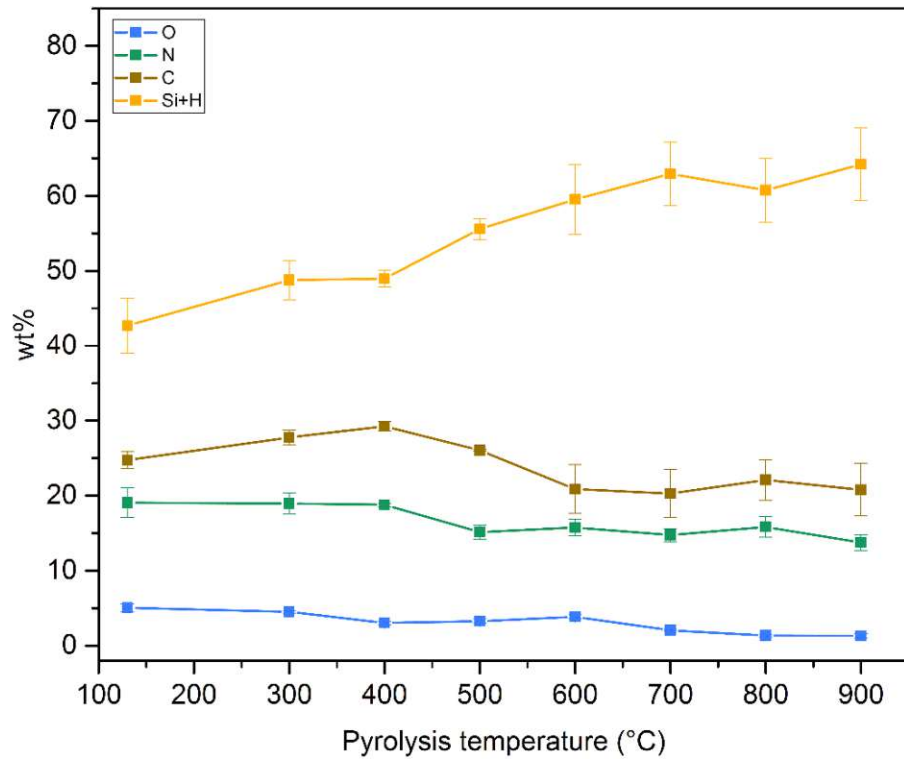


Figure 115: Elemental composition of PSZ after crosslinking at 130 °C and after pyrolysis at temperatures between 300-900°C.

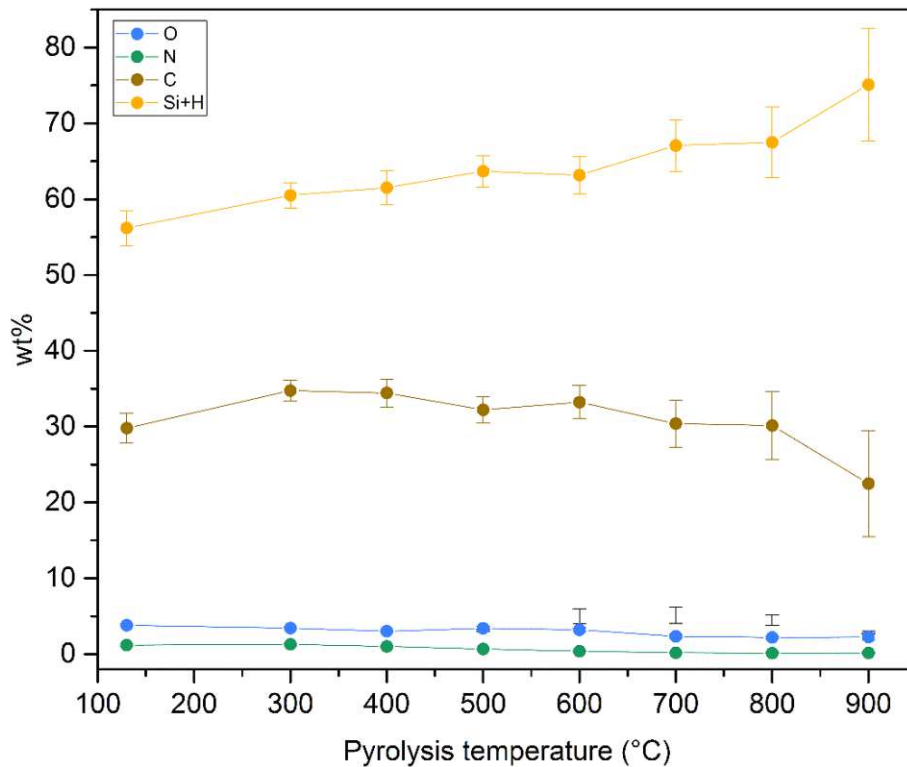


Figure 116: Elemental composition of PCS after crosslinking at 130 °C and after pyrolysis at temperatures between 300-900°C.

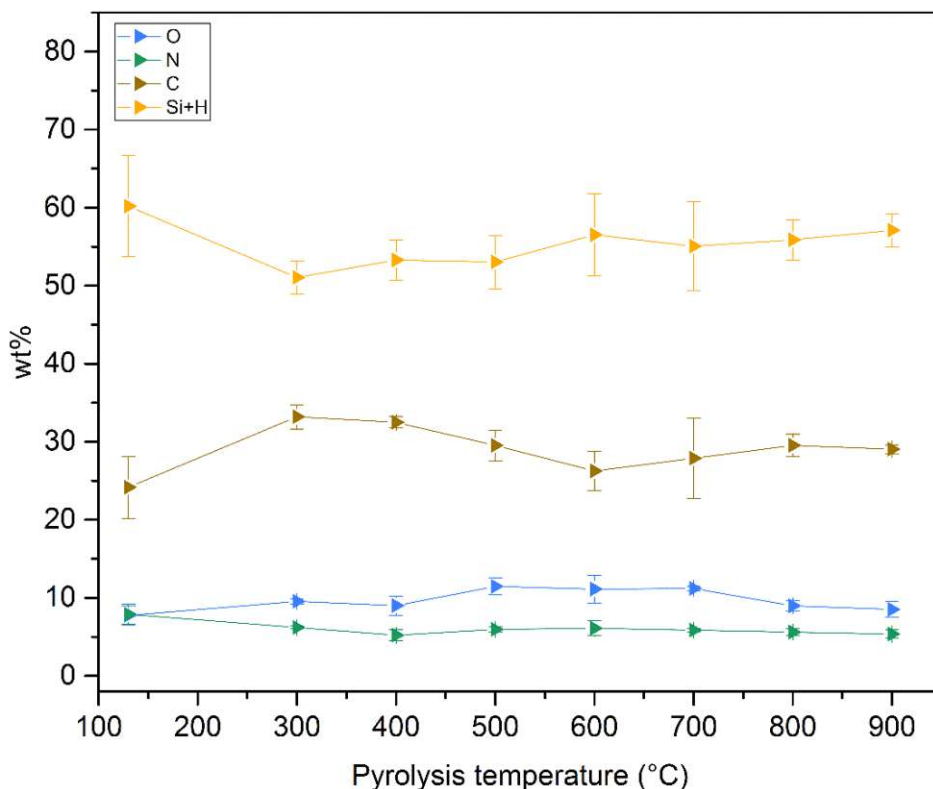


Figure 117: Elemental composition of PSZPCS after crosslinking at 130 °C and after pyrolysis at temperatures between 300-900 °C.

#### 10.2.4 ATR-IR

The ATR-IR spectra of the **PSZ** samples pyrolyzed from 300-900 °C were recorded and are shown in Figure 118 with a shift in y-axis. In addition, the spectrum of crosslinked PSZ (130 °C) is shown and was normalized with respect to the Si-CH<sub>3</sub> band to show the changes during the low temperature range better. In general, the spectra weren't normalized because none of the bands can be assumed to stay constant. Because of that, the intensity of the spectra was adjusted in a way where the main band is in the same intensity range. Therefore, only the relation of bands to each other can be evaluated as well as their presence or absence. Generally, it can be said that organic groups, especially the Si-CH<sub>3</sub> group, can be seen in the spectra up to 700 °C. Between 130 °C and 300 °C, the major changes can be found for the N-H and Si-H bands. Also, the finger print area slightly shifts to higher wave numbers. The aliphatic C-H deformation at ~1400 cm<sup>-1</sup> shows an interesting phenomenon at 500 °C, where the single signal splits up in two signals, one still being at 1400 cm<sup>-1</sup>, the other one at ~1350 cm<sup>-1</sup>. The latter one dominates at 600 °C. This phenomenon happens simultaneously with the disappearance of the N-H signal. The signal could thus be caused by C-N-stretching due to forming of new bonds.

The spectra for **PCS** are shown in the same way in Figure 119. Organic groups are found up to temperatures of 600 °C. Even Si-H is still present at 600 °C. The major change up to 300 °C is the decrease of the Si-H signal. In addition, there is a slight shift of the spectra to lower wave numbers which is the opposite trend than for PSZ. This trend can be found for the Si-H signal up to 600 °C. A reason could be that more Si-atoms are in the close environment of the bond due to structural rearrangement and therefore shift the signal to lower values.

The ATR-IR spectra of the mixtures of **PSZPCS** are shown in Figure 120. Organic groups can be found up to a pyrolysis temperature of 600 °C. The N-H vibrations can barely be seen, which is due to the mixture of polymers. The N-H deformation vibrations can be found as a little shoulder up to 500 °C. The Si-H signal is clearly visible up to 500 °C. At 600 °C, there is still a signal left but the signal to noise ratio is too low to state that with certainty. In contrast to the spectra of the pure materials, there is no shift of the Si-H band with increasing pyrolysis temperature.

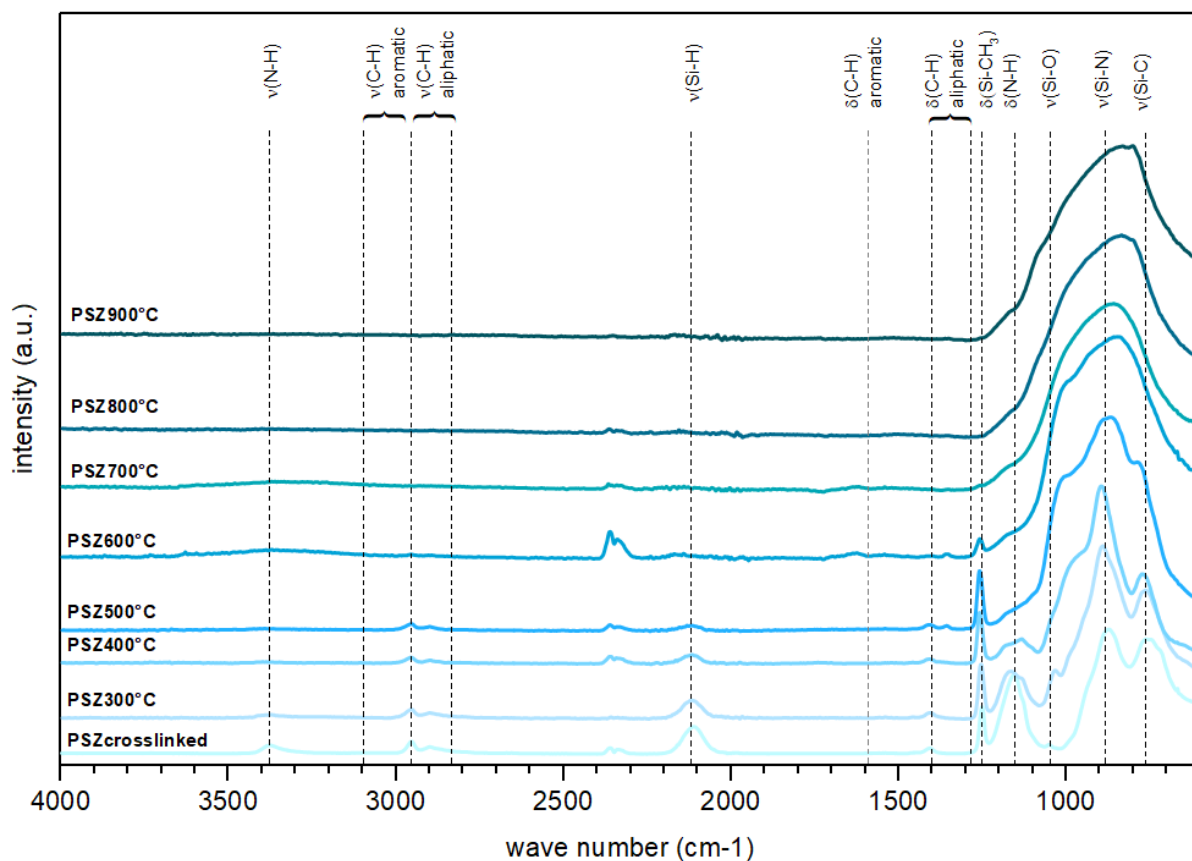


Figure 118: ATR-IR spectra of PSZ after crosslinking at 130 °C and after pyrolysis at temperatures between 300-900°C.



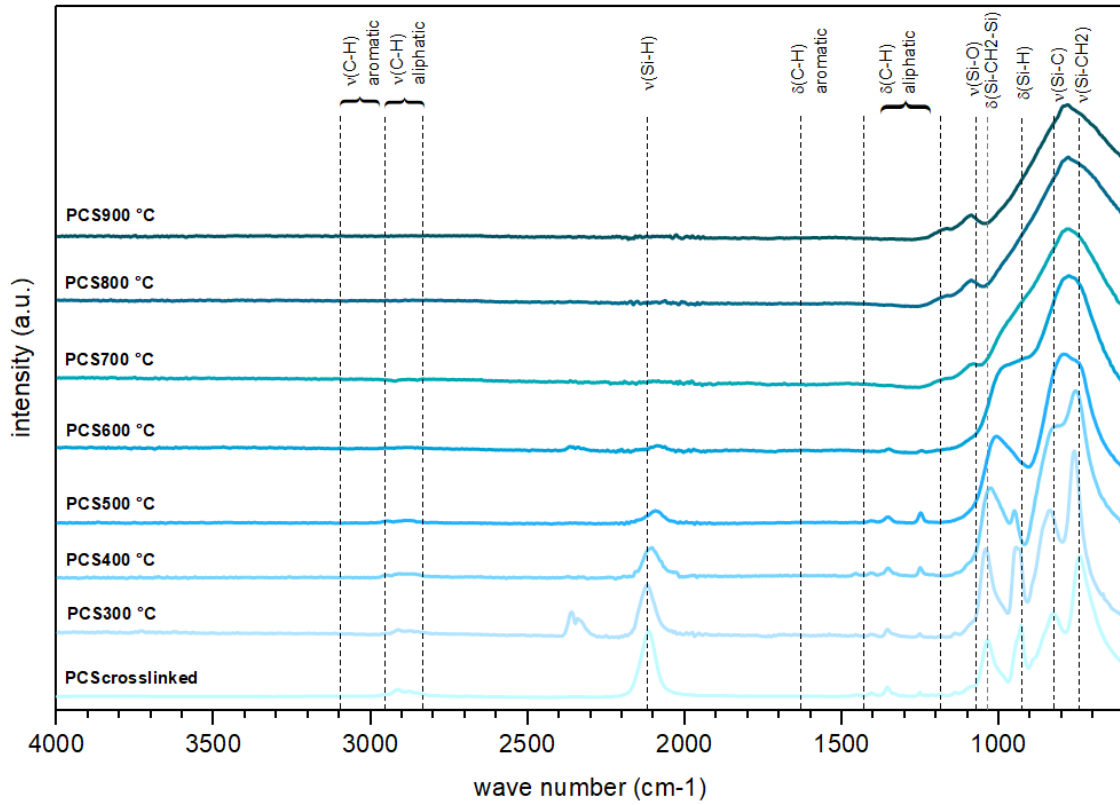


Figure 119: ATR-IR spectra of PCS after crosslinking at 130 °C and pyrolysis at temperatures between 300-900°C.

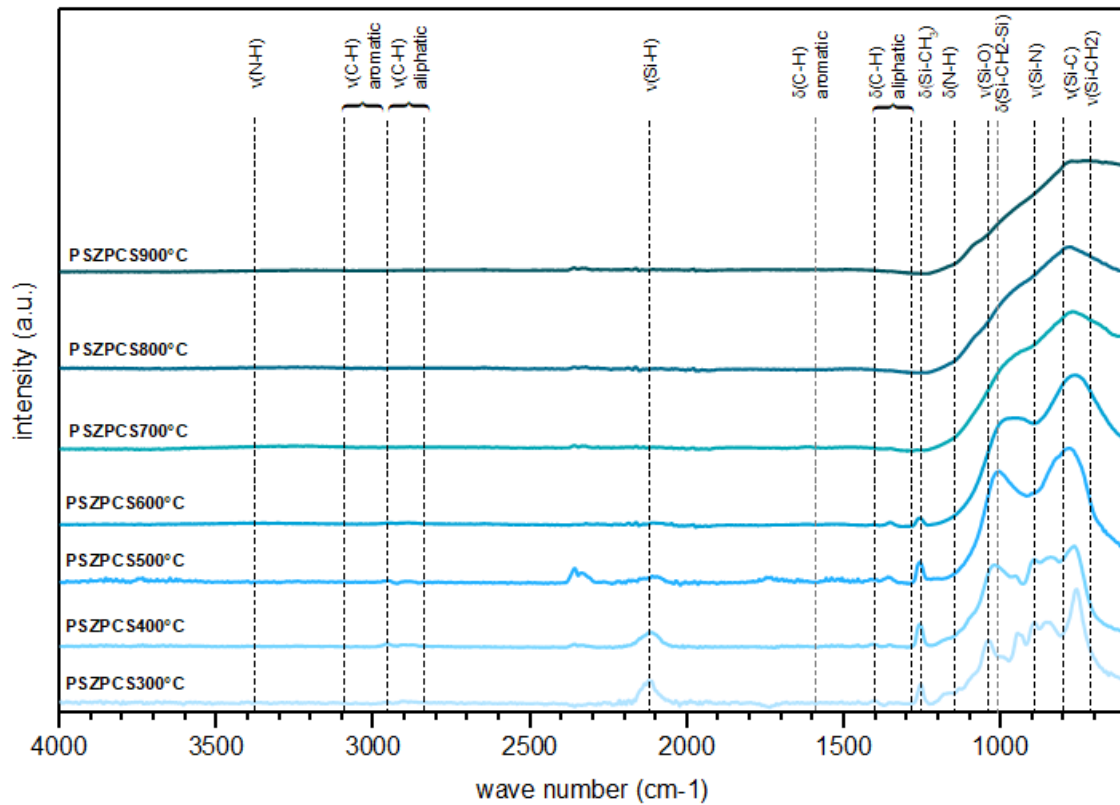


Figure 120: ATR-IR spectra of PSZPCS after crosslinking at 130 °C and pyrolysis at temperatures between 300-900°C.

### 10.2.5 N<sub>2</sub>-Physisorption

The pore characteristics of the samples dependant on the pyrolysis temperature were investigated using N<sub>2</sub> physisorption. The resulting isotherms as well as the calculated parameters are summarized in Table 39. The isotherms for PSZ at various pyrolysis temperatures are displayed in Figure 121 and the corresponding pore size distributions are shown in Figure 122. The isotherms of PSZ, PCS and PSZPCS after pyrolysis at 600 °C are shown in Figure 123.

The porosity in PSZ seems to evolve during a certain temperature window, before collapsing again, since there is almost no porosity present (type II/VI isotherm) at 400 °C and very high specific surface areas together with the type I isotherms, which are typical for microporous materials, at 500 °C and 600 °C. The highest specific surface area is found at 500 °C, before the specific surface area and the pore size decreases when reaching 600 °C and goes down to close to 0 m<sup>2</sup>/g at 700 °C, which is in accordance with the findings of Konegger et al. [12] regarding the closure of pores.

As can be seen in Figure 121, only PSZ yields high specific surface areas at 600 °C, while PCS in contrast shows no porosity accessible by nitrogen. Against the expectation, the mixture doesn't show a combination of the two pure materials, but is almost non-porous, although the shape of the isotherm is like that of a type I isotherm with the sharp rise in the low pressure region. An explanation could be, that there are PSZ and PCS domains formed and the nonporous PCS domains block most of the PSZ micropores.



Table 39: Type of isotherm, BET specific surface area ( $S_{BET}$ ), maximum of the pore size distribution ( $PSD_{max}$ ) and micropore volume ( $V_{micro}$ ) of PSZ crosslinked with different amounts of DVB as linker or using DCP.

	Isotherm	$S_{BET}$ (m <sup>2</sup> /g)	$PSD_{max}$ (nm)	$V_{micro}$ (cm <sup>3</sup> /g)	Comment
<b>PSZ400°C</b>	Type II/ VI	63 ± 1	1.13	-	Macro- or nonporous
<b>PSZ500°C</b>	Type I	350 ± 16	0.88	0.17	Microporous
<b>PSZ600°C</b>	Type I	195 ± 6	0.84	0.10	Microporous
<b>PSZ700°C</b>	Type VI	5 ± 0.5	-	-	Macro- or nonporous
<b>PCS600°C</b>	Type VI	29 ± 1	-	-	Micro- and mesoporous
<b>PSZPCS600°C</b>	Type I/II	20 ± 1	-	-	Micro- /nonporous

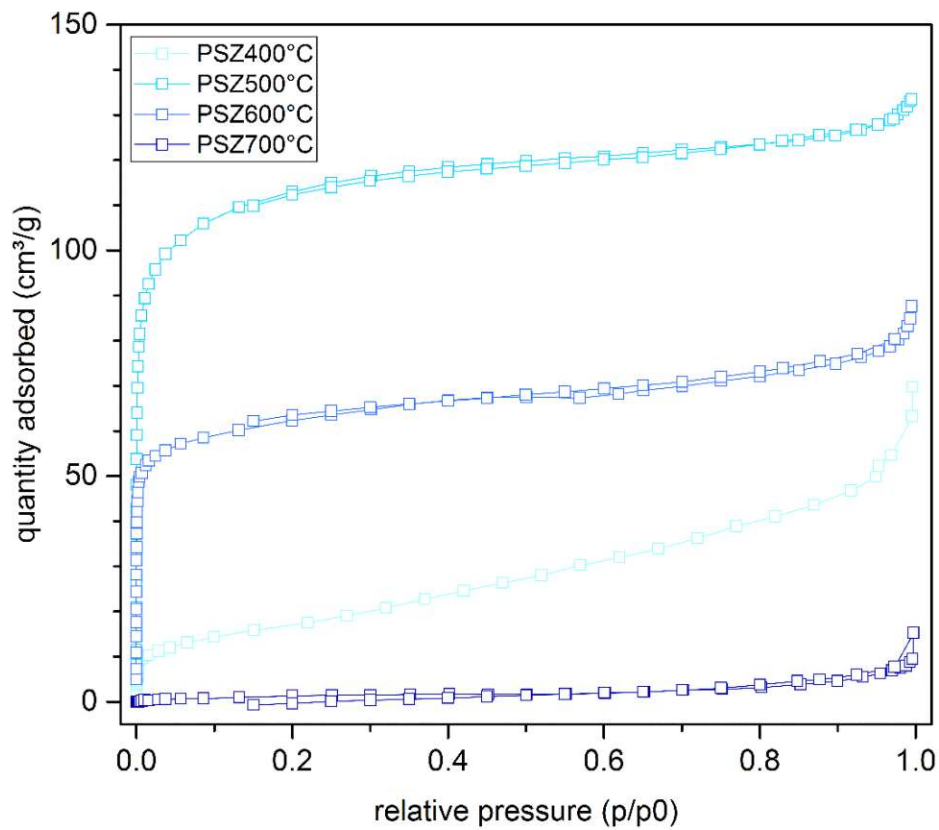


Figure 121:  $N_2$  physisorption isotherms of PSZ after pyrolysis at temperatures between 400-700°C.

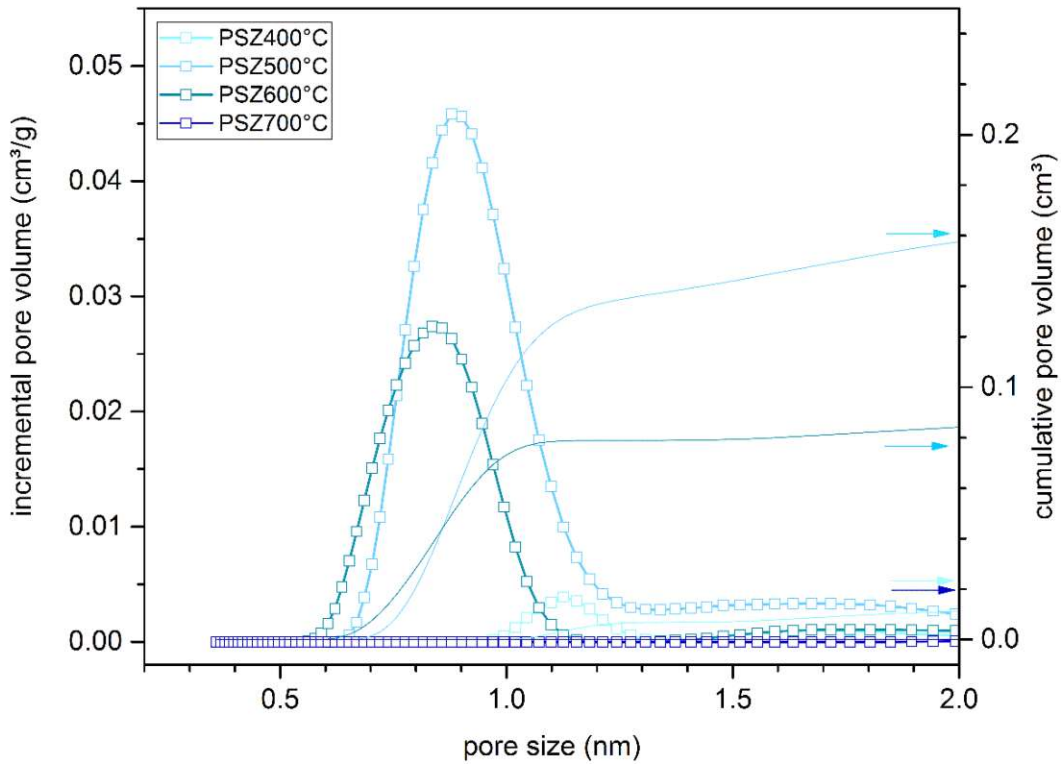


Figure 122: PSDs of PSZ after pyrolysis at temperatures from 400-700 °C, calculated from the  $N_2$  physisorption data using NL-DFT.

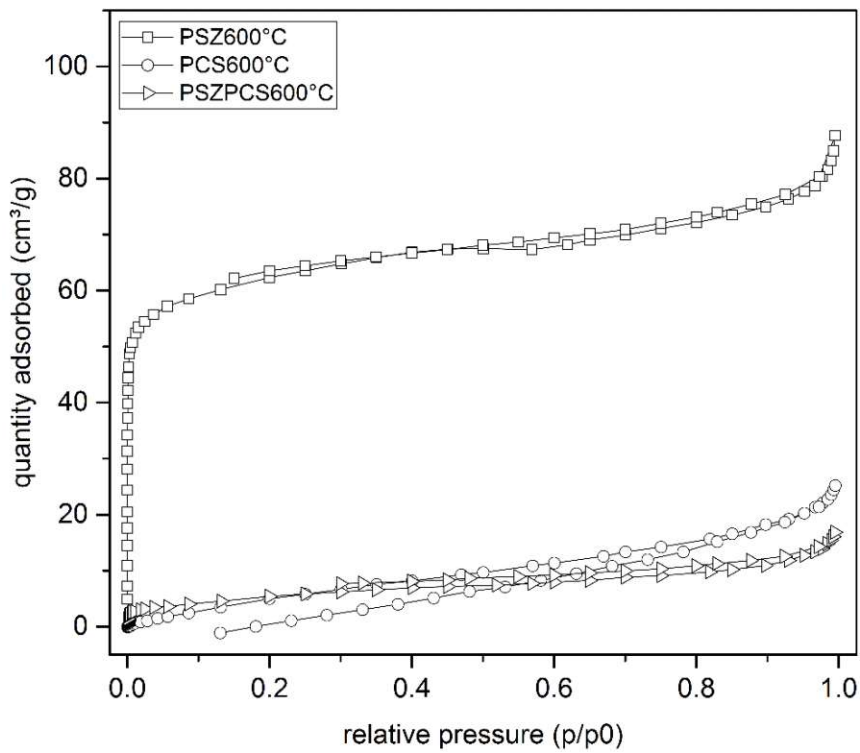


Figure 123:  $N_2$  physisorption isotherms of PSZ, PCS and PSZPCS after pyrolysis (600°C).

### 10.3 Conclusions - Pyrolysis in nitrogen atmosphere

Benchmark values for PSZ, PCS and PSZPCS were generated by pyrolysis under nitrogen atmosphere for comparison to the following experiments using ammonia.

The mass loss of the pure compounds is in accordance with the TGA-curves (see section 6.2.3.1), but surprisingly, the mixture shows a higher ceramic yield than either of the pure compounds which indicates favoured crosslinking of the different polymers with each other than with themselves.

Although the properties of the mixture are lying inbetween those of the pure compounds regarding elemental composition and IR spectroscopy, the porosity does not. While PSZ yields type I isotherms, the mixture behaves mainly like PCS, showing almost no porosity at this pyrolysis temperature. Still, a small sharp increase of adsorbed gas quantity indicates partially type I behaviour. This could be a sign for the formation of rather PSZ and rather PCS rich domains, with the nonporous PCS blocking the micropores present in the PSZ domains.

## 10.4 Results - Pyrolysis in diluted ammonia

### 10.4.1 Diluted ammonia treatment at maximum temperature

To check the influence of ammonia as reactive atmosphere on the properties of SiCN-ceramics derived from PSZ, various preliminary experiments with diluted ammonia were conducted in a temperature range from 300-900 °C. In a first series of experiments, the samples were heated up under nitrogen and then held at the maximum temperature for 1 h under flowing diluted ammonia (10 %). In the second series, the samples were heated up to 800 °C in flowing nitrogen and in a temperature window from 500 °C to 700°C or 500 to 800 °C, respectively, the atmosphere was changed to flowing diluted ammonia. In the last series, the whole heating part of the pyrolysis was conducted under flowing diluted ammonia either up to 600 °C, 700 °C or 800 °C. In addition to the last series, all samples were subsequently heat treated in nitrogen at 800 °C.

#### 10.4.1.1 Optical appearance

The color of the samples changes during processing, from a colorless or light yellow sample in the crosslinked stage and at lower pyrolysis temperatures to (dark) brown and black if going up to 900 °C. Since pyrolysis under reactive atmosphere affects the carbon content of the samples, it is plausible that the sample colour could be affected too. Therefore, images of the samples for both the samples pyrolyzed in flowing nitrogen and the ones held at maximum temperature for an hour in flowing diluted ammonia were taken.

These are shown in Figure 124 for PSZ. There is a difference for the 500 °C and 600 °C samples – the samples additionally treated with ammonia have a lighter color than the corresponding nitrogen samples, which indicates a reaction although the maximum temperature was already reached under inert atmosphere. For 300 °C and 400 °C, it is not possible to see any difference since the samples are colorless anyways.

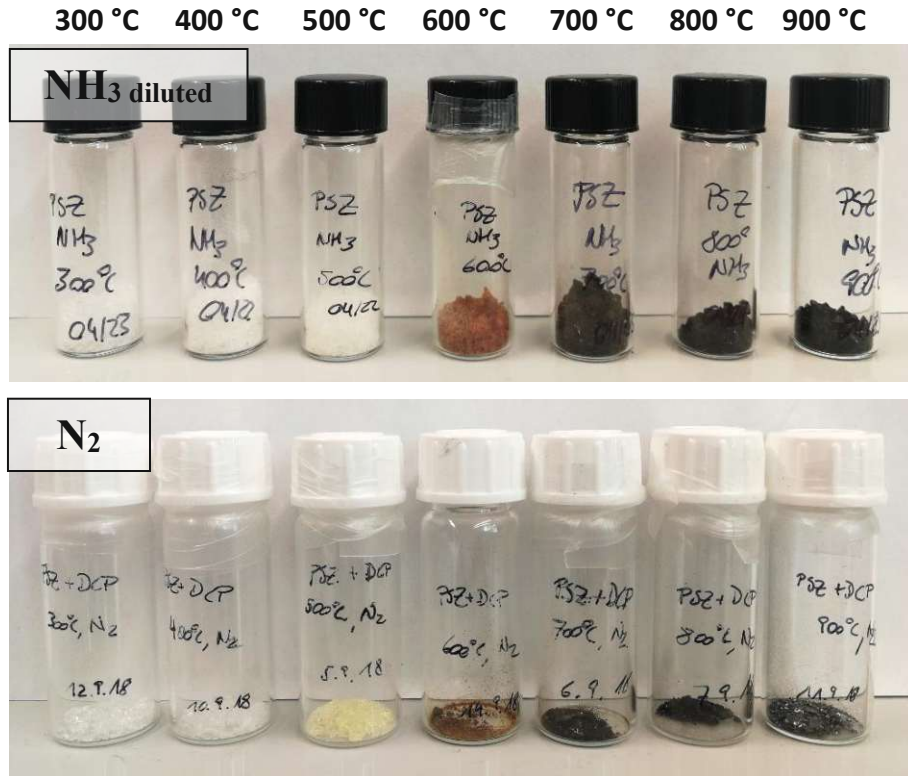


Figure 124: Sample images for PSZ for pyrolysis from 300-900 °C (f.l.t.r.) under nitrogen (bottom) or diluted ammonia at the maximum temperature (top)

#### 10.4.1.2 Mass change

The samples were weighed before and after pyrolysis to calculate the mass loss. The results are shown below.

The results are shown in Figure 125 in comparison to the samples pyrolyzed solely under nitrogen, with the samples held at the maximum temperature for an hour under flowing diluted ammonia showed in dashed lines.

In general, it can be said that there is not much difference for the treatments in different atmospheres – maybe the influence of the treatment only at the maximum temperature is too small. Up to 500 °C, the curves for PSZ fit the expectation, that the mass loss is higher for the samples treated in ammonia. Above 500 °C, the tendencies switch and the mass loss of the ammonia samples is lower.

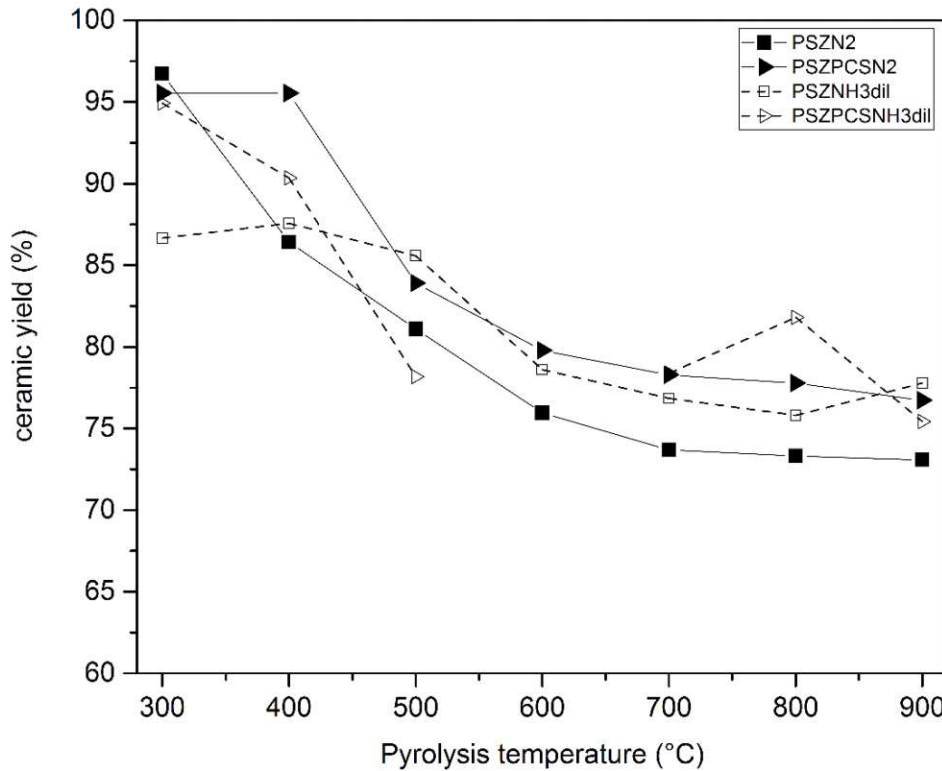


Figure 125: Mass loss during pyrolysis under  $N_2$  or diluted  $NH_3$  at the maximum temperature for 1 h (300-900°C).

#### 10.4.1.3 Elemental analysis

The elemental composition of the samples treated with ammonia at a certain pyrolysis temperature is shown in Figure 126. The results of the samples additionally treated in diluted ammonia are displayed using dashed lines.

Most of the values overlap for the two series of experiments. The main difference can be found for the carbon content and temperature between 300 and 500 °C, where the carbon content is lower for the diluted ammonia treated sample. The diluted ammonia has no influence on the elemental composition anymore at temperatures above 600°C.

Schitco et al. [14], who conducted the experiments with pure ammonia, reached carbon contents around 3 wt% for PSZ after ammonolysis at 600 °C, which is way below the values reached in the experiments conducted in this work. Therefore, the influence of diluted ammonia at the maximum temperature is not effective enough.

Generally, the carbon content decreases constantly up to a temperature of 700 °C and then slightly increases again. The reason for that could be further decomposition with hydrogen as decomposition product. A similar trend can be observed for nitrogen, where the content decreases until 600 °C and then starts to increase again. Oxygen, in contrast, decreases

constantly with the 600 °C sample as exception, which indicates that it is consumed by one of the decomposition products, for example hydrogen. In addition, an increase of standard deviation with pyrolysis temperature can be observed for both the samples, especially for the carbon content, which could mean that some kind of domains form with increasing temperature, making the sample less homogenous.

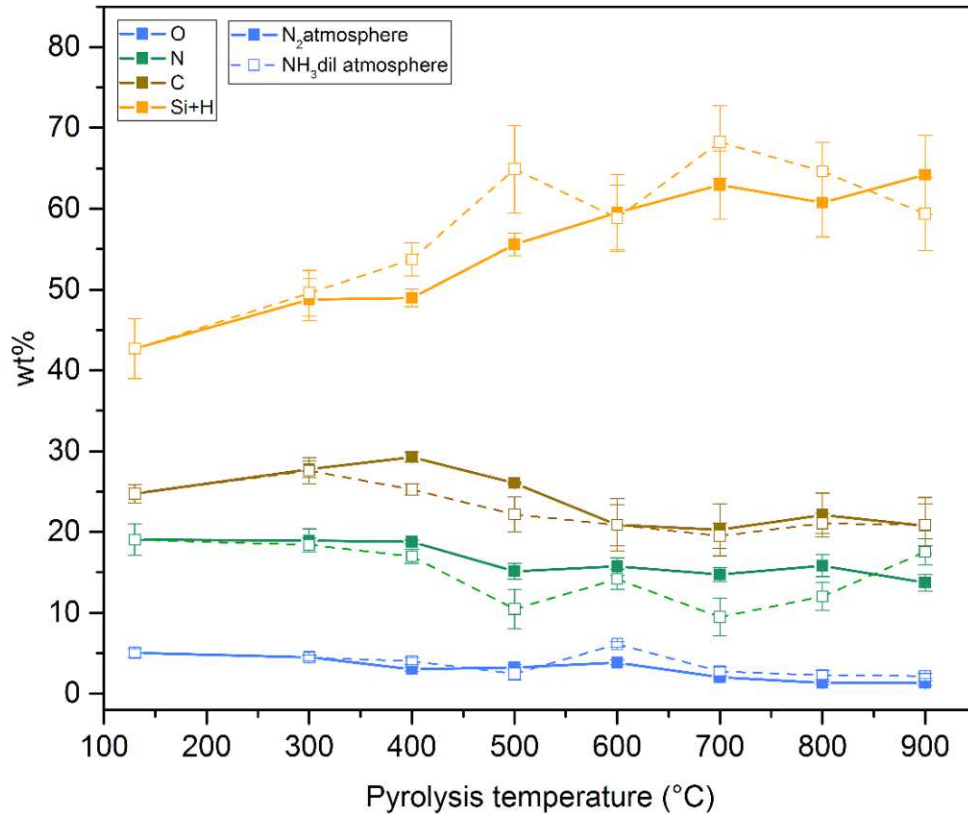


Figure 126: Elemental composition of PSZ after treatment with diluted ammonia at the maximum temperatures between 300-900°C or with nitrogen as atmosphere; O, N, and C content are measured, Si+H is calculated as remainder to 100 wt%.

#### 10.4.1.4 ATR-IR

The ATR-IR spectra of the samples treated with ammonia at the maximum pyrolysis temperature for 1 h are shown in Figure 127. Since none of the bands can be expected to remain unaffected, the spectra weren't normalized but the intensities were adapted to be in the same range.

Organic groups can be found up to temperatures of 700 °C. At higher temperatures, there are small signals at the wavenumber of the Si-CH<sub>3</sub>-band, but the signal is in the same intensity range as the background signal which results from slight variations in the composition of air.



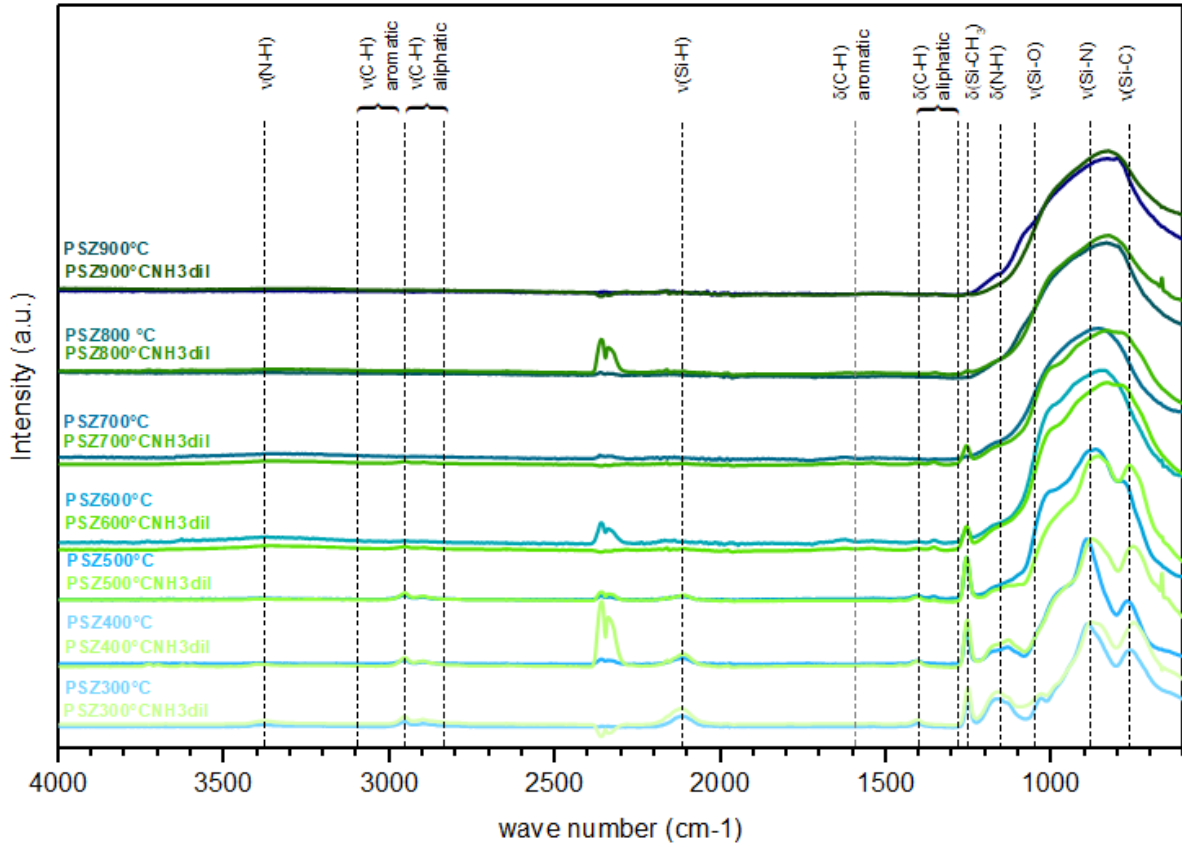


Figure 127: ATR-IR spectra of PSZ after treatment with diluted ammonia at the maximum temperatures between 300-900°C or with nitrogen as atmosphere.



## 10.4.2 Diluted ammonia treatment in a certain temperature range of the pyrolysis

### 10.4.2.1 Optical appearance

As can be seen in Figure 128, the samples are both dark brown/black, and look like the sample pyrolyzed up to 800 °C solely under nitrogen. Diluted ammonia does not affect elemental composition of the sample enough to change the sample color.



Figure 128: Sample images for PSZ treated with ammonia during a temperature window of 500-700 °C (left) and 500-800 °C (right) and up to a maximum temperature of 800 °C.

### 10.4.2.2 Mass change

Since there are only two temperature windows that were investigated, 500-700 °C and 500-800 °C, the data is not shown in a diagram but in Table 40. For comparison, the values of the samples pyrolyzed up to 800 °C under nitrogen are also shown, since the 500-700 °C sample was further heated up to 800 °C under nitrogen too. For both samples, the mass loss is lower when heat treated in ammonia in the critical temperature region. Apparently, there is still an influence when increasing the temperature from 700 °C to 800 °C. The expectation would have been that ammonia increases the mass loss, but the opposite can be observed. An explanation could be nitrogen incorporation (see next section).

Table 40: Mass change of the samples treated with ammonia during a temperature window.

	$\Delta m_{\text{crossl.-pyro, \%}}$
800N <sub>2</sub>	-26.7
500-700NH <sub>3</sub>	-20.6
500-800NH <sub>3</sub>	-19.1

### 10.4.2.3 Elemental composition

The elemental composition of the samples which were treated with diluted ammonia during a temperature window from either 500-700 or 500-800 °C is given in Figure 129. The maximum pyrolysis temperature was 800 °C in both cases, which is why the composition of the samples pyrolyzed up to 800 °C solely under nitrogen atmosphere is shown for comparison. The nitrogen content increases with the duration of the ammonia treatment and is significantly higher than for the sample solely pyrolyzed in nitrogen, which has a nitrogen content of 16 wt%. The carbon content on the other hand is lower for the ammonia treated samples (15 wt% compared to 22 wt%), which indicates that the ammonia treatment has an influence on the carbon content even though it is diluted. Still, the oxygen content of the samples pyrolyzed in diluted ammonia is significantly higher, which could also be the reason for the lower carbon content.

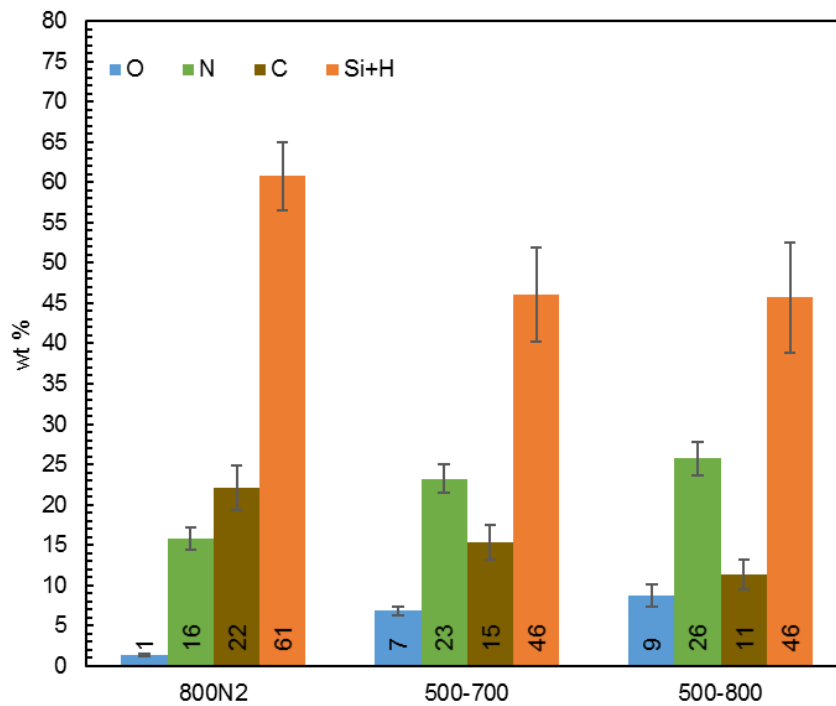


Figure 129: Elemental composition of PSZ after treatment with diluted ammonia during a temperature window and pyrolysis up to a maximum temperature of 800 °C or with nitrogen as atmosphere; O, N, and C content are measured, Si+H is calculated as remainder to 100 wt%.

#### 10.4.2.4 ATR-IR

The ATR-IR spectra of the samples treated with diluted ammonia during a certain temperature window of pyrolysis are shown in Figure 130 for **PSZ** compared to the spectrum of the sample pyrolyzed up to 800 °C under nitrogen (PSZ800°C). There is only a minor shift in the spectra to higher wave numbers which could be caused by a higher nitrogen content. The sample treated with ammonia up to 800 °C shows two maxima, with the bigger one in the Si-N region. As shown by elemental analysis, the sample also has a slightly higher nitrogen content than the one from 500-700 °C, with 26 wt% compared to 23 wt% and both higher than that of the sample pyrolyzed up to 800 °C in nitrogen, which has a nitrogen content of 16 wt%.

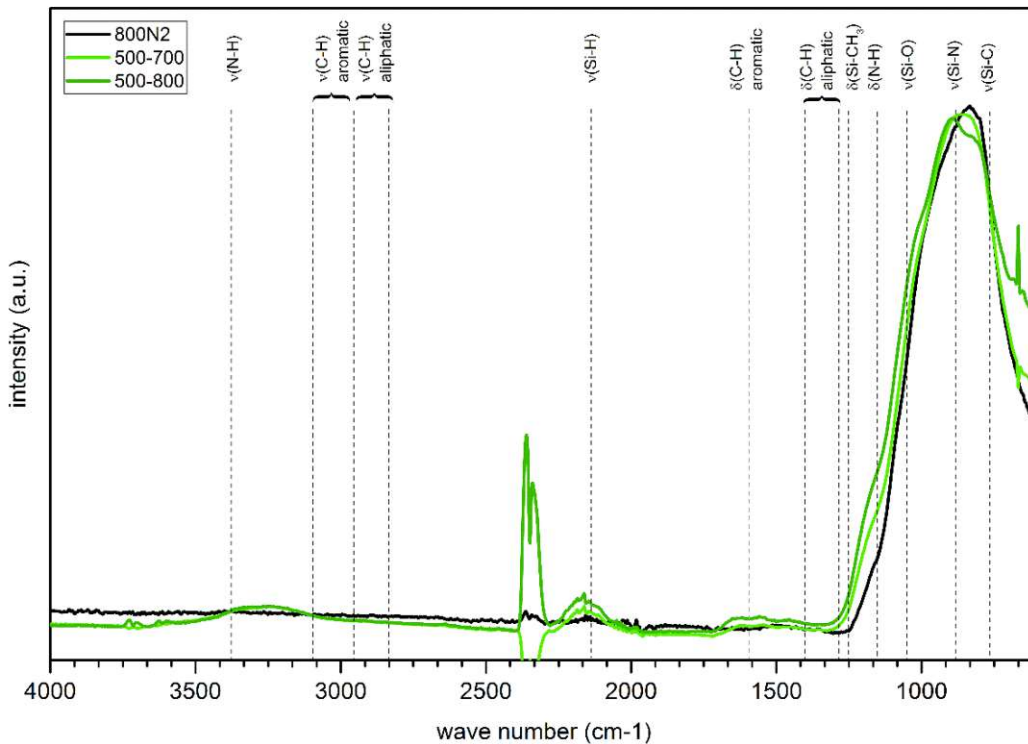


Figure 130: ATR-IR spectra of PSZ after treatment with diluted ammonia during a temperature window and pyrolysis up to a maximum temperature of 800 °C, or with nitrogen as atmosphere.

### 10.4.3 Diluted ammonia treatment during whole heating period

#### 10.4.3.1 Optical appearance

The samples treated with diluted ammonia during the whole heating period and after a second heat treatment under nitrogen are shown in Figure 131.

The biggest difference was found for the PSZ sample 0-600 °C, which is light brown, compared to a medium brown for the ammonia treatment at maximum temperature and a relatively dark brown for the nitrogen sample. Also, the sample 0-700 °C is lighter brown than the corresponding 700 °C samples (diluted ammonia and nitrogen). This indicates a bigger influence, if the whole heating period is done under reactive atmosphere. After the second treatment, all samples have the same color and the same color as the corresponding inert sample.

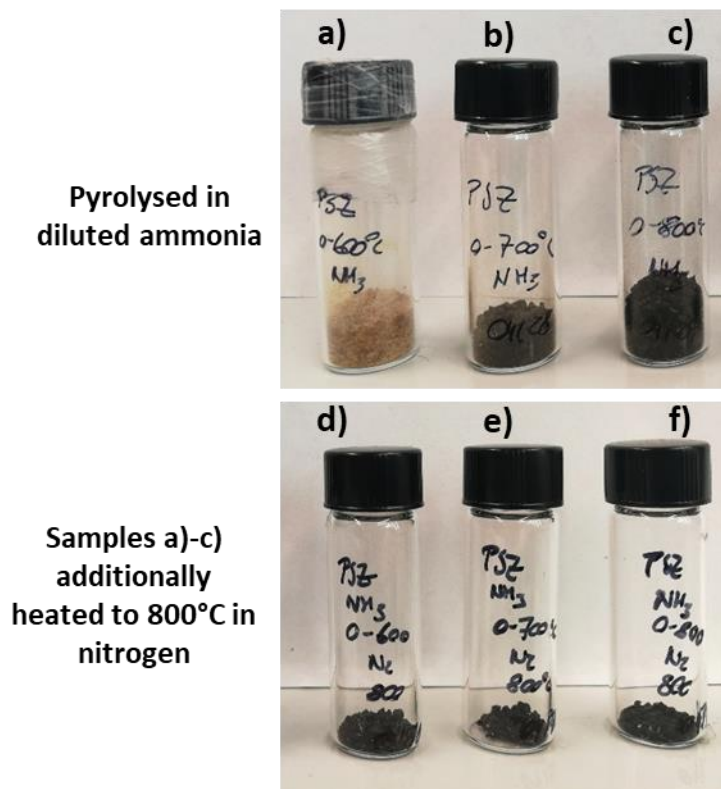


Figure 131: Sample images for PSZ treated with diluted ammonia during the whole heating period (top) and after second heat treatment under nitrogen (bottom); a) 0-600°C b) 0-700°C c) 0-800°C; d)-f) are the corresponding samples heat treated in nitrogen.

### 10.4.4 Mass change

In Table 41, the mass change of the samples using diluted ammonia as atmosphere during the whole heating part of the pyrolysis is shown. The corresponding samples pyrolyzed under nitrogen flow are given too for reasons of better comparability. For PSZ, one of the values (0-700NH<sub>3</sub>) can't be taken into account, because sample was spilt during removing the crucible from the furnace. The trend shows that the mass loss is lower than for the samples pyrolyzed in nitrogen, which is in accordance with the previously described experiments.

Table 41: Mass loss of the samples treated with ammonia during the whole heating period.

	$\Delta m_{\text{crossl.-pyro, \%}}$
600N <sub>2</sub>	-24.0
<b>0-600NH<sub>3</sub></b>	<b>-20.4</b>
700N <sub>2</sub>	-26.3
<b>0-700NH<sub>3</sub></b>	<b>-40.4<sup>a</sup></b>
800N <sub>2</sub>	-26.7
<b>0-800NH<sub>3</sub></b>	<b>-21.5</b>

<sup>a</sup> sample spilt while removing the crucible from the furnace

In addition to these experiments, parts of these samples were heat treated in nitrogen at 800 °C, to see if the sample behavior during pyrolysis changes due to the previous ammonolysis step.

Table 42 shows the mass loss of each the treatment of the ammonolysis step, the treatment in nitrogen at 800 °C, and the sum of the two. In addition, the mass loss of the sample heated up to 800 °C solely using nitrogen as atmosphere is given. PSZ shows a high additional mass loss for the samples previously pyrolyzed in ammonia up to 600 °C and much lower additional mass losses for the samples with 700 °C and 800 °C, while the latter two are almost equal. This indicates that the influence of the ammonia treatment is most important – at least as far as it can be seen from the mass loss data - up to 700 °C.

Table 42: Mass change up to 800 °C of the samples previously heat treated in ammonia.

	$\Delta m, \%$		
	NH <sub>3</sub> step	N <sub>2</sub> step	total
800N <sub>2</sub>			<b>-26.7</b>
<b>0-600NH<sub>3</sub> + 800N<sub>2</sub></b>	-20.4	-5.6	<b>-26.0</b>
<b>0-700NH<sub>3</sub> + 800N<sub>2</sub></b>	-40.4 <sup>a</sup>	-1.7	<b>-42.1<sup>a</sup></b>
<b>0-800NH<sub>3</sub> + 800N<sub>2</sub></b>	-21.5	-1.4	<b>-22.9</b>

<sup>a</sup> sample spilt while removing the crucible from the furnace

10.4.4.1 Elemental analysis

The elemental compositions after pyrolysis under diluted ammonia during the heating period as well as after an additional heat treatment under nitrogen up to 800 °C are given in Figure 132, together with the sample pyrolyzed with nitrogen as atmosphere.

If the pyrolysis from 0-600 °C under ammonia is compared to the value for the pyrolysis solely under nitrogen atmosphere (O: 2wt%, N: 16 wt%, C: 21 wt%), nitrogen and carbon content are both a little lower for the ammonia treated sample. For 0-700 °C, the nitrogen content is nearly the same, the carbon content is slightly lower for the ammonia treated sample (15 wt% vs. 20 wt%). For 0-800 °C, the same trend – higher nitrogen and lower carbon content – can be found. The elemental compositions of the samples after an additional heat treatment under nitrogen at 800 °C converge.

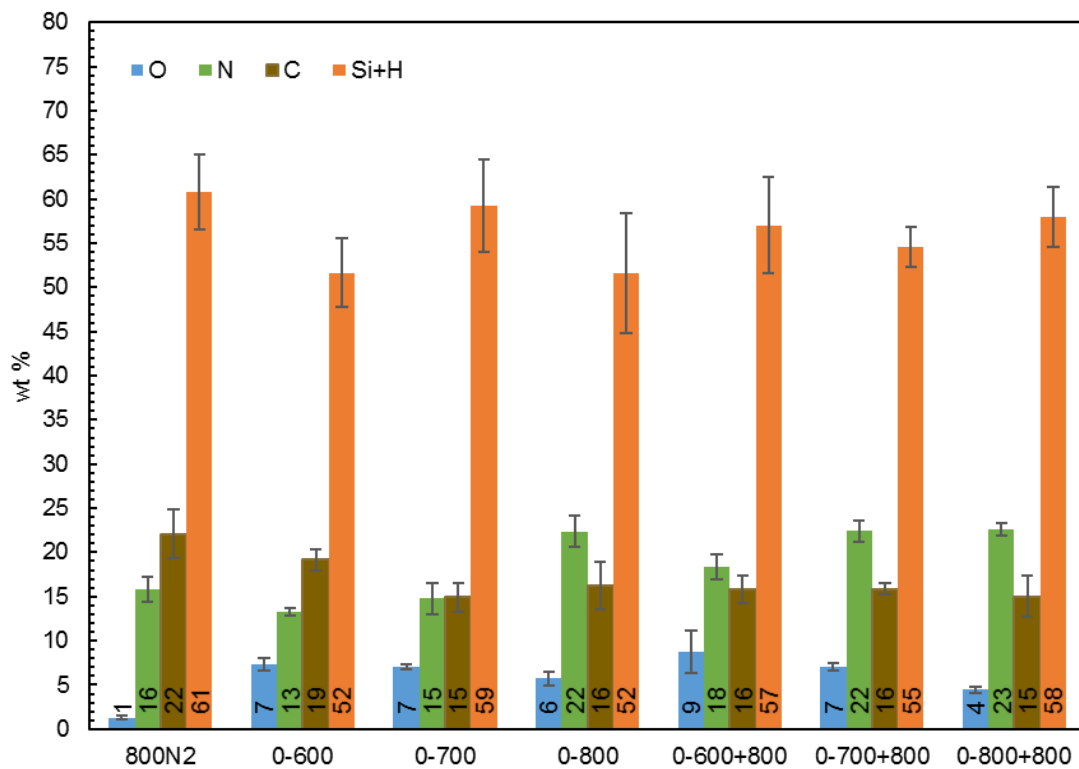


Figure 132: Elemental composition of PSZ after pyrolysis with diluted ammonia or with nitrogen as atmosphere during the heating period, or after an additional nitrogen heat treatment after the first pyrolysis with diluted ammonia; O, N, and C content are measured, Si+H is calculated as remainder to 100 wt%.

### 10.4.4.2 ATR-IR

Three pyrolysis experiments up to 600 °C, 700 °C and 800 °C in flowing diluted ammonia were carried out. The spectra are compared with those of the corresponding nitrogen pyrolyses in Figure 133.

Only minor differences can be seen, especially because the spectra cannot be normalized on any band. At 600 °C, there are more signals in the aliphatic C-H regions.

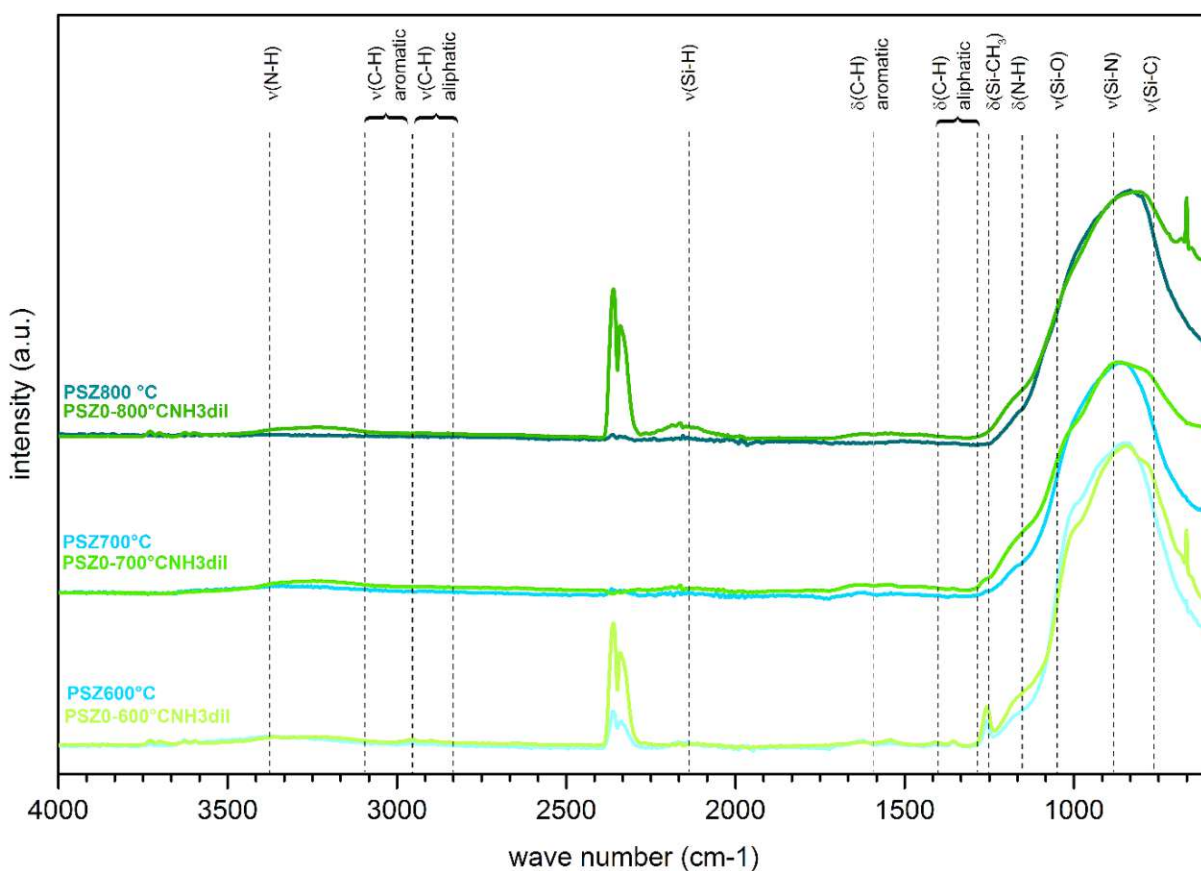


Figure 133: ATR-IR spectra of PSZ after pyrolysis with diluted ammonia or with nitrogen as atmosphere during the heating period.



### 10.4.4.3 N<sub>2</sub>-Physisorption

Since previous samples were always pyrolyzed at 600 °C, the first sample investigated using N<sub>2</sub>-physisorption was the sample pyrolyzed at 600 °C with diluted ammonia during the whole heating period (PSZNH<sub>3</sub>dil0-600°C). The isotherm is shown in Figure 134, the PSD in Figure 135, each with the values of PSZ600°C for comparison. The isotherm is mainly type I and the PSD has a maximum at 0.86 nm. The pore size maximum is close to that of the benchmark sample, showing that the influence of the treatment with diluted ammonia is only minor. Still, the slightly higher pore size could indicate that the reactive atmosphere removed part of the carbon and consequently increased the pore size. The sample has a BET specific surface area of 121 m<sup>2</sup>/g, which is lower than for the benchmark sample. This could be due to partial oxidation of the sample, leading to a closure of the pores, which is in accordance with the higher oxygen content was measured for the samples treated with diluted ammonia.

Selected other samples were analyzed using 5-point-BET without measuring the whole isotherm. The results are listed in Table 43. As can be seen, the specific surface area decreases drastically if the pyrolysis temperature exceeds 600 °C, as for the pyrolysis under nitrogen atmosphere. The specific surface area of PSZNH<sub>3</sub>dil0-700 °C lies at 22 m<sup>2</sup>/g, showing that almost no (accessible) porosity is left. For PSZNH<sub>3</sub>dil 0-800 °C, the sample has quasi lost its open porosity with a specific surface area of 9 m<sup>2</sup>/g.

The sample PSZNH<sub>3</sub>dil0-600°C heat treated a second time in nitrogen at 800 °C shows a surface area of only 2 m<sup>2</sup>/g, which means that the sample is practically non porous. The diluted ammonia apparently didn't have enough effect on the microporosity to stabilize it up to 800 °C as it was shown (for 750 °C and concentrated) by Schitco et al. [14].

Table 43: Type of isotherm, BET specific surface area ( $S_{BET}$ ), maximum of the pore size distribution ( $PSD_{max}$ ) and micropore volume ( $V_{micro}$ ) of PSZ after pyrolysis with diluted ammonia or with nitrogen as atmosphere during the heating period.

	Isotherm	$S_{BET}$ (m <sup>2</sup> /g)	$PSD_{max}$ (nm)	$V_{micro}$ (cm <sup>3</sup> /g)	Comment
<b>600°C</b>	Type I	195 ± 6	0.84	0.10	Microporous
<b>0-600°CNH<sub>3</sub>dil</b>	Type I	121 ± 6	0.86	0.08	Microporous
<b>0-700°CNH<sub>3</sub>dil</b>	just BET	22 ± 2	-	-	Non porous
<b>0-800°CNH<sub>3</sub>dil</b>	just BET	9 ± 1	-	-	Non porous
<b>0-600°CNH<sub>3</sub>dil</b> <b>+ 800 N<sub>2</sub></b>	just BET	2 ± 0	-	-	Non porous



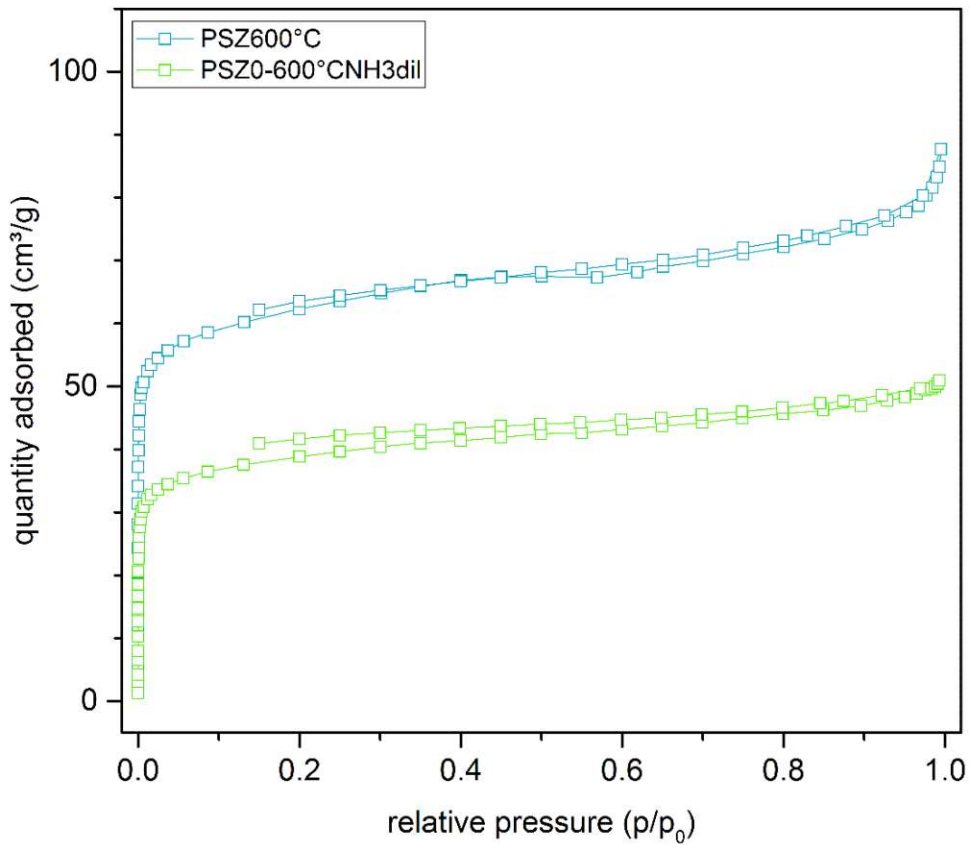


Figure 134:  $N_2$  physisorption isotherms of PSZ after pyrolysis up to 600 °C under diluted ammonia or solely under nitrogen atmosphere.

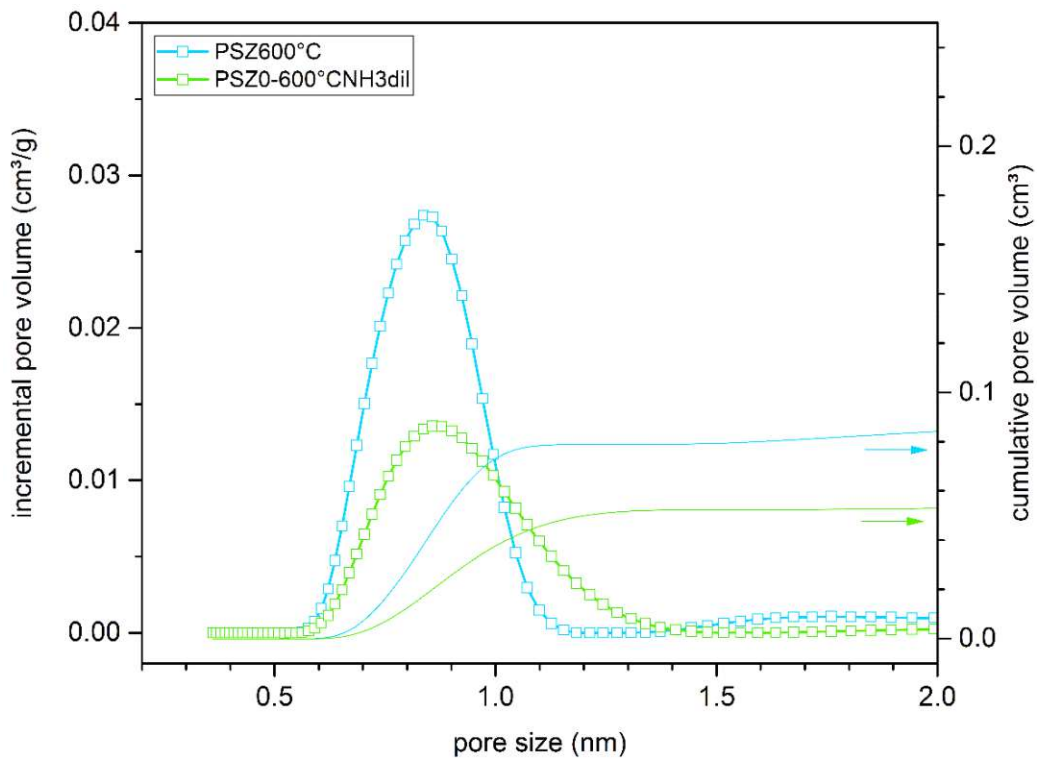


Figure 135: PSDs PSZ after pyrolysis up to 600 °C under diluted ammonia or solely under nitrogen atmosphere, calculated from the  $N_2$  physisorption data using NL-DFT.

## 10.5 Conclusions – Pyrolysis in diluted ammonia

Although many experiments were conducted using diluted ammonia as reactive atmosphere, the findings didn't show a clear and consistent effect on the properties of the materials.

Although the weight loss was slightly higher for the samples treated in diluted ammonia, which is expected to happen due to carbon removal by reaction with ammonia, the effect is only minor and almost in the range of weighing errors, especially due to problems when removing the crucibles from the furnace.

The elemental composition showed a slight decrease in carbon content going along with a slight increase of nitrogen content.

All these findings would fulfil the expectations from the ammonia treatment, still no influence on the pore stability or –size was found.

Apparently, the concentration was too low to lead to significant changes.

## 10.6 Results - Pyrolysis in concentrated ammonia

### 10.6.1 Influence of different grain sizes

Using the standard material, PSZ, and the standard pyrolysis temperature, 600 °C, the influence of the grain size on the resulting ceramic using ammonia as pyrolysis atmosphere was tested. Since ammonia is a reactive pyrolysis atmosphere, interacting with the material during the heat treatment and not just serving as inert atmosphere to protect the material from oxidation, the grain size could influence the properties of the resulting ceramics.

#### 10.6.1.1 Optical appearance

The different sieve fractions of PSZ after pyrolysis under ammonia up to 600 °C are shown in Figure 136. The smaller the grain size, the lighter the color, which could indicate a stronger decrease in carbon content and therefore a dependency of the resulting ceramic on the grain size of the crosslinked material. But, when grinding the ceramics, the color becomes lighter, too, so the elemental analysis has to be taken into account.

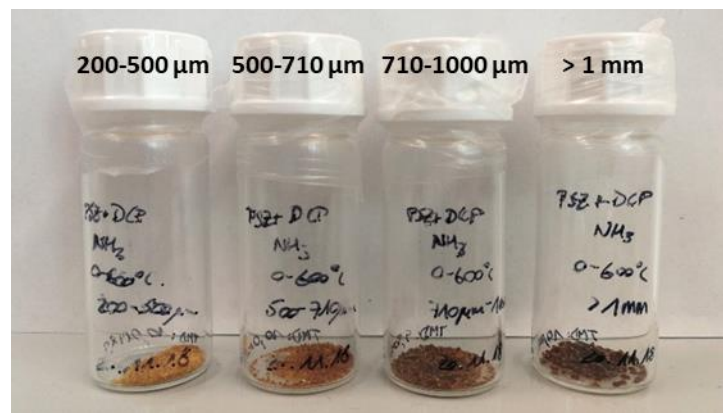


Figure 136: Sample images of the grain size variation of PSZ and pyrolysis up to 600 °C under concentrated ammonia.

#### 10.6.1.2 Mass change

The mass change of the four different sieving fractions is listed in Table 44. The mass loss increases with decreasing grain size, indicating that reactions are facilitated by the smaller grain size, because higher areas of the powder are accessible by the reactive atmosphere. Since only small amounts of each sieving fraction were used, the values have to be seen with care due to weighing errors; still, a trend is visible.

Table 44: Mass change for different sieving fractions pyrolyzed under concentrated ammonia at 600 °C.

	$\Delta m_{\text{crossl.-pyro, \%}}$
>1mm	-27.0
710 $\mu\text{m}$ -1mm	-27.8
500-710 $\mu\text{m}$	-29.2
200-500 $\mu\text{m}$	-30.0

### 10.6.1.3 Elemental composition

Different sieving fractions of crosslinked PSZ were pyrolyzed at 600 °C in concentrated ammonia to check if the grain size has an influence on the resulting ceramic. According to the results that are listed in Table 45, the grain size has a minor effect, at least if it is below 1 mm. The oxygen content increases with decreasing grain size, which is plausible due to the higher specific surface area. The nitrogen contents increase with decreasing grain size, but have high deviations. The carbon content is constant except for the fraction >1mm.

Table 45: Elemental analysis of different sieving fractions of PSZ pyrolyzed at 600 °C under ammonia.

	O, wt%	N, wt%	C, wt%	Si+H, wt%
mixed	6.2 ± 0.8	30.8 ± 4.4	7.8 ± 0.9	55.2
>1mm	5.3 ± 0.4	28.0 ± 3.2	9.0 ± 0.1	57.8
710 $\mu\text{m}$ -1mm	6.1 ± 0.2	30.5 ± 1.7	6.9 ± 0.5	56.5
500-710 $\mu\text{m}$	8.0 ± 0.5	38.0 ± 4.1	6.9 ± 0.7	47.1
200-500 $\mu\text{m}$	8.0 ± 0.4	35.1 ± 3.2	6.6 ± 0.2	50.3

### 10.6.2 Interim conclusions

The experiments in the following sections were always carried out with a mixture of these sieving fractions (c.f. “mixed”). Mixed grain sizes are used for the following experiments for several reasons. Already for the experiments using nitrogen as pyrolysis atmosphere, as well those with diluted ammonia, mixtures were used. Although mass loss and nitrogen content indicate that the reactions are facilitated if smaller grain sizes are used, there is also a higher degree of oxidation visible for these samples. Therefore, using the grain size mixture is a good trade-off, with the restriction that no grains bigger than 1 mm are used.

### 10.6.3 Influence of dwell time and temperature window of the reactive atmosphere

Besides a standard heating program up to the maximum pyrolysis temperature followed by cooling without dwell time and the use of the reactive atmosphere during the heating period only, several variations using dwell times or ammonia during a longer/shorter part of the pyrolysis were tested. An overview of the conditions and sample names is listed in Table 46. 700 °C was chosen as maximum temperature, because during a first trial to test the ammonia set up at 600°C and 700°C, the 600 °C sample showed no difference in elemental composition, but the 700 °C sample did in comparison with the corresponding samples pyrolyzed in nitrogen.

Table 46: Pyrolysis conditions for the investigations regarding influence of dwell time, heating - and cooling period and corresponding sample names.

sample name	Precursor	dwell time at $T_{\max}$	NH <sub>3</sub> while heating	NH <sub>3</sub> while cooling
<b>0-700(_NH<sub>3</sub>conc)</b>	PSZ+DCP	-	0-700 °C	-
<b>300-700(_NH<sub>3</sub>conc)</b>	PSZ+DCP	-	300-700 °C	-
<b>500-700(_NH<sub>3</sub>conc)</b>	PSZ+DCP	-	500-700 °C	-
<b>0-700-300(_NH<sub>3</sub>conc)</b>	PSZ+DCP	-	0-700 °C	700-300 °C
<b>700_1h(_NH<sub>3</sub>conc)</b>	PSZ+DCP	1 h	0-700 °C	-
<b>700_4h(_NH<sub>3</sub>conc)</b>	PSZ+DCP	4 h	0-700 °C	-

#### 10.6.3.1 Optical appearance

For the samples shown in Figure 137, no difference in optical appearance can be seen; all of the different variations with a maximum temperature at 700 °C are dark brown/almost black in color.

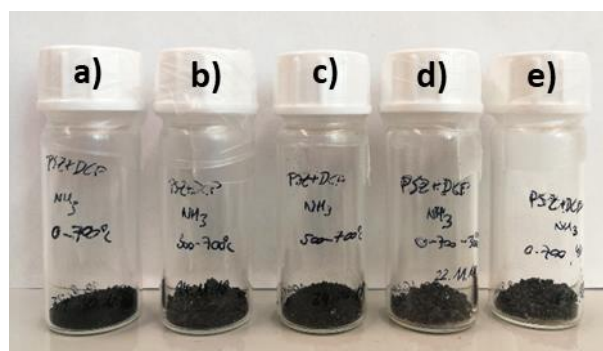


Figure 137: Sample images of the variations of the heating program with 700 °C as maximum temperature for PSZ; a) 0-700\_NH<sub>3</sub>conc b) 300-700\_NH<sub>3</sub>conc c) 500-700\_NH<sub>3</sub>conc d) 0-700-300\_NH<sub>3</sub>conc e) 0-700\_4h\_NH<sub>3</sub>conc.

### 10.6.3.2 Mass change

The mass change of the samples with varied versions of the heating program with 700 °C as maximum temperature is listed in Table 47, investigating the influence of varying dwell times and temperature regions using the reactive atmosphere. The atmosphere during the cooling period doesn't seem to have a significant impact on the mass loss. The low temperature region, in contrast, does; when changing the atmosphere to ammonia at 300 °C, the mass loss is ~2 % lower than when using ammonia during the whole heating period. Surprisingly, changing the atmosphere at 500 °C leads to a mass loss lower than for all other samples, even the one pyrolyzed in nitrogen. Due to the short time ammonia is used in this program, it was one of the first experiments done and therefore undergoing some problems with the neutralization of ammonia leading to a pressure increase inside the furnace, which could possibly explain the discrepancies with the other samples. The mass loss increases with increasing dwell time from 32 % with 0 h dwell time to 35 % with 4 h dwell time.

Table 47: Mass loss of the samples pyrolyzed using varying heating programs and atmospheres with a maximum pyrolysis temperature of 700 °C.

	$\Delta m_{\text{crossl.-pyro, \%}}$
PSZ700°C (N <sub>2</sub> )	-26.2
0-700_NH <sub>3</sub> conc	-32.2
300-700_NH <sub>3</sub> conc	-29.6
500-700_NH <sub>3</sub> conc	-19.9
0-700-300_NH <sub>3</sub> conc	-31.9
700_1h_NH <sub>3</sub> conc	-32.8
700_4h_NH <sub>3</sub> conc	-34.8

### 10.6.3.3 Elemental analysis

All elemental compositions of the samples pyrolyzed with varying heating programs up to 700 °C are shown in Figure 138.

The influence of the dwell time can be seen in the diagrams on the left side, each compared to the corresponding sample pyrolyzed in nitrogen. Regarding the nitrogen content, there is a slight trend of an increase of nitrogen with increasing dwell time noticeable. The carbon content

slightly decreases with increasing dwell time for PSZ. The influence of the temperature window in which ammonia is used as atmosphere shows that the cooling period doesn't change the elemental composition significantly. Starting the use of ammonia at 300 °C, however, increases the nitrogen content compared to starting at 500 °C as well as room temperature.

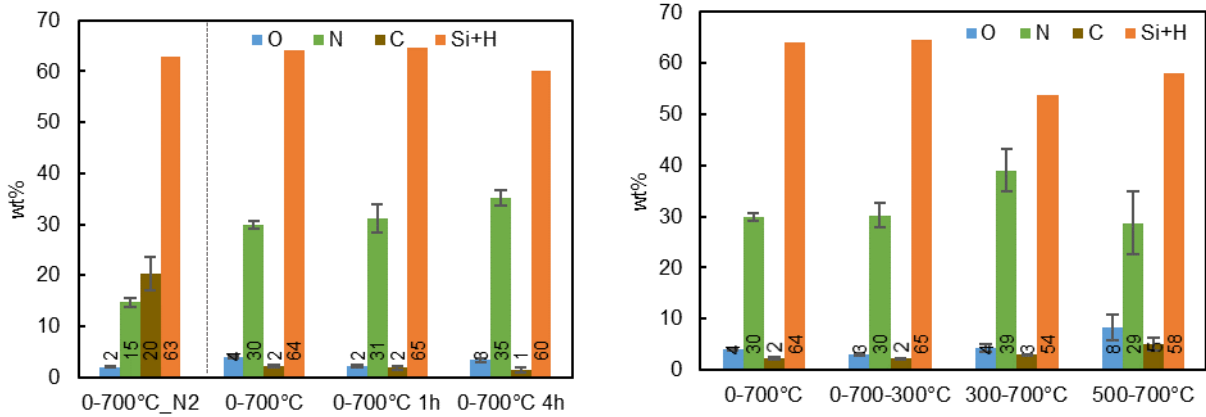


Figure 138: Elemental composition of PSZ after parameter variations during pyrolysis under concentrated ammonia with a maximum temperature of 700 °C; O, N, and C content are measured, Si+H is calculated as remainder to 100 wt%.

### 10.6.3.4 ATR-IR

As can be seen in Figure 139, the variations of the heating program only have a minor influence on the IR-spectra of the ceramics, since most of the curves are congruent. The two curves that are shifted are the ones where ammonia wasn't used as atmosphere during the whole heating part of the pyrolysis (300-700\_NH3conc and 500-700\_NH3conc) and are also the samples that show slightly different results in elemental composition and a different mass change.

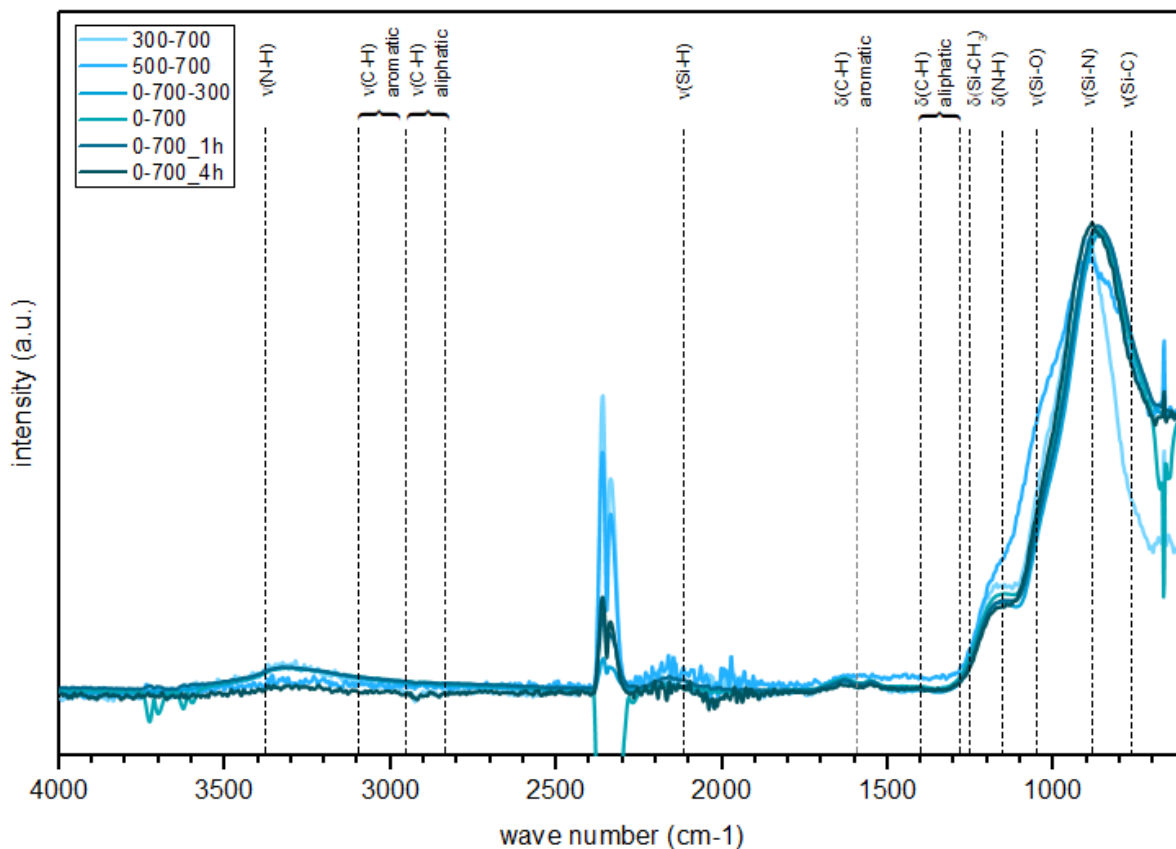


Figure 139: ATR-IR spectra of PSZ after parameter variations during pyrolysis under concentrated ammonia with a maximum temperature of 700 °C.



### 10.6.3.5 Conclusions

Various experiments were conducted using the same maximum pyrolysis temperature but different dwell times or temperature windows during which the reactive atmosphere was used, to find the shortest temperature program with the minimum usage of ammonia.

The dwell time at 700° C seems to have a minor effect on the properties.

The atmosphere during the cooling period has no influence on the resulting ceramics, the dwell time has only a minor influence. The heating rate is apparently low enough to enable the reactions of ammonia with the sample already during the heating period.

Although the influence of the low temperature region is only of minor extent, the reactive atmosphere was – for all following experiments – already used from room temperature on, because it is easier to provide a reproducible process if the atmosphere can be adjusted before starting the program.

The pyrolysis program for the following experiments was therefore set with the following parameters:

- 3K/min up to 300 °C
- 1K/min up to the maximum temperature
- No dwell time at the maximum temperature
- 3K/min cooling to room temperature
- Ammonia during the heating period, nitrogen during the cooling period

### 10.6.4 Pyrolysis in concentrated ammonia during the heating period

Experiments with PSZ, PCS and PSZPCS in concentrated ammonia were conducted up to maximum temperatures between 500-900 °C. The cooling period was carried out in nitrogen. The heating program results from the previous experiments and can be seen in section 10.6.3.5.

#### 10.6.4.1 Optical appearance

When comparing the sample images in Figure 140, samples pyrolyzed in ammonia show lighter versions of the colors than samples pyrolyzed in nitrogen, which can best be seen up to 600 °C. A possible explanation could be the reduced carbon content of the samples due to the reactive atmosphere, as confirmed by elemental analysis (see next section).

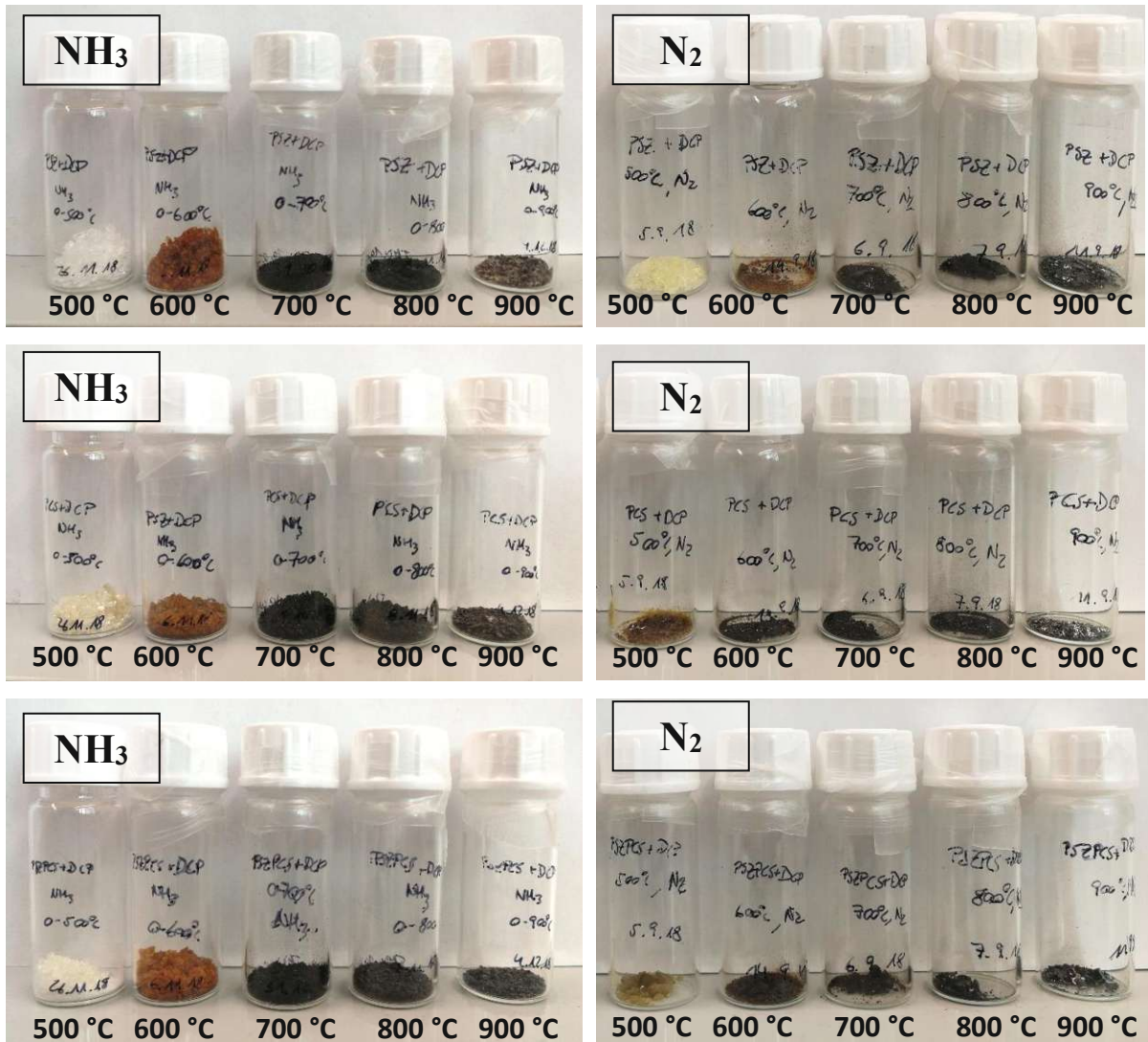


Figure 140: Sample images of PSZ (top), PCS (middle) and PSZPCS (bottom) for pyrolysis temperatures from 500-900 °C (f.l.t.r.) under concentrated ammonia (left) or nitrogen (right).

### 10.6.4.2 Ceramic yield

The ceramic yield of the samples is shown in Figure 141.

When comparing the dashed lines ( $\text{NH}_3$ ) with the values for pyrolysis under nitrogen, one can see that the trends are not the same for the three materials. While the mass loss for PSZ and PSZPCS is higher if ammonia is used as pyrolysis atmosphere, there is almost no difference between the two atmospheres for PCS, with the two lines crossing twice. All three materials show a value that doesn't fit in the trend of the other temperatures at a pyrolysis temperature of 800 °C, which could result from a change in atmosphere that wasn't as precise as for the other samples or possibly from a temporarily reduced flow through a partially blocked pipe.

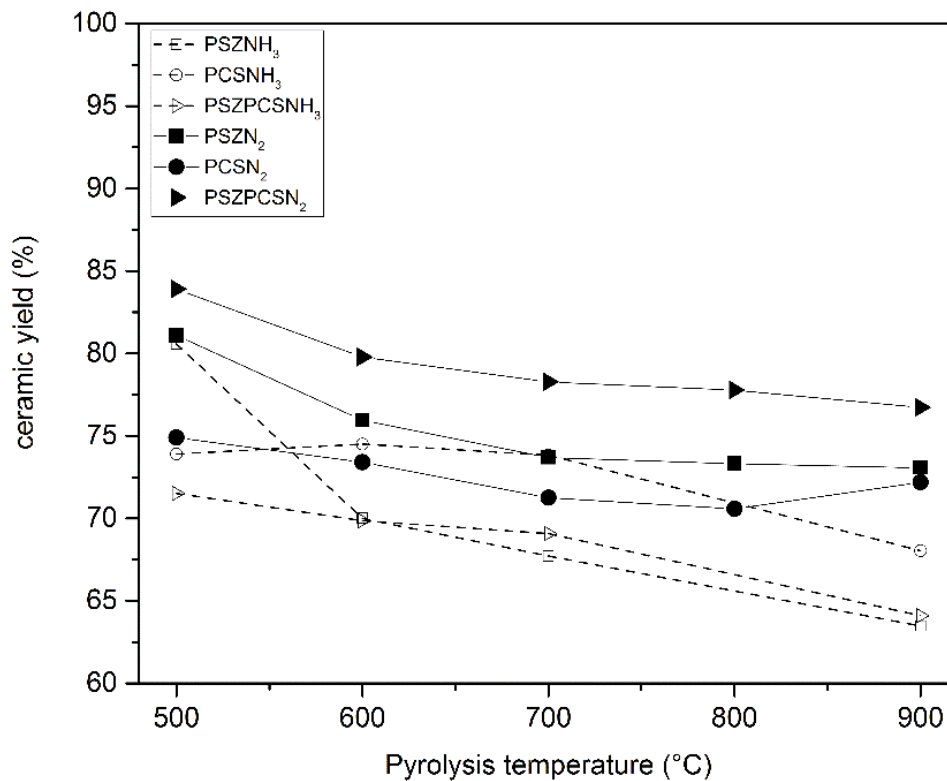


Figure 141: Ceramic yield of PSZ, PCS and PSZPCS pyrolyzed under concentrated ammonia or under nitrogen after pyrolysis at temperatures from 500-900 °C.

### 10.6.4.3 Elemental composition

The elemental composition of the samples pyrolyzed in ammonia is compared to the corresponding samples pyrolyzed in nitrogen in Figure 142, Figure 143 and Figure 144.

While the compositions of the two **PSZ** samples are similar at 500 °C, the values at 600 °C differ strongly. The carbon content decreases to half the value of the sample pyrolyzed in nitrogen with <10 wt% compared to 20 wt%, respectively. The difference in carbon content becomes more drastic with increasing pyrolysis temperature, since the carbon content for the samples pyrolyzed in nitrogen stays approximately constant with ~20 wt%, whereas the carbon content in samples pyrolyzed in ammonia constantly decreases to ~1 wt%. The nitrogen content in the samples increases to ~30 wt% if ammonia is used as pyrolysis atmosphere when compared to the constant value of ~16 wt% for the nitrogen samples. At first sight, it looks as if the nitrogen content is increasing due to carbon removal. Therefore, the nitrogen content was calculated by using the composition of the samples pyrolyzed in nitrogen and setting the carbon content to zero. The calculated value for e.g. 500 °C is 21 %, which is way below the measured value of 30 wt%. Therefore, either nitrogen is incorporated due to the reactive atmosphere or silicon/hydrogen are removed to a higher extent than in the inert nitrogen atmosphere.

For **PCS**, the composition already differs at 500 °C. The nitrogen content, which is almost zero if pyrolysis is conducted in nitrogen atmosphere, increases to 10 wt% at 500 °C and then further to 20 wt% and even 25 wt% at the highest tested temperatures in ammonia. This is almost as high as the nitrogen content of PSZ, although there was no nitrogen in the starting material. This also strengthens the assumption that additional nitrogen is incorporated in PSZ during pyrolysis in ammonia. Also, as for PSZ, the carbon content decreases strongly which can be seen from the results starting at 600 °C, where instead of ~30 wt% for the nitrogen samples, there are only ~20 wt% carbon in the samples pyrolyzed in ammonia and the content decreases further to less than 10 wt% at a pyrolysis temperature of 900 °C.

The influence of the pyrolysis atmosphere on the elemental composition of **PSZPCS** is similar to the other two starting materials. With rising pyrolysis temperature, the nitrogen content increases, while the carbon content decreases. The carbon content reaches almost zero at the maximum pyrolysis temperature of 900 °C (c.f. ~0 wt% for PSZ, ~8 wt% for PCS).

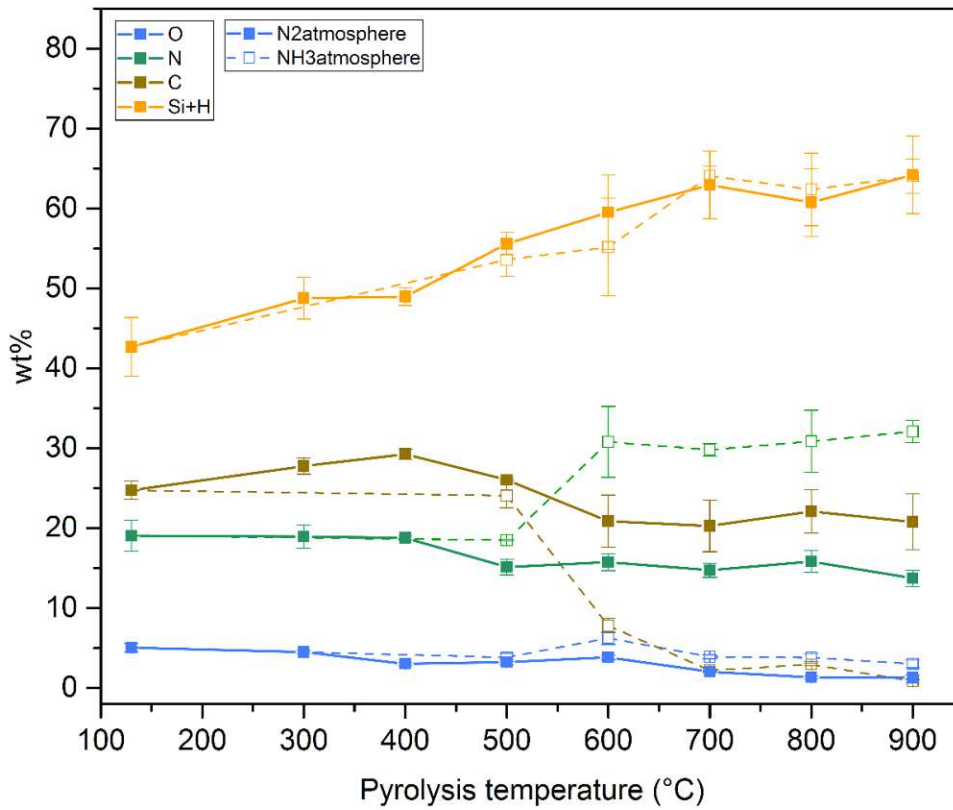


Figure 142: Elemental composition of PSZ after pyrolysis under concentrated ammonia or nitrogen up to maximum temperatures between 500-900°C; O, N, and C content are measured, Si+H is calculated as remainder to 100 wt%.

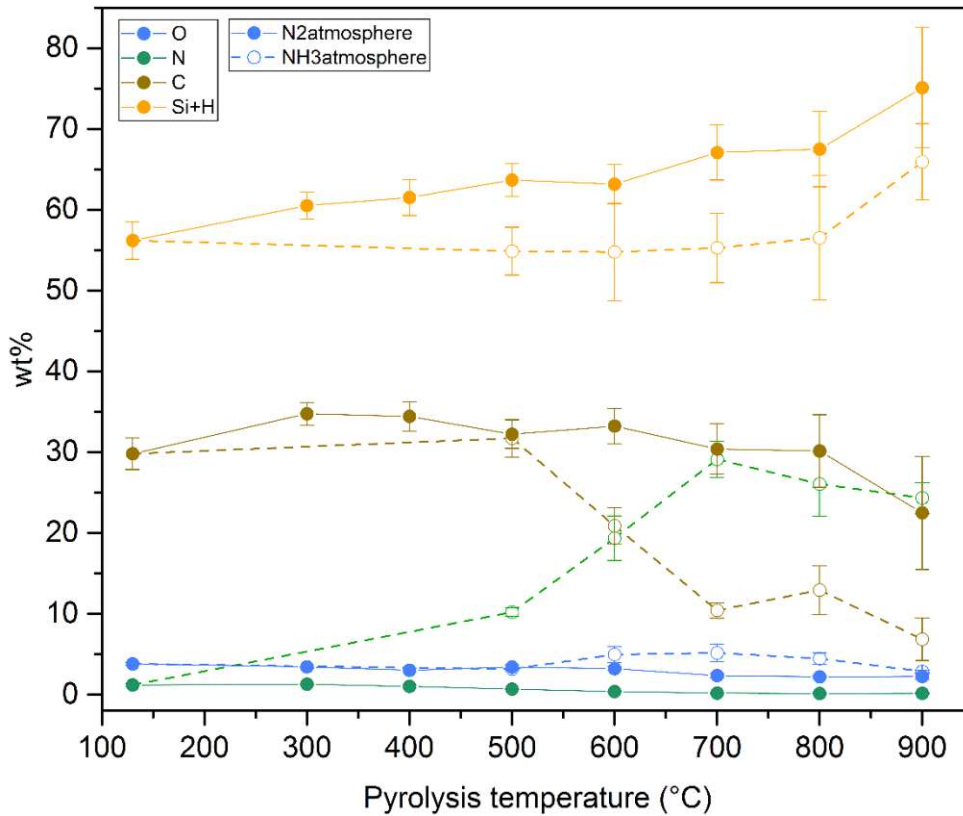


Figure 143: Elemental composition of PCS after pyrolysis under concentrated ammonia or nitrogen up to maximum temperatures between 500-900°C; O, N, and C content are measured, Si+H is calculated as remainder to 100 wt%.



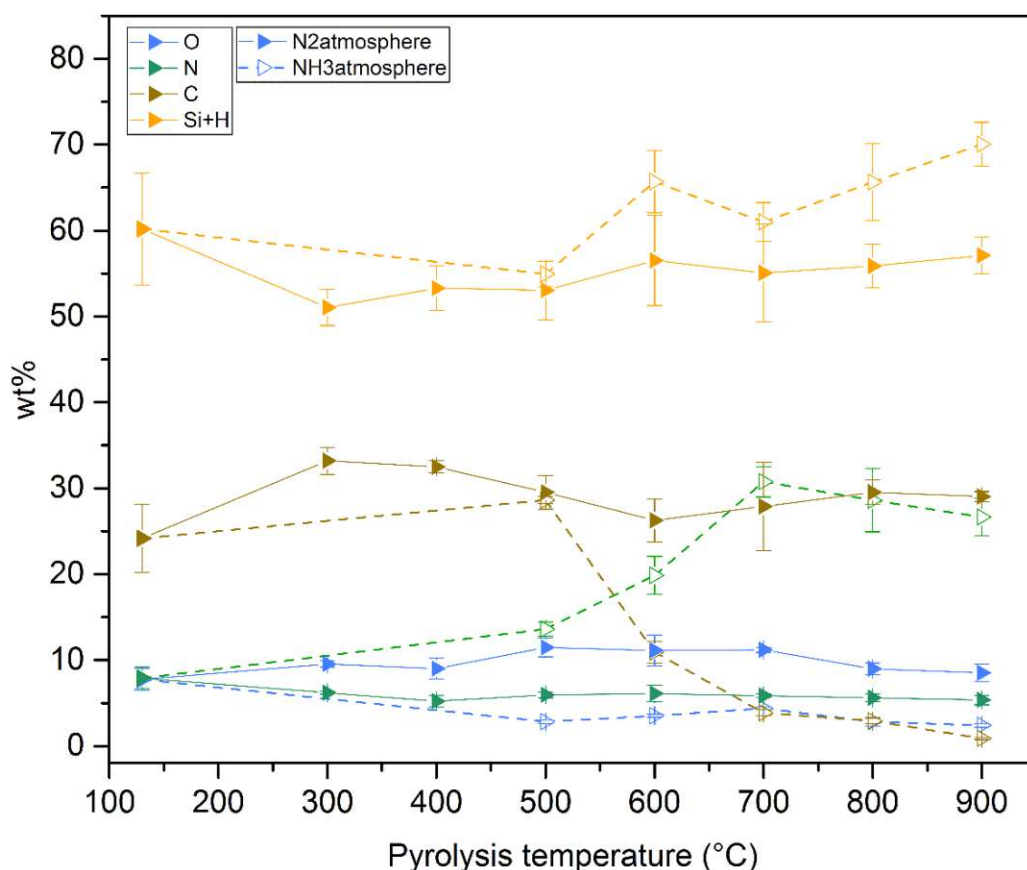


Figure 144: Elemental composition of PSZPCS after pyrolysis under concentrated ammonia or nitrogen up to maximum temperatures between 500-900°C; O, N, and C content are measured, Si+H is calculated as remainder to 100 wt%.

#### 10.6.4.4 ATR-IR

The spectra for **PSZ** pyrolyzed up to temperatures of 500-900 °C in ammonia or nitrogen are shown in Figure 145, with the green spectra showing the results with ammonia as pyrolysis atmosphere and the blue versions the corresponding results for nitrogen. The main differences can be found in the finger print region below 1500  $\text{cm}^{-1}$ , especially around 1150  $\text{cm}^{-1}$ , where the N-H signals are located. At 500 °C it looks as if there were still N-H groups left in the sample pyrolyzed in ammonia, according to the shape of the band. For the other samples starting with the one at 600 °C, the band is shaped as for the samples pyrolyzed with nitrogen as atmosphere, but with a higher intensity relative to the main signal. A reason could be that the signal is now caused by C-N bonds.

The results for **PCS** are shown in Figure 146. The difference between the samples pyrolyzed using ammonia as atmosphere and the ones using nitrogen are clearly visible, with the differences becoming more obvious at higher temperatures. At 500 °C, the major difference is the shoulder at 1150  $\text{cm}^{-1}$  that can also be found for the spectra of PSZ and is related to N-

containing bonds, either N-H bonds at lower temperatures and C-N bonds at higher temperatures. Since the shape of the signals changed, it is more likely that they are caused by C-N bonds. At 600 °C, the intensity of that shoulder increases to the level of the PSZ samples. The main signal changes shape, the maximum at 1000  $\text{cm}^{-1}$  increases in relation to the one at 800  $\text{cm}^{-1}$ . With a further increase in temperature, the maximum shifts to higher wave numbers, which can be attributed to the decreasing carbon content and the increasing nitrogen content (see previous section). Surprisingly, the maximum is located at higher wavenumbers than the same sample with PSZ as starting material and at higher wave numbers than the expected Si-N signal.

The spectra of **PSZPCS** are shown in Figure 147. Again, there is a signal around 1050  $\text{cm}^{-1}$  for the samples pyrolyzed in ammonia, which is not present in the samples pyrolyzed in nitrogen. The maximum of the main signal shifts to higher wave numbers, which is the same trend as for the PCS samples.

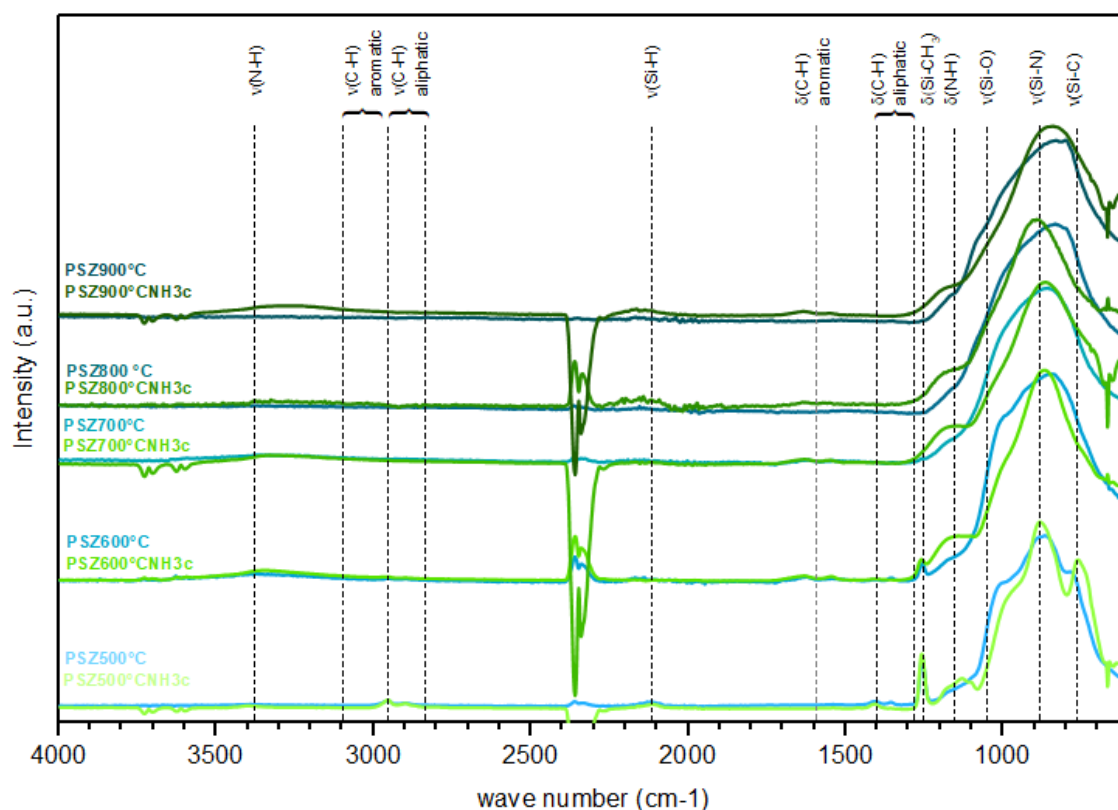


Figure 145: ATR-IR spectra of PSZ after pyrolysis under concentrated ammonia or nitrogen up to maximum temperatures between 500-900°C.

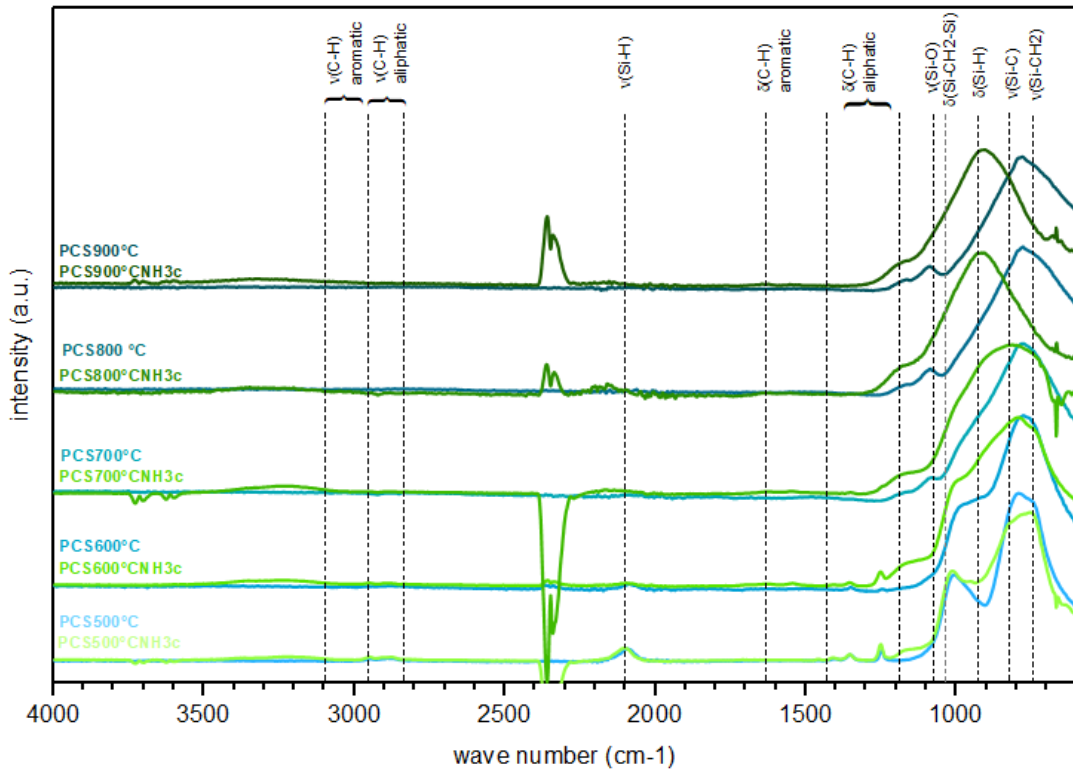


Figure 146: ATR-IR spectra of PCS after pyrolysis under concentrated ammonia or nitrogen up to maximum temperatures between 500-900°C.

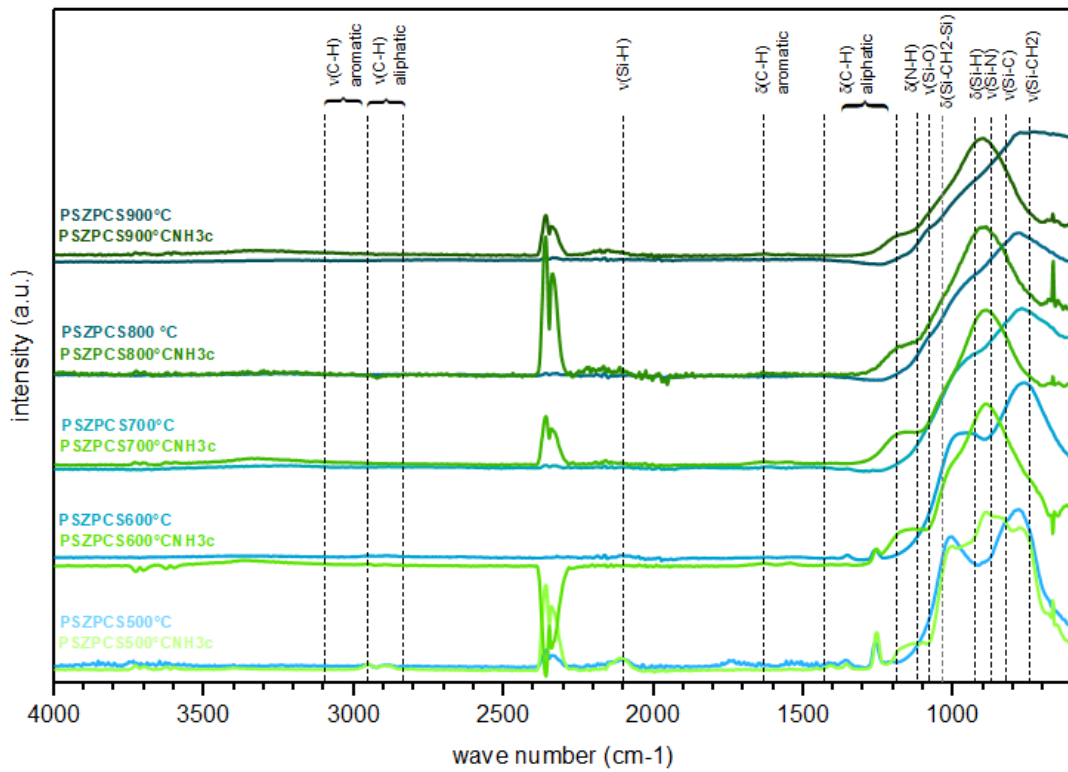


Figure 147: ATR-IR spectra of PSZPCS after pyrolysis under concentrated ammonia or nitrogen up to maximum temperatures between 500-900°C.



#### 10.6.4.5 N<sub>2</sub>-Physisorption

The results of the gas sorption investigations with the samples pyrolyzed using concentrated ammonia are summarized in Table 48. For easier comparison, the results of the samples pyrolyzed using nitrogen atmosphere for the whole pyrolysis are listed, too.

The isotherms of **PSZ** pyrolyzed using ammonia are shown in Figure 148, the corresponding PSDs in Figure 149. Even up to temperatures of 900 °C, the isotherms are all of type I and the materials therefore microporous. The reactive atmosphere apparently has a stabilizing effect on the ceramics. In addition, the specific surface areas calculated using the BET method are all around 200 m<sup>2</sup>/g or above for the sample with the highest porosity (pyrolyzed at 500°C). Against the expectation, the pore size decreases when using the reactive atmosphere instead of nitrogen, although it is expected to remove the carbon (which is proven by the elemental analysis) and the logical consequence would be an increase in pore size. Since not only carbon is removed by the ammonolysis, but - according to the elemental composition - also nitrogen integrated in the network, this change in composition could be a possible explanation for the decrease in pore size, since the composition of the micropore forming entities is changed, which is similar to the findings during the crosslinking studies with hydrosilylation using DVB as linker. Another interesting phenomenon is, that the pore size distribution for most of the samples shows one main maximum, but reaching the highest pyrolysis temperature – 900°C – there is a second maximum at higher pore size visible. This could possibly be explained by the further removal of carbon that was initially expected to increase the pore size but seems to be compensated by the nitrogen integration.

The use of a reactive atmosphere also has a drastic effect on the ceramics resulting from the two other starting materials, **PCS** and **PSZPCS**. While both are nonporous according to the physisorption investigations if pyrolyzed under nitrogen, both materials turn out to be microporous if ammonia is used as reactive atmosphere at the same pyrolysis temperature. The isotherms and corresponding PSDs are shown in Figure 150 and Figure 151 at 600 °C and in Figure 152 and Figure 153 at 900 °C.

Table 48: Type of isotherm, BET specific surface area ( $S_{BET}$ ), maximum of the pore size distribution ( $PSD_{max}$ ) and micropore volume ( $V_{micro}$ ) of PSZ crosslinked with different amounts of DVB as linker or using DCP.

	Isotherm	$S_{BET}$ (m <sup>2</sup> /g)	$PSD_{max}$ (nm)	$V_{micro}$ (cm <sup>3</sup> /g)	Comment
<b>PSZ400°C</b>	Type II/ VI	63 ± 1	1.13	-	Macro- or nonporous
<b>PSZ500°C</b>	Type I	350 ± 16	0.88	0.17	Microporous
<b>PSZ600°C</b>	Type I	195 ± 6	0.84	0.10	Microporous
<b>PSZ700°C</b>	Type VI	5 ± 0.5	-	-	Macro- or nonporous
<b>PCS600°C</b>	Type VI	29 ± 1	-	-	Micro- and mesoporous
<b>PSZPCS600°C</b>	Type I/II	20 ± 1	1.10	0.01	Micro- /nonporous
<b>PSZ500°CNH<sub>3</sub>c</b>	Type I	385 ± 17	0.90	-	Microporous
<b>PSZ600°CNH<sub>3</sub>c</b>	Type I	271 ± 14	0.70	0.13	Microporous
<b>PSZ700°CNH<sub>3</sub>c</b>	Type I	208 ± 12	0.67	0.11	Microporous
<b>PSZ800°CNH<sub>3</sub>c</b>	just BET	210 ± 8	-	-	Microporous
<b>PSZ900°CNH<sub>3</sub>c</b>	Type I	186 ± 10	0.62, 0.93	0.10	Microporous
<b>PCS600°CNH<sub>3</sub>c</b>	Type I	119 ± 1	0.76	0.10	Microporous
<b>PSZPCS600°CNH<sub>3</sub>c</b>	Type I	243 ± 8	0.67	0.10	Microporous
<b>PCS900°CNH<sub>3</sub>c</b>	Type I	158 ± 8	0.64, 0.95	0.10	Microporous
<b>PSZPCS900°CNH<sub>3</sub>c</b>	Type I	215 ± 11	0.62, 0.93	0.11	Microporous

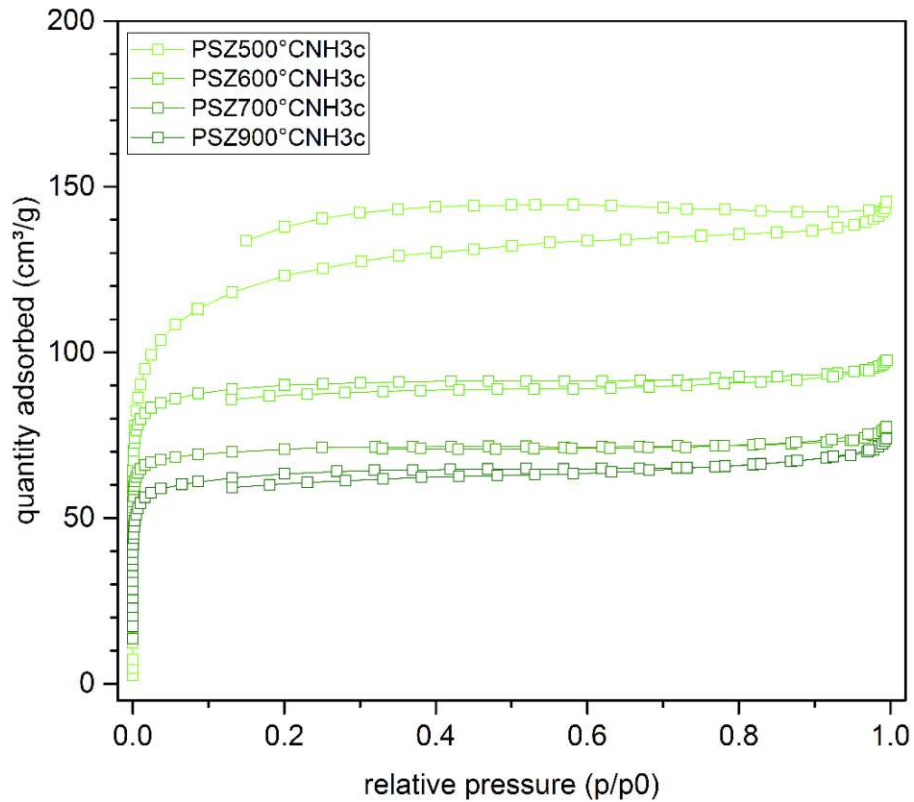


Figure 148:  $N_2$  physisorption isotherms of PSZ after pyrolysis at temperatures between 500-900°C using concentrated ammonia as atmosphere during the heating period.

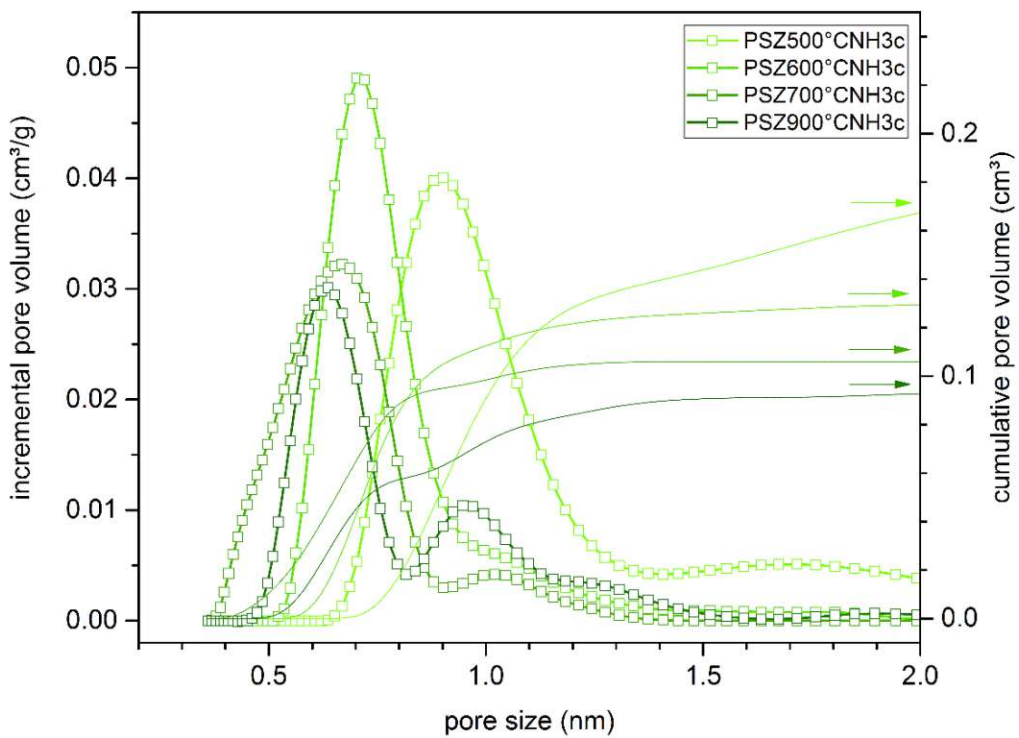


Figure 149: PSDs of PSZ after pyrolysis at temperatures from 500-900°C using concentrated ammonia as atmosphere during the heating period, calculated from the  $N_2$  physisorption data using NL-DFT.

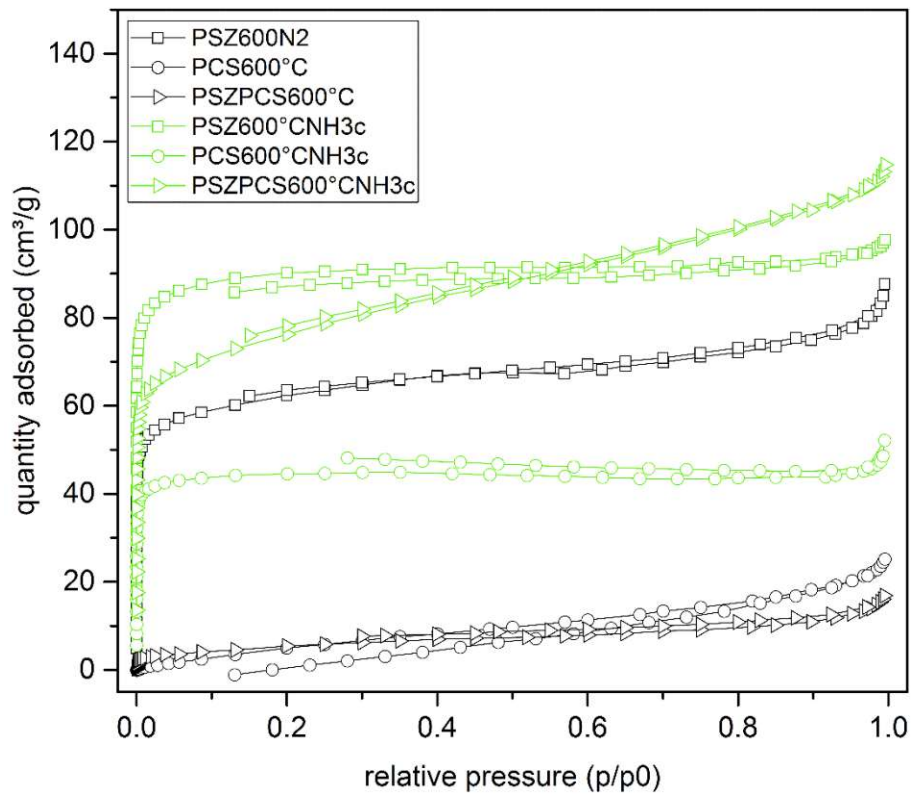


Figure 150:  $N_2$  physisorption isotherms of PSZ, PCS and PSZPCS after pyrolysis at  $600^\circ\text{C}$  using concentrated ammonia or nitrogen as atmosphere during the heating period.

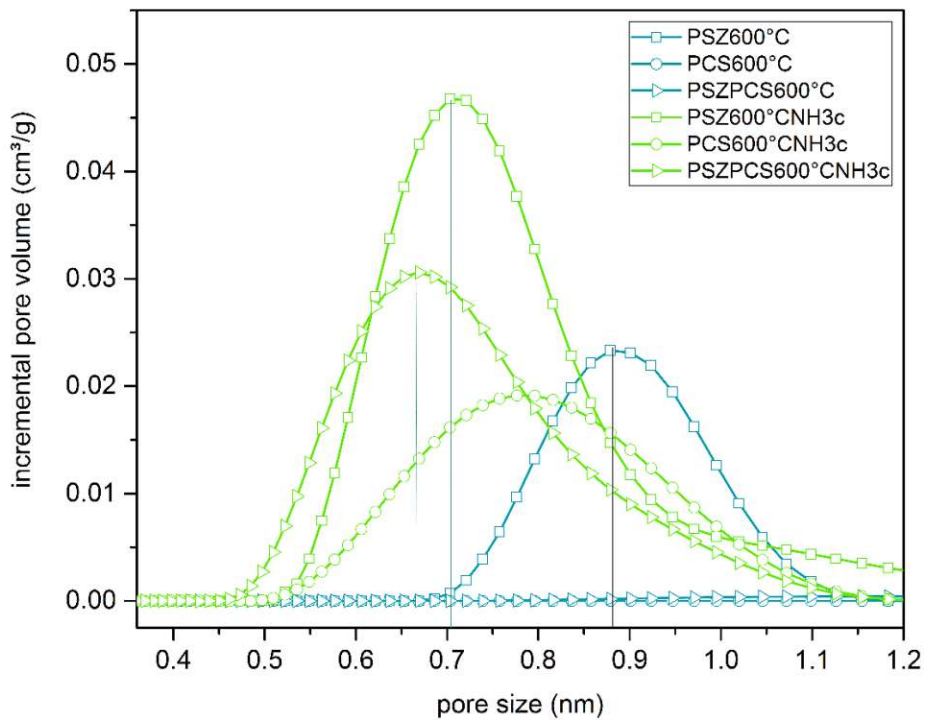


Figure 151: PSDs of PSZ, PCS and PSZPCS after pyrolysis at  $600^\circ\text{C}$  using concentrated ammonia or nitrogen as atmosphere during the heating period, calculated from the  $N_2$  physisorption data using NL-DFT.

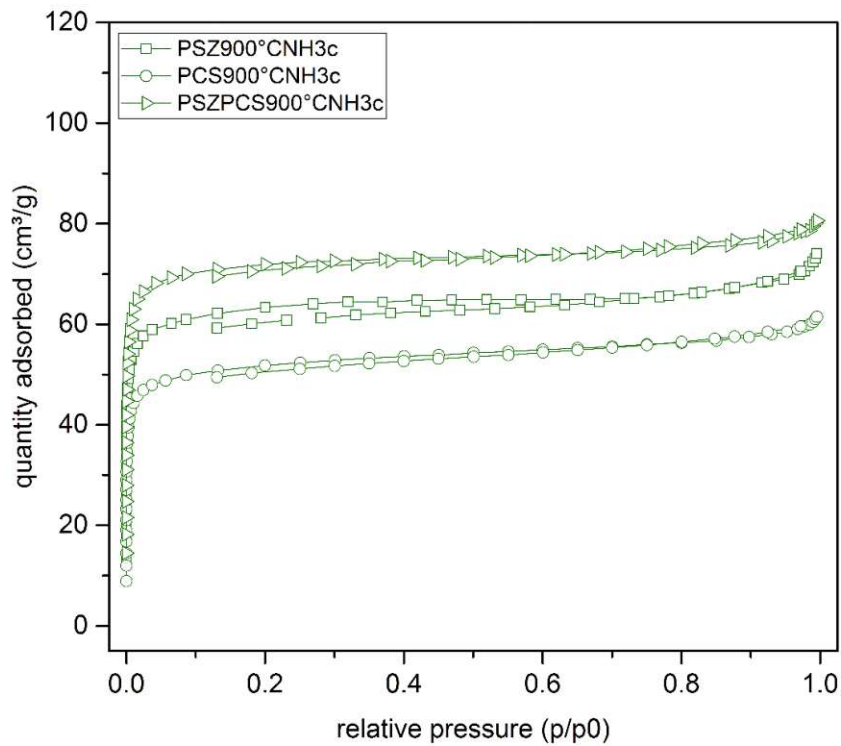


Figure 152:  $N_2$  physisorption isotherms of PSZ, PCS and PSZPCS after pyrolysis at  $900^\circ\text{C}$  using concentrated ammonia as atmosphere during the heating period..

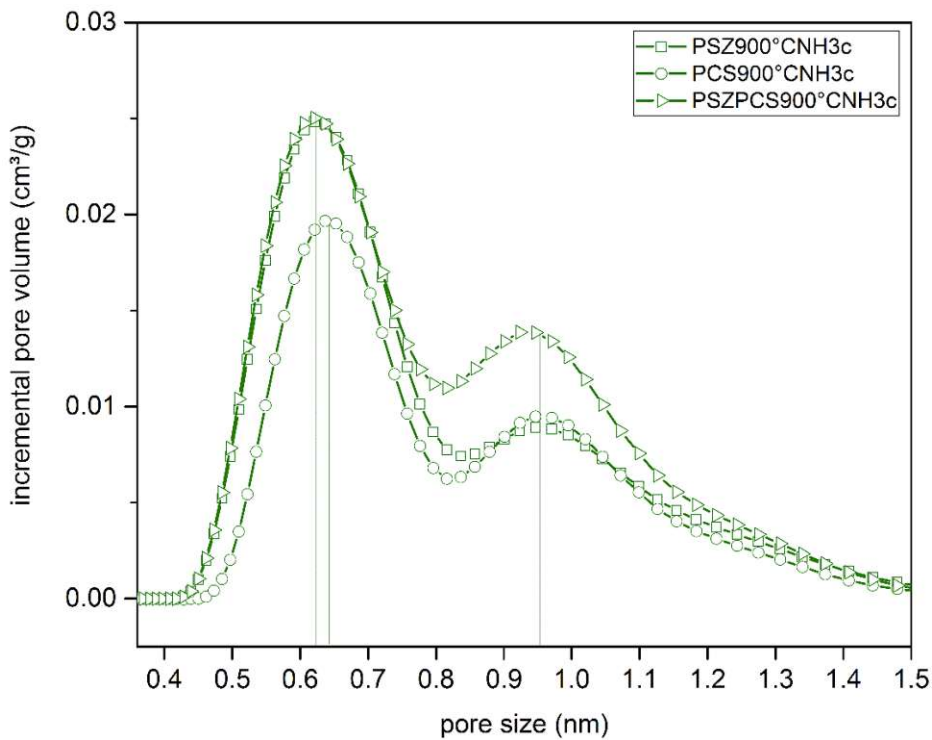


Figure 153: PSDs of PSZ, PCS and PSZPCS after pyrolysis at  $900^\circ\text{C}$  using concentrated ammonia as atmosphere during the heating period, calculated from the  $N_2$  physisorption data using NL-DFT.

## 10.6.5 Pair distribution function investigations

The PDF method is used in this work, because the pyrolysis experiments with concentrated ammonia showed that - independent of the starting precursor composition - similar micropore sizes were found after pyrolysis at 900 °C. This was accompanied by a converging elemental composition of the three samples PSZ, PCS and PSZPCS with increasing pyrolysis temperature in ammonia. To control if the interatomic distances are really similar in the samples, PDF was chosen to investigate the samples. The pair distribution function  $G(r)$  describes the probability of finding two atoms separated by a distance  $r$ . Since the method does not presume a periodicity in the material, it is a great method to investigate structural features in amorphous materials. Since pyrolysis temperatures in this work are below the crystallization temperatures of the PDCs, standard XRD measurements would not be successful.

### 10.6.5.1 Experimental procedure

For amorphous solids, traditional X-ray based structure analysis does not give much information. PDF analysis of these data helps to reveal the short range order by determining average distances between the nearest neighbouring atoms. Since fitting is difficult for the results of amorphous samples, the values have to be taken with care and are rather used for comparison of samples under each other than for evaluation of absolute values.

The samples that were investigated are listed in Table 49.

They were ground to a fine powder and filled in a polyimide capillary with 1 mm diameter (Cole-Parmer, 12" long, cut in shorter pieces) till approximately 2 cm of the capillary were filled with close packed sample. The capillaries were then sealed with a two-component glue on both sides. One empty capillary was used for the background measurement.

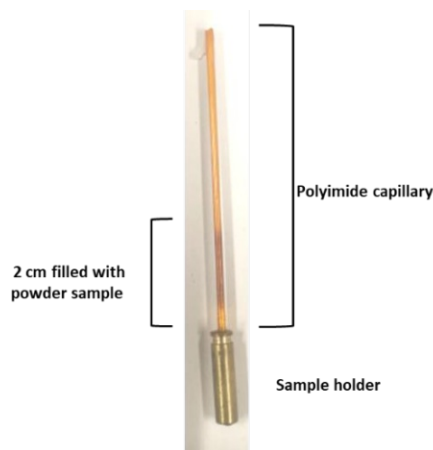


Figure 154: Sample preparation for the PDF investigations.



Table 49: Maximum of the PSD and elemental composition of the samples that were investigated using PDF.

	PSD <sub>max</sub> (nm)	Comment	O (wt%)	N (wt%)	C (wt%)	Si+H (wt%)
<b>PSZ900°C</b>	-	Nonporous	1 ± 0	14 ± 1	21 ± 4	64 ± 5
<b>PSZ600°CNH<sub>3</sub>c</b>	0.70	Microporous	6 ± 1	31 ± 4	8 ± 1	55 ± 6
<b>PSZ900°CNH<sub>3</sub>c</b>	0.62, 0.93	Microporous	3 ± 0	32 ± 1	1 ± 0	64 ± 1
<b>PCS900°CNH<sub>3</sub>c</b>	0.64, 0.95	Microporous	3 ± 1	24 ± 2	7 ± 3	66 ± 6
<b>PSZPCS900°CNH<sub>3</sub>c</b>	0.62, 0.93	Microporous	2 ± 0	27 ± 2	1 ± 0	70 ± 2

X-ray diffraction measurements were performed on a PANalytical X'Pert PRO MPD system. An X-ray tube with a silver anode was used as X-ray source, delivering Ag K $\alpha$  radiation with a wavelength of 0.0561 nm. Scans along the 2 $\theta$  axis were made up to an angle of 160 degrees corresponding to a scattering vector Q of 22 Å<sup>-1</sup>.

The typical steps after performing the total Xray diffraction measurement are:

- Background correction (using an empty capillary), correction of Compton scattering, detector dead-time, absorption, diffraction geometry and polarization
- The corrected X-ray diffraction data is scaled into electron units and the reduced structure function is calculated
- The structure function is Fourier transformed into the atomic pair distribution function:  $G(r) = 4\pi r (\rho(r) - \rho_0)$  with  $\rho(r)$  being the local atom number density, and  $\rho_0$  being the mean atom number density.

### 10.6.5.2 Results

A total X-ray study was performed to find out more about the atomic distances in selected samples. Still, reference values for interesting atomic distances are given in Table 50 as rough interpretation guideline, which were taken from Schitco et al. [15].

The results of the pair correlation functions for PSZ600NH<sub>3</sub>c and PSZ900NH<sub>3</sub>c are given in Figure 155. These two are compared to check if the interatomic distances differ at higher pyrolysis temperatures. Two main maxima were found at 1.65 Å and 3.07 Å for the sample pyrolyzed in ammonia at 600°C. 3.07 Å is a typical value for Si-Si bonds, 1.65 Å are close to the interatomic distance of Si-N. Still, they are slightly shifted to lower radii. A possible explanation is that at 600 °C, there's still hydrogen present in the sample (forming mixed Si-N-H species), which can influence the strength of the Si-N interaction and therefore the

interatomic distance. The maxima for PSZ pyrolyzed in ammonia at 900°C are slightly shifted. The smaller radius is at 1.68 Å, which is again in the region of Si-N distances, but probably with less contribution of other elements, since polymer-ceramic conversion is in a progressed stage at 900°C. The second radius is now at 2.97 Å. A possible reason for the shift is that - according to elemental analysis – nitrogen is incorporated in the sample. This could influence the composition of the structural elements in sample and therefore influence the interatomic distances. Overall, the change from 600°C to 900°C in concentrated ammonia is minor.

The results for a nonporous sample, PSZ900°C, compared to a microporous sample PSZ900NH3c are shown in Figure 156. The sample pyrolyzed under nitrogen shows the same Si-Si distances as the sample pyrolyzed under ammonia, but the second main radius is shifted to higher distances with 1.78 Å. Since this value lies between the values of Si-N and Si-C distances, it could result from mixed Si-C-N species, which is reasonable, since carbon is still present in the sample if an inert atmosphere is used. Regarding these investigations, the main difference between the microporous sample and the nonporous sample is the presence/absence of carbon.

The three different materials PSZ, PCS and PSZPCS had a comparable elemental composition and a similar pore size distribution after pyrolysis at 900 °C in concentrated ammonia. The results for these three samples are shown in Figure 157. All three samples show the exact same maxima of the pair correlation function at 1.68 Å and 2.97 Å. By using a reactive atmosphere, the elemental composition of different starting materials can be adjusted and consequently also the interatomic distances in the materials. This could in further consequence confirm that the elemental composition of the micropore forming entities is determining the pore size.

Table 50: Typical values for the interatomic distances of relevant atom-pairs taken from [15]

Atom- pair	Interatomic distance Å
Si-N	1.72
Si-C	1.88
Si-O	1.59
Si-Si	3.07
Si-H	1.5



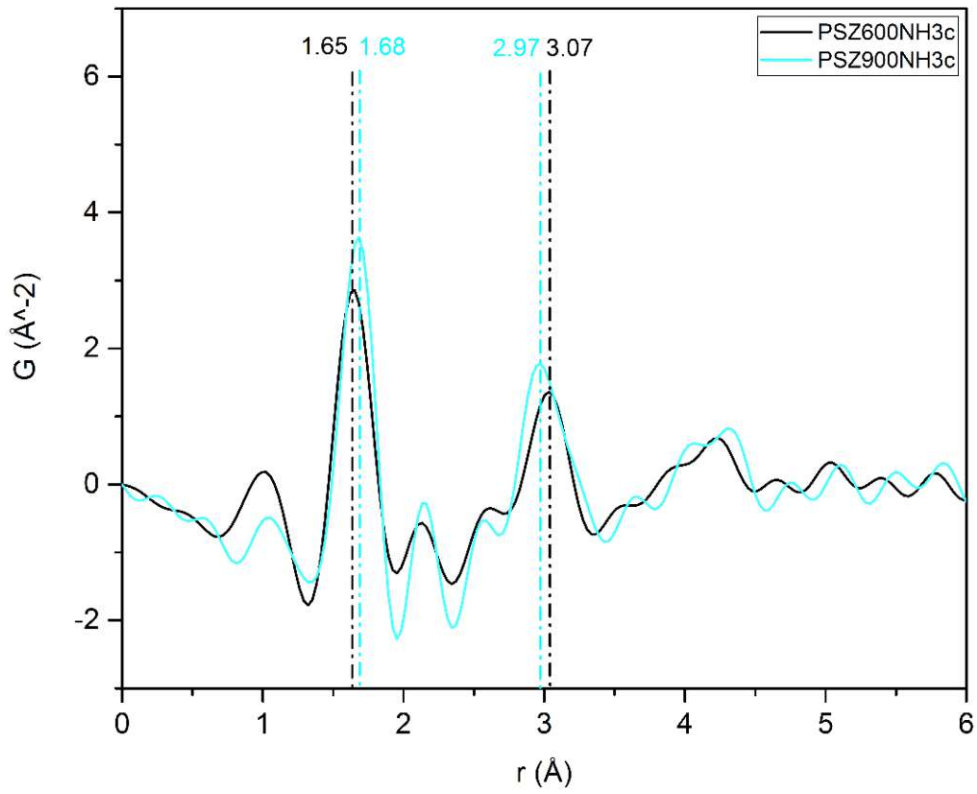


Figure 155: The total X-ray pair correlation functions ( $G(r)$ ) of PSZ after pyrolysis at 600 °C or 900 °C under concentrated ammonia.

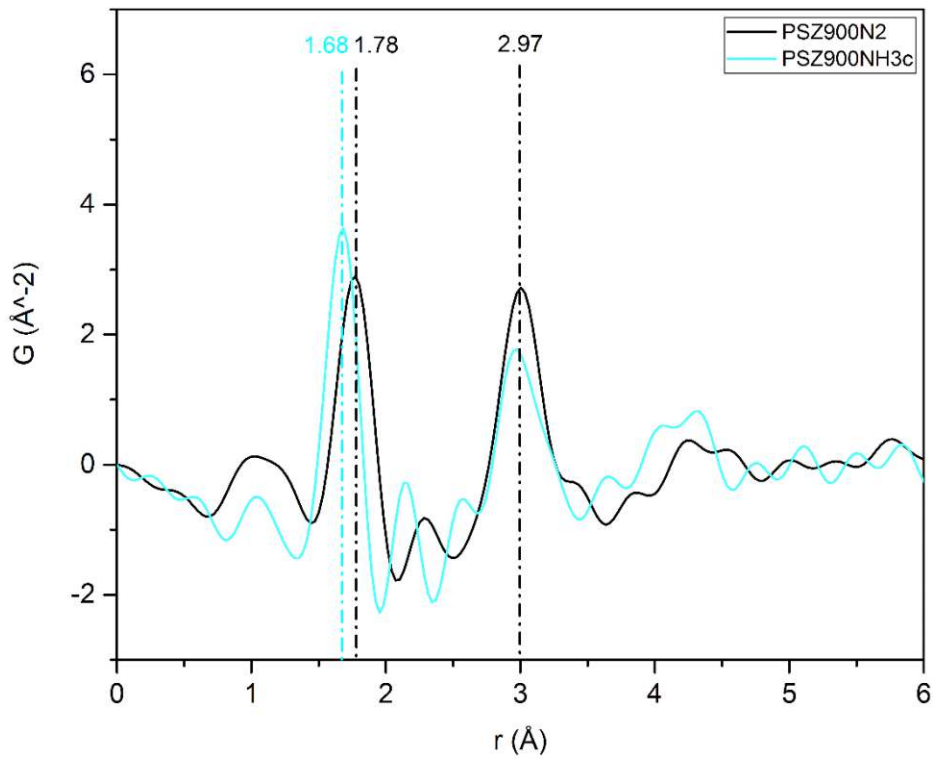


Figure 156: The total X-ray pair correlation functions ( $G(r)$ ) of PSZ after pyrolysis at 900 °C under nitrogen or concentrated ammonia.

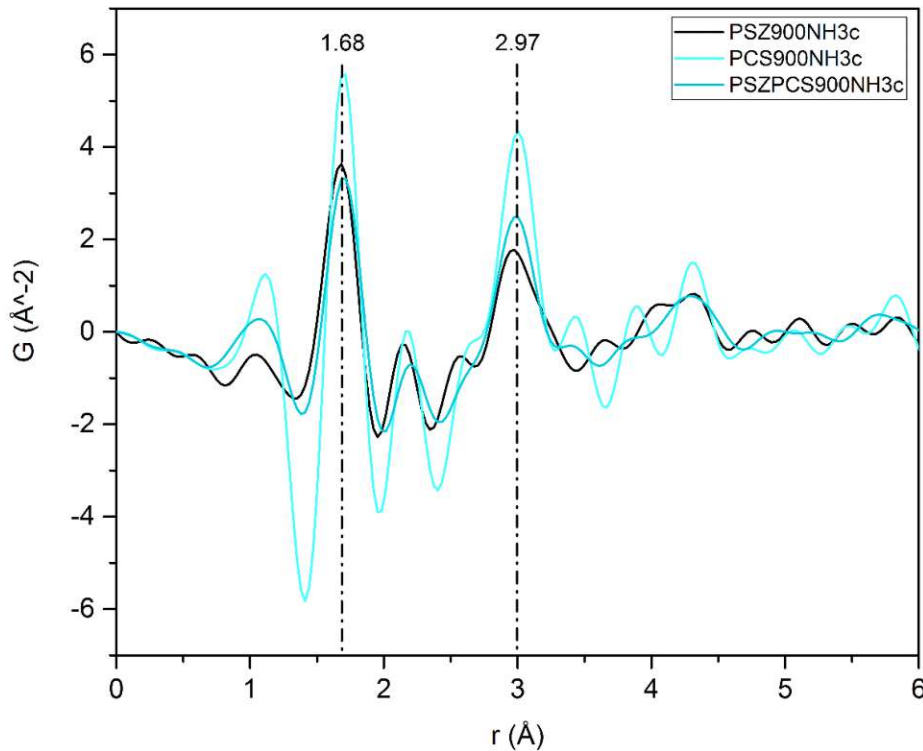


Figure 157: The total X-ray pair correlation functions ( $G(r)$ ) of PSZ, PCS and PSZPCS after pyrolysis at 900 °C under concentrated ammonia.

## 10.7 Conclusions - Pyrolysis in concentrated ammonia

The use of the concentrated reactive ammonia atmosphere has a drastic effect on the properties of the resulting ceramics, both in terms of elemental composition and structural elements present in the ceramic, with corresponding change of pore size and stability region of the pores.

It was found that carbon removal starts at temperatures around 500 °C and continues up to the maximum temperature of 900 °C investigated in this work. Simultaneously, the nitrogen content increases significantly. This incorporation of nitrogen already starts in the low temperature region for PCS and PSZPCS. This leads to the phenomenon that although the three materials have a different starting composition, the composition converges step by step, until at 900 °C the elemental composition is almost the same for the three materials.

The higher nitrogen and lower carbon content of the samples is also visible in the IR spectra, showing a shift of the broad maximum to higher wavenumbers, which is attributed most likely to Si-N bonds.

In contrast to pyrolysis in inert atmosphere, all materials are microporous in the investigated temperature region up to 900 °C (e.g. for PSZ, the micropores collapse above 600 °C in nitrogen

atmosphere). For PCS and PSZPCS the influence is even stronger, since both appear nonporous after pyrolysis at 600 °C in nitrogen and are microporous if ammonia is used as pyrolysis atmosphere even up to 900 °C.

This is a strong indication that the hypothesis of micropore forming entities, whose composition is responsible for pore size and stability, is true.

Another interesting finding is that the pore size distribution becomes bimodal at 900 °C in ammonia. The lower value ( $\sim 0.65$  nm) is lying below the pore size of the samples pyrolyzed at 600 °C (in both atmospheres), which could be caused by shrinkage of the pores due to e.g. viscous flow. This is strengthened by the specific surface area decrease of PSZ when going from 600 °C to 900 °C. For PCS, the specific surface area increases with increasing pyrolysis temperature, which could be explained by further carbon removal, which takes place up to that temperature while the carbon content was already completely removed for PSZ at temperatures around 700 °C. The second pore size maximum is most likely caused by carbon removal, leading to an increase of pore size.

PDF investigations were conducted to obtain information about the interatomic distances present in selected samples. When comparing two microporous PSZ samples prepared at pyrolysis temperatures of 600 °C and 900 °C in ammonia, there is a little change in the interatomic distance from 1.65 to 1.68 Å and 3.07 to 2.97 Å. This change could be explained by hydrogen contribution to bonds at 600°C. Apart from that, there is not much of a difference between the samples, showing that the major influence of ammonia treatment was already made at 600 °C, which correlates with the minor differences also in porosity.

When comparing a micro- and a nonporous PSZ sample (900 °C in nitrogen or ammonia atmosphere), there are most likely mixed Si-C-N species in the nonporous sample, which is in accordance with the elemental composition of the samples. Since the carbon content is the major difference between the two samples, it probably plays an important role regarding the pore stability.

The three different materials PSZ, PCS and PSZPCS pyrolyzed in ammonia at 900 °C have the exact same maxima in the pair correlation function at 1.68 Å and 2.97 Å. By using a reactive atmosphere, the elemental composition of different starting materials can be adjusted and consequently also the interatomic distances in the materials. This could in further consequence confirm that the elemental composition of the micropore forming entities is determining the pore size.

## 10.8 Results - Further pyrolysis experiments with 80DVB in nitrogen

Since a change of micropore size could be found for the samples with DVB as linker (see section 9.2.6), further samples were prepared at different pyrolysis temperatures and under different atmospheres. According to the TGA-MS measurements (see section 9.2.6.5), the DVB hinders reactions during pyrolysis, and using samples prepared at various temperatures in this temperature range, it can be investigated when the influence of DVB begins and if it increases the pore stability, too. The pyrolysis experiments were carried out only with the sample with the highest DVB content (80DVB), because the clearest changes were visible for this sample.

### 10.8.1 Ceramic yield

The ceramic yield of 80DVB in comparison to that of PSZ in the same temperature range is displayed in Figure 158. As can be seen, the mass loss is drastically higher already at 400 °C and the curves have a similar shape from then on. This shows that part of the DVB is decomposed during the pyrolysis process already at low temperatures.

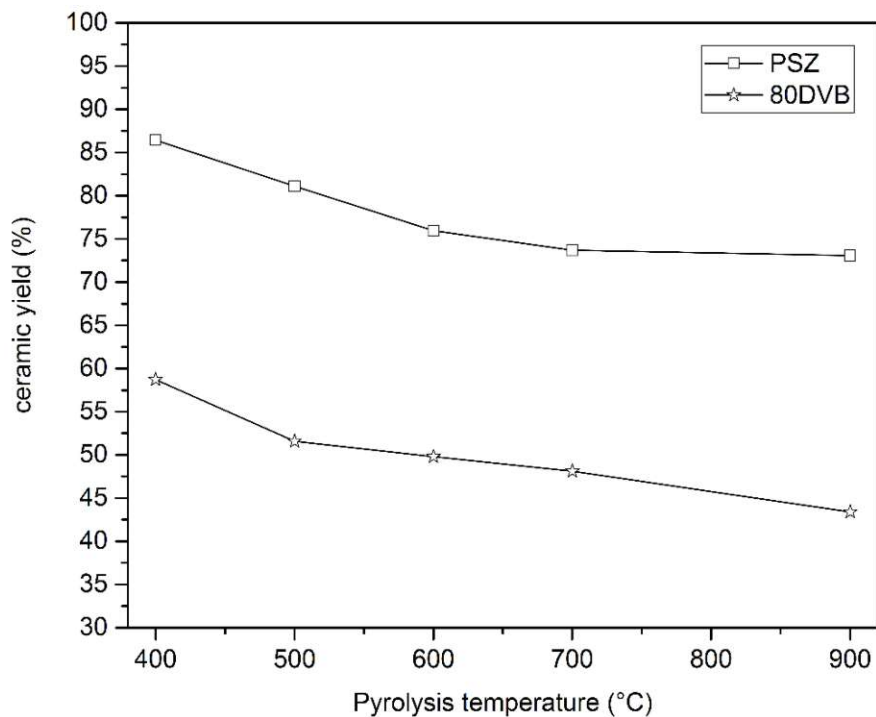


Figure 158: Ceramic yield of 80DVB and PSZ pyrolyzed under nitrogen at temperatures from 400 to 900 °C.

### 10.8.2 Elemental composition

The elemental composition of 80DVB and PSZ after crosslinking and pyrolysis at various temperatures is shown in Figure 159. The pyrolyzed samples have a comparable oxygen content, which is due to the oxygen already present in the precursor polymer, with a slight increase in case of the 80DVB samples due to the handling procedure. Even though the mass loss is drastically higher for the 80DVB samples, the carbon content is still significantly higher at all pyrolysis temperatures, which shows that DVB or resulting decomposition products stay integrated in the samples. While the nitrogen content decreases for pure PSZ when going to higher temperatures, it stays almost constant for 80DVB, which goes along with the TGA-MS results that are shown in section 9.2.6.5. These show that transamination reactions are hindered by the presence of DVB molecules, which separate the PSZ oligomers and therefore prevent them from interacting with each other. Since transamination reactions lead to the loss of nitrogen through ammonia formation, this gives an explanation for the higher amount of nitrogen remaining in the 80DVB samples.

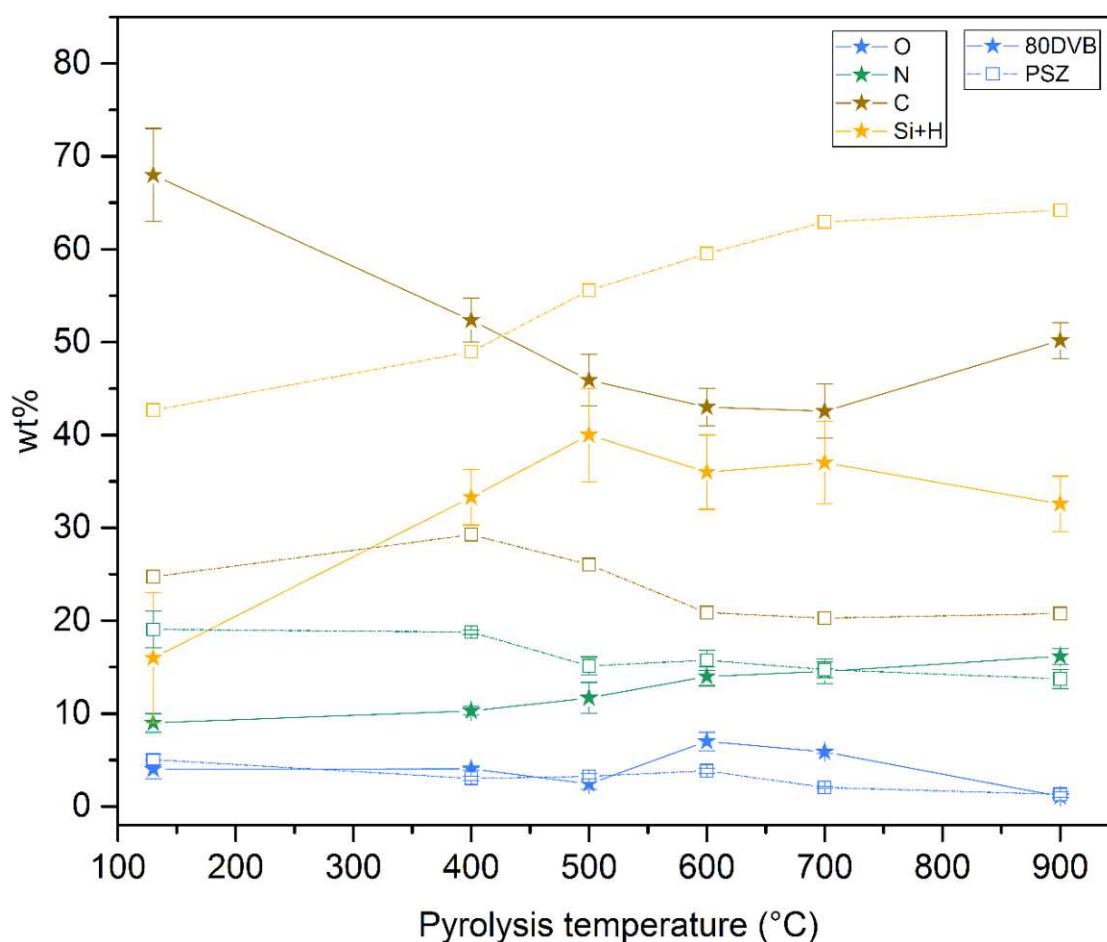


Figure 159: Elemental composition of 80DVB and PSZ after crosslinking and pyrolysis under nitrogen at temperatures between 400-900°C; O, N, and C content are measured, Si+H is calculated as remainder to 100 wt%.

### 10.8.3 ATR-IR

The spectra recorded of 80DVB and PSZ after crosslinking and pyrolysis at temperatures between 400-700 °C are displayed in Figure 160. The crosslinked stage was already discussed in section 9.2.6.4. There are several differences in the spectra of the pyrolyzed samples. First, the Si-H signal is only present up to temperatures of 400 °C in case of 80DVB instead of 500 °C, which probably results from an increased number of hydrosilylation reactions at elevated temperatures with the DVB molecules providing a high number of yet unreacted unsaturated bonds. In addition, aromatic signals can be found even at 700 °C for the 80DVB samples, which confirms that the DVB molecules or their decomposition products stay integrated in the samples even after pyrolysis. Since the broad main signal at 600 °C and 700°C, which is most likely composed of overlapping Si-C and Si-N vibrations, is shifted to lower wave numbers in case of 80DVB, the ratio between Si-C and Si-N bonds changes. More carbon containing bonds are present, since Si-C bonds are formed during the hydrosilylation reaction. This is most likely the explanation for the shift to lower wave numbers.

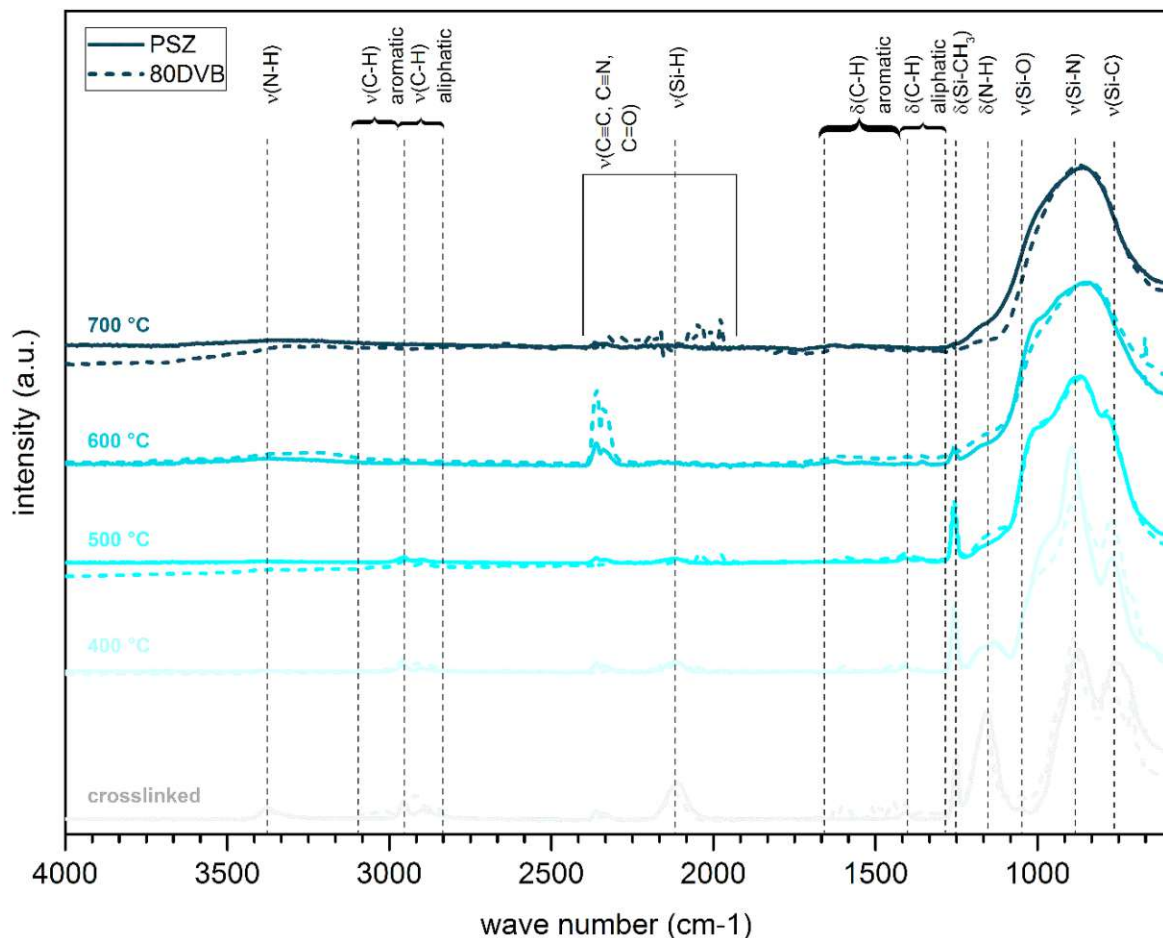


Figure 160: ATR-IR spectra of 80DVB and PSZ after crosslinking and pyrolysis under nitrogen at temperatures between 400-700°C.



### 10.8.4 Pore characterization

The pore characteristics for the samples pyrolyzed at temperatures between 400-700 °C were investigated both using physisorption and SAXS measurements.

#### 10.8.4.1 N<sub>2</sub>-Physisorption

The physisorption data of 80DVB in comparison to PSZ is shown in Figure 161, and the calculated pore size distributions are shown in Figure 162. The calculated parameters are listed in Table 51. PSZ yields isotherms of type I at 500 °C and 600 °C, with the pores collapsing at higher temperatures leading to a type VI isotherm. At 400 °C, which is the lowest temperature investigated, the isotherm is of type II/VI, which is typical for a non- or macroporous material. 80DVB shows a similar behaviour, with an increasing pore volume and the pores collapsing at temperatures above 600 °C. The pores again seem to evolve with increasing temperature, reaching the maximum pore volume at 500 °C and then collapse again. In addition to the micropore part, the DVB samples show a hysteresis loop, indicating the presence of additional mesopores, which, according to the DFT calculations, are only present in a minor extent.

The pore size distributions of PSZ calculated from the type I isotherms of the samples pyrolyzed at 500 °C and 600 °C have their maxima at 0.88 and 0.84 nm, respectively. At a pyrolysis temperature of 400 °C, it is difficult to evaluate the pore size distribution, because of the low adsorbed quantity, but the PSD yielded a maximum at 1.13 nm. Above 600°C, the pores collapse, hence there was no PSDmax calculated for PSZ700°C.

The results for 80DVB are showing the same general trends. The sample pyrolyzed at 400 °C has the maximum of the pore size distribution at 1.13 nm as well. The two type I/type IV isotherms for pyrolysis temperatures of 500 °C and 600 °C have their pore size maxima both at 0.70 nm. The low amount of mesopores, which cause the hysteresis loop, range from 10-50 nm, but contribute to the pore volume only to a minor extent. No maxima in the micropore range were found for the 80DVB700°C sample.

Overall, DVB does not affect the maximum temperature up to which the micropores are stable, since both materials show the highest specific surface areas at 500 °C with the pores closing at higher temperatures. Although the influence on the pore stability is minor, the presence of DVB shifts the size of micropores to smaller values for the type I isotherms, while the pore size is the same for both materials at 400 °C.

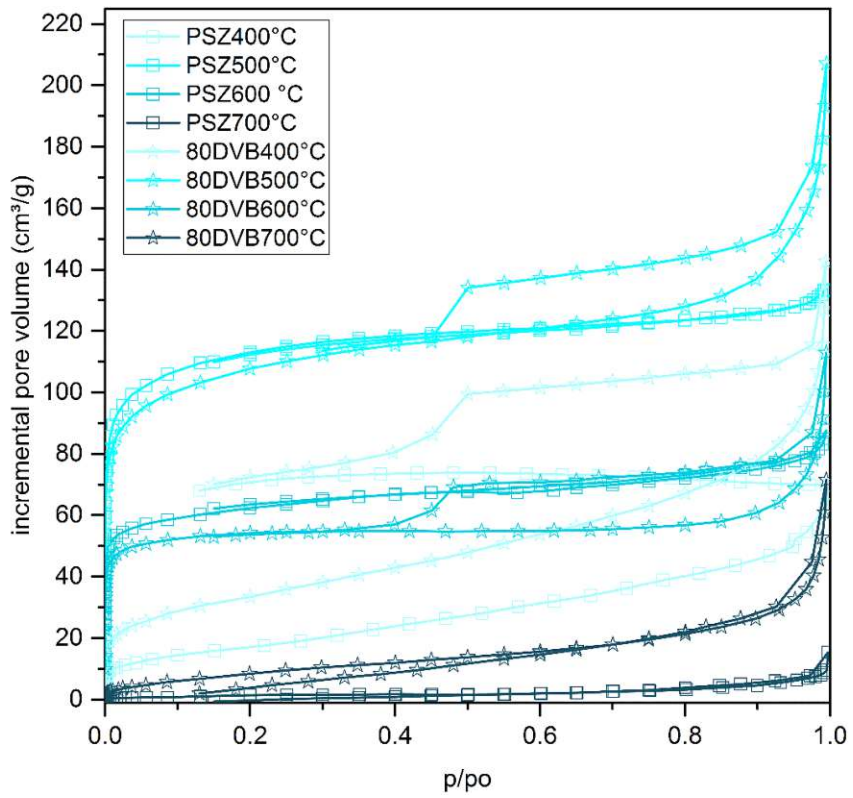


Figure 161:  $N_2$  physisorption isotherms of PSZ and 80DVB after pyrolysis at 400 to 700 °C.

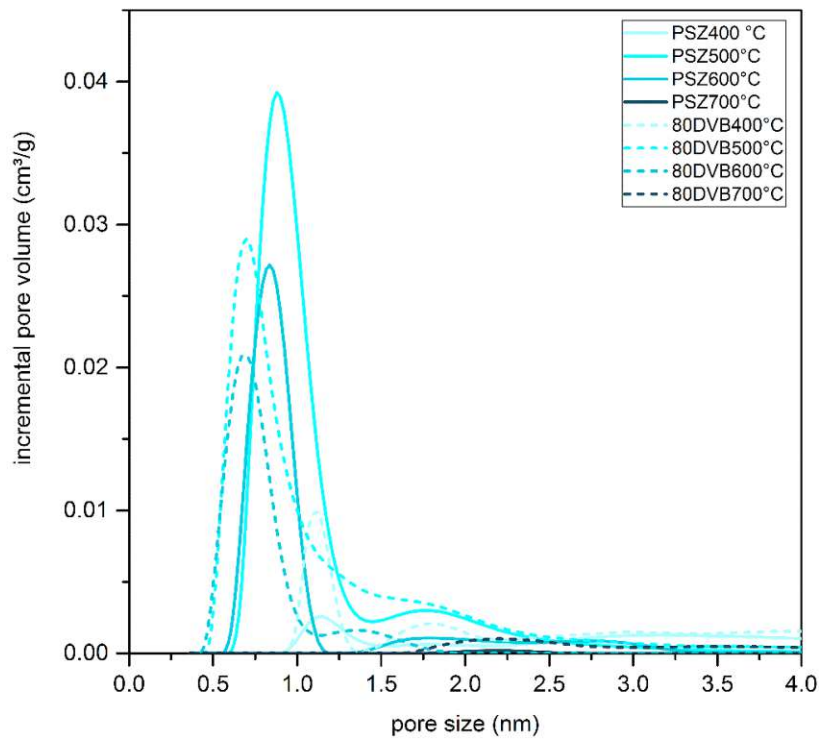


Figure 162: PSDs of PSZ and 80DVB after pyrolysis at 400 to 700 °C, calculated from the  $N_2$  physisorption data using NLDFT models.



Table 51: Type of isotherm, BET specific surface area ( $S_{BET}$ ), maximum of the pore size distribution ( $PSD_{max}$ ) in the micropore range, and micropore volume ( $V_{micro}$ ) of PSZ and DVB pyrolyzed at temperatures between 400 and 700 °C (data from gas physisorption using  $N_2$  at 77 K).

	Isotherm	$S_{BET}$ (m <sup>2</sup> /g)	$PSD_{max}$ (nm)	$V_{micro}$ (cm <sup>3</sup> /g)	Comment
<b>PSZ400 °C</b>	Type II/VI	63 ± 1	1.13	0.02	Non- or macroporous
<b>PSZ500 °C</b>	Type I	350 ± 16	0.88	0.17	Microporous
<b>PSZ600 °C</b>	Type I	195 ± 6	0.84	0.10	Microporous
<b>PSZ700 °C</b>	Type VI	5 ± 0.5	-	-	Non porous
<b>80DVB400 °C</b>	Type II/VI	119 ± 1	1.13	0.02	Non- or macroporous
<b>80DVB500 °C</b>	Type I/IV	338 ± 14	0.70	0.16	Micro – and mesoporous
<b>80DVB600 °C</b>	Type I/IV	164 ± 9	0.70	0.08	Micro- and mesoporous
<b>80DVB700 °C</b>	Type VI	36 ± 1	-	-	Non porous

#### 10.8.4.2 SAXS

In addition to physisorption studies, SAXS investigations were carried out. The experimental SAXS data are shown in Figure 163. The parameters calculated from the fitted model are summarized in Table 52.

The diameter of gyration ( $2R_g$ ), which is assumed to correspond to the size of micropores, confirms the trends found by the physisorption experiments. There is almost no difference for the two materials PSZ and 80DVB after pyrolysis at 400 °C. When increasing the pyrolysis temperature, the pore size in PSZ first increases to values of 0.67 nm and 0.71 nm at 500 °C and 600 °C, respectively before shrinking again. In contrast, the pore size in 80DVB first increases to 0.52 nm, where it reaches a plateau, and stays almost constant at higher temperatures.

All samples have a fractal dimension  $D$  of  $\sim 4$ , which can be interpreted as sharp interface between pores and bulk material. The trends for the hard sphere radius  $R_{hs}$ , in contrast, which is a measure for the distance between the scattering objects, are different for the two materials, as well as those of the hard sphere volume fraction  $\eta$ . The distance between the pores increases strongly from 400 °C to 500 °C in case of PSZ, and then stays almost constant. The increasing distance between the pores. This can be explained by the formation of pores through

decomposition of organic groups, which grow up to temperatures of 600 °C and shrink again above this temperature.

For 80DVB, there is almost no change in  $R_{hs}$  as a function of pyrolysis temperature, but the agglomeration ( $\eta$ ) decreases significantly from 400-500°C. If the assumption is true that PSZ and DVB domains form in the crosslinked sample, and that micropores are located mainly in the PSZ domains, this behaviour can be explained by the decomposition of DVB. DVB domains then do not separate the PSZ-derived domains anymore, in which the pores are agglomerated and they are therefore more homogeneously distributed in the material.

DVB leads to lower values for the pore size when compared to PSZ, with a shift from 0.7 to 0.5 nm, but comparable values at the lowest pyrolysis temperature of 400 °C. The distance between the pores is higher for 80DVB and also shows a higher degree of agglomeration. Both findings can be explained by the formation of DVB and PSZ domains, and the micropores being mainly present in the PSZ rich domains.

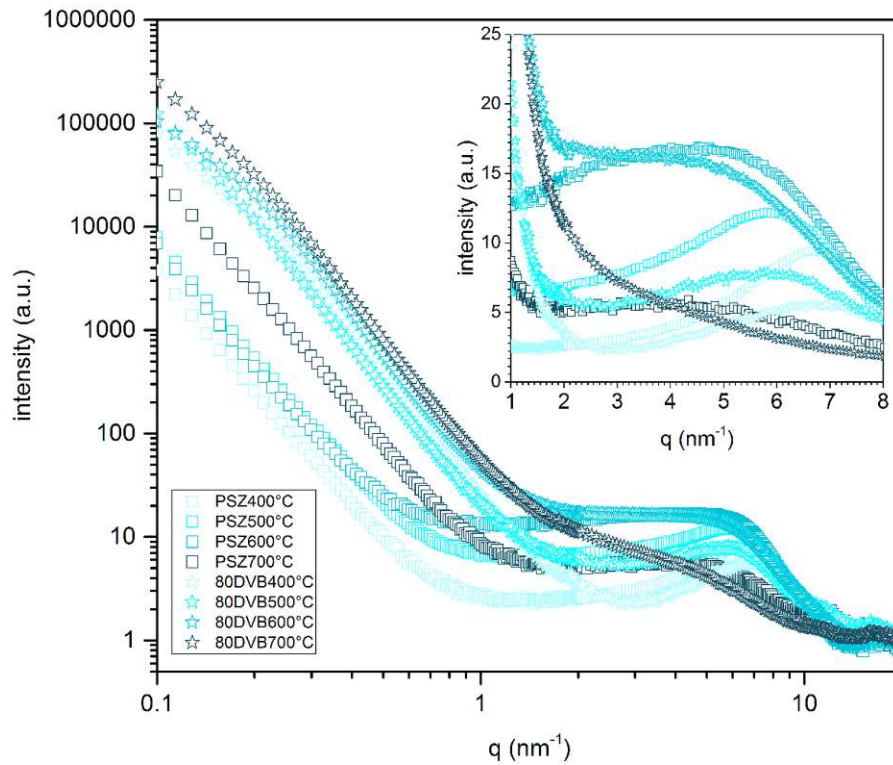


Figure 163: Experimental SAXS curves of 80DVB and PSZ pyrolyzed at temperatures from 400-700°C.

Table 52: Parameters obtained from applying a model fit to the SAXS data: Radius of gyration ( $R_g$ ), fractal dimension ( $D$ ), hard sphere radius ( $R_{hs}$ ), and hard sphere volume fraction ( $\eta$ ).

	$2R_g$ (nm)	$D$	$2R_{hs}$ (nm)	$\eta$
<b>PSZ400 °C</b>	0.44	3.5	0.44	0.12
<b>PSZ500 °C</b>	0.67	3.81	0.93	0.25
<b>PSZ600 °C</b>	0.71	3.85	0.89	0.19
<b>PSZ700 °C</b>	0.53	3.82	1.10	0.11
<b>80DVB400 °C</b>	0.42	4	0.86	0.42
<b>80DVB500 °C</b>	0.52	4	0.90	0.17
<b>80DVB600 °C</b>	0.48	4	-	-
<b>80DVB700 °C</b>	0.66	4	-	-

## 10.9 Conclusions - Pyrolysis experiments with 80DVB

Further pyrolysis experiments were conducted with the material 80DVB, because the experiments at 600 °C showed a significant influence of the presence of the linker molecules on the pore size and decomposition behaviour. Based on these findings, several possible explanations for the origin of micropore formation can be strengthened or excluded.

One of the assumptions made was that the reactions that are hindered by the presence of DVB are responsible for the pore formation or an overall shift of the temperature region of pore formation is caused by the delay of the reactions during polymer-ceramic conversion. Because of the same pore size at 400 °C, for PSZ and DVB, a temperature where transamination reactions already take place in the pure PSZ material, a direct influence of the transamination reactions on the micropore formation is not likely. Since the porosity of the 80DVB sample collapses at the same temperatures as that of PSZ, a general temperature shift of the pore evolution can most likely be excluded.

Another possible explanation for the shift in micropore size was that the change in elemental composition yields a different composition of structural elements responsible for the pore formation and stability. This assumption is strengthened by these findings, because the nitrogen content in the 80DVB sample is higher due to hindered transamination reactions.

## 11. FOCUS VI – IN SITU SAXS INVESTIGATIONS

In-situ investigations of the pore evolution during the pyrolysis in different atmospheres can help to clarify the origin of pore formation in PDCs. Therefore, a new methodological approach was designed to enable measurements under elevated temperatures and simultaneous gas flow, even with aggressive gases like ammonia.

### 11.1 Design of the sample holder

The sample holder is displayed in Figure 164, the gas flow through the sample holder is shown in Figure 165. The requirements were:

- Stable up to temperatures as high as 900 °C for the parts that are inside or close to the furnace
- Gas flow at temperatures as high as 900 °C
- Resistance against aggressive gases like ammonia even at 900 °C
- Sufficiently high intensity reaching the detector → quartz glass with wall thickness below 100 µm
- Easy sample changes
- Limited space in the SAXS instrument chamber
- Flexible tubing

Therefore, all metal parts were made of stainless steel, the tubes were made out of PTFE, the sealing material was a high temperature silicone and a standard quartz mark tube was used to put the sample in (wall thickness <10 µm, commercially available). A union tee (vacuum tube fitting, Fitok 1/4'') was the central piece of the sample holder, connecting gas inlet, gas outlet and quartz tube. The mark tube is fragile and can't be connected to the union tee directly. Hence, high temperature silicone was used to glue the mark tube into a 1/4'' stainless steel tube, which can easily be connected to the union tee. Tube pieces with a length of approximately 3 cm were used and the total length with the mark tube was adjusted to 10.9 cm (the length is adjusted to the optimal sample position in the furnace). A stainless steel cannula is used to bring the gas directly to the sample. Because of the desired low gas flow rates and the small diameter of the cannula, the gas inlet was reduced from 1/4'' to a 1/8'' to prevent a pressure increase at the cannula. The connection to the gas bottle is a 1/8'' PTFE tube. The gas outlet is a 1/4'' stainless steel tube connected to a PTFE tubing with the same diameter. To seal the connection gas tight, a shrinking tube is used.

The gas-supply also contains an ammonia gas bottle and a nitrogen gas bottle for rinsing the whole set up after doing the experiments with a stainless steel pressure regulator for ammonia with a hetero gas rinsing possibility connected to the two bottles. The gas flow was then regulated using a needle valve. The gas outlet was connected to two washing bottles, again using a shrinking tube. The first one was filled with water to take up the main part of the ammonia. The second bottle was filled with a ~30 %  $\text{H}_2\text{SO}_4$  solution to neutralize the remaining ammonia.

The flow was adjusted with nitrogen by controlling the bubble formation in the washing bottles. Since low gas flows are desired, ~1 bubble per second was set as flow. Considering the size of a bubble approximately the size of a droplet, it has approximately 0.3 ml, which equals a gas flow of ~0.02 l/min. For the ammonia measurements, the flow is adjusted using nitrogen while purging the set up.

The whole measurement set up, including the newly designed sample holder, is shown in Figure 166.

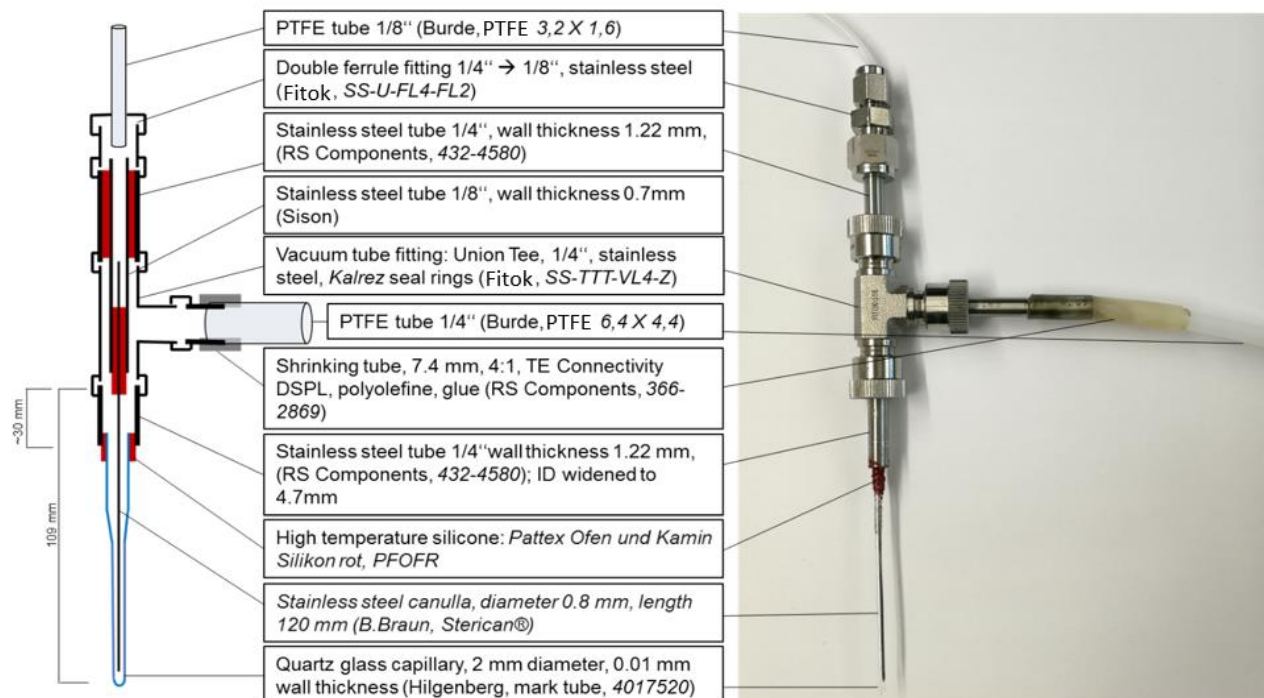


Figure 164: Core piece of the in situ SAXS sample holder; schematically on the left and photographed on the right with the description of the parts in the middle.

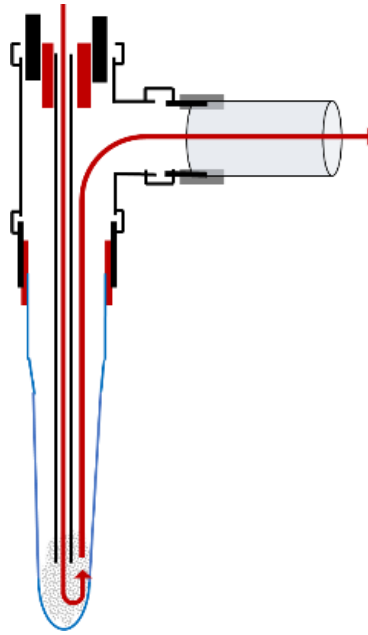


Figure 165: Gas flow through the SAXS sample holder.



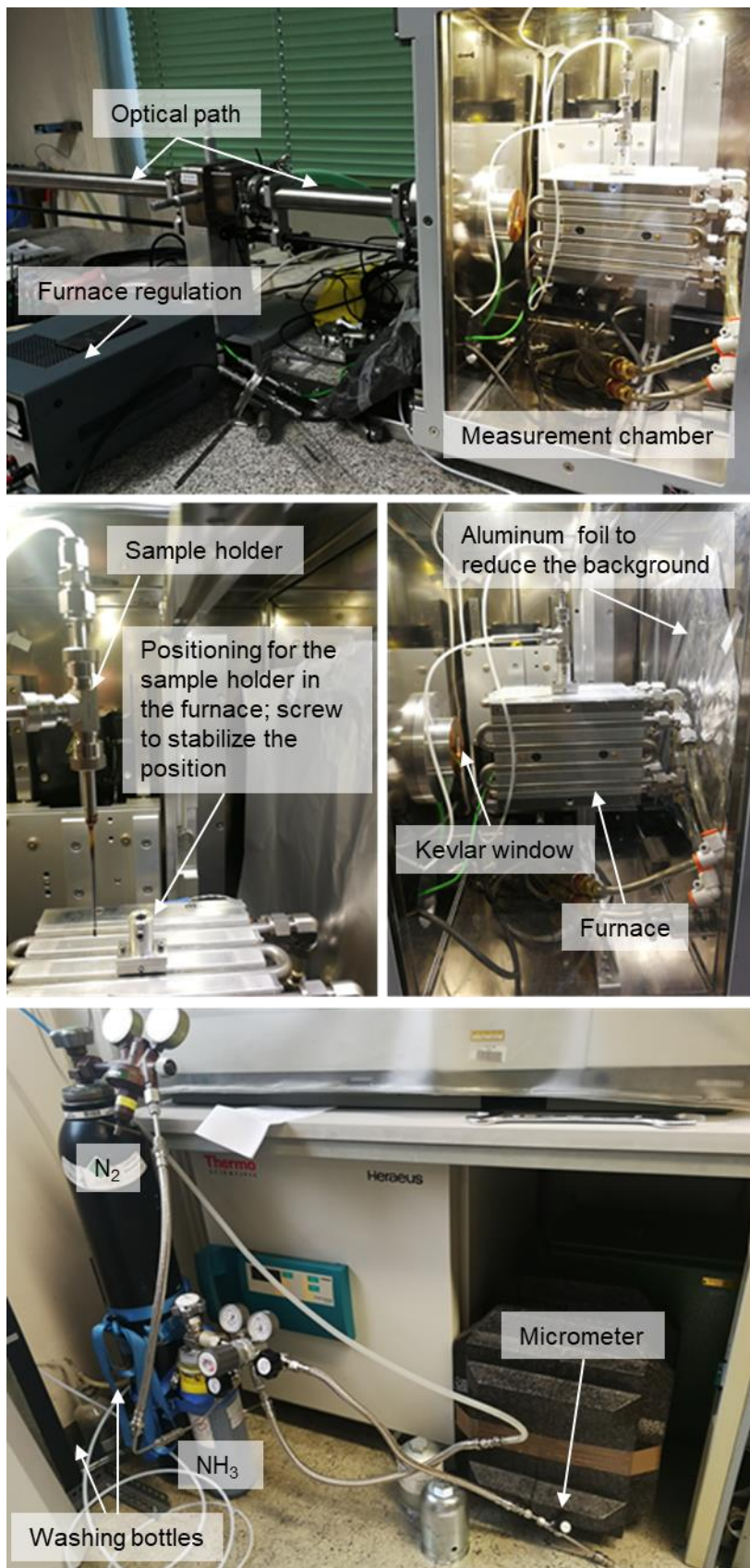


Figure 166: Various parts of the set up during or before the measurement, showing the measurement chamber including the furnace and sample holder on top, the gas supply at the bottom and a closer display of the inside of the measurement chamber in the two pictures in the middle.

## 11.2 Experimental procedure – Focus VI

Four different materials were investigated using in-situ SAXS, PSZ, PCS, PSZPCS and 80DVB.

SAXS investigations were carried out using a Bruker Nanostar equipped with a microfocus source (Incoatec High Brilliance, Germany) and a 2D position sensitive detector (Vantec 2000, Bruker AXS).

The crosslinked samples were ground and filled in the newly designed sample holder (up to the tip of the canulla), the whole set up was purged with nitrogen and a flow of 0,2 l/min of either ammonia or nitrogen was adjusted using a needle valve. The steel canulla was used as reference point for the measurement spot (approximately 2 mm below the tip of the canulla, since the material is shrinking during pyrolysis). Then the pyrolysis was started with a heating rate of approximately 10 K/min and a measurement was performed every 50 °C during the heating period and every 200 °C during the cooling period (measurement time at each datapoint: 10 min). An empty capillary was measured using the same procedure to get a temperature correlated background signal. The data was normalized on the amplitude maximum. Collected X-ray data were radially integrated and background corrected to obtain scattering intensities in dependence on the scattering vector  $q$ . In addition to the small pores already investigated in the ex-situ measurements, long slit like pores were found and fitted accordingly.

## 11.3 Results – Focus VI

The experimental data generated in the in-situ SAXS experiments is displayed in Figure 167. Already from the raw data, one can see clear differences between the two atmospheres. More distinct evolution of ordered pores in all four materials can be seen by the sharper maxima around  $q$  values of  $5 \text{ nm}^{-1}$ .

The data showed that there are not only the well-investigated micropores forming during the polymer-ceramic conversion (scattering objects, in our case designated as small pores), but also some long pores or cracks, that are closing again during the cooling period, which is shown in Figure 168, schematically as well as with the underlying data. The characteristic parameters that are extracted from the data are shown in Figure 169 for PSZ, PCS, PSZPCS and 80DVB in nitrogen and ammonia atmosphere. The data for the heating period is only shown for temperatures above 300 °C, because below that temperature, the polymer structure is causing the signal and not the pores yet. There are huge differences visible between the inert pyrolysis



atmosphere and the reactive one, as expected. All three materials show the same behaviour in nitrogen, however, PSZ seems to be the only material being equally vulnerable to crack formation in ammonia. Generally, the cracks start to form around 500 °C in nitrogen and approximately 50 °C earlier in the reactive atmosphere. This formation of long pores is only visible because of the in-situ technique. If investigated with a standard set-up, one only has access to the last data point after the cooling period, and cannot separately make any declaration on the processes during the original pore formation. The cracks were found to have a radius of gyration  $r_g$  of  $\sim 1.5$  nm.

The hard sphere radius  $r_{HS}$ , is a measure for the distance between the scattering objects (i.e., the pores), the hard sphere volume ratio  $\eta$  is a measure for the degree of agglomeration of pores. These two parameters are displayed together with the radius of gyration in Figure 167 for the small pores as well as their amplitude. For PSZ as starting material, there is a significant difference in the occurrence of these small pores. Whereas they are forming around 500 °C in nitrogen, they seem to be already present at this temperature if pyrolysis is conducted in ammonia. There is almost no change for PCS regarding the course of the amplitude. For PSZPCS, one can see an interesting phenomenon. There is a bimodal maximum for both atmospheres, always located at the temperatures of maxima of the two pure materials. The pore formation seems to be completely independent from each other. The same findings are visible in the size of the pores – the PSZPCS mixture shows two maxima which are at the same radii as those of the pure materials. The reactive atmosphere apparently influences the two precursor types in a similar manner if they are in a mixture and if they are used in a pure form.

The hard sphere volume ratio shows the formation of agglomerated ordered pores in the temperature region of the main polymer-ceramic-conversion and with even higher temperatures drifting apart, which is probably caused by the reduced radius of the scattering objects. This can be also seen in the hard sphere radius, which is measure for the distance of the scattering objects.

For 80DVB, the amplitude of small pores increases if pyrolysis is conducted in ammonia. This is probably because ammonia is reacting with the carbon phase in the DVB rich domains. Since micropores are most likely located in the PSZ derived domains, the removal of the carbon leads to an increase content of micropores present in the material. This is also displayed by the hard sphere radius, which is higher if the measurement is conducted in nitrogen, since the micropore containing domains are separated by the DVB derived carbon rich domains.

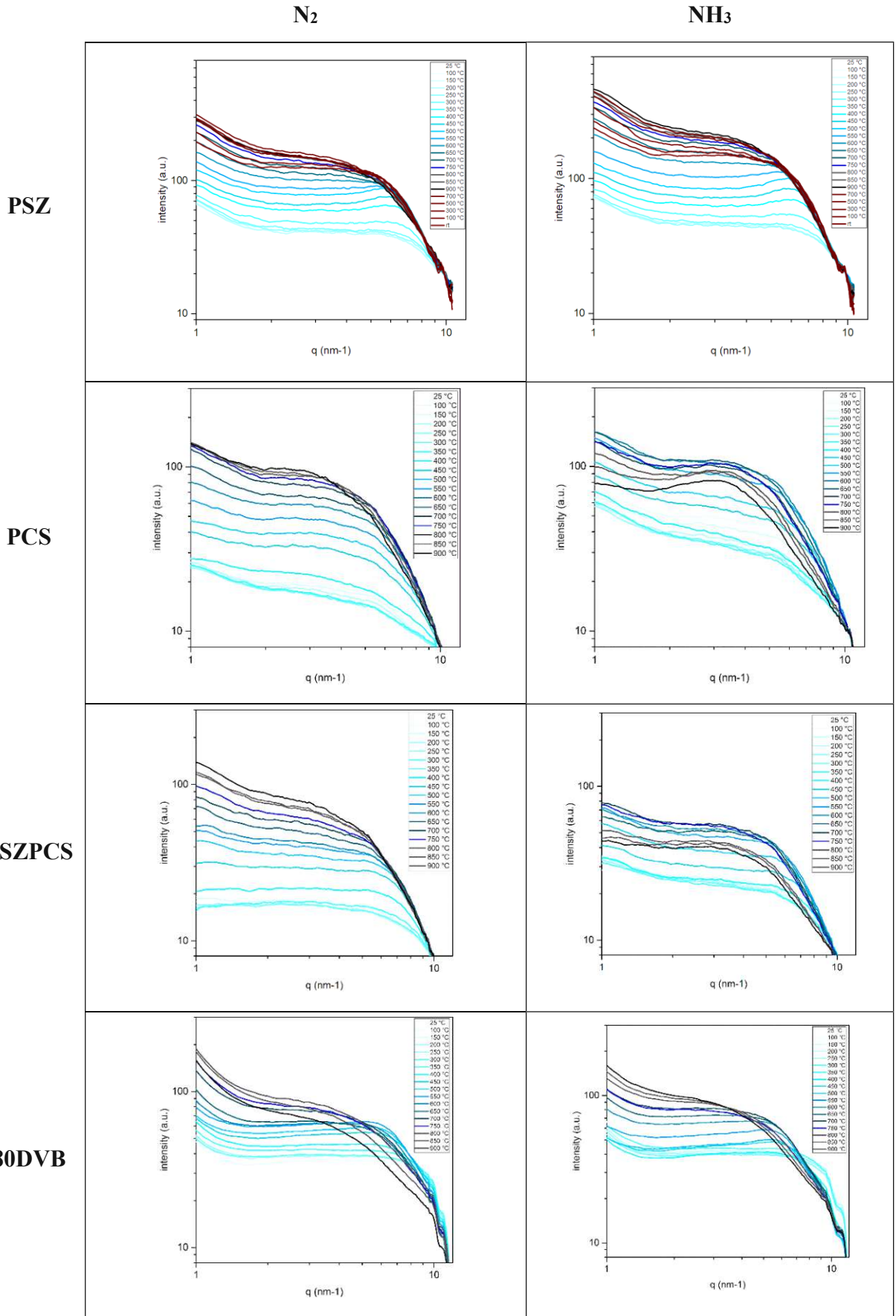


Figure 167: In situ SAXS data of the four samples PSZ, PCS, PSZPCS and 80DVB pyrolyzed in nitrogen (left) or ammonia atmosphere (right) up to 900 °C.

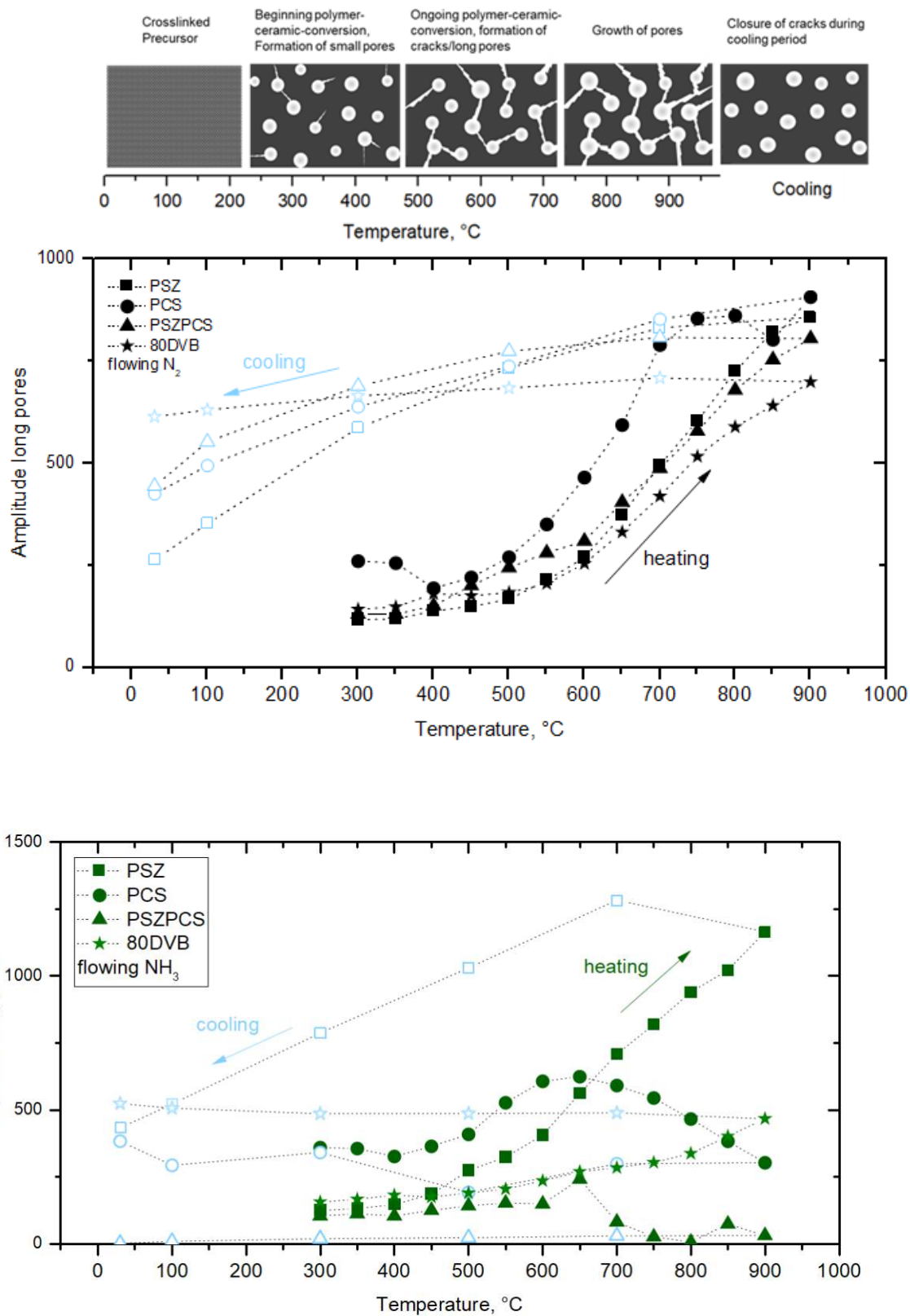


Figure 168: Schematic display of the pore formation in PDCs according to the in-situ SAXS data, with the amplitude of long pores over the whole temperature program calculated from the fitted SAXS data, representing the amount of cracks present in the sample in nitrogen and ammonia.

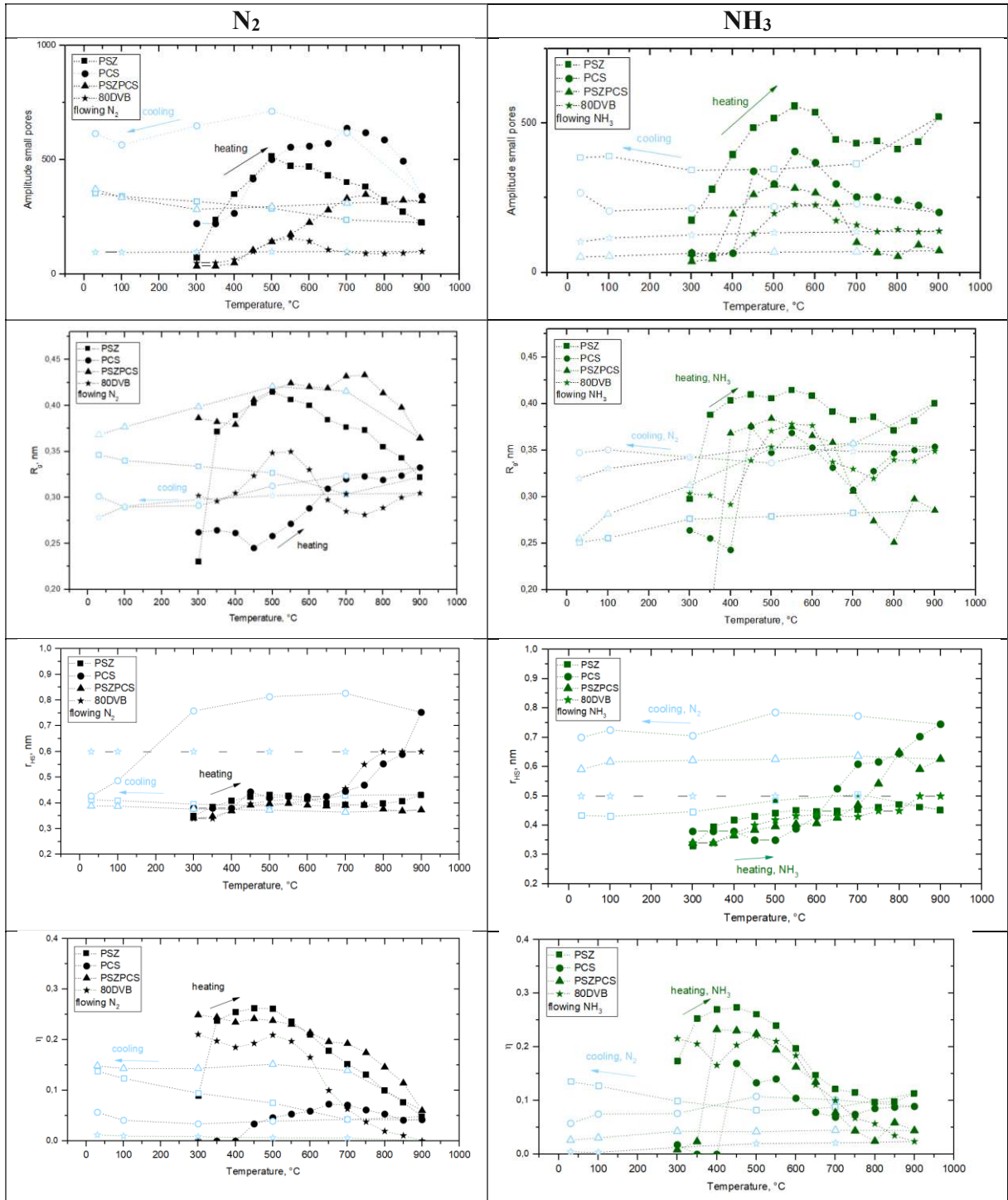


Figure 169: Parameters obtained from in-situ SAXS data: Radius of gyration ( $R_g$ ), amplitude of the small pores, hard sphere radius ( $R_{hs}$ ), and hard sphere volume fraction ( $\eta$ ) for pyrolysis under nitrogen/ammonia.

Die approbierte gedruckte Originalversion dieser Dissertation ist an der TU Wien Bibliothek verfügbar. The approved original version of this doctoral thesis is available in print at TU Wien Bibliothek.

## 11.4 Conclusions – Focus VI

The pore formation in the materials was investigated in detail using a newly introduced SAXS technique, enabling the in-situ observation of the pore formation under simulated pyrolysis conditions even under reactive atmospheres, revealing new information about this pore generation by making it possible to separate the initial formation during the heating period and the influence of the cooling period. Significant differences for the two different atmospheres were found, not only regarding the starting temperature of pore formation, but also the additional occurrence of cracks in the material in case of nitrogen atmosphere, which are closing again during the cooling period, probably making the actual micropores inaccessible for the probe molecule during physisorption. This assumption is strengthened by the second maximum in the PSD of the materials pyrolyzed in ammonia at 900 °C, which could be caused by the shrank large pores/cracks that were found.

The two precursor types seem to act independent from each other in the mixture, which can be seen from the bimodal amplitudes and radii of small pores comparable to the two different maxima of the pure materials.

According to the in-situ SAXS results, it is possible to get a bimodal pore size in the material by simply mixing two different precursors. Also, the findings would suggest an “in-place” pyrolysis of the membrane at separation conditions in case of applications in separation or catalysis processes.

## 12. FOCUS VII – STABILITY AGAINST OXIDATION

### 12.1 Experimental procedure – Focus VII

Selected materials were tested towards their stability in harsh environments, hot air and steam. The materials and their physisorption results are listed in Table 53. The samples were finely ground and sieved, and the fractions with grain sizes of 125-200  $\mu\text{m}$  were chosen for the stability testing experiments. Approximately 100 mg of samples of these sieving fractions were then heated to 500 °C (1K/min) either in air or steam, held at that temperature for 12 hours and characterized afterwards using the usual methods. 500°C were chosen because this temperature is below the pyrolysis temperatures and therefore doesn't influence the pore size by further polymer-ceramic conversion.

For the testing in air at 500 °C, an open furnace was used. After the heat treatment, the samples were stored in glass vials until characterization was started.

For the hydrothermal stability testing, a supplement to the furnace was used (Figure 171; the whole set up was isolated during the experiment and the tubing was heated before the experiment was started), where the nitrogen is purged through water using a frit. The water was heated to 60 °C using a water bath to yield a higher steam concentration. According to data shown in Figure 170, approximately 130 g water per  $\text{m}^3$  air (consequently a similar value for  $\text{N}_2$ ) were achieved.

Table 53: Type of isotherm, BET specific surface area ( $S_{\text{BET}}$ ), maximum of the pore size distribution ( $\text{PSD}_{\text{max}}$ ) and micropore volume ( $V_{\text{micro}}$ ) of the tested samples before testing.

	Isotherm	$S_{\text{BET}}$ ( $\text{m}^2/\text{g}$ )	$\text{PSD}_{\text{max}}$ (nm)	$V_{\text{micro}}$ ( $\text{cm}^3/\text{g}$ )	Comment
<b>PSZ600°C</b>	Type I	$195 \pm 6$	0.84	0.10	Microporous
<b>80DVB600 °C</b>	Type I/IV	$164 \pm 9$	0.70	0.08	Micro- and mesoporous
<b>PSZ600°C<math>\text{CNH}_3\text{c}</math></b>	Type I	$271 \pm 14$	0.70	0.13	Microporous
<b>PSZ700°C<math>\text{CNH}_3\text{c}</math></b>	Type I	$208 \pm 12$	0.67	0.11	Microporous



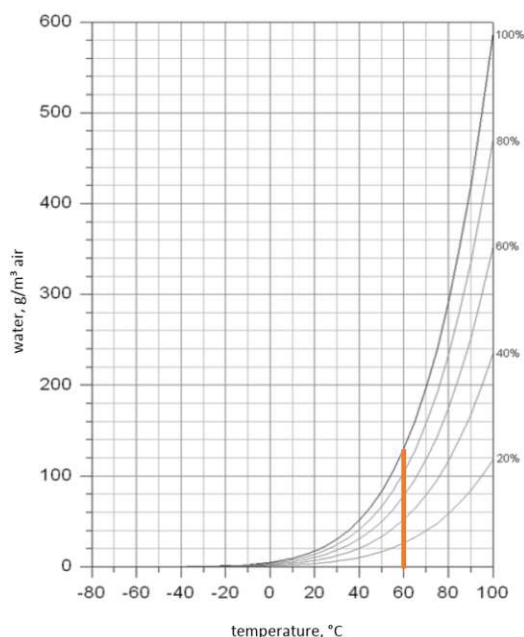


Figure 170: Temperature dependency of the maximum steam concentration, after [134]

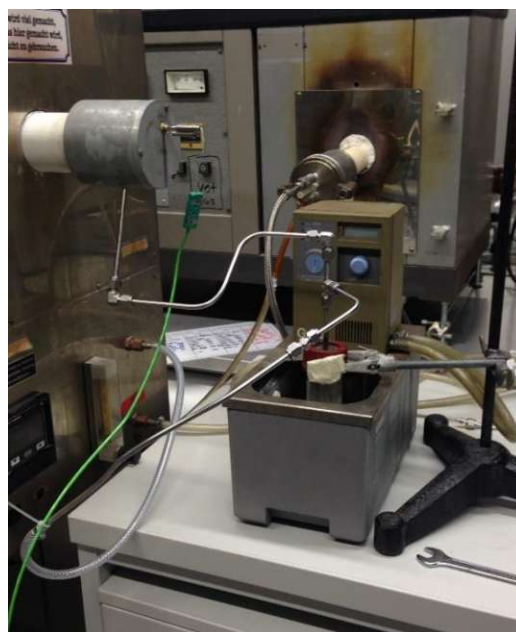


Figure 171: Supplement to the furnace left) for hydrothermal stability testing (the tubing was heated).

## 12.2 Results – Focus VII

### 12.2.1 Treatment at 500 °C in air

#### 12.2.1.1 Mass loss

The mass change of the samples tested regarding their oxidation stability is listed in Table 54, with extremely different results for the different samples. All samples have high specific surface areas, leading to strong oxidation of the sample. Because there is already only a minor amount of carbon left in the ammonia treated samples, there is not much carbon left to be removed by the reaction with oxygen anymore, which leads to an increase in mass. The opposite is the case for the DVB sample, in which there are free carbon domains, originating from the DVB domains, which can react with the oxygen and lead to relatively high mass losses up to -20 %.



Table 54: Mass change of the samples after the stability testing in air at 500 °C for 12 h.

	$\Delta m, \%$
OX500PSZ600°C	+9
OX500PSZ600°CNH <sub>3c</sub>	+2
OX500PSZ700°CNH <sub>3c</sub>	-3
OX50080DVB600°C	-18

### 12.2.1.2 Elemental analysis

The elemental composition of the samples after the oxidation in air at 500 °C is given in Table 55. All samples show strong oxidation, which can be attributed to the high specific surface area providing enough contact area for the oxygen. Since there is still carbon present in the sample OX500PSZ600°C, it is likely that some of the pores closer to the surface close before the whole carbon can be removed.

Table 55: Elemental composition of the samples after the stability testing in air at 500 °C for 12 h; O, N, and C content are measured, Si+H is calculated as remainder to 100 wt%.

	O, wt%	N, wt%	C, wt%	Si+H, wt%
OX500PSZ600°C	23 ± 3	12 ± 3	10	55
OX500PSZ600°CNH <sub>3c</sub>	33 ± 1	51 ± 2	0	16
OX500PSZ700°CNH <sub>3c</sub>	21 ± 3	41 ± 4	1	37
OX50080DVB600°C	31 ± 4	46 ± 4	3	20
PSZ600 °C	2 ± 0	12 ± 3	19 ± 1	63 ± 7
PSZ600°CNH <sub>3c</sub>	6 ± 1	31 ± 4	8 ± 1	55 ± 6
PSZ700°CNH <sub>3c</sub>	4 ± 0	30 ± 1	2 ± 0	64 ± 1
80DVB600°C	4 ± 0	9 ± 0	68 ± 5	20 ± 6

### 12.2.1.3 ATR-IR

The IR spectra of the different samples tested regarding their oxidation stability are shown in Figure 172 together with the benchmark sample PSZ600°C. The stronger the oxidation/the higher the oxygen content of the samples, the stronger visible is the typical Si-O vibration at 1090 cm<sup>-1</sup>. In addition, the bands caused by Si-N and Si-C vibrations are still visible, but less

intense compared to the Si-O vibrations. Also, the main signal is split up in two overlapping signals more clearly, and the Si-N bands are dominant over the Si-C bands, which is in accordance with the elemental composition, showing that there is almost no carbon left in the samples in case of the materials prepared in ammonia.

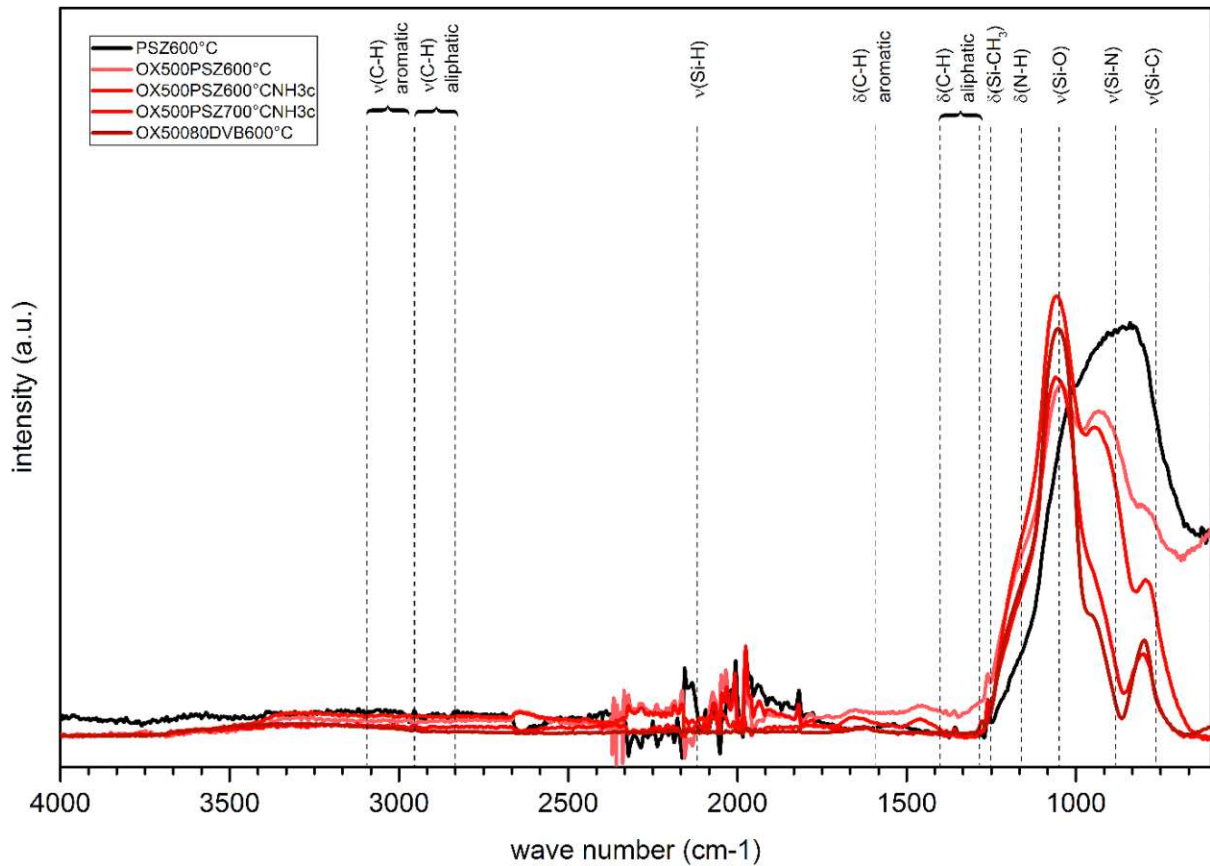


Figure 172: ATR-IR spectra of the samples tested regarding their stability against oxidation at 500 °C in air.

#### 12.2.1.4 N<sub>2</sub>-Physisorption

According to the physisorption experiments, the samples are nonporous after the oxidation heat treatment, which leads to very low specific surface areas and isotherms of type VI, which are typical for nonporous samples. The parameters are summarized in Table 56.

Table 56: Type of isotherm and specific surface area for the samples after treatment in hot air.

	Isotherm	BET specific surface area, m <sup>2</sup> /g	PSD maximum (micropores), nm
OX500PSZ700_N <sub>2</sub>	Type VI	8 ± 0.5	-
OX500PSZ700_NH <sub>3</sub> conc	Type VI	18 ± 2	-
OX500PSZ600_NH <sub>3</sub> conc	Type VI	6 ± 0.5	-

## 12.2.2 Treatment at 500 °C in steam

### 12.2.2.1 Mass change

The mass change of the samples tested on their oxidation stability using steam is listed in Table 57. Similar behaviour as in hot air can be observed. Because there is already only a minor amount of carbon left in the ammonia treated samples, there is not much carbon left to be removed by the reaction with oxygen anymore, which leads to an increase in mass by oxygen uptake. In case of the DVB sample, there is a high amount of free carbon in the sample, which can react with the steam, leading to a high mass loss.

Table 57: Mass change of the samples treated in hot steam for 12 h at 500 °C.

	$\Delta m, \%$
H <sub>2</sub> OPSZ600N2	1
H <sub>2</sub> OPSZ600NH3	7
H <sub>2</sub> OPSZ700NH3	-6
H <sub>2</sub> O80DVB600N2	-24

### 12.2.2.2 Elemental composition

The elemental composition of the samples after the oxidation under steam at 500 °C is given in Table 58. As for the samples treated in hot air, severe oxidation of all the samples can be observed.

Table 58: Elemental composition of the samples after the stability testing under air at 500 °C for 12 h; O, N, and C content are measured, Si+H is calculated as remainder to 100 wt%.

	O, wt%	N, wt%	C, wt%	Si+H, wt%
H <sub>2</sub> OPSZ600N2	22.0 ± 4.5	19.1 ± 2.4	7	52.9
H <sub>2</sub> OPSZ600NH3	29.6 ± 2.1	48.1 ± 1.9	3	19.3
H <sub>2</sub> OPSZ700NH3	27.4 ± 1.9	45.6 ± 3.9	4	23.0
H <sub>2</sub> O80DVB600N2	33.2 ± 2.8	42.6 ± 4.4	3	21.2

### 12.2.2.3 N<sub>2</sub>-Physisorption

According to the physisorption experiments, the samples are nonporous after the oxidation heat treatment, which leads to very low specific surface areas and isotherms of type VI, which are typical for nonporous samples. The parameters are summarized in Table 59. The only exception is the DVB sample, showing a type I and type IV isotherm (cf. Figure 173), which means that some porosity is retained even after treatment in moisture at elevated temperatures. The PSD of the sample is shown in Figure 174. Additionally, there are mesopores distributed over the whole pore size range up to 50 nm. The retained porosity is probably due to the reaction of the oxygen with free carbon instead of closure of the pores.

Table 59: Type of isotherm and specific surface area for the samples after treatment in hot air.

	<b>Isotherm</b>	<b>BET SSA, m<sup>2</sup>/g</b>	<b>PSD maximum (micropores), nm</b>	<b>V<sub>micro</sub> (cm<sup>3</sup>/g)</b>	<b>V<sub>meso</sub> (cm<sup>3</sup>/g)</b>
<b>H<sub>2</sub>OPSZ600N2</b>	Type VI	32 ± 2	-	-	
<b>H<sub>2</sub>OPSZ600NH3</b>	Type VI	12 ± 1	-	-	
<b>H<sub>2</sub>OPSZ700NH3</b>	Type VI	28 ± 4	-	-	
<b>H<sub>2</sub>O80DVB600N2</b>	Type I/IV	122 ± 6	~1 nm, 5-50 nm	0.05	0.05
<b>80DVB600 °C</b>	Type I/IV	164 ± 9	0.70	0.08	0.03

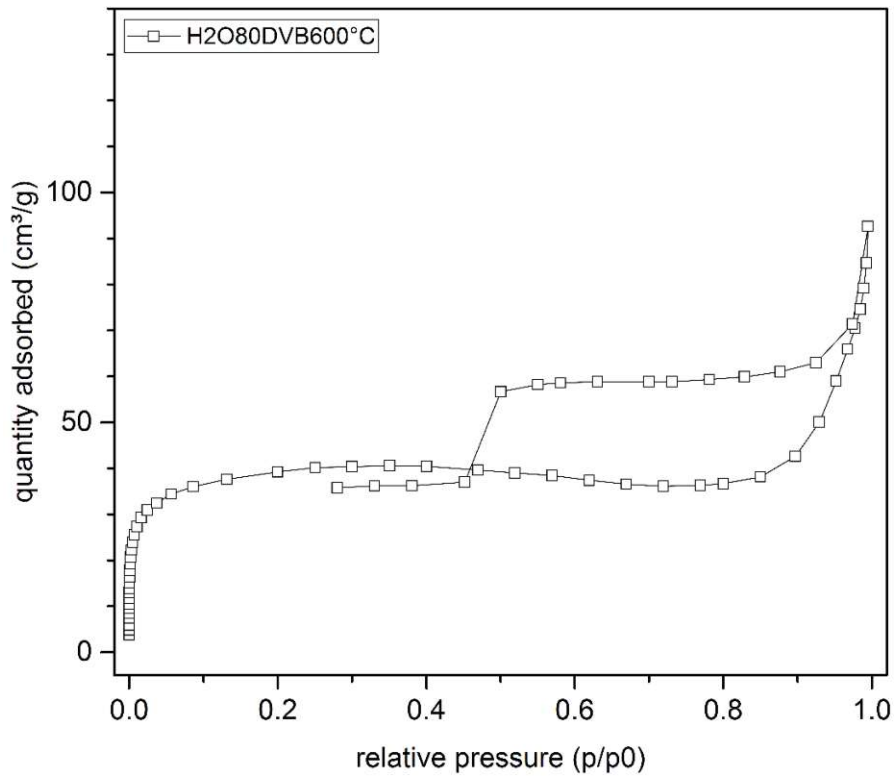


Figure 173:  $N_2$  physisorption isotherms of 80DVB after treatment in hot steam for 12 h at 500 °C.

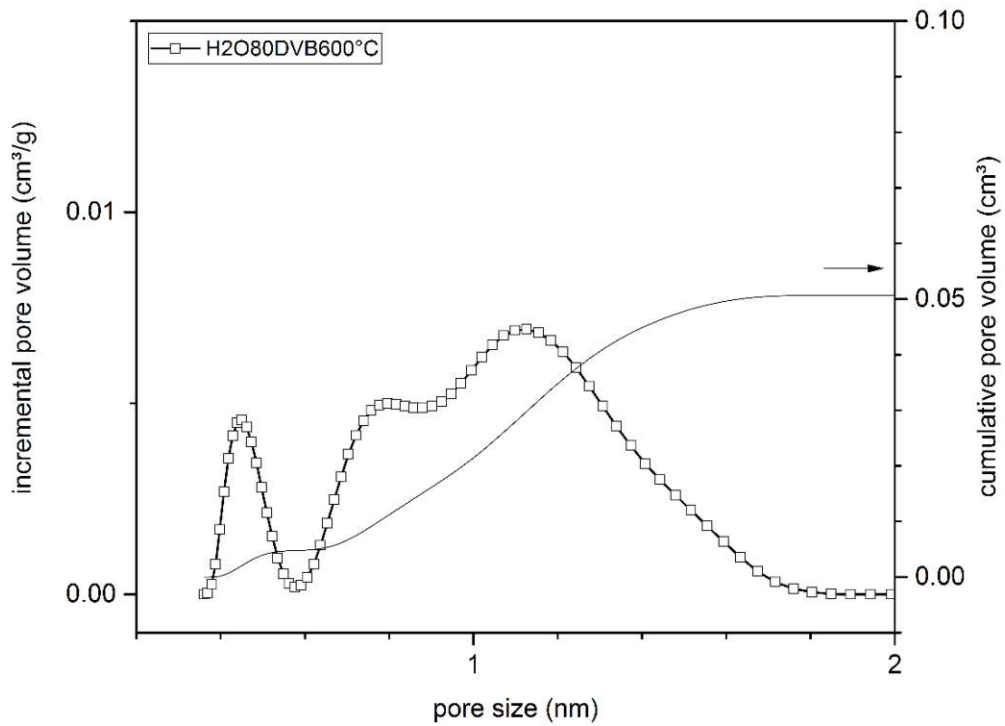


Figure 174: PSDs of 80DVB after treatment in hot steam for 12 h at 500 °C, calculated from the  $N_2$  physisorption data using NL-DFT.

### 12.3 Conclusions – Focus VII

Selected microporous samples were tested under conditions which simulate those of prospective applications, which means oxidizing atmosphere at elevated temperatures. Hot air and steam at 500 °C were chosen as testing conditions. Severe oxidation was found for all the samples leading to a complete removal of the carbon in most of the samples, except for OX500PSZ600N2 and H2OPSZ600N2. The reaction with oxygen probably leads to closure of the pores before the remaining carbon can be removed.

Due to the strong oxidation, the pores close and almost all samples show type VI isotherms, which are characteristic for nonporous samples, which is confirmed by very low specific surface areas. The only exception is the DVB containing sample 80DVB, which still shows porosity and a isotherm similar to that before oxidation treatment. The isotherm is a mixture between type I and type IV, which indicates the presence of micro- and mesopores in the material. This is probably due to reaction of the moisture primarily with the free carbon phase, leading to increased mesoporosity, while the micropores are rarely influenced.

## 13. SUMMARY

To clarify the reactions and mechanism that are responsible for the pore formation in PDCs, a variety of modifications of the precursor as well as processing parameters was successfully conducted during this thesis. Different focuses were set to test different hypotheses regarding the origin of pore formation.

### 13.1 Focus I – Unaltered Precursors

A full characterization of the two polymer precursors PSZ and PCS and their products if undergoing a standard procedure was done using various characterization methods.

According to TGA, the ceramic yield is around 75 % for both polymers. The polymer-ceramic-conversion takes place between 500-800 °C for PSZ and 450-700 °C for PCS if methane formation is used as indicator. Elemental composition and IR-spectra are comparable to the literature. Solid state NMR investigations showed that PSZ600°C consists of mixed Si-C-N-(H) tetrahedra. Surprisingly, there is also a free carbon phase present already at these pyrolysis temperatures. PCS600°C consists most likely of SiC<sub>4</sub> tetrahedra at this pyrolysis temperature; there was no free C phase found.

The N<sub>2</sub>-physisorption investigations showed the expected type I isotherm for the pyrolyzed PSZ600°C with a main pore size around 0.86 nm. The BET specific surface area of PSZ600°C is satisfactorily high at 195 ± 6 m<sup>2</sup>/g, which is also in accordance with the literature. [12] PCS in contrast follows a type II isotherm and according to this is non- or macroporous. The BET surface area is low; the pore size is in the mesoporous range. CO<sub>2</sub> physisorption showed no benefits in comparison to the nitrogen measurements, which is why N<sub>2</sub> is preferred as adsorbat, since it gives information about a wider pore size range.

### 13.2 Focus II and III - Modifications in the precursor stage

In this part, the influence of the molecular weight and copolymerisation with styrene (as possible porogen) were investigated. While the high molecular weight compounds yielded nonporous samples, the copolymers with styrene led to slight increases in the specific surface area and development of mesopores, which could make them interesting for asymmetric membrane materials (pore size gradient over the membrane). Due to the great effort going in the preparation of the copolymers, they are not suitable for an easy modification of the pore size towards an application as membran.



The second approach in the precursor stage was supposed to substitute the N-H group in the polymer-backbone by an organic group, that is supposed to serve as template for the pores and to split off during pyrolysis leading to a change in pore size. The main investigations were carried out using a benzyl group and a butyl group. Although a procedure for the substitution of the N-H group was successfully established and almost complete substitution was achieved in case of the aromatic group, there was no significant influence on the pore size. The TGA measurements revealed that the organic group decomposes already at temperatures below the start of the polymer-ceramic conversion of PSZ, which indicates that this temperature region  $> 300\text{ °C}$  is the crucial one regarding the pore formation.

### 13.3 Focus IV – Modifications in the crosslinking stage

Various changes were performed in the crosslinking step; a change in amount and type of initiator, change of crosslinking mechanism and the use of linker molecules. A linear and an aromatic linker were chosen, 1,5-hexadiene (HDE) and different concentrations of divinylbenzene (DVB).

Most of the variations showed no effect on the properties of the resulting ceramics regarding microporosity. The crosslinking mechanism itself has a minor impact on the pore generation in this specific polysilazane precursor. The addition of linker molecules during the crosslinking step, in contrast, led to changes in the decomposition behaviour of PSZ, which consequently caused differences in elemental composition, structural features present in the resulting ceramics and even to a shift of the PSD maximum, which lies in the micropore range, to lower values. (Figure 175) This effect is already present at understoichiometric amounts of DVB-linker present in the network, but becomes more obvious when looking at the overstoichiometric sample 80DVB. The pore size (PSDmax) is shifted from 0.86 nm to 0.70 nm, with the trends being confirmed also by SAXS investigations showing an even stronger shift from 0.70 nm to 0.48 nm for 2Rg. TGA-investigations revealed the influence of DVB on the decomposition behaviour of PSZ. The DVB molecules hinder specific reactions taking place during the pyrolytic conversion or shift them to higher temperatures. Almost no signal of ammonia, which is related to further crosslinking of the PSZ oligomers through transamination reactions, was found in TGA investigations. The reactions attributed to the polymer-ceramic conversion under formation of methane and hydrogen are shifted to higher temperatures. The presence of DVB therefore affects the elemental composition in two ways, directly by the increase of carbon content due to the DVB itself (which forms carbon rich domains in the ceramic) and on the other hand by a different decomposition behaviour leading

for example to a reduced loss of nitrogen and therefore an effectively higher nitrogen content in the PSZ domains. An explanation for the influence on the pore size shift could be that the reactions that are hindered are responsible for the pore formation, or that the change in elemental composition yields a different composition of structural elements, that are responsible for the pore formation and stability. Further pyrolysis experiments were conducted at temperatures between 400-700 °C. Since the porosity of the 80DVB sample collapses at the same temperatures as that of PSZ (above 600°C), a general shift of the pore evolution can most likely be excluded. The samples prepared at 400 °C showed similar pore size for both the 80DVB and PSZ sample. Since transamination reactions in PSZ have already taken place at these temperatures for pure PSZ, a different pore size should be found if transamination reactions themselves are the crucial factor for the pore generation in PSZ. These findings strengthen the assumption that the indirect change of composition of micropore forming entities leads to different pore sizes.

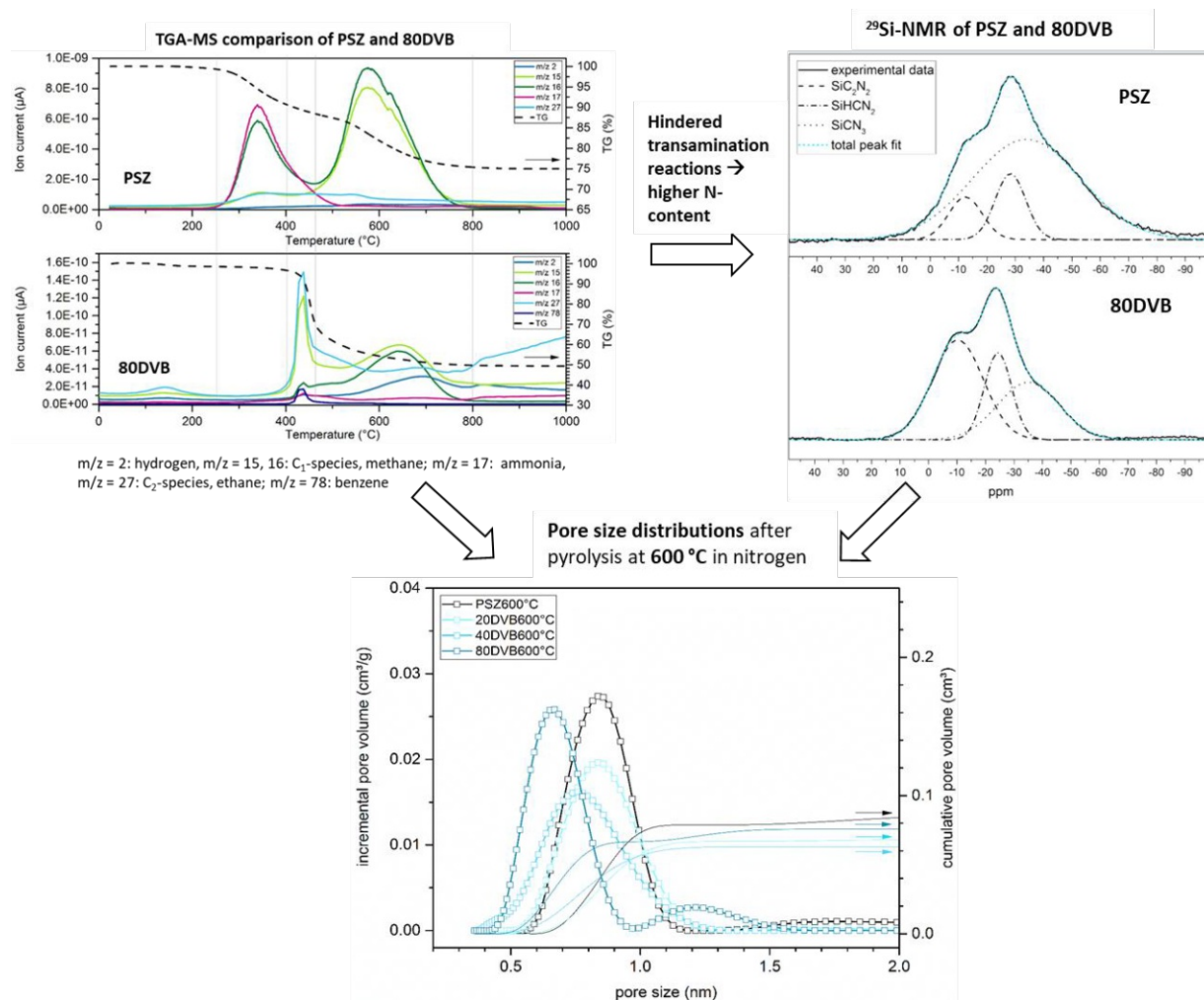


Figure 175: Summary of the results with DVB as linker molecule of Focus IV. The comparison of the TGA-MS investigations showing the absence of transamination reactions, the resulting more nitrogen rich structural features displayed by the solid state NMR and the resulting pore size distribution.

### 13.4 Focus V and VI – Effect of pyrolysis conditions on the microporosity

The use of the concentrated reactive ammonia atmosphere has a drastic effect on the properties of the resulting ceramics, both in terms of elemental composition and structural elements present in the ceramic, with corresponding change of pore size and stability region of the pores.

In contrast to pyrolysis in inert atmosphere, all materials are microporous in the investigated temperature region up to 900 °C (e.g. for PSZ, the micropores collapse above 600 °C in nitrogen atmosphere). It was found that carbon removal starts at temperatures around 500 °C and continues up to the maximum temperature of 900 °C investigated in this work. Simultaneously, the nitrogen content increases significantly. This incorporation of nitrogen already starts in the low temperature region for PCS and PSZPCS. This leads to the phenomenon that although the three materials have a different starting composition, the composition converges step by step, until at 900 °C the elemental composition is almost the same for the three materials.

The higher nitrogen and lower carbon content of the samples is also visible in the IR spectra, showing a shift of the broad maximum to higher wavenumbers, which is attributed most likely to Si-N bonds.

This is a strong indication that the theory of micropore forming entities, whose composition is responsible for pore size and stability, is true.

Another interesting finding is that the pore size distribution becomes bimodal at 900 °C in ammonia. The lower value (~ 0.65 nm) is lying below the pore size of the samples pyrolyzed at 600 °C (in both atmospheres), which could be caused by shrinkage of the pores due to e.g. viscous flow. The second pore size maximum is most likely caused by carbon removal, leading to an increase of pore size.

These results are summarized in Figure 176.

PDF investigations were conducted to obtain information about the interatomic distances present in selected samples. The three different materials PSZ, PCS and PSZPCS pyrolyzed in ammonia at 900 °C have the exact same maxima in the pair correlation function at 1.68 Å and 2.97 Å. By using a reactive atmosphere, the elemental composition of different starting materials can be adjusted and consequently also the interatomic distances in the materials. This could in further consequence confirm, that the elemental composition of the micropore forming entities is determining the pore size.

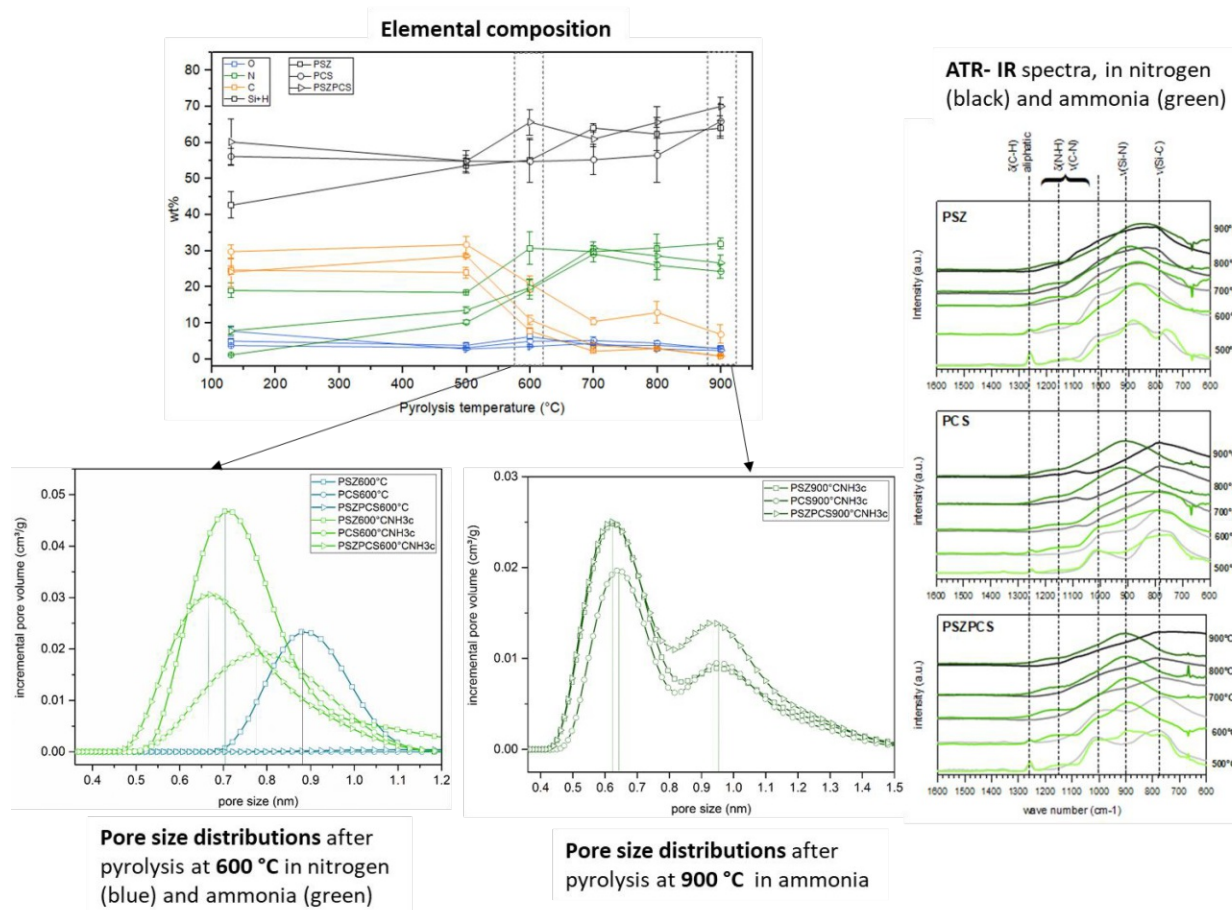


Figure 176: Summary of the results of Focus V showing the converging elemental composition of the three starting materials with increasing pyrolysis temperature in concentrated ammonia, the pore size distributions at 600 °C and 900 °C and the ATR-IR spectra in nitrogen and ammonia for all three materials.

The pore formation in the materials was investigated in detail using a recently introduced SAXS technique, enabling the in-situ observation of the pore formation under simulated pyrolysis conditions even under reactive atmospheres, revealing new information about this pore generation by making it possible to separate the initial formation during the heating period and the influence of the cooling period. The occurrence of cracks in the materials, which are closing again during the cooling period was found and is probably making the actual micropores inaccessible for the probe molecule during physisorption. (Figure 177) This assumption is strengthened by the second maximum in the PSD of the materials pyrolyzed in ammonia at 900 °C, which could be caused by the shrunk large pores/cracks that were found. (Figure 176) These findings would suggest an “in-place” pyrolysis of the membrane at separation conditions in case of applications in separation or catalysis processes.

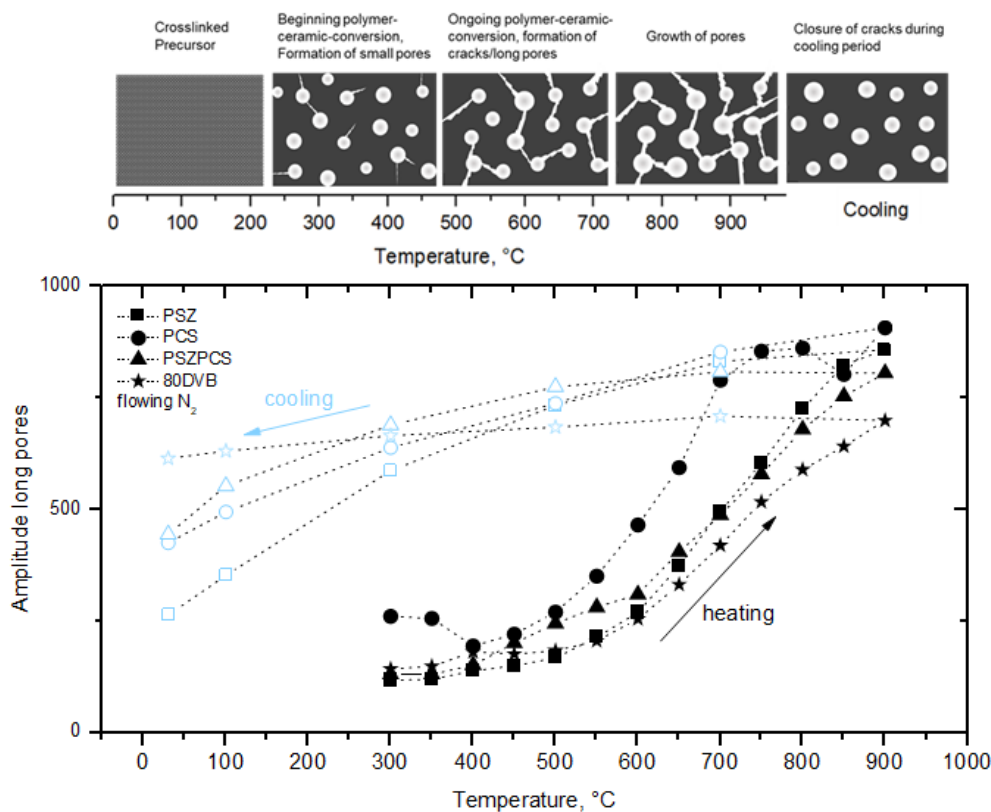


Figure 177: Schematic display of the pore formation in PDCs according to the in-situ SAXS data, with the amplitude of long pores over the whole temperature program calculated from the fitted SAXS data, representing the number of cracks present in the sample in nitrogen.

The two precursor types seem to act independent from each other in the mixture, which can be seen from the bimodal amplitudes and radii of small pores comparable to the two different maxima of the pure materials. (Figure 178) According to the in-situ SAXS results, it is therefore possible to get a bimodal pore size in the material by simply mixing two different precursors.

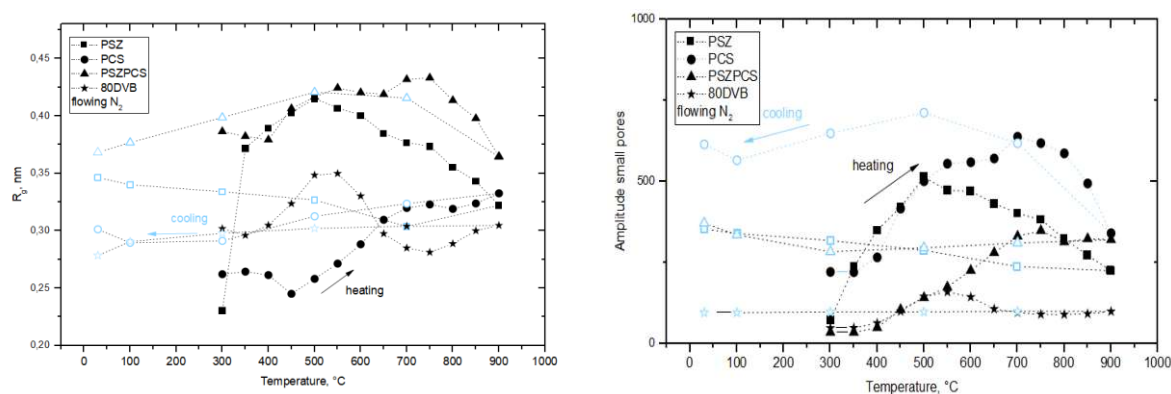


Figure 178:  $R_g$  and amplitude of these pores for PSZ, PCS, PSZPCS and 80DVB for pyrolysis in nitrogen.

### 13.5 Focus VII - Oxidation stability

The stability of selected samples against oxidation was tested at 500 °C in air and steam, but unfortunately showed closure of the pores in the various PSZ samples. Only the 80DVB600°C showed retained micro-and mesoporosity which is probably caused by favoured interaction of the oxygen with the free carbon phase which prevents the interaction with the micropores. DVB therefore leads to a possibility to shift the pore size maximum to lower values and additionally prevent closure of the porosity at least over a time period of 12 h.



## 14. CONCLUSIONS

Several hypotheses (Figure 1, taken from section 3) about the origin of micropores were tested by experiments in all processing stages of two commercially available polymer precursors.

- The micropore size is predefined by the structural elements in the precursor.
- The pores are caused simply by the release of gaseous species during the polymer-ceramic conversion, independent of the structural arrangements in the material. [26]
- There are certain micropore forming entities, which, depending on the elemental composition, yield different pore sizes. [14]
- Voids that are forming during crosslinking of the polymer chains are responsible for the micropores.

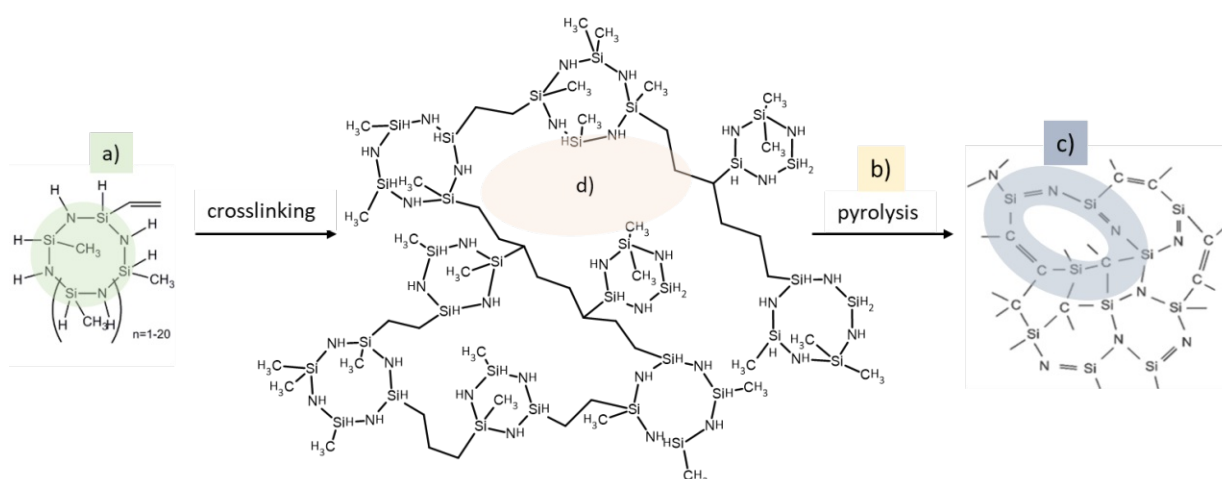


Figure 179: Schematic illustration of the processing stages from precursor polymer to PDC; the highlighted areas showing where the pores would originate from if a) they are already present in the precursor b) they were caused simply by the release of gaseous species during pyrolysis c) their size is defined by the composition of micropore forming entities d) they are caused by the voids that form during crosslinking.

Based on the results, some of the hypotheses can be excluded and some are strongly supported.

Various experiments contradict with hypothesis a), which assumes the pore size is already predefined by the structure of the precursor. The experiments in the precursor stage showed that the different structures (e.g. by introduction of organic side groups or increased molecular weight) had no influence on the resulting pore size. Pyrolysis experiments with ammonia showed that similar pore sizes can be obtained in the final ceramic independent of the starting precursor.



Also hypothesis d) is not supported by the experiments conducted in this work. Neither the increased amount of initiator, nor the change of crosslinking mechanisms, which lead to different bonds forming during crosslinking, showed a difference regarding microporosity in the final ceramics. Even the use of large linker molecules such as DVB did not increase, but even decrease the pore size compared to the benchmark sample. Therefore, it is unlikely that the voids formed by the crosslinking-bridges are the origin of the micropores in PDCs.

Hypothesis b) is very general and can therefore neither be excluded nor strengthened by the experiments.

The experiments in this thesis strongly indicate that there are, as according to hypothesis c), certain micropore forming entities in the amorphous ceramics, which depending on their composition define the pore size. The first hints were found during the crosslinking experiments with DVB as linker molecule. It indirectly influences the elemental composition, since transamination reactions during crosslinking are hindered, and the nitrogen content in the PSZ-domains stays higher. This consequently led to more nitrogen rich structural features, which were confirmed by  $^{29}\text{Si}$ -solid state NMR investigations. The pore size in the DVB-containing samples was smaller than in the ceramics derived from pure PSZ, which was found in the physisorption measurements as well as by SAXS investigations. The pyrolysis experiments with concentrated ammonia further strengthened the assumption of micropore forming entities in the ceramics, because independent of the starting precursor, the elemental composition and consequently the pore size can be adjusted. All three starting materials, PSZ, PCS and PSZPCS, had a similar pore size distribution after pyrolysis at  $900^\circ\text{C}$  and comparable elemental compositions. These findings were confirmed by PDF investigations, showing that the interatomic distances in the three samples after pyrolysis at  $900^\circ\text{C}$ , are the same.

## 15. OUTLOOK

Based on the findings of this work, further experiments to systematically vary the elemental composition of the precursor should be carried out. The focus should be set on the backbone of the precursor rather than on the side groups, since side groups are prone to react and split off during pyrolysis.

Using the newly introduced in-situ SAXS method, the formation of cracks and especially their closure should be investigated further, e.g. measurements up to 600 °C, to check whether the cracks close or stay open.

The next step would be the application of the material on a support structure to test its gas separation properties. Besides testing the materials themselves one by one, multilayer systems or in-situ fabrication of the membranes would be interesting:

- Multilayer systems: Using e.g. a solely PSZ based layer inbetween two DVB-PSZ-layers could protect the PSZ layer from oxidation and closure of the pores. The DVB containing layers react with the environment as “sacrificial” layer, which can lead to the formation of mesopores, keeping the PSZ layer accessible.
- Since the in-situ SAXS investigations showed the formation of cracks and their closure during cooling of the sample, an in-situ preparation of the membranes at their site of application (or a test rig) could clarify if the cracks are necessary to keep the pores accessible and consequently make the materials applicable at higher temperatures than they would be if manufactured ex-situ.

Overall, this work contributed towards a deeper understanding of the origin of micropore formation and therefore gave the future investigations a new direction/focus.

## REFERENCES

1. Seishi, Y., H. Josaburo, and O. Mamoru, *CONTINUOUS SILICON CARBIDE FIBER OF HIGH TENSILE STRENGTH*. Chemistry Letters, 1975. **4**(9): p. 931-934.
2. Sarkar, S. and L. Zhai, *Polymer-Derived Non-Oxide Ceramic Fibers*; Past, Present and Future. Materials Express, 2011. **1**(1): p. 18-29.
3. Barroso, G., et al., *Polymeric and ceramic silicon-based coatings – a review*. Journal of Materials Chemistry A, 2019. **7**(5): p. 1936-1963.
4. Riedel, R., et al., *Silicon-based polymer-derived ceramics: Synthesis properties and applications-A review*. Nippon Seramikkusu Kyokai Gakujutsu Ronbunshi/Journal of the Ceramic Society of Japan, 2006. **114**(1330): p. 425-444.
5. Schulz, M., *Polymer derived ceramics in MEMS/NEMS – a review on production processes and application*. Advances in Applied Ceramics, 2009. **108**(8): p. 454-460.
6. Colombo, P., et al., *Polymer-Derived Ceramics: 40 Years of Research and Innovation in Advanced Ceramics*. Journal of the American Ceramic Society, 2010. **93**(7): p. 1805-1837.
7. Kikuchi, E., et al., *Steam reforming of methane in membrane reactors: Comparison of electroless-plating and CVD membranes and catalyst packing modes*. Catalysis Today, 2000. **56**(1-3): p. 75-81.
8. Iwamoto, Y., *Precursors-derived ceramic membranes for high-temperature separation of hydrogen*. J. Ceram. Soc. Jpn., 2007. **115**(12): p. 947-954.
9. Prasad, R.M., *Polymer-Derived Microporous Ceramics for Membranes and Sensors for High Temperature Hydrogen Purification and Sensing*. 2012, TU Darmstadt. p. 230.
10. Verweij, H., Y.S. Lin, and J. Dong, *Microporous Silica and Zeolite Membranes for Hydrogen Purification*. MRS Bulletin, 2006. **31**(10): p. 756-764.
11. Wach, R.A., et al., *Molecular sieve SiC-based membrane for hydrogen separation produced by radiation curing of preceramic polymers*. Materials Science and Engineering: B, 2007. **140**(1-2): p. 81-89.
12. Konegger, T., et al., *Asymmetric polysilazane-derived ceramic structures with multiscalar porosity for membrane applications*. Microporous and Mesoporous Materials, 2016. **232**: p. 196-204.
13. Dismukes, J.P., et al., *Chemical Synthesis of Microporous Nonoxide Ceramics from Polysilazanes*. Chemistry of Materials, 1997. **9**(3): p. 699-706.
14. Schitco, C., et al., *NH<sub>3</sub>-assisted synthesis of microporous silicon oxycarbonitride ceramics from preceramic polymers: A combined N<sub>2</sub> and CO<sub>2</sub> adsorption and small angle X-ray scattering study*. Journal of Materials Chemistry A, 2015. **3**(2): p. 805-818.
15. Schitco, C., et al., *Silicon oxycarbonitrides synthesized by ammonia-assisted thermolysis route from polymers: A total X-ray scattering, solid-state NMR, and TEM structural study*. Journal of the European Ceramic Society, 2016. **36**(4): p. 979-989.
16. Seifollahi Bazarjani, M., et al., *High-Temperature Stability and Saturation Magnetization of Superparamagnetic Nickel Nanoparticles in Microporous Polysilazane-Derived Ceramics and their Gas Permeation Properties*. ACS Applied Materials & Interfaces, 2014. **6**(15): p. 12270-12278.
17. Seifollahi Bazarjani, M., et al., *Nanoporous Silicon Oxycarbonitride Ceramics Derived from Polysilazanes In situ Modified with Nickel Nanoparticles*. Chemistry of Materials, 2011. **23**(18): p. 4112-4123.
18. Zaheer, M., et al., *Robust Microporous Monoliths with Integrated Catalytically Active Metal Sites Investigated by Hyperpolarized <sup>129</sup>Xe NMR*. Chemistry of Materials, 2012. **24**(20): p. 3952-3963.
19. Wen, Q., et al., *Single-source-precursor synthesis of dense SiC/HfCxNi<sub>1-x</sub>-based ultrahigh-temperature ceramic nanocomposites*. Nanoscale, 2014. **6**(22): p. 13678-13689.
20. Corriu, R.J.P., et al., *Mechanism of pyrolysis of polycarbosilanes: Poly(silylethylene) and poly(dimethylsilylethylene)*. Organometallics, 1993. **12**(2): p. 454-462.
21. Bahloul, D., M. Pereira, and C. Gerardin, *Pyrolysis chemistry of polysilazane precursors to silicon carbonitride*. Journal of Materials Chemistry, 1997. **7**(1): p. 109-116.

22. Breuning, T., *Study of pyrolysis of polysilazane precursor in Si-C(O,N) system*. Journal of Analytical and Applied Pyrolysis, 1999. **49**(1–2): p. 43-51.
23. Li, Y., et al., *Thermal cross-linking and pyrolytic conversion of poly(ureamethylvinyl)silazanes to silicon-based ceramics*. Applied Organometallic Chemistry, 2001. **15**(10): p. 820-832.
24. Suda, H., et al., *Structural Evolution during Conversion of Polycarbosilane Precursor into Silicon Carbide-Based Microporous Membranes*. Journal of the Ceramic Society of Japan, 2006. **114**(1330): p. 539-544.
25. Chen, W. and J. Zhou, *Study on the pyrolysis behavior of polycarbosilane*. Journal of Wuhan University of Technology-Mater. Sci. Ed., 2015. **30**(4): p. 679-683.
26. Kroke, E., et al., *Silazane derived ceramics and related materials*. Materials Science and Engineering R: Reports, 2000. **26**(4): p. 197-199.
27. Okamura, K., et al., *SiC-based ceramic fibers prepared via organic-to-inorganic conversion process—a review*. Journal of the Ceramic Society of Japan, 2006. **114**(1330): p. 445-454.
28. Liew, L.-A., et al., *Fabrication of SiCN ceramic MEMS using injectable polymer-precursor technique*. Sensors and Actuators A: Physical, 2001. **89**(1): p. 64-70.
29. Liew, L.-A., et al., *Fabrication of SiCN MEMS by photopolymerization of pre-ceramic polymer*. Sensors and Actuators A: Physical, 2002. **95**(2): p. 120-134.
30. Yang, H., et al., *Fabrication of High Performance Ceramic Microstructures from a Polymeric Precursor Using Soft Lithography*. Advanced Materials, 2001. **13**(1): p. 54-58.
31. Viard, A., P. Miele, and S. Bernard, *Polymer-derived ceramics route toward SiCN and SiBCN fibers: From chemistry of polycarbosilazanes to the design and characterization of ceramic fibers*. Journal of the Ceramic Society of Japan, 2016. **124**(10): p. 967-980.
32. Cross, T., et al. *Fabrication process for ultra high aspect ratio polysilazane-derived MEMS*. in *Proceedings of the IEEE Micro Electro Mechanical Systems (MEMS)*. 2002.
33. Bahloul, D., et al., *Preparation of Silicon Carbonitrides from an Organosilicon Polymer: I, Thermal Decomposition of the Cross-linked Polysilazane*. Journal of the American Ceramic Society, 1993. **76**(5): p. 1156-1162.
34. Seitz, J., et al., *Structural investigations of Si/C/N-ceramics from polysilazane precursors by nuclear magnetic resonance*. Journal of the European Ceramic Society, 1996. **16**(8): p. 885-891.
35. Greil, P., *Active-Filler-Controlled Pyrolysis of Preceramic Polymers*. Journal of the American Ceramic Society, 1995. **78**(4): p. 835-848.
36. Greil, P., *Polymer-filler derived ceramics with hierarchical microstructures*, in *Key Engineering Materials*. 1999. p. 339-346.
37. Riedel, R., et al., *Polymer-derived Si-based bulk ceramics, part I: Preparation, processing and properties*. Journal of the European Ceramic Society, 1995. **15**(8): p. 703-715.
38. Clarke, D.R. and S.R. Phillpot, *Thermal barrier coating materials*. Materials Today, 2005. **8**(6): p. 22-29.
39. Günthner, M., et al., *Advanced coatings on the basis of Si(C)N precursors for protection of steel against oxidation*. Journal of the European Ceramic Society, 2009. **29**(10): p. 2061-2068.
40. Lee, K.N., *Current status of environmental barrier coatings for Si-Based ceramics*. Surface and Coatings Technology, 2000. **133–134**: p. 1-7.
41. Biasetto, L., *Functional ceramic foams from preceramic polymers*. 2007.
42. Colombo, P. and E. Bernardo, *Macro- and micro-cellular porous ceramics from preceramic polymers*. Composites Science and Technology, 2003. **63**(16): p. 2353-2359.
43. Kumar, B.V.M. and Y.W. Kim, *Processing of polysiloxane-derived porous ceramics: A review*. Science and Technology of Advanced Materials, 2010. **11**(4): p. 044303.
44. Lu, K., *Porous and high surface area silicon oxycarbide-based materials—A review*. Materials Science and Engineering: R: Reports, 2015. **97**: p. 23-49.
45. Vakifahmetoglu, C., D. Zeydanli, and P. Colombo, *Porous polymer derived ceramics*. Materials Science and Engineering: R: Reports, 2016. **106**: p. 1-30.
46. Obmann, R., et al., *Porous polysilazane-derived ceramic structures generated through photopolymerization-assisted solidification templating*. Journal of the European Ceramic Society, 2019. **39**(4): p. 838-845.

47. Xue, F., et al., *Porous SiC ceramics with dendritic pore structures by freeze casting from chemical cross-linked polycarbosilane*. *Ceramics International*, 2018. **44**(6): p. 6293-6299.
48. Zhang, H., et al., *Hierarchically ordered micro/meso/macroporous polymer-derived ceramic monoliths fabricated by freeze-casting*. *Journal of the European Ceramic Society*, 2016. **36**(1): p. 51-58.
49. Mikl, G., et al., *Pore Morphology Tailoring in Polymer-Derived Ceramics Generated through Photopolymerization-Assisted Solidification Templating*. *Advanced Engineering Materials*, 2019. **21**(6): p. 1900052.
50. *Structural Ceramics Derived from a Pre ceramic Polymer*, in *14th Annual Conference on Composites and Advanced Ceramic Materials: Ceramic Engineering and Science Proceedings*. p. 1387-1394.
51. Schonfeler, H., F. Aldinger, and R. Riedel, *Silicon carbonitrides-a novel class of materials*. *Journal De Physique*, 1993. **3**(7 pt 2): p. 1293-1298.
52. Riedel, R., et al., *Synthesis of dense silicon-based ceramics at low temperatures*. *Nature*, 1992. **355**(6362): p. 714-717.
53. Erny, T., et al., *Microstructure Development of Oxycarbide Composites during Active-Filler-Controlled Polymer Pyrolysis*. *Journal of the American Ceramic Society*, 1993. **76**(1): p. 207-213.
54. Seibold, M. and P. Greil, *Thermodynamics and microstructural development of ceramic composite formation by active filler-controlled pyrolysis (AFCOP)*. *Journal of the European Ceramic Society*, 1993. **11**(2): p. 105-113.
55. Hahn, B., et al., *ESR investigation of MoSi<sub>2</sub> powders used as reactive fillers in polymer-derived ceramics*. *Colloids and Surfaces A: Physicochemical and Engineering Aspects*, 1996. **115**: p. 291-295.
56. Greil, P., *Near Net Shape Manufacturing of Polymer Derived Ceramics*. *Key Engineering Materials*, 1997. **132-136**: p. 1981-1984.
57. Greil, P., *Near Net Shape Manufacturing of Polymer Derived Ceramics*. *Journal of the European Ceramic Society*, 1998. **18**(13): p. 1905-1914.
58. Scheffler, M., et al., *Si-C-O Ceramics from Pre ceramic Polymers: Reaction Mechanism between the Si-Filler and the Polymer Derived Matrix during Pyrolytic Conversion*. *Key Engineering Materials*, 2001. **206-213**: p. 289-292.
59. Xie, Z., S. Wang, and Z. Chen, *Active Filler (Aluminum-Aluminum Nitride) Controlled Polycarbosilane Pyrolysis*. *Journal of Inorganic and Organometallic Polymers and Materials*, 2006. **16**(1): p. 69-81.
60. Mayer, J., et al., *Polymer-derived Si-based bulk ceramics, part II: Microstructural characterisation by electron spectroscopic imaging*. *Journal of the European Ceramic Society*, 1995. **15**(8): p. 717-727.
61. Blum, Y.D., R.M. Platz, and E.J. Crawford, *Glass Strengthening by Polymer-Derived Ceramic Coatings*. *Journal of the American Ceramic Society*, 1990. **73**(1): p. 170-172.
62. Anderson, H.U., et al., *Polymeric synthesis of perovskite powders and films*. *NIST Special Publication*, 1991(804): p. 179-184.
63. Ueno, K., S. Kose, and M. Kinoshita, *Toughness enhancement by polycarbosilane coating on SiC whiskers incorporated in Si<sub>3</sub>N<sub>4</sub> matrix composite*. *Journal of Materials Science*, 1993. **28**(21): p. 5770-5774.
64. Bill, J. and D. Heimann, *Polymer-derived ceramic coatings on C/C-SiC composites*. *Journal of the European Ceramic Society*, 1996. **16**(10): p. 1115-1120.
65. Petersen, R., et al., *Pyrolysis of Poly(ferrocenylsilanes): Synthesis and Characterization of Ferromagnetic Transition-Metal-Containing Ceramics and Molecular Depolymerization Products*. *Chemistry of Materials*, 1995. **7**(11): p. 2045-2053.
66. Burns, G.T., et al., *High-temperature chemistry of the conversion of siloxanes to silicon carbide*. *Chemistry of Materials*, 1992. **4**(6): p. 1313-1323.
67. Su, K., et al., *Synthesis, characterization, and ceramic conversion reactions of borazine-modified hydridopolysilazanes: new polymeric precursors to silicon nitride carbide boride (SiNCB) ceramic composites*. *Chemistry of Materials*, 1993. **5**(4): p. 547-556.



68. Xu, Y., et al., *Microstructure and Microchemistry of Polymer-Derived Crystalline SiC Fibers*. Journal of the American Ceramic Society, 1993. **76**(12): p. 3034-3040.
69. Dando, N.R., et al., *Methylhydridopolysilazane and its pyrolytic conversion to silicon nitride-silicon carbide (Si<sub>3</sub>N<sub>4</sub>/SiC) ceramics*. Chemistry of Materials, 1993. **5**(11): p. 1624-1630.
70. Laine, R.M. and F. Babonneau, *Pre-ceramic polymer routes to silicon carbide*. Chemistry of Materials, 1993. **5**(3): p. 260-279.
71. Song, Y.C., et al., *Synthesis and pyrolysis of polysilazane as the precursor of Si<sub>3</sub>N<sub>4</sub>/SiC ceramic*. Journal of Materials Science, 1994. **29**(21): p. 5745-5756.
72. Toreki, W., et al., *Polymer-derived silicon carbide fibers with low oxygen content and improved thermomechanical stability*. Composites Science and Technology, 1994. **51**(2): p. 145-159.
73. Monthieux, M. and O. Delverdier, *Thermal behavior of (organosilicon) polymer-derived ceramics. V: Main facts and trends*. Journal of the European Ceramic Society, 1996. **16**(7): p. 721-737.
74. Liu, Q., et al., *Synthesis of Polycarbosilane/Siloxane Hybrid Polymers and Their Pyrolytic Conversion to Silicon Oxycarbide Ceramics*. Chemistry of Materials, 1997. **9**(11): p. 2434-2441.
75. Baldus, H.P. and M. Jansen, *Novel High-Performance Ceramics - Amorphous Inorganic Networks from Molecular Precursors*. Angewandte Chemie (International Edition in English), 1997. **36**(4): p. 329-343.
76. Kleebe, H.-J., *Microstructure and Stability of Polymer-Derived Ceramics; the Si-C-N System*. physica status solidi (a), 1998. **166**(1): p. 297-313.
77. Gabriel, A.O., et al., *Thermal Decomposition of Poly(methylsilsesquicarbodiimide) to Amorphous Si-C-N Ceramics*. Chemistry of Materials, 1999. **11**(2): p. 412-420.
78. Delverdier, O., et al., *Thermal behavior of polymer-derived ceramics. IV. SiCNO fibers from an oxygen-cured polycarbosilazane*. Journal of the European Ceramic Society, 1994. **14**(4): p. 313-325.
79. Ziegler, G., et al., *Synthesis, microstructure and properties of SiCN ceramics prepared from tailored polymers*. Materials Chemistry and Physics, 1999. **61**(1): p. 55-63.
80. Iwamoto, Y., et al., *Crystallization Behavior of Amorphous Silicon Carbonitride Ceramics Derived from Organometallic Precursors*. Journal of the American Ceramic Society, 2001. **84**(10): p. 2170-2178.
81. Wideman, T., et al., *Reactions of Monofunctional Boranes with Hydridopolysilazane: Synthesis, Characterization, and Ceramic Conversion Reactions of New Processible Precursors to SiNCB Ceramic Materials*. Chemistry of Materials, 1997. **9**(10): p. 2218-2230.
82. Aldinger, F., M. Weinmann, and J. Bill, *Precursor-derived Si-B-C-N ceramics*, in *Pure and Applied Chemistry*. 1998. p. 439.
83. Müller, A., et al., *Correlation of boron content and high temperature stability in Si-B-C-N ceramics*. Journal of the European Ceramic Society, 2000. **20**(14): p. 2655-2659.
84. Schmidt, W.R., et al., *Pyrolysis chemistry of an organometallic precursor to silicon carbide*. Chemistry of Materials, 1991. **3**(2): p. 257-267.
85. Gérardin, C., F. Taulelle, and D. Bahloul, *Pyrolysis chemistry of polysilazane precursors to silicon carbonitride: Part 2. - Solid-state NMR of the pyrolytic residues*. Journal of Materials Chemistry, 1997. **7**(1): p. 117-126.
86. Bao, X. and M.J. Edirisinghe, *Polycyclodisilazane: a new polymeric precursor for silicon nitride-based ceramics*. Journal of Materials Chemistry, 2000. **10**(2): p. 395-401.
87. Maddocks, A.R., et al., *Heterogeneously catalysed crosslinking of polycarbosilane with divinylbenzene*. Journal of Materials Science, 2008. **43**(8): p. 2666-2674.
88. Liu, Q., et al., *Investigation of the Pyrolytic Conversion of Poly(silylenemethylene) to Silicon Carbide*. Chemistry of Materials, 1999. **11**(8): p. 2038-2048.
89. Reid, A.W., B. Rand, and R.J.P. Emsley. *Nanoporosity in ceramics from polymeric precursors*. in *Materials Research Society Symposium - Proceedings*. 1994.
90. Sorarù, G.D., et al., *Role of Precursor Molecular Structure on the Microstructure and High Temperature Stability of Silicon Oxycarbide Glasses Derived from Methylene-Bridged Polycarbosilanes*. Chemistry of Materials, 1998. **10**(12): p. 4047-4054.

91. Schmidt, W.R., et al., *Silicon Nitride Derived from an Organometallic Polymeric Precursor: Preparation and Characterization*. Journal of the American Ceramic Society, 1990. **73**(8): p. 2412-2418.
92. Galusek, D., et al., *In-Situ Carbon Content Adjustment in Polysilazane Derived Amorphous SiCN Bulk Ceramics*. Journal of the European Ceramic Society, 1999. **19**(10): p. 1911-1921.
93. Prasad, R.M., et al., *Thermal decomposition of carbon-rich polymer-derived silicon carbonitrides leading to ceramics with high specific surface area and tunable micro- and mesoporosity*. Journal of the European Ceramic Society, 2012. **32**(2): p. 477-484.
94. Williams, H.M., et al., *High temperature ceramics for use in membrane reactors: the development of microporosity during the pyrolysis of polycarbosilanes*. Journal of Materials Chemistry, 2002. **12**(12): p. 3754-3760.
95. Maddocks, A.R., et al., *Synthesis of nanoporous silicon carbide via the preceramic polymer route*. Materials Chemistry and Physics, 2009. **113**(2-3): p. 861-867.
96. Colombo, P., *Engineering porosity in polymer-derived ceramics*. Journal of the European Ceramic Society, 2008. **28**(7): p. 1389-1395.
97. Colombo, P. and J.R. Hellmann, *Ceramic foams from preceramic polymers*. Materials Research Innovations, 2002. **6**(5-6): p. 260-272.
98. Colombo, P., *Conventional and novel processing methods for cellular ceramics*. Philosophical Transactions of the Royal Society A: Mathematical, Physical and Engineering Sciences, 2006. **364**(1838): p. 109-124.
99. Vakifahmetoglu, C., et al., *Highly porous macro- and micro-cellular ceramics from a polysilazane precursor*. Ceramics International, 2009. **35**(8): p. 3281-3290.
100. Vakifahmetoglu, C. and P. Colombo, *A Direct Method for the Fabrication of Macro-Porous SiOC Ceramics from Preceramic Polymers*. Advanced Engineering Materials, 2008. **10**(3): p. 256-259.
101. Fukushima, M. and P. Colombo, *Silicon carbide-based foams from direct blowing of polycarbosilane*. Journal of the European Ceramic Society, 2012. **32**(2): p. 503-510.
102. Naviroj, M., et al., *Directionally aligned macroporous SiOC via freeze casting of preceramic polymers*. Journal of the European Ceramic Society, 2015. **35**(8): p. 2225-2232.
103. Wang, X., et al., *Additive manufacturing of ceramics from preceramic polymers: A versatile stereolithographic approach assisted by thiol-ene click chemistry*. Additive Manufacturing, 2019. **27**: p. 80-90.
104. Wei, L., et al., *Fabrication of SiOC ceramic with cellular structure via UV-Assisted direct ink writing*. Ceramics International, 2020. **46**(3): p. 3637-3643.
105. Li, S., et al., *Additive manufacturing of SiBCN/Si<sub>3</sub>N<sub>4</sub>w composites from preceramic polymers by digital light processing*. RSC Advances, 2020. **10**(10): p. 5681-5689.
106. Espinal, L., *Porosity and Its Measurement*, in *Characterization of Materials*. p. 1-10.
107. *MANUAL OF SYMBOLS AND TERMINOLOGY FOR PHYSICOCHEMICAL QUANTITIES AND UNITS*. 2001; Available from: [https://old.iupac.org/reports/2001/colloid\\_2001/manual\\_of\\_s\\_and\\_t/node16.html](https://old.iupac.org/reports/2001/colloid_2001/manual_of_s_and_t/node16.html). (last accessed 02/2020)
108. Thommes, M., et al., *Physisorption of gases, with special reference to the evaluation of surface area and pore size distribution (IUPAC Technical Report)*. Pure and Applied Chemistry, 2015. **87**(9-10): p. 1051-1069.
109. Brunauer, S., P.H. Emmett, and E. Teller, *Adsorption of Gases in Multimolecular Layers*. Journal of the American Chemical Society, 1938. **60**(2): p. 309-319.
110. Anton Paar, W. *BET Theory*. Available from: <https://wiki.anton-paar.com/at-de/bet-theorie/>. (last accessed 02/2020)
111. Rouquerol, J., et al., *Recommendations for the characterization of porous solids (Technical Report)*, in *Pure and Applied Chemistry*. 1994. p. 1739.
112. Seaton, N.A., J.P.R.B. Walton, and N. Quirke, *A new analysis method for the determination of the pore size distribution of porous carbons from nitrogen adsorption measurements*. Carbon, 1989. **27**(6): p. 853-861.



113. Landers, J., G.Y. Gor, and A.V. Neimark, *Density functional theory methods for characterization of porous materials*. Colloids and Surfaces A: Physicochemical and Engineering Aspects, 2013. **437**: p. 3-32.
114. Landers, J., G. Gor, and A. Neimark, *Density functional theory methods for characterization of porous materials*. Colloids and Surfaces A: Physicochemical and Engineering Aspects, 2013. **437**: p. 3-32.
115. Wiki, A.P. *SAXS nanostructure analysis*. Available from: <https://wiki.anton-paar.com/en/saxs-nanostructure-analysis/>. (last accessed 02/2020)
116. Wu, Z. and X. Xing, *Small Angle X-ray Scattering and Its Applications*, in *Synchrotron Radiation Applications*. p. 225-285.
117. Schmidt, P.W., et al., *Small-angle x-ray scattering from the surfaces of reversed-phase silicas: Power-law scattering exponents of magnitudes greater than four*. The Journal of Chemical Physics, 1991. **94**(2): p. 1474-1479.
118. Porod, G., *Die Röntgenkleinwinkelstreuung von dichtgepackten kolloiden Systemen*. Kolloid-Zeitschrift, 1951. **124**(2): p. 83-114.
119. Konegger, T., C.C. Tsai, and R.K. Bordia, *Preparation of polymer-derived ceramic coatings by dip-coating*, in *Materials Science Forum*. 2015. p. 645-652.
120. Kaur, S., R. Riedel, and E. Ionescu, *Pressureless fabrication of dense monolithic SiC ceramics from a polycarbosilane*. Journal of the European Ceramic Society, 2014. **34**(15): p. 3571-3578.
121. Beaucage, G. and D.W. Schaefer, *Structural studies of complex systems using small-angle scattering: a unified Guinier/power-law approach*. Journal of Non-Crystalline Solids, 1994. **172-174**: p. 797-805.
122. Kinning, D.J. and E.L. Thomas, *Hard-sphere interactions between spherical domains in diblock copolymers*. Macromolecules, 1984. **17**(9): p. 1712-1718.
123. Kenneth J.D. MacKenzie, M.E.S., *Multinuclear Solid-State Nuclear Magnetic resonance of Inorganic Materials*. Vol. 6. 2002: Pergamon materials series.
124. Toni, B., *Fabrication of porous ceramics by phase separation*. 2017, TU Wien.
125. Nghiem, Q.D., C.T. Nguyen, and D.-P. Kim, *Controlled/living radical polymerization of vinylcyclosilazane by RAFT process and their block copolymers*. Journal of Polymer Science Part A: Polymer Chemistry, 2008. **46**(13): p. 4594-4601.
126. Flores, O., et al., *Selective cross-linking of oligosilazanes to tailored meltable polysilazanes for the processing of ceramic SiCN fibres*. Journal of Materials Chemistry A, 2013. **1**(48): p. 15406-15415.
127. Li, Y.H., X.D. Li, and D.P. Kim, *Acrylation of polyvinylsilazane with allyl bromide for an UV photosensitive inorganic polymer*. Journal of Organometallic Chemistry, 2007. **692**(23): p. 5303-5306.
128. Moore, J.L., S.M. Taylor, and V.A. Soloshonok, *An efficient and operationally convenient general synthesis of tertiary amines by direct alkylation of secondary amines with alkyl halides in the presence of Huenig's base*. Arkivoc, 2005. **2005**(6): p. 287-292.
129. Nebel, M., *Modification of Preceramic Polymers and Investigation of their Porosity Development*. 2019, TU Wien.
130. Liu, G., et al., *Electrochemical performance of DVB-modified SiOC and SiCN polymer-derived negative electrodes for lithium-ion batteries*. Electrochimica Acta, 2013. **106**(Supplement C): p. 101-108.
131. *NIST Webbook*. Available from: <https://webbook.nist.gov/chemistry/>. (last accessed 05/2021)
132. Zhang, Q., et al., *Synthesis and structural evolution of dual-boron-source-modified polysilazane derived SiBCN ceramics*. New Journal of Chemistry, 2016. **40**(8): p. 7034-7042.
133. Zera, E., et al., *Out-of-furnace oxidation of SiCN polymer-derived ceramic aerogel pyrolyzed at intermediate temperature (600–800 °C)*. Journal of the European Ceramic Society, 2016. **36**(3): p. 423-428.
134. <https://de.wikipedia.org/wiki/Luftfeuchtigkeit>. (last accessed 10/2019)

**CV - CHRISTINA DRECHSEL**

### Personal Information

---

**Acad. Degree:** Dipl.Ing. BSc.  
**Date of Birth:** 30 June 1992  
**Citizenship:** Austria

### Education

---

- Since 10/2016: **Doctoral programme in Technical Sciences**, TU Wien – Technical University of Vienna, Institute of Chemical Technologies and Analytics, Austria  
 Specialization: Fundamental research in the field of polymer-derived ceramics  
 Title of the PhD project: *Micropore evolution in polymer-derived ceramics with tailored gas separation functionality*
- 02/2018 - 05/2018: **Research stay at the Clemson University (USA)**, Department of Materials Science and Engineering
- 04/2014 - 09/2016: **Master's program Technical Chemistry**, TU Wien – Technical University of Vienna, passed with distinction, Specialization: High Performance Materials  
 Title of the Master's Thesis: *Polymer-derived ceramic layer structures with multi-scale porosity*
- 10/2010 - 04/2014: **Bachelor's program Technical Chemistry**, TU Wien – Technical University of Vienna  
 Title of the Bachelor's Thesis: *Influence of a precipitation heat treatment on the thermal and electrical conductivity of AgSi- and AlSi-alloys*
- 09/2002 - 06/2010: **AHS Friesgasse**, Schulzentrum der SSND, 1150 Vienna, Austria

### Work Experience

---

- Since 04/2020: Chemist R&D, Materialdevelopment for Semperform IM/CM, Semperit Technische Produkte GmbH, Austria
- 10/2016-03/2020: Research assistant, TU Wien – Technical University of Vienna, Institute of Chemical Technologies und Analytics  
 Title of the project: *Micropore development in polymer-derived ceramics (FWF)*
- 07/2013 - 08/2013: Employment at the TU Wien – Technical University of Vienna, Institute of Chemical Technologies und Analytics  
 Research Focus: Preparation and characterization of Al- and Ag-diamond composites

Vienna, 02 May 2021